UNIVERSIDADE FEDERAL DO RIO GRANDE DO SUL
INSTITUTO DE PESQUISAS HIDRÁULICAS

Dinâmica Espacial e Temporal do Metabolismo Aquático em Sistemas Subtropicais

José Rafael de Albuquerque Cavalcanti

Tese submetida ao Programa de Pós-Graduação em Recursos Hídricos e Saneamento Ambiental da Universidade Federal do Rio Grande do Sul como requisito parcial para a obtenção do título de Doutor em Recursos Hídricos e Saneamento Ambiental

Orientador: David da Motta-Marques
Co-Orientador: Carlos Ruberto Fragoso Júnior

Banca Examinadora

Prof. Dr. Juan Martin Bravo	IPH - UFRGS
Prof. Dr. Daniel G. Allasia	UFSM
Prof. Dra. Marie-Paule Bonnet	IRD - França

Porto Alegre, Março de 2017

Dinâmica Espacial e Temporal do Metabolismo Aquático em Sistemas Subtropicais

José Rafael de Albuquerque Cavalcanti

Trabalho Aprovado. Porto Alegre, Março de 2017

Banca Examinadora

Prof. Dr. David da Motta-Marques
Orientador

Prof. Dr. Carlos Ruberto Fragoso Júnior
Co-Orientador

Prof. Dr. Juan Martin Bravo

Prof. Dr. Daniel G. Allasia

Prof. Dra. Marie-Paule Bonnet

Porto Alegre, Março de 2017

"I used to think the top environmental problems were biodiversity loss, ecosystem collapse and climate change. I thought that with 30 years of good science we could address those problems. But I was **wrong**.
The top environmental problems are selfishness, greed, and apathy. And to deal with those we need a spiritual and cultural transformation...
... And we scientists **don't know** how to do that."

- Gus Speth

Agradecimentos

Existem muitos a quem devo agradecer. Cada um que entra no nosso caminho, seja por um breve momento ou compartilhando momentos importantes, é parte daquilo que nos faz chegar ao nosso objetivo. Sendo assim, começo meus agradecimentos pelo nosso pai, que mesmo escrevendo por linhas tortas nos permite sempre alcançar nosso potencial. O caminho para chegar até aqui foi difícil, mas basta um dia de sol ou uma noite com chuva na janela para lembrarmos que ainda tem muita coisa boa além dos problemas e preocupações diárias.

É difícil escolher alguém para vir depois, visando evitar mágoas vou agradecer a CAPES e ao CNPq pelos recursos que me foram disponibilizados e que me permitiram dedicação integral ao desenvolvimento desta tese. Ainda gostaria de agradecer ao IPH pela estrutura e apoio ao longo do trabalho.

Não posso demorar a agradecer meus orientadores, Prof. David da Motta Marques e Prof. Carlos Ruberto Fragoso Junior, por toda a atenção e ensinamentos ao longo deste trabalho. Hoje sinto nosso grupo não apenas com estudantes e alunos, mas com parceiros de trabalho com visões e vontades similares entre si. Estamos crescendo e cada vez mais me sinto grato por fazer parte desta história. Ainda sobre professores, não posso esquecer de agradecer aos amigos que também fazem parte do nosso grupo ou do IPH: Prof. Juan Martin, Profa. Lúcia Rodrigues, Profa. Luciana Cardoso, Profa. Luciane Crossetti, Prof. Walter Collischonn, Prof. Rodrigo Paiva, Profa. Edith Beatriz e tantos outros que me auxiliam ao longo desses anos de casa. Ainda no tópico "professores", tenho que agradecer ao Prof. Vincezo Casulli e ao prof. Michael Dumbser pelo apoio e ensinamentos dados ao longo dos seis meses que passei em Trento.

Agora vem a hora de agradecer aos amigos. São tantos que corro o risco de esquecer alguém importante aqui. Caso isto ocorra, espero que o esquecido(a) seja amigo(a) o suficiente para entender sua importância apesar de não estar explícita aqui. Vou começar pelos amigos de IPH, que dividiram comigo as noites sem dormir estudando, a hora do café entre as aulas, os churrascos divertidos e os jogos de bola. Amigos como: Paulo, Rosane, Mino, Fernando Fan, Fernando Bike, Ada, Carlos Henrique, Benício, Erick, Carolina, Fran, Nestor, Fernando, Gabriel, Leonardo, Felipe, Marco e outros que me foram importantes ao longo deste caminho. Agradeço também aos companheiros de grupo de pesquisa: Juliana, Andressa, Mônica, Marla, Luidi, Thiago, Rafa Souza, Mauricio, Vinicius, Daniela e Glaucia pelas discussões e o apoio nos momentos difíceis. Extendo os agradecimentos também aos amigos

Marcus, Marlos, Publius, Victor, Samuca, Rodrigos, Saed e Aquiles, pelas boas horas de lazer que tivemos juntos e viagens inesquecíveis!

Os agradecimentos mais especiais ficam para a minha família, principalmente meus pais, Claudius e Liliane que suportaram toda a distância e nunca deixaram de apoiar meus sonhos. Vocês são os exemplos vivos que mais agradeço por ter a oportunidade de observar. Agradeço também aos familiares que a vida me deu, meu irmãos Eugênio e Carlos e minhas "mães" Claudia e Irma, que sempre estiveram ao meu lado durante os anos morando longe de casa. Continuando, não posso esquecer de agradecer minhas irmãs, Julianne e Erica por toda a ajuda dada ao longo da vida e ao meu tio Marcus, um exemplo de pessoa que tenho a felicidade de poder conviver nessa existência.

Por último, mas não menos importante, gostaria de agradecer a minha companheira Luana, que soube a hora certa de aparecer na minha vida. Creio que estamos nos tornando pessoas melhores ao lado um do outro. Este é só o primeiro objetivo que vamos alcançar juntos!!

"Sonho que se sonha só,
é só um sonho que se sonha só...
...Mas sonho que se sonha junto é realidade!"

- Prelúdio, Raul Seixas

Resumo

A tese investigou o uso de uma ferramenta computacional para avaliar a dinâmica espaço-temporal do metabolismo em ecossistemas aquáticos onde a hidrodinâmica possui papel de destaque na estruturação das comunidades planctônicas. A modelagem matemática foi realizada utilizando o modelo IPH-ECO, uma ferramenta computacional complexa capaz de integrar processos físicos, químicos e biológicos em três dimensões. O trabalho foi dividido em quatro capítulos principais, tendo como base os processos físicos e biológicos que influenciam as estimativas de metabolismo (Capítulos #02 e #03) e melhorias nos métodos numéricos utilizados no modelo IPH-ECO (Capítulos #04 e #05). Os primeiros dois capítulos apresentam o desenvolvimento e aplicação de um algoritmo computacional capaz de quantificar as estimativas de metabolismo aquático baseado (em termos de Produção Primária Bruta - GPP, Respiração do ecossistema - R e Produção Líquida do Ecossistema - NEP = GPP - R) em processos biológicos individuais que influenciam o balanço de oxigênio dissolvido em ecossistemas aquáticos (*e.g.*, respiração de zooplâncton, produção primária de macrófitas aquáticas). A implementação deste algoritmo no modelo IPH-ECO permitiu quantificar as estimativas de metabolismo aquático na Lagoa Mangueira, sul do Brasil, avaliando a importância relativa de diferentes processos individuais e o efeito da hidrodinâmica sobre os processos que compõem o metabolismo da lagoa. O metabolismo aquático da Lagoa Mangueira apresentou um gradiente espacial com maiores valores na região Litorânea e menores na região Pelágica. Além da heterogeneidade espacial, foi possível observar uma heterogeneidade temporal, com valores de produção primária mais elevados durante o verão e primavera e menores durante o inverno e outono. Esta heterogeneidade espacial e temporal acarreta em alterações no estado trófico (autotrófico - NEP positivo ou heterotrófico - NEP negativo) da lagoa, dependendo do local sendo avaliado (zona litorânea ou zona pelágica) e da época do ano. A simulação de diferentes cenários de vento (cinco no total) demonstraram que os padrões de circulação da água podem alterar a dinâmica das estimativas de metabolismo na Lagoa Mangueira, alterando a forma como o sistema é classificado (autotrofia *vs.* heterotrofia) e influenciando os diferentes processos biológicos que compõem estas estimativas.

Os Capítulos #04 e #05 apresentam o desenvolvimento de um novo esquema numérico visando auxiliar na simulação de problemas de qualidade de água. O novo esquema é baseado no método dos Volumes Finitos e permite a integração numérica de equações de transporte utilizando um passo de tempo localizado, calculado a partir da condição de estabilidade de Courant-Friedrich-Lewy (condição *CFL*). A nova solução numérica é diretamente acoplada a um modelo hidrodinâmico

tridimensional em grades triangulares não-estruturadas (e.g, modelo UnTRIM), que utiliza uma solução numérica semi-implícita (Crank-Nicholson) baseada em diferenças finitas e volumes finitos. Diferentes testes clássicos e idealizados são simulados e é realizada uma comparação entre o método com esquema numérico localizado (LTS - *Local Time Stepping*) e o método tradicional (GTS - *Global Time Stepping*). Ambos os métodos se mostraram conservativos considerando uma, duas e três dimensões, e ainda foi respeitada uma condição de estabilidade baseada nos valores máximos e mínimos sendo transportados (*i.e.*, não são criados novos valores máximos nem mínimos). Os métodos também foram avaliados de forma acoplada com escoamentos a superfície livre, levando em conta substâncias conservativas e não-conservativas (*e.g.*, balanço de temperatura na água), assim como situações onde a hidrodinâmica é controlada por vento (forte mistura vertical e horizontal) e onde a hidrodinâmica é controlada por um gradiente de pressão (*e.g.*, maré). Além disso, situações onde a secagem e inundação de células computacionais ocorrem foram testadas e os métodos se mostraram estáveis e conservativos. O esquema numérico LTS se mostrou mais rápido do ponto de vista computacional, exigindo menos tempo de simulação em praticamente todos os testes realizados. Além disso, o esquema mostrou resultados similares ao obtidos utilizando o esquema GTS tradicional. Os testes mostraram que a eficiência do esquema LTS é maior quando ocorre a combinação de altas velocidades e pequenos elementos (alta restrição dada pela condição *CFL*), como a simulação da interface entre rios e lagos, entradas de água rápida (*e.g.*, tromba d'água, *Dam-Break*) e estuários (efeito de maré).

Palavras-Chave: Metabolismo Aquático; Hidrodinâmica; GPP; R; NEP; Heterogeneidade Espacial; Estratificação; Processos Físicos; Processos Biológicos; Modelos Matemáticos; Métodos Numéricos; Volumes Finitos; Passo de Tempo Localizado

Abstract

This thesis investigated the use of a mathematical model to evaluate the space-time dynamics of aquatic metabolism in ecossystems where hydrodynamics plays a key role in structuring the planktonic community. The mathematical model used was the IPH-ECO model, a complex tridimensional model capable of integrating physical, chemical, and biological processes in aquatic environments. The thesis was divided into four main chapters with focus in studying the biological processes and aquatic metabolism estimates (Chapters #2 and #3), and also the improvement of numerical methods used in the IPH-ECO model (Chapters #4 and #5). The first two chapters show the development and application of a computational algorithm capable of quantifying the aquatic metabolism estimates (in terms of Gross Primary Production - GPP, Ecosystem Respiration - R, and Net Ecosystem Production - NEP = GPP-R) based on individual biological processes affecting the dissolved oxygen budget in aquatic ecosystems (*e.g.*, zooplankton respiration, aquatic macrophyte primary production). The numerical algorithm implemented on the IPH-ECO model allowed the quantification of aquatic metabolism estimates (GPP, R, and NEP) at Lake Mangueira, South of Brazil, and the evaluation of the relative importance of different individual processes and how the lake hydrodynamic can change the complex dynamics of the biological processes comprising the lake metabolism estimates. Lake Mangueira's metabolism estimations showed a well-marked spatial gradient with higher values observed in the littoral zone and lower values observed in the pelagic zone. Besides the spatial heterogeneity, it was also possible to notice a strong seasonal heterogeneity, with increased values of GPP and R during summer and spring and lower values during winter and autumn. This space-time heterogeneity leads to a switching in the trophic state of the lake (autotrophic - Positive NEP or heteotrophic - Negative NEP), depending on the site being evaluated (littoral or pelagic) and also the time of the year being assessed. The simulation of different wind scenarios (a total of five) showed that the water circulation patterns can change the metabolism estimates dynamics in Lake Mangueira, changing the system trophic status (net autotrophy *v.s.* net heterotrophy) e also affecting the dynamics of individual biological processes composing the metabolism estimates.

Chapters #4 and #5 show the development of a new numerical scheme capable of accelerate water quality simulations. The new numerical method is based on a Finite Volume framework and allows for numerical integration of scalar transport equations using a local time step, chosen based on the Courant-Friedrich-Lewy stability criteria (the *CFL* condition). This new solution is directly linked to a tridimensional hydrodynamic model on triangular unstructured mesh (e.g., UnTRIm

model), using a semi-implicit solution based on finite differences and finite volume. Different classical and idealized test-cases were simulated and the results from using the new Local Time Stepping (LTS) numerical method is compared against the usage of a traditional Global Time Stepping method (GTS). Both implemented methods showed precise mass conservation in one, two, and three dimensions, moreover, a discrete max-min property was observed in all simulations (*i.e.*, no new maximum nor minimum was created). The methods were also tested when the coupling with hydrodynamic models of free-surface flows is simulated, accounting both conservative (*e.g.*, Salt) and non-conservative substances (*e.g.*, water temperature). The idealized coupled test-cases accounted for situations where hydrodynamics is controled by the wind (strong vertical and horizontal mixing), and situations where hydrodynamics is driven by pressure gradients (*e.g.*, tidal currents). Furthermore, situations where an intense wet- and dry-ing of computational cells is observed was tested and the methods showed stability and precise mass conservation. In a general manner, the new LTS scheme was faster from a computational point-of-view, requiring less simulation time in praticaly all tests. In addition, the new scheme presented concentration fields similar to the ones computed by a traditional GLS algorithm. Our findings suggested that the efficiency of the LTS algorithm is increased when a combination of high velocities and small polygons is observed (elevated *CFL* stability restriction), such as the simulation of the interface between rivers and lakes, fast water inflow (*e.g.*, Dam-Break), and estuaries (Tidal effect).

Key-Word: Aquatic Metabolism; Hydrodynamics; GPP; R; NEP; Spatial Heterogeneity; Vertical Stratification; Physical Processes; Biological Processes; Mathematical Models; Numerical Methods; Finite Volume; Local Time Stepping

Sumário

Lista de Figuras

Capítulo 1

Introdução

O metabolismo em ambientes aquáticos é um importante parâmetro capaz de integrar a atividade biológica do ecossistema, permitindo avaliar seu estado trófico, saúde ambiental, e, numa escala mais ampla, a forma como o carbono é consumido/gerado nestes ambientes. Estudos de metabolismo aquático são uma importante forma de avaliar o funcionamento do ecossistema aquático, visando gerar informações sobre seus principais condicionantes e sua dinâmica espacial e temporal. No entanto, ambientes aquáticos são conhecidos por sua intensa dinâmica temporal, com alterações sendo processadas em escalas temporais curtas, de segundos ou minutos. Avaliar o funcionamento do ecossistema aquático e sua relação com ambientes externos (e.g., pareamento bacia-lagoa) é um desafio que permanece em aberto, uma vez que processos externos ocorrem numa escala de tempo maior (dias, anos), quando comparados aos processos internos nestes ambientes. Além disso, sistemas aquáticos podem apresentar uma variabilidade espacial intensa, com regiões apresentando funcionamento diferente ao longo de um mesmo corpo hídrico (e.g., zonas pelágicas e litorâneas).

Visando contornar estas questões, o uso de ferramentas matemáticas computacionais vem crescendo e suas aplicações vão desde de processos externos (e.g., geração de vazão e cargas oriundas da bacia) a processos internos (e.g., geração de gases em camadas de sedimentos). Estes modelos são capazes de representar de maneira integrada a dinâmica do ecossistema aquático e seus principais processos físicos, químicos e biológicos. Contudo, devido a complexidade em descrever com precisão os processos hidrodinâmicos e biológicos em ecossistemas aquáticos diversos modelos matemáticos vem sendo desenvolvidos, com vantagens e desvantagens inerentes a sua solução computacional. Desta forma, este trabalho visa: i) utilizar uma ferramenta computacional complexa para avaliar o metabolismo de ambientes aquáticos; ii) melhorar os métodos numéricos existentes e utilizados em modelos matemáticos para qualidade de água. A seguir, esta seção apresenta uma introdução sobre Metabolismo Aquático, Modelagem Hidrodinâmica e Ecológica, e os objetivos

do trabalho, juntamente com a divisão dos capítulos que formam esta tese.

1.1 Metabolismo Aquático

O metabolismo é um importante parâmetro capaz de integrar a atividade biológica de diferentes níveis tróficos em ecossistemas aquáticos (Fig. 1.1). Esta atividade pode ser relacionada à dinâmica de gás carbônico e oxigênio na água, por meio da produção primária bruta do ecossistema (GPP, do inglês *Gross Primary Production*) e da Respiração do Ecossistema (R). GPP é definido como o processo de assimilação de carbono inorgânico (CO_2) e liberação de oxigênio (O_2), por meio da fotossíntese. R é a oxidação do carbono orgânico em carbono inorgânico realizado por organismos heterotróficos e autotróficos. A porção do carbono inorgânico assimilado (GPP) que não é remineralizado (R) é chamado produção líquida do ecossistema (NEP = GPP-R, do inglês *Net Ecosystem Production*) e possui dois principais destinos no ambiente aquático: (1) armazenamento dentro do sistema (na forma de biomassa, viva e morta, ou armazenamento abiótico); ou (2) exportação para outros ambientes (Cole et al., 2007). O NEP pode ainda ser utilizado como indicador do estado trófico de um ecossistema (Odum, 1956), sendo considerados ecossistemas heterotróficos aqueles onde NEP possui valor negativo (GPP $<$ R) e ecossistemas autotróficos aqueles onde NEP possui valor positivo (GPP $>$ R).

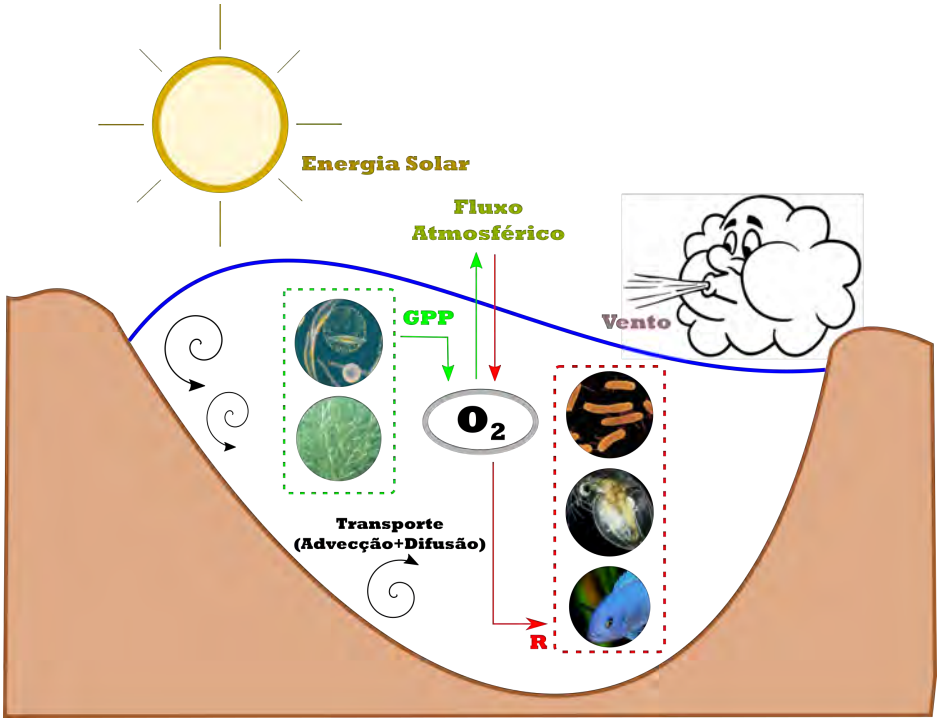

Figura 1.1: Processos envolvidos nas estimativas de metabolismo em ambientes aquáticos. Fonte: Arquivo pessoal.

Diversas metodologias podem ser aplicadas para avaliar GPP, R e NEP, impossibilitando destacar uma técnica específica dentre as mais utilizadas nos diferentes ambientes aquáticos (Kemp & Testa, 2011; Staehr et al., 2012b). Em lagos, duas metodologias ganharam destaque ao longo dos anos, são elas: o método das incubações e os métodos conhecidos como "*free-water*", baseados no balanço entre produção e consumo de oxigênio em curtas escalas de tempo (Odum, 1956). As estimativas de metabolismo aquático baseadas em incubação, consistem na coleta de amostras de água em locais específicos da região de estudo (coluna d'água, camada de sedimento, zona litorânea ou pelágica). Estas amostras são coletadas em duplicata, sendo um recipiente exposto a uma fonte de luz, utilizado para medir produção primária, enquanto o outro recipiente é mantido no escuro, para medir a taxa de respiração na amostra. A integração dos resultados entre as diferentes localizações coletadas gera uma estimativa de GPP, R, e consequentemente, NEP para o sistema como um todo (e.g. Gazeau et al., 2005; Kemp et al., 1997). Apesar de ainda utilizada em alguns trabalhos, esta metodologia possui algumas limitações dentre as quais pode-se destacar (van de Bogert et al., 2007): a) o recipiente utilizado pode causar alterações nas estimativas de metabolismo aquático; e b) elevada incerteza nas estimativas quando extrapoladas para ambientes amplos.

A metodologia "*free-water*" consiste na medição em alta-frequência (escala de minutos) da concentração de gases na água, principalmente oxigênio e dióxido de carbono (e.g. Brighenti et al., 2015; Cole et al., 2000; Hanson et al., 2003; Laas et al., 2012; Staehr et al., 2012b; van de Bogert et al., 2007). A principal desvantagem no uso desta metodologia é que o sinal de alta frequência obtido das sondas automáticas pode apresentar "ruído", dificultando a elaboração de estudos sem o correto tratamento dos mesmos (Batt & Carpenter, 2012; Holtgrieve et al., 2010; Rose et al., 2014) (ver Fig. 1.2 (c)). Portanto, é necessário uma avaliação prévia da série, tentando isolar diferentes processos bióticos e abióticos que possam causar alterações nas concentrações de gases dissolvidos (Winslow et al., 2016). Estas alterações pontuais na concentração de gases dissolvidos na água medidos pelas sondas automáticas não remetem apenas a atividade metabólica e fluxos com a atmosfera, mas também a cargas afluentes, interações físico-químicas e foto-degradação do carbono orgânico dissolvido (Hanson et al., 2003). O uso generalizado de sensores posicionados apenas na zona pelágica (ou apenas na zona litorânea) do lago pode resultar em sub- ou super-estimação dos processos de GPP, R e NEP (Staehr et al., 2012b), principalmente devido ao entorno e o uso da bacia de contribuição próximo a estes pontos (Fig. 1.2 (a) e (b)). A presença ou ausência de macrófitas aquáticas em zonas litorâneas, por exemplo, pode ocasionar diferenças na dinâmica dos gases dissolvidos nestes ambientes, alterando as estimativas de GPP, R e NEP e impossibilitando a generalização dos resultados obtidos para todo o sistema (e.g. Devlin et al., 2016; Lauster et al., 2006; Obrador & Petrus, 2013).

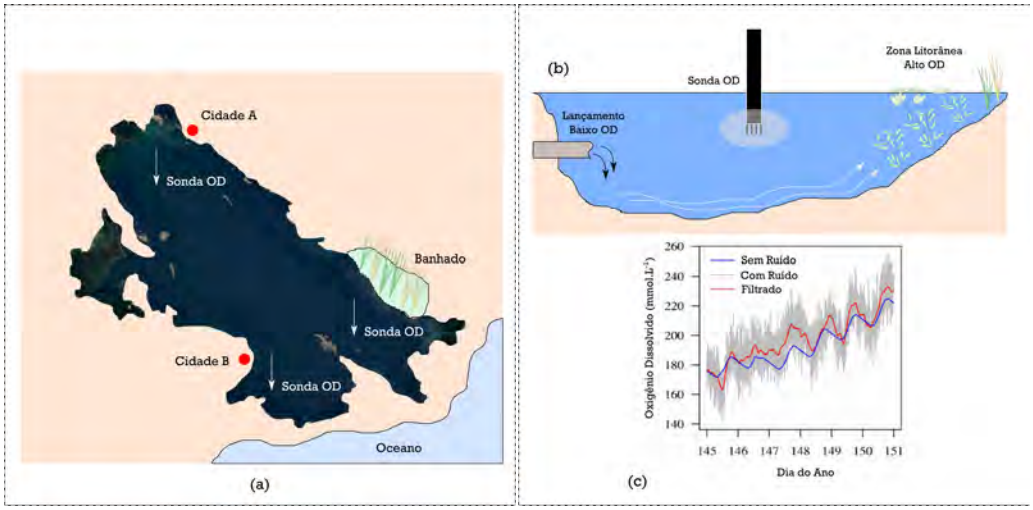

Figura 1.2: Influência da localização da sonda nas estimativas de oxigênio dissolvido em lagos. (a) Dimensão espacial da área de estudo e a influência das proximidades. Uma seta branca indica possíveis posições da sonda (Fonte: Arquivo pessoal.); (b) Influência de diferentes localidades na dinâmica do oxigênio dissolvido. Linhas brancas demonstram uma possível circulação de água (Fonte: Arquivo pessoal.); (c) Efeito do ruído nos resultados de oxigênio dissolvido obtidos por sondas (adaptado de Batt & Carpenter (2012)).

Recentemente, um grande esforço vem sendo empregado visando estimar a influência de processos físicos sobre as estimativas de metabolismo aquático (e.g., Brighenti et al., 2015; Tonetta et al., 2016; van de Bogert et al., 2012). Uma das formas de avaliar esta influência é entender como o processo de troca gasosa na interface ar-água (fluxo atmosférico) é estimado (Hanson et al., 2008; Vachon & Prairie, 2013; Vachon et al., 2010), levando em conta não apenas as tradicionais equações relacionadas apenas a velocidade dos ventos na superfície da água (Cole & Caraco, 1998; Wanninkhof, 1992) mas também a turbulência interna do sistema devido a movimentação de correntes de densidade (MacIntyre et al., 2010; Tedford et al., 2014). Outra forma de avaliar a influência de processos físicos é estimar com maior precisão as correntes hidrodinâmicas existentes no ambiente aquático. Estes processos de mistura podem fortalecer ou enfraquecer a heterogeneidade espacial e temporal das estimativas de metabolismo, levando a conclusões apenas parciais do real estado trófico em ambientes aquáticos quando não contabilizados de forma eficiente (Coloso et al., 2011; Obrador et al., 2014; Sadro et al., 2011). Alguns estudos sugerem o uso de modelos matemáticos capazes de integrar processos físicos e biológicos para avaliar o efeito da hidrodinâmica sobre as estimativas de metabolismo (Hanson et al., 2008; Staehr et al., 2012b). Neste caso, a ideia principal é incluir diferentes mecanismos de transporte no balanço de oxigênio

dissolvido, por meio da solução de Equações de Conservação (Fig. 1.3).

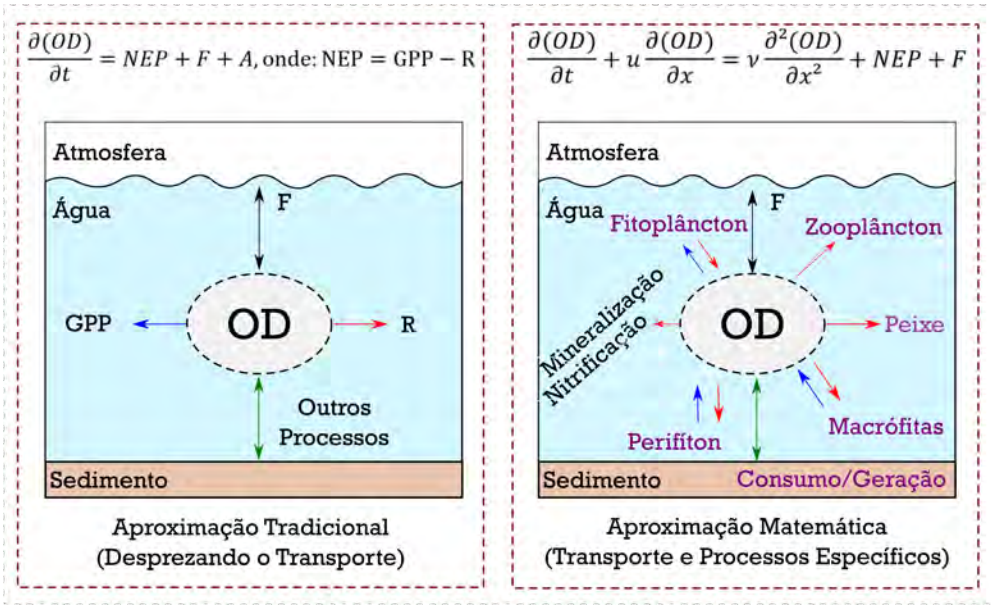

Figura 1.3: Abordagem tradicional, desprezando mecanismos de transporte (a) e abordagem baseada em modelos matemáticos, levando em conta mecanismos de transporte e processos biológicos específicos (b). Setas com coloração diferentes indicam processos consumindo e gerando oxigênio em ambientes aquáticos. Fonte: Arquivo pessoal.

Apesar de concluir com relativo sucesso o objetivo de incluir mecanismos de transporte nas estimativas de oxigênio dissolvido (e.g., Antenucci et al., 2013; McNair et al., 2013), os modelos atuais idealizam o conjunto de processos biológicos individuais que compõem as taxas de metabolismo aquático como funções pré-estabelecidas que dependem de fatores internos e externos no local de estudo (e.g., intensidade luminosa, temperatura média da água, concentração média de carbono orgânico dissolvido) (e.g., Hanson et al., 2008; McNair et al., 2015). A hidrodinâmica é levada em conta e sua influência nas concentrações de oxigênio estimada pela utilização de mecanismos de transporte (advecção e difusão), no entanto, a complexa dinâmica existente nos processos de geração e consumo de matéria orgânica dentro da cadeia trófica aquática (e.g. Karlsson et al., 2012; Kluijver et al., 2015; McCallister & del Giorgio, 2008; Silva et al., 2014; Zimmer et al., 2016) não é inteiramente descrita por estes modelos. Levar em conta contribuições individuais de cada elemento da cadeia trófica permite avaliar a dinâmica de grupos funcionais e suas contribuições nas mudanças de estado trófico (heterotrófico ou autotrófico) do metabolismo aquático (Cremona et al., 2014).

A hidrodinâmica é um importante fator influenciando as estimativas de metabolismo aquático. No entanto, diversos outros fatores agindo em diferentes escalas temporais e espaciais, tais como entradas de carbono no sistema e fluxos com a atmosfera e sedimento, também podem controlar as taxas de metabolismo de lagos (e.g. Coloso et al., 2011; Hanson et al., 2006; Staehr & Sand-Jensen, 2007). Variações de longo prazo normalmente estão relacionadas à disponibilidade de fósforo, a concentração de clorofila-a e ao carbono dissolvido na água (Sand-Jensen & Staehr, 2007, 2009), enquanto variações de curto prazo estão relacionadas a produção primária, temperatura da água, e trocas entre diferentes compartimentos devido a circulação hidrodinâmica (Hanson et al., 2006; Staehr & Sand-Jensen, 2007). A heterogeneidade espacial do metabolismo aquático de lagos pode estar relacionado a morfometria e a processos hidrodinâmicos no sistema (Staehr et al., 2012a; Tonetta et al., 2016; van de Bogert et al., 2012, 2007). Além disso, o grau de isolamento entre essas zonas biológicas (pelágica e litorânea) pode depender do tamanho do lago e de sua morfologia, área total da região litorânea, magnitude e direção dos ventos prevalecentes, e aspectos do balanço de calor do lago como a estabilidade térmica e a heterogeneidade espacial existente (Sadro et al., 2011).

1.2 Modelagem Hidrodinâmica e Ecológica

O progresso da tecnologia e o desenvolvimento de computadores levou ao crescimento do uso de ferramentas computacionais capazes de integrar aspectos físicos, químicos e biológicos, em diferentes escalas espaciais e temporais. Neste contexto, modelos matemáticos de qualidade da água se tornaram ferramentas importantes para a proteção, gestão e geração de conhecimento em ecossistemas aquáticos (Fragoso Jr. et al., 2009; Jorgensen & Fath, 2011). Usualmente, estes modelos são compostos por dois, ou mais, módulos acoplados (Fig. 1.4). Um módulo deve representar os principais elementos capazes de descrever processos físicos (e.g., padrões de circulação, efeito de maré, estratificação térmica) enquanto os outros módulos devem representar de maneira eficaz os principais processos físicos, químicos e biológicos que compõem a dinâmica da qualidade de água em ecossistemas aquáticos (Hamilton & Schladow, 1997). Atualmente é possível observar o uso de módulos numa escala mais ampla (Modelos Hidrológicos), utilizados para melhor descrever fluxos quantitativos (volume de água) e qualitativos (transporte de materiais) entre a bacia hidrográfica e o ecossistema aquático (e.g. Fragoso Jr et al., 2011; Liu et al., 2015; Trolle et al., 2014). Estudos de qualidade de água e limnologia utilizando ferramentas computacionais necessitam de uma boa descrição dos principais processos físicos (e.g., hidrodinâmica, estratificação térmica) e biológicos (e.g., produção primária, degradação de matéria orgânica) existentes no ecossistema. Portanto, podemos destacar o módulo hidrodinâmico e o módulo de

Limnologia como os principais constituintes de um modelo matemático para avaliar a dinâmica de nutrientes, gases dissolvidos e comunidades ecológicas em ambientes aquáticos.

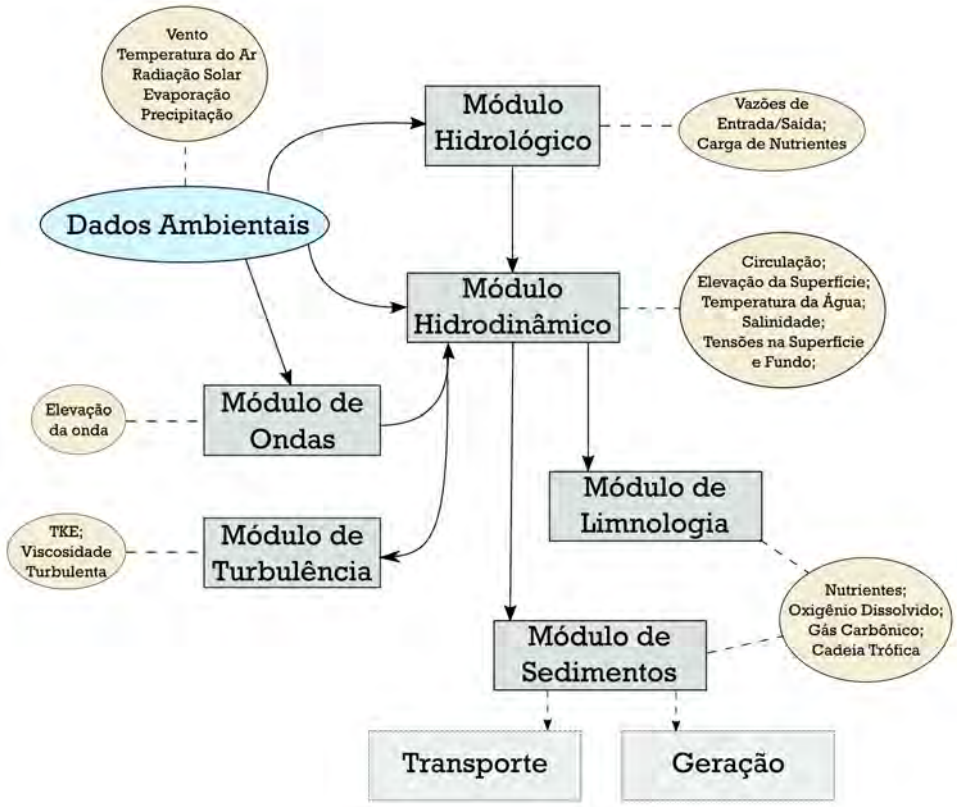

Figura 1.4: Principais módulos utilizados em modelos matemáticos para simulações de qualidade de água. Dados ambientais geram as principais forçantes utilizadas na modelagem de ambientes aquáticos. Fonte: Arquivo pessoal.

O módulo hidrodinâmico, ou modelo hidrodinâmico, é baseado em alguma forma das equações de Navier-Stokes, complementada com um equação de conservação para o volume de água. Existem diversos modelos hidrodinâmicos disponíveis, com diferentes características quanto a estabilidade numérica e discretização espacial. A discretização computacional do domínio real pode ser feita utilizando grades estruturadas [1] (TRIM (Casulli & Cheng, 1992), ELCOM (Hodges et al., 2000), ROMS (Shchepetkin & McWilliams, 2005)) ou não-estruturada [2] (QUODDY (Lynch & Werner, 1991), SEOM (Iskandarani et al., 2003), SUNTANS (Fringer et al., 2006),

[1] quadrados
[2] triângulos, hexágonos

UnTRIM (Casulli & Walters, 2000), ELCIRC (Zhang et al., 2004), FVCOM (Chen et al., 2003), SELFE (Zhang & Baptista, 2008)). A estabilidade numérica depende do tipo de solução computacional utilizada pelo modelo, sendo tipicamente baseados no método das Diferenças Finitas (POM, TRIM, ELCOM, ROMS), Elementos Finitos (ADCIRC, SEOM, SELFE) ou numa mistura de métodos numéricos envolvendo diferenças finitas e Volumes Finitos (UnTRIM, SUNTANS, FVCOM, ELCIRC). Além do tipo de solução numérica utilizada, alguns modelos se destacam pela integração computacional empregada, sendo os modelos baseados em esquemas semi-implícitos (e.g., TRIM/UnTRIM) os mais utilizados atualmente, se tornando a nova geração de modelos de circulação, principalmente por sua elevada precisão numérica e tempo de simulação reduzido, em relação a outras soluções numéricas utilizadas (Zhang & Baptista, 2008). A principal desvantagem nos modelos considerados do tipo TRIM/UnTRIM está na condição de ortogonalidade necessária para a discretização do domínio, principalmente devido a forma como a pressão é descrita na solução numérica (Fringer et al., 2006; Ham et al., 2005). A principal vantagem destes modelos é a utilização de passos de tempo elevados, devido a utilização do método semi-implícito combinado a um esquema Euleriano-Lagrangiano utilizado na solução dos termos explícitos de relacionados aos campos de velocidade. Neste contexto, as restrições ao passo de tempo dependem apenas da viscosidade horizontal e no caso de escoamentos barotrópicos (i.e., diferentes densidades) da máxima velocidade de propagação das ondas internas (Cheng et al., 1993; Gross et al., 1998), que normalmente é menor que a velocidade de propagação das ondas de superfície. Num caso bidimensional no plano X-Z, estas restrições podem ser descritas como:

$$\Delta t \leq \frac{1}{\frac{2\nu_x}{(\Delta x)^2}},\ e\ \Delta t \leq \frac{\Delta x}{\sqrt{g\frac{(\rho_B-\rho_T)}{\rho_T}\frac{H}{4}}} \tag{1.1}$$

onde Δt é o passo de tempo utilizado nas simulações; ν é o coeficiente de viscosidade turbulenta do meio; Δx é a discretização horizontal; g é a aceleração da gravidade; ρ_B e ρ_T são as densidades do fluido numa camada no topo (T) e no fundo (B); e H é a profundidade total do sistema.

A ligação entre o módulo hidrodinâmico e o módulo limnológico é realizada por meio da solução de Equações de Transporte do tipo:

$$\frac{\partial \phi}{\partial t} + \underbrace{\nabla \mathbf{u}\phi}_{\text{Advecção}} = \overbrace{\nabla\left(\mathbf{K}\nabla\phi\right)}^{\text{Difusão}} + \underbrace{S_\phi}_{\text{Reação}} \tag{1.2}$$

onde ϕ é a grandeza escalar sendo transportada, podendo ser assumida como Massa ($\phi = M = \text{C}.V$, com C sendo a concentração e V o volume do elemento computacional) quando o transporte de nutrientes, gases dissolvidos e biomassa é computado ou como Energia Específica ($\phi = e$) quando o transporte de energia é

computado; $\nabla = (\partial/\partial x, \partial/\partial y, \partial/\partial z)$ é o operador matemático derivacional; $\mathbf{u}$ é o campo de velocidades e $\mathbf{K}$ é o tensor de difusividades, ambos calculados pelo módulo hidrodinâmico; e S_ϕ é um termo reativo não ocasionado devido aos mecanismos de transporte. A solução computacional da Eq. 1.2 pode ser realizada utilizando diferentes métodos numéricos. Uma solução unidimensional utilizando o método das diferenças finitas é dada por:

$$\phi_i^{n+1} = \phi_i^n - u\frac{\Delta t}{\Delta x}\left(\phi_{i+1}^n - \phi_i^n\right) + K_x\frac{\Delta t}{(\Delta x)^2}\left(\phi_{i+1}^n - 2\phi_i^n + \phi_{i-1}^n\right) + \Delta t.S(\phi_i^n) \quad (1.3)$$

onde ϕ_i^{n+1} é o valor transportado no i-ésimo elemento num passo de tempo posterior $t^{n+1} = t^n + \Delta t$;/u é a componente horizontal na direção x da velocidade; K_x é a difusividade horizontal na direção x; e $S(\phi_i^n)$ é o termo reativo calculado para o i-ésimo elemento no tempo anterior (n). Para que um método numérico utilizado na solução de Equações Diferenciais Parciais se mantenha estável, é necessário que a solução num passo de tempo posterior (n+1) esteja confinada num intervalo entre os valores máximos e mínimos existente no tempo anterior (n). A partir da Eq. 1.3, é possível observas a seguinte restrição ao passo de tempo para que o valor futuro ϕ_i^{n+1} seja uma média ponderada entre seu valor no tempo presente ϕ_i^n e seus vizinhos ϕ_{i+1}^n e ϕ_{i-1}^n:

$$\Delta t \leq \frac{1}{\frac{u}{\Delta x} + \frac{2K_x}{(\Delta x)^2} + S(\phi_i)} \quad (1.4)$$

Esta restrição pode ser suavizada no transporte de substâncias com taxas de reação lentas, desprezando-se o termo reativo $S(C_i)$ na restrição ao passo de tempo. É importante ressaltar que este termo deve ser mantido na solução final dada pela Eq. 1.3. As restrições diferentes no passo de tempo entre a solução do módulo hidrodinâmico (Eq. 1.1) e das equações de transporte (Eq. 1.4) pode acarretar em problemas na integração das soluções. O uso de passos de tempo elevados acarreta na perda de estabilidade na solução de transporte, além disso, devido a presença de restrições advectivas que mudam constantemente ao longo da simulação hidrodinâmica (campo de velocidades), é difícil prever um passo de tempo baseado na máxima velocidade das ondas de gravidade. Visando superar estes obstáculos, é comum o uso de sub-passos de tempo, onde a solução de transporte é integrada utilizando um passo de tempo igual ou menor que o passo de tempo utilizado no módulo hidrodinâmico (Casulli & Zanolli, 2005; Wang et al., 2008).

O módulo de limnologia deve ser capaz de descrever os principais elementos que definem a qualidade de ambientes aquáticos, como: dinâmica de nutrientes (e.g., Carbono, Fósforo, Nitrogênio); concentração de gases dissolvido e sal, assim como o balanço térmico (e.g. Cole & Buchak, 1995; Rosman, 2001). O grau de complexidade do módulo de limnologia varia dependendo do nível de descrição utilizado, sendo possível acoplar diferentes objetos de estudo, como a dinâmica da

cadeia trófica e efeitos tóxicos de determinadas substâncias (e.g. Fragoso Jr et al., 2009; Hamilton & Schladow, 1997; Park et al., 2008) (Fig. 1.5).

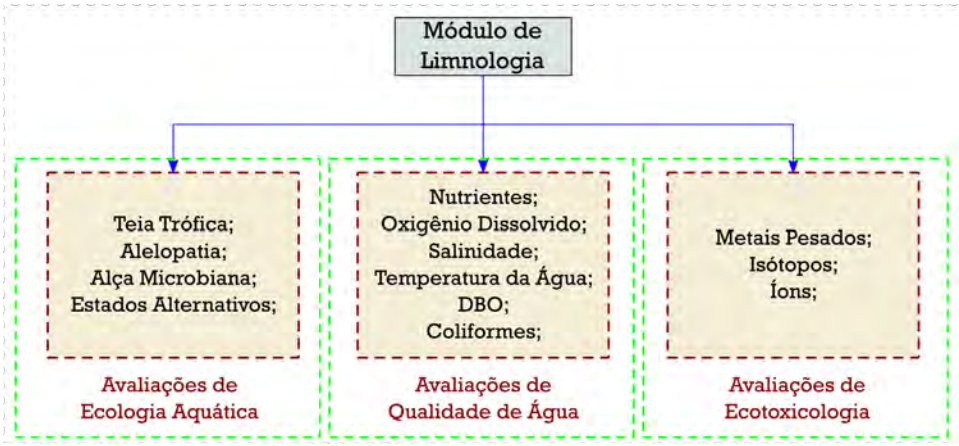

Figura 1.5: Possíveis níveis de complexidade presente num módulo de Limnologia dependendo do tipo de estudo a ser utilizado. É possível utilizar combinações entre diferentes complexidades. Fonte: Arquivo pessoal.

Avaliações de limnologia em geral são realizadas pela correta descrição de diversas variáveis de estado, ou seja, cada elemento que se deseja avaliar por meio da simulação computacional. Cada variável possui um chamado termo fonte ($S(\phi_i)$ na Eq. 1.3) que descreve matematicamente por meio de uma relação empírica ou determinística os principais processos envolvidos na sua dinâmica (Hamilton & Schladow, 1997; Jorgensen & Fath, 2011). Por exemplo, um modelo matemático simples descrevendo a dinâmica do fitoplâncton na coluna d'água pode ser descrita pelo seguinte conjunto de processos (Fragoso Jr. et al., 2009):

$$\frac{d(Fit)}{dt} = PP - Resp - Pred - Sed + Res + Q_{Fit} \tag{1.5}$$

onde PP é a produção primária; $Resp$ é a respiração; $Pred$ é a perda por predação na malha trófica; Sed é uma perda por sedimentação ao longo da coluna d'água para a camada de sedimentos; Res é um ganho por resuspensão de material a partir da camada de sedimentos para a coluna d'água; e Q é uma carga externa que pode aumentar ou reduzir a biomassa de fitoplâncton (e.g., entradas e saídas para rios, estuários e oceanos). Cada processo proposto para cada variável de estado é então avaliado e diferentes aproximações matemáticas podem ser propostas para sua correta descrição (e.g., Asaeda & Van Bon, 1997; Boulion & Hakanson, 2003; Hamilton & Schladow, 1997; Hipsey et al., 2008). Além disso, o efeito combinado de diferentes componentes simulados entre si pode ser levados em conta, aumentando

a complexidade do modelo e a necessidade de novas equações para cada processo de geração ou consumo no ambiente aquático (Fig. 1.6).

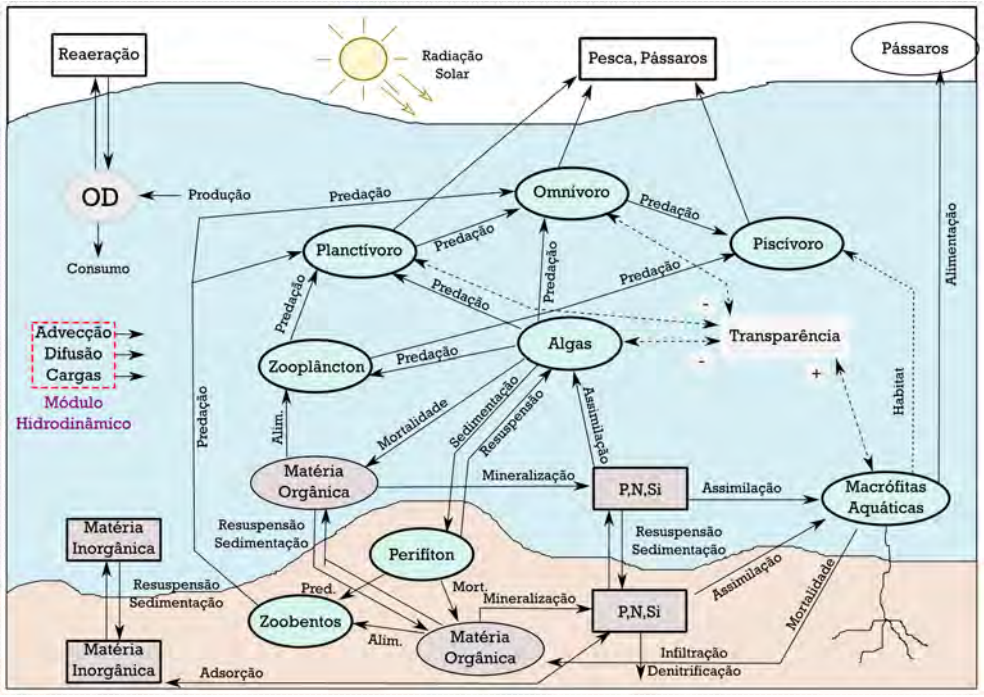

Figura 1.6: Esquema simplificado de processos integrando diversos componentes simulados no ambiente aquático. As linhas sólidas representam fluxos de transporte e linhas pontilhadas indicam relações empíricas para efeitos indiretos. Adaptado de Fragoso Jr. (2009)

Apesar da complexidade, o uso de diferentes processos físicos, químicos e biológicos integrados no ambiente aquático é a base do modelo matemático IPH-ECO (Fragoso Jr et al., 2009). Mais informações sobre a solução numérica utilizada nesta tese, resumo do desenvolvimento do modelo IPH-ECO e os principais processos levados em conta pelo modelo podem ser encontrados no Capítulo 7.

1.3 Objetivos

O objetivo geral desta tese de doutorado foi contribuir para o entendimento da dinâmica do metabolismo aquático em lagos subtropicais, utilizando um modelo matemático baseado em processos. Desta forma, este trabalho buscou avaliar os processos físicos, químicos e biológicos que integram os fluxos de produção e consumo de Oxigênio (O_2) em ambientes aquáticos. Um objetivo adicional

foi melhorar as soluções numéricas utilizadas em modelos de qualidade da água, buscando um método numérico conservativo e capaz de acelerar simulações de longo prazo.

No contexto apresentado acima, são abordados neste trabalho as seguintes questões científicas gerais:

- **Q1** - Como se desenvolve a dinâmica espacial e temporal do metabolismo aquático de lagos rasos subtropicais e quais os principais elementos controladores desta dinâmica?
- **Q2** - Sistemas onde a hidrodinâmica é um fator-chave podem apresentar influência dos processos de mistura nas estimativas de metabolismo ou apenas processos biológicos influenciam nas estimativas?
- **Q3** - É possível melhorar os métodos numéricos existentes e tradicionalmente utilizados em modelos de qualidade da água?

1.3.1 Organização do Trabalho

A fim de responder as questões científicas propostas, foi desenvolvida uma série de estudos que são apresentados nos capítulos 2 a 5 na forma de artigos:

- **Capítulo 2**:
  Cavalcanti, J.R.; Motta-Marques, D.; Fragoso Jr., C.R. Process-based modeling of shallow lake metabolism: Spatio-temporal variability and relative importance of individual processes. *Ecological Modelling*, 323, pages: 28-40, DOI: j.ecolmodel.2015.11.010, 2016. Aplicação na Lagoa Mangueira.
- **Capítulo 3**:
  Cavalcanti, J.R. *et. al.* The role of wind-driven hydrodynamics on the process-based modeling of shallow lake metabolism. Aplicação na Lagoa Mangueira. *Em preparação.*
- **Capítulo 4**:
  Cavalcanti, J.R.; Dumbser, M.; Motta-Marques, D.; Fragoso Jr., C.R. A Conservative Finite Volume Scheme with Time-Accurate Local Time Stepping for Scalar Transport on Unstructured Grids. *Advances in Water Resources*, 86, pages: 217-230, DOI: j.advwatres.2015.10.002, 2015. Aplicação no Lago Guaíba.
- **Capítulo 5**:
  Cavalcanti, J.R.*et. al.* A Conservative three-dimensional Finite Volume

Scheme with Time-Accurate Local Time Stepping for water quality applications on unstructured grids. Aplicação no Reservatório do Faxinal. *Em preparação.*

A Figura 1.7 apresenta uma visão geral dos temas abordados em cada capítulo e a relação entre eles. Apresenta-se a seguir um resumo das respectivas contribuições de cada capítulo para o tema geral proposto nesta tese.

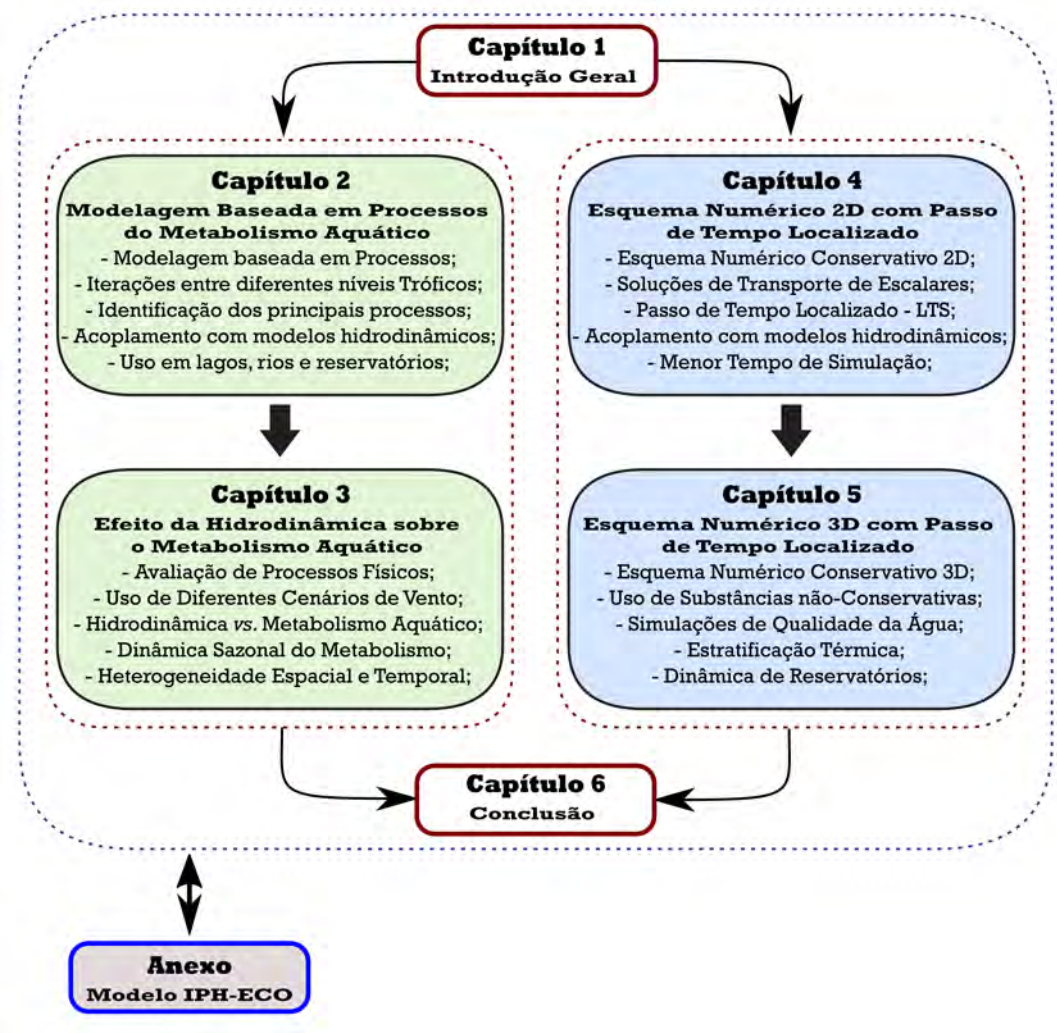

Figura 1.7: Visão geral e relação entre os temas abordados na tese.

O trabalho desenvolvido ao longo da tese tem início no Capítulo 2, onde um novo algoritmo para estimar metabolismo aquático baseado em processos foi desenvolvido e testado. O algoritmo se mostrou capaz de estimar o metabolismo

aquático da Lagoa Mangueira de maneira eficaz, sendo possível determinar processos individuais que mais influenciam ou controlam o metabolismo aquático em grandes lados subtropicais.

O Capítulo 3 apresenta um experimento numérico visando determinar como os processos químicos e biológicos se relacionam com o campo de vento (intensidade e direção) existente sobre a lagoa. Uma vez que o vento é o principal agente controlador da hidrodinâmica da Lagoa Mangueira, é esperado que o sistema mude seu comportamento para diferentes padrões de vento.

Paralelamente ao desenvolvimento do algoritmo para estimar metabolismo aquático, foi desenvolvido um modelo hidrodinâmico capaz de simular domínios irregulares com maior precisão, utilizando elementos triangulares. O Capítulo 4 apresenta o desenvolvimento de um esquema numérico bidimensional conservativo em Volumes Finitos para grades não-estruturadas. Este esquema numérico além de preciso e eficaz utiliza uma integração temporal independente, chamada passo de tempo localizado. Este esquema permite que cada célula avance no tempo de forma independente, permitindo simulações mais rápidas que esquemas com passo de tempo global.

Seguindo as ideias desenvolvidas no Capítulo 4, o Capítulo 5 estende o esquema numérico para três dimensões e acrescenta soluções na equação de transporte para os fluxos difusivos e reações que podem consumir ou produzir alterações num elemento específico sendo simulado. Este novo esquema tridimensional é então utilizado para simular a dinâmica de temperatura da água em um reservatório profundo (Reservatório do Faxinal).

No capítulo 6, apresenta-se um resumo das conclusões da tese assim como perspectivas para pesquisas futuras. E no Capítulo 7 são apresentados detalhes técnicos do modelo hidrodinâmico-ecológico IPH-ECO desenvolvido e utilizado ao longo da construção desta tese.

Capítulo 2

Process-based modeling of shallow lake metabolism: Spatio-temporal variability and relative importance of individual processes

J. Rafael Cavalcanti
David da Motta Marques
Carlos Ruberto Fragoso Junior

Artigo publicado no periódico "*Ecological Modelling*", Fator de Impacto (ISI): 2.321, Qualis CAPES: Engenharias I - A1.

Process-based modeling of shallow lake metabolism: Spatio-temporal variability and relative importance of individual processes

J. Rafael Cavalcanti[a,*], David da Motta-Marques[a], Carlos Ruberto Fragoso Jr[b]

[a] *Universidade Federal do Rio Grande do Sul, Instituto de Pesquisas Hidráulicas, CP 15029, Porto Alegre, RS, Brazil*
[b] *Universidade Federal de Alagoas, Centro de Tecnologia, 57072-970, Maceió, AL, Brazil.*

Abstract

A process-based model was used to evaluate distributed estimates of aquatic metabolism and the importance of different individual processes related to dissolved-oxygen dynamics in a large shallow subtropical lake, Lake Mangueira, on the southern coast of Brazil. In order to assess spatial differences in metabolism estimates, the lake was divided into three geographical areas (North, Central, and South) and each area was subdivided into two biological zones (littoral and pelagic). A well-marked littoral to pelagic gradient was observed, with significant differences in the metabolism estimates between the biological zones of each compartment. In addition, a significant longitudinal difference in metabolism between the North and other lake areas was also apparent. Temporal dynamics featured continuous switching between net autotrophic and net heterotrophic conditions. Phytoplankton primary production and respiration were the main individual processes controlling gross primary production and ecosystem respiration, respectively, for the entire lake. Our findings indicated that spatially distributed estimates of lake metabolism led to different conclusions than did overall metabolism estimates based on single points. Also, individual processes must be taken into account in order to fully understand their relative importance on different spatial and temporal scales for the overall metabolism of aquatic ecosystems.

Keywords: Gross Primary Production, Ecosystem Respiration, Net Ecosystem Production, Spatial Pattern, Process-Based Modelling.

1. Introduction

The aquatic metabolism is an important parameter integrating the biological activity of an aquatic ecosystem. Several factors acting on different temporal and spatial scales, such as carbon inputs and air-water-sediment fluxes, can control lake metabolism (e.g. Hanson et al., 2006; Staehr and Sand-Jensen, 2007; Coloso et al., 2011b). Spatial heterogeneity of the aquatic metabolism in lakes can be related to lake morphometry and hydrodynamic processes within the system (van de Bogert et al., 2007; Staehr et al., 2010; Coloso et al., 2011a; Staehr et al., 2012a; van de Bogert et al., 2012; Brighenti et al., 2015). Long-term variability is often related to phosphorus availability and the concentrations of chlorophyll-*a* and dissolved carbon in the water (Sand-Jensen and Staehr, 2007, 2009). Short-term variability of the aquatic metabolism is suggested to respond to primary production, water temperature, and exchanges among the different compartments due to hydrodynamics (Hanson et al., 2006; Staehr and Sand-Jensen, 2007).

Estimates of lake metabolism are often based on a single dissolved-oxygen sensor in the pelagic zone (e.g. Cole et al., 2000; Hanson et al., 2003, 2006; Tsai et al., 2008; Staehr et al., 2010; Brighenti et al., 2015). However, dissolved-oxygen concentration is spatially variable, and metabolism estimates performed at single points, usually in the pelagic zone, fail to capture the existing spatial-temporal ecosystem heterogeneity (van de Bogert et al., 2012). Estimation of the metabolism based on a single dissolved-oxygen sensor has been suggested to be very different from the metabolism of the entire system, for many reasons: (a) lake zones (i.e. littoral, pelagic, photic, aphotic, and

*Corresponding Author.
Email address: rafael.cavalcanti@ufrgs.br (J. Rafael Cavalcanti)

benthic) can contribute in different ways (Lauster et al., 2006; Sadro et al., 2011a; Giordano et al., 2012; van de Bogert et al., 2012); (b) a point assessment can mask the influence of hydrodynamics (van de Bogert et al., 2007, 2012); (c) a dissolved-oxygen sensor is unable to track oxygen variations due to the sediments, where benthic organisms can cause significant variations (Sadro et al., 2011b); and (d) the variability of dissolved oxygen is not related exclusively to metabolism-related activities and air-water fluxes, but also to groundwater input, physical and chemical interactions, photo-respiration of dissolved organic carbon, and external forces such as wind and precipitation (Hanson et al., 2003, 2006). Therefore, a complete representation of the lake metabolism using process-based models that include physical, chemical, and biological processes might be an useful alternative to better represent the aquatic metabolism (Coloso et al., 2011a; Staehr et al., 2012b).

Process-based models are commonly used to assess water quality in aquatic environments (e.g. Straskraba, 1979; Hamilton and Schladow, 1997; Brookes et al., 2004; Fragoso Jr et al., 2011; Trolle et al., 2014). These models can be useful for understanding the spatial heterogeneity in systems such as large shallow lakes (Fragoso Jr et al., 2011), because of the potential differences between the littoral and pelagic zones (Zanden and Vadeboncoeur, 2002; Vadeboncoeur et al., 2008). In lakes where hydrodynamic processes are intense, the aquatic metabolism may be spatially and temporally heterogeneous (Antenucci et al., 2013; van de Bogert et al., 2007; Coloso et al., 2011a; Hanson et al., 2008), and may be associated with the spatial patchiness of phytoplankton and nutrients (Cardoso et al., 2012; Cardoso and Motta-Marques, 2003, 2004, 2009; Fragoso Jr et al., 2008). The use of empirical/mathematical models to estimate lake metabolism is recent (e.g. Holtgrieve et al., 2010; Holtgrieve and Schindler, 2011; McNair et al., 2013). The process-based approach allows us to estimate, amongst other things, hydrodynamic effects on the ecosystem (Fragoso Jr et al., 2011; Trolle et al., 2014) and metabolism (Antenucci et al., 2013; McNair et al., 2013). This approach also allows continuous diel estimates of ecosystem respiration, which is an advantage over the classic free-water approach (McNair et al., 2013).

Recent studies using an empirical single-point approach have suggested that the hydrodynamics may influence the estimates of lake metabolism in tropical and temperate lakes (van de Bogert et al., 2007; Coloso et al., 2011a; Staehr et al., 2012b; Brighenti et al., 2015). Nonetheless, the authors were unable to quantify the degree to which physical processes affect dissolved-oxygen dynamics. In large shallow lakes, the influence of hydrodynamics on limnological variables (such as nutrient concentration and phytoplankton biomass) can be strong, especially for wind-driven hydrodynamics (Cardoso and Motta-Marques, 2009; Fragoso Jr et al., 2011), which may increase the effect of hydrodynamic processes on dissolved oxygen concentration. Recent publications regarding process-based modeling of lake metabolism use hydrodynamic models linked to metabolism estimates in order to understand these dynamics (Antenucci et al., 2013; McNair et al., 2013). However, these studies indirectly represent the individual processes that compose gross primary production and ecosystem respiration estimates (Cremona et al., 2014a).

Metabolism in aquatic ecosystems is spatially and temporally dynamic, and many individual processes make significant and different contributions. In this study, we used a complex and spatially distributed ecosystem model, in order to evaluate individual processes (physical, chemical, and trophic web) on the metabolism of a shallow subtropical lake, based on the dissolved-oxygen budget, and considering spatial and temporal heterogeneity.

2. Methodology

2.1. Study area

Lake Mangueira (Fig. 1) is a large shallow lake in southern Brazil, located between 32°20'S and 33°00'S, and 052°20'W and 052°45'W. The lake surface area is approximately 820 km^2, with a mean depth of 2.6 m and maximum depth of 6.5 m, elongated, with a maximum length of 90 km and width of 10 km. The trophic state varies from oligotrophic to mesotrophic, with a mean annual PO_4 concentration of 35 $mg.m^{-3}$, ranging from 5 to 51 $mg.m^{-3}$. The lake is surrounded by dunes and two wetlands. This heterogeneous landscape harbors an exceptional biological diversity, which motivated the Brazilian federal authorities to protect part of the entire hydrological system as the TAIM Ecological Station, in 1991 (Motta-Marques et al., 2002). The watershed (ca. 415 km^2) is used primarily for rice production.

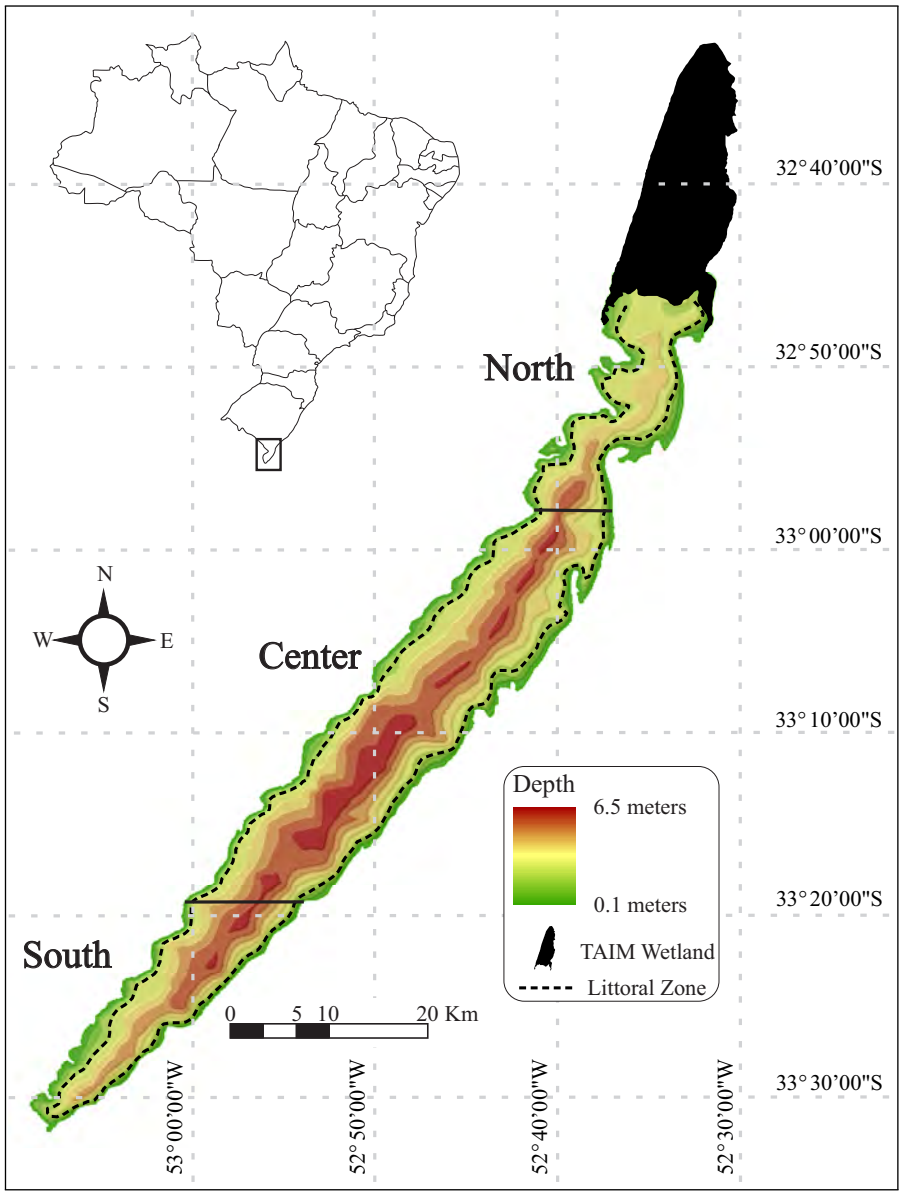

Figure 1: Lake Mangueira areas and zones. The dashed line (–) marks the estimated border between the littoral and pelagic zones. The continuous line (—) marks the limits of the North (N), Central (C), and South (S) areas.

2.2. Model description

The IPH-TRIM3D-PCLake model (Fragoso Jr et al., 2009), also known as IPH-ECO (freely available in: `https://sites.google.com/site/iphecomodel`), describes the main physical (water temperature and density, velocity fields, and free-water elevation), chemical and biological (e.g. nutrients and trophic structure) processes existing in the aquatic ecosystem. The model can be used in an individual assessment, allowing the user to evaluate physical and water-quality processes separately, or it can be used to evaluate physical processes, water-quality processes, and biological structures simultaneously in one, two, or three dimensions.

The IPH-ECO hydrodynamic module solves the Reynolds-Averaged Navier-Stokes Equation using a semi-implicit discretization on structured staggered grids (see Casulli and Cheng, 1992; Cheng et al., 1993, for more details). The non-linear convective terms existing in the TRIM solution (Cheng et al., 1993) are solved using an explicit Eulerian-Lagrangian finite-difference scheme. To increase the stability and accuracy, the θ-method was also implemented

(Casulli and Cattani, 1994). The parameter of horizontal eddy viscosity can be calibrated manually, and vertical eddy viscosity is modeled as an empirical relationship (Pacanowski and Philander, 1981). To perform the coupling between physical and biological processes, IPH-ECO uses an explicit finite-difference scheme to solve an advection-diffusion-reaction type equation of the form:

$$\frac{\partial C}{\partial t} + \nabla(\mathbf{v}C) = \nabla(\Gamma\nabla(C)) + S_C \tag{1}$$

where C is the scalar concentration being transported, which can be regarded as different ecosystem variables (e.g., nutrients, biomass, chlorophyll-*a*, or water temperature); **v** is the velocity field, which is given by the hydrodynamic model; Γ is the diffusivity tensor, regarded in the model as turbulent eddy diffusivity; and S_C is a source/sink term that takes into account a wide variety of processes that can cause changes in the scalar concentration (e.g., settling, resuspension, and biological processes).

The water quality-module of IPH-ECO, i.e., the chemical and biological dynamics in the water column and sediment bed, is based largely on PCLake (Janse, 2005). Each water-quality variable has its own source/sink term, allowing IPH-ECO to describe nutrients (phosphorus, nitrogen, and silica) and dissolved-oxygen dynamics based on different processes. The model is also able to describe biological biomasses, splitting the phytoplankton and fish biomasses into three functional groups, the aquatic macrophytes into four functional groups, and the zooplankton as one functional group, and the zooplankton as one functional group; and describes in a simplified manner the benthic fluxes and sediment diagenesis. Some improvements have been added to the model since its first release, such as a resuspension flux that is a function of wind fetch (Fragoso Jr et al., 2011), and the day length as a function of latitude. In order to evaluate the metabolism dynamically, we implemented a process-based algorithm to evaluate the aquatic metabolism based on individual processes composing O_2 dynamics, which is described next.

2.3. Process-based algorithm for aquatic metabolism

Our process-based algorithm for aquatic metabolism was based on the assumption that processes involved in the dissolved-oxygen (O_2) budget are related to NEP (Odum, 1956). The mathematical formulation proposed here and implemented in IPH-ECO describes O_2 dynamics in a more detailed form, taking into account more trophic levels than the previous algorithm used in the model (Fig. 2). Along with the effects of hydrodynamics on O_2 concentration (Eq. 1), the new source/sink term (S_C) for dissolved oxygen in IPH-ECO is implemented as follows:

$$\begin{aligned}\frac{\partial O_2}{\partial t} &= f_{min}(T, DO, Det) + f_{nit}(T, DO, NH_4) + f_{SOD}(Min_{sed}, Nit_{Sed}) \\ &\quad + f_{atm}(T, W) + f_{PP}(Phyt, Mac, Peri, T) \\ &\quad + f_{resp}(Phyt, Mac, Peri, Zoo, Fish, Benthos, T)\end{aligned} \tag{2}$$

where *Min*, *Nit*, *SOD*, *atm*, *PP*, and *resp* are, respectively: mineralization, nitrification, sediment oxygen demand, reaeration, primary production, and respiration fluxes; T is the water temperature in °C; W is the wind velocity in $m.s^{-1}$; DO is the dissolved oxygen concentration in $g.m^{-3}$, Det is the detritus concentration in $g.m^{-3}$; NH_4 is the ammonium concentration in $g.m^{-3}$; and Phyt, Mac, Peri, Zoo, Fish, and Benthos are the biomasses of phytoplankton, macrophytes, periphyton, zooplankton, fish and zoobenthos, respectively, in $g.m^{-3}$ of dry weight. The effects of the different processes (or functions, as in Eq. 2) on OD dynamics are described by the model as empirical relationships (see Janse, 2005, for more details).

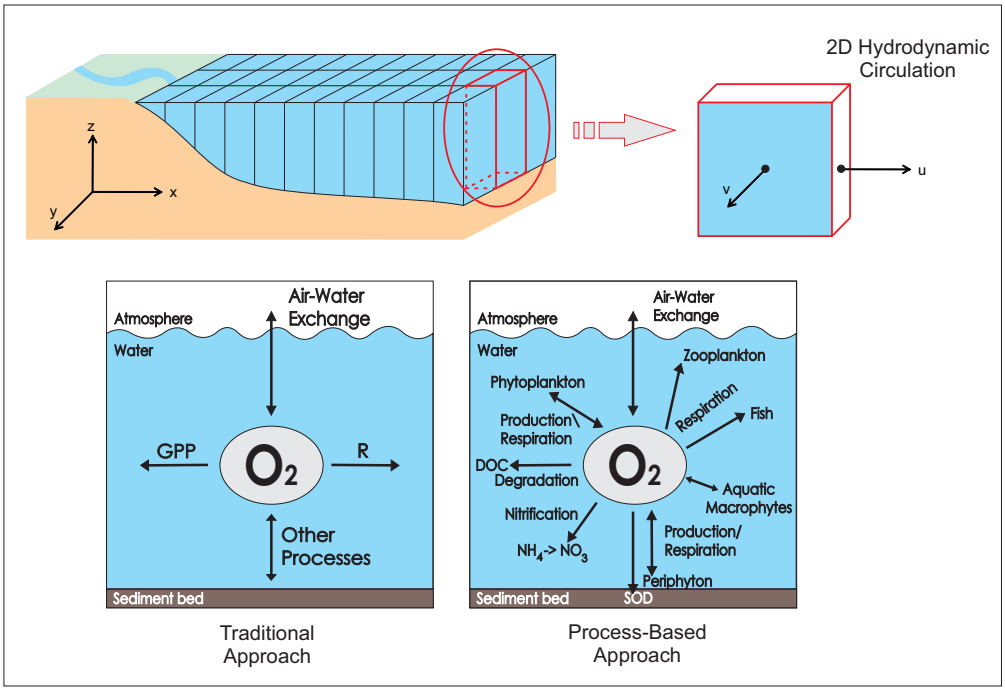

Figure 2: Schematic view of the process-based approach used in this study. The IPH-ECO hydrodynamic module generates physical circulation, and the water-quality module generates process-based estimates of lake metabolism.

The large variety of processes implemented in IPH-ECO that constitute the metabolism were divided into representative variables, based on Odum's equation (Odum, 1956):

$$\frac{\Delta O_2}{\Delta t} = NEP - F - A \tag{3}$$

where $NEP = GPP - R$ is the Net Ecosystem Production; GPP is the Gross Primary Production; and R is the Ecosystem Respiration. F is the atmospheric exchange of O_2 at the lake surface, and A represents other processes that may alter the dissolved-oxygen concentration (Table 1). Physical processes derived from water circulation (i.e., advection and diffusion) are taken into account by the numerical solution of (Eq. 1).

Table 1: Separation of variables representing metabolism processes. The first column shows the variables of Odum's equation; the second column shows the IPH-ECO processes used to describe lake metabolism.

Term in Odum's equation	IPH-ECO model associated processes
GPP	Primary production of phytoplankton, submerged macrophyte, and periphyton
R	Mineralization, nitrification, respiration of phytoplankton, submerged macrophyte, periphyton, zooplankton, fish, and zoobenthos
F	Atmospheric reaeration flux
A	Nitrate uptake from phytoplankton, submerged macrophyte, and periphyton

2.4. Model parameterization and simplifications

Lake Mangueira was horizontally discretized using a regular grid with 500x500 m resolution. Only one vertical layer was used, due to the lake's daily mixing and brief stratification period (hours), resulting in a two-dimensional vertically integrated model. The model parameterization and calibration, meteorological data used, watershed simulation, and water abstraction estimates were presented in detail in a recent article (Fragoso Jr et al., 2011). We retained the model structure and simplifications used previously, including (a) only one functional group for phytoplankton, zooplankton and macrophytes; (b) exclusion of the module for strictly planktivorous fishes; (c) omnivorous and piscivorous fishes were modeled dynamically, with a distinction between juvenile and adult stages for the omnivore community.

The model was calibrated using field data obtained from 2001 to 2006, and collected at three field stations located in the North, Central, and South areas of the lake (see Fragoso Jr et al., 2011, for more details). The simulation was performed from 01/01/2001 through 12/31/2006, and the model was calibrated by comparing simulated against median field data for: water level, water temperature, dissolved oxygen, dissolved nitrogen, orthophosphate PO_4-P, ammonium NH_4-N, and chlorophyll-*a*. Since we are focusing on evaluating Lake Mangueira metabolism estimates using the calibrated period, a validation phase was not necessary. In order to eliminate possible effects of initial conditions on the distributed simulations, the model outcomes for the first summer were discarded. The model time step was set to 30 s and the output was set to 3600 s, allowing us to analyze hourly estimates of lake metabolism.

The lake was divided into four spatial compartments to simplify the analysis of the results: North, Central and South areas, as well as Lake Mangueira as a whole (Fig. 1). In addition, each compartment was divided into two biological zones, pelagic and littoral, according to a depth criterion that relates the depth of the euphotic zone to the Secchi disk depth, as follows (Ji, 2008):

$$D = -\ln\left(\frac{I(D)}{I_s}\right).\frac{Z_s}{C_s} \tag{4}$$

where $I(D)/I_s = 0.01$ is the percentage of luminous energy that reaches the limit of the euphotic zone, C_s is a constant with typical values that range from 1.7 to 1.9 (here we adopted the mean value, 1.8), and Z_s is the Secchi disk depth, which was adopted as the mean Secchi depth observed for Lake Mangueira in the field data for the simulation period (0.89 m, see Fragoso Jr et al., 2011, for more details). The critical depth for the littoral zone was then calculated as 2.3 m.

2.5. Data analysis

In order to assess the spatial differences, the Analysis of Variance (ANOVA) confidence level was set to 0.05. A post-hoc analysis using Tukey's HSD (Honestly Significant Difference) test was performed in order to evaluate the significance of spatial differences. The time series for each compartment of the lake was obtained by using all cells composing the specific compartment (geographical areas and biological zones). The metabolism time series for each compartment of the lake was obtained by using a volumetric-averaged value for all cells composing one compartment for each hourly output. The hourly output was then time-averaged using a 24-h interval (daily mean).

3. Results

3.1. Model Calibration

The IPH-ECO model was calibrated for the period of January 2001 through December 2007. Most model outcomes showed a reasonable fit with the field data (Fig. 3) despite the large spatial variation of the data used to calibrate the model. The heat budget reproduced the water temperature in all years of simulation, showing good agreement with the observed data (R=0.82, Table 2). For oxygen concentration, the model produced the same seasonal dynamics as were measured. However, it tended to underestimate the values measured in the summer of 2005 (R=0.43, Table 2). The seasonal patterns of chlorophyll-*a*, PO_4, dissolved nitrogen and Secchi depth were tracked reasonably well by the model (R>0.22, Table 2). We could capture the large uptake of NO_3 and PO_4 by phytoplankton in summer, and a relatively higher nutrient availability in winter, due to low uptake and input of allochthonous material. However, the variability of PO_4 and dissolved N in the winter within the simulated period was overestimated most of the time. The large spatial variability of NH_4 both within and between years was much more difficult to predict (R=0.23, Table

2); only the mean concentration could be reproduced by IPH-ECO. NH_4 seems to be strongly dependent on local conditions.

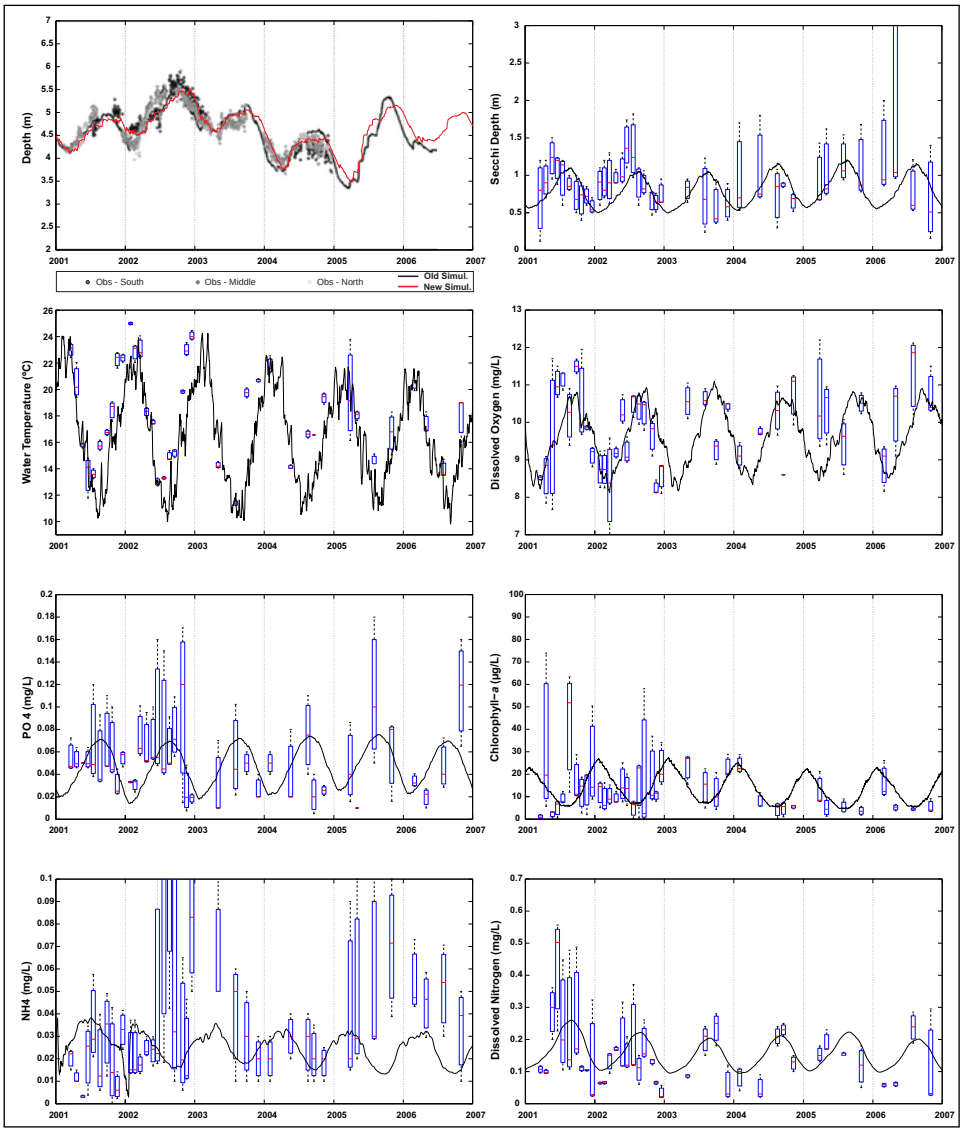

Figure 3: Model calibration for some physical, chemical, and biological variables in Lake Mangueira, from 2001 through 2007. Simulated (line plots) and observed (boxplot) values for water level, water temperature, dissolved oxygen, dissolved N, NH_4, PO_4, and chlorophyll-*a*. Each boxplot compiles all monthly data monitored spatially along Lake Mangueira. It presents five statistical summaries for spatial data: the smallest observation (sample minimum), lower quartile (Q1), median (Q2), upper quartile (Q3), and largest observation (sample maximum).

165 The hydrological balance determined the water level in Lake Mangueira. The simulated water level agreed with the field data, though the levels obtained in this study are slightly different from those found in a previous simulation of the lake (Fig. 3).

Table 2: Statistical comparison between model simulations and field measurements (median values) of water surface temperature and concentrations of dissolved oxygen (DO), Secchi disk, dissolved nitrogen, ammonium (NH_4), orthophosphate (PO_4), and chlorophyll-*a* over the calibration period (Cal., January 2001-December 2006) RMSE stands for Root Mean Square Error, and *R* is the correlation coefficient.

	R	**RMSE**
Water Temperature	0.82	2.80
Dissolved Oxygen	0.43	0.90
Secchi Disk	0.25	0.24
Dissolved Nitrogen	0.48	0.08
NH_4	0.23	0.03
PO_4	0.27	0.03
Chlorophyll-*a*	0.13	10.26

3.2. Metabolism Estimates

Lake Mangueira's metabolism showed a wide day-to-day variation and well-defined seasonal patterns for GPP, R, and NEP (Fig. 4), for each geographical area (North, Central, and South) and biological zone (pelagic and littoral). GPP and R showed higher estimates during early summer and lower estimates during winter. Higher values of GPP and R were found in the littoral zone during late summer (Fig. 5). NEP estimated values were higher for spring and autumn and lower during winter, with a constant shift between autotrophic and heterotrophic conditions during the entire year (Fig. 4).

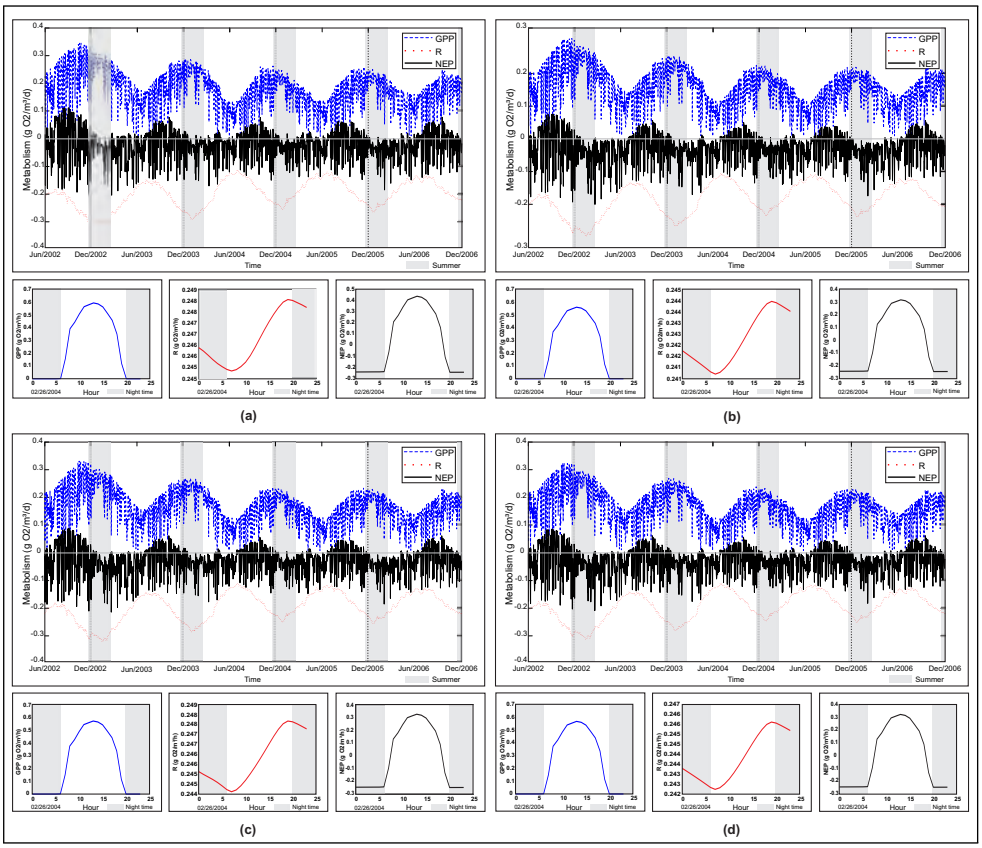

Figure 4: Seasonal variation (daily means) for Gross Primary Production (GPP), dashed line (–); Ecosystem Respiration (R), dotted line (.); and Net Ecosystem Production (NEP), thick solid line (-) for pelagic zones: (a) North, (b) Central, (c) South, and (d) Lake Mangueira as a whole. A thin vertical line indicates the beginning of a new year. Small windows show the diel metabolism for 02/26/2004 in g $O_2.m^{-3}.h^{-1}$.

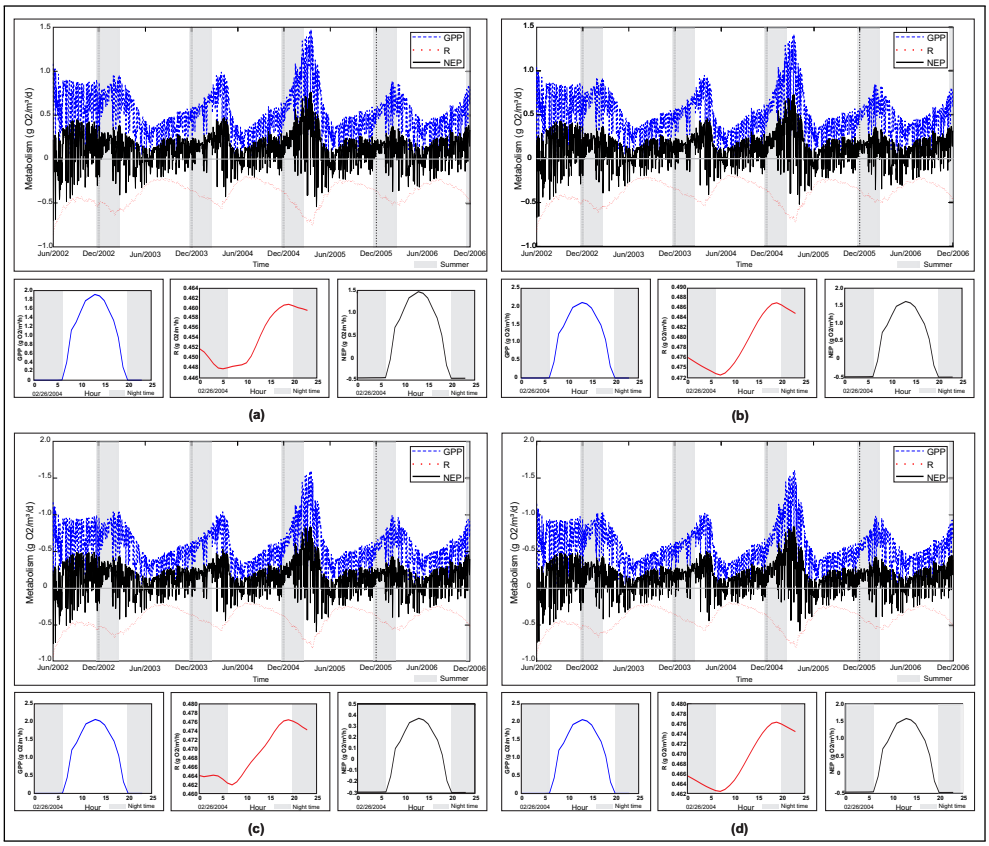

Figure 5: Seasonal variation (daily means) for Gross Primary Production (GPP), dashed line (–); Ecosystem Respiration (R), dotted line (.); and Net Ecosystem Production (NEP), thick solid line (-) for littoral zones: (a) North, (b) Central, (c) South, and (d) Lake Mangueira as a whole. A thin vertical line indicates the beginning of a new year. Small windows show the diel metabolism for 02/26/2004 in g $O_2.m^{-3}.h^{-1}$.

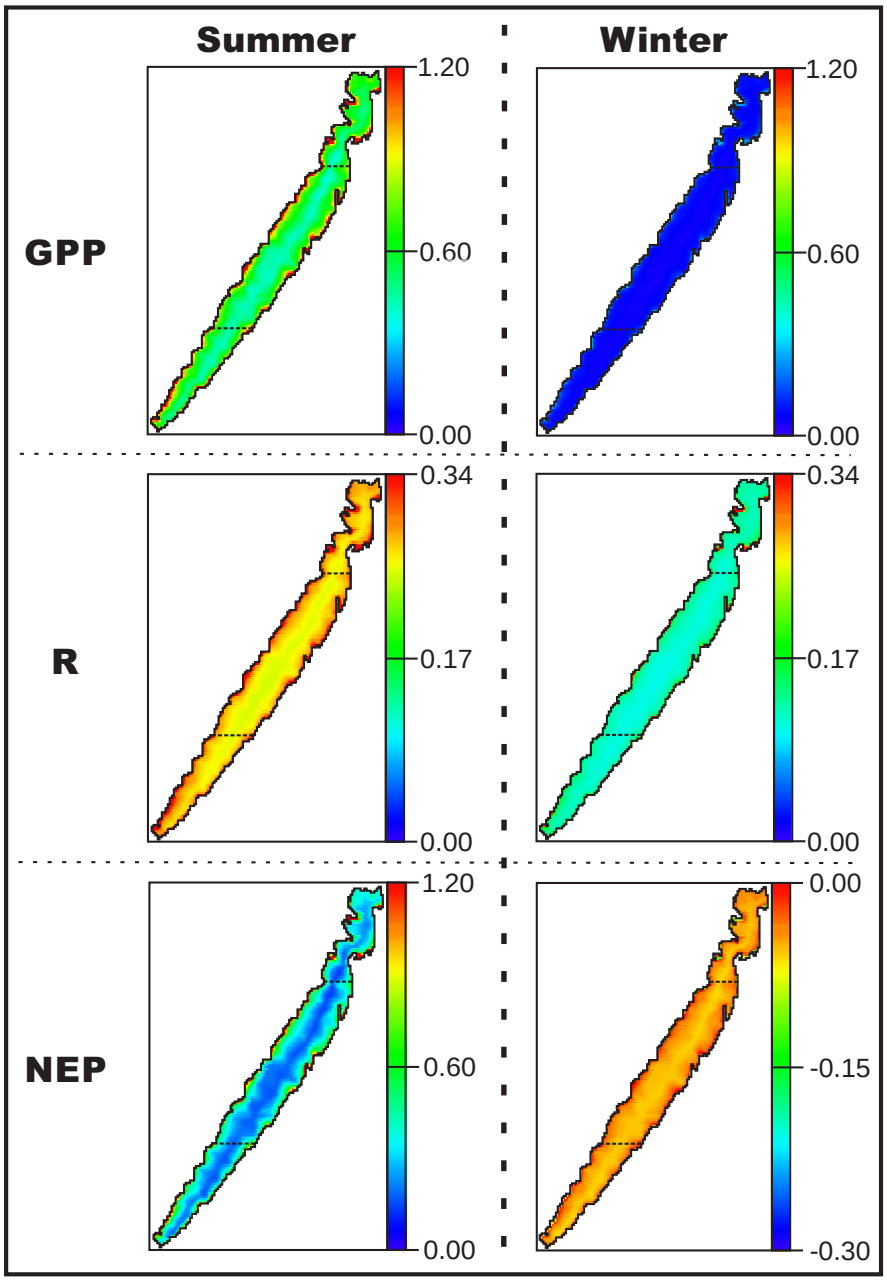

Figure 6: Spatial distribution during summer (first column) and winter (second column) for Gross Primary Production (GPP, first row), Ecosystem Respiration (R, second row), and Net Ecosystem Production (NEP, third row). A dashed line separates the main areas of the lake. Values in g $O_2.m^{-3}.d^{-1}$.

Table 3: Mean, standard deviation, minimum, and maximum calculated for Lake Mangueira metabolism estimates in each compartment (biological zones and geographical areas). GPP stands for Gross Primary Production, R for Ecosystem Respiration, and NEP for Net Ecosystem Production.

		Pelagic				Littoral				Entire region			
		Mean	Stand. Dev.	Min	Max	Mean	Stand. Dev.	Min	Max	Mean	Stand. Dev.	Min	Max
North Region	GPP	0.17	0.07	0.01	0.33	0.50	0.24	0.02	1.41	0.22	0.08	0.01	0.42
	NEP	-0.02	0.05	-0.20	0.11	0.12	0.17	-0.67	0.73	0.00	0.07	-0.24	0.16
	R	0.19	0.05	0.11	0.30	0.38	0.13	0.19	0.83	0.22	0.05	0.12	0.35
Central Region	GPP	0.16	0.06	0.01	0.31	0.55	0.27	0.02	1.63	0.18	0.07	0.01	0.35
	NEP	-0.03	0.05	-0.20	0.08	0.15	0.20	-0.73	0.87	-0.02	0.05	-0.21	0.10
	R	0.18	0.05	0.11	0.30	0.40	0.14	0.19	0.91	0.20	0.05	0.11	0.32
South Region	GPP	0.16	0.06	0.01	0.32	0.54	0.26	0.02	1.54	0.20	0.08	0.01	0.38
	NEP	-0.03	0.05	-0.21	0.09	0.14	0.19	-0.72	0.80	-0.01	0.06	-0.23	0.12
	R	0.19	0.05	0.11	0.31	0.40	0.14	0.19	0.89	0.21	0.05	0.11	0.34
Lake Mangueira	GPP	0.16	0.06	0.01	0.31	0.53	0.26	0.02	1.54	0.19	0.07	0.01	0.37
	NEP	-0.03	0.05	-0.20	0.08	0.14	0.19	-0.71	0.81	-0.01	0.06	-0.22	0.12
	R	0.19	0.05	0.11	0.30	0.39	0.14	0.19	0.88	0.21	0.05	0.11	0.33

Regarding spatial variability, GPP varied among the geographical areas and biological zones, varying from north to south, and from littoral to pelagic (Fig. 6 first row, summer and winter). Higher estimated values of GPP were found in the littoral zone, and also in the North area (Table 3). This spatial heterogeneity was lower during winter, with a much more homogeneous behavior (Fig. 6, first row, second column). The differences observed for GPP were statistically significant (p<0.05) for all littoral vs. pelagic zones of each compartment, while the opposite was found in comparing the pelagic zones separately (Table 4). In comparing the entire zones (pelagic and littoral) against each other, a significant difference was noted only for the North area, while the Central and South areas and the lake as a whole did not differ significantly from each other (Table 4). Phytoplankton production was the main individual process composing the GPP estimates for each geographical area and biological zone (Fig. 7).

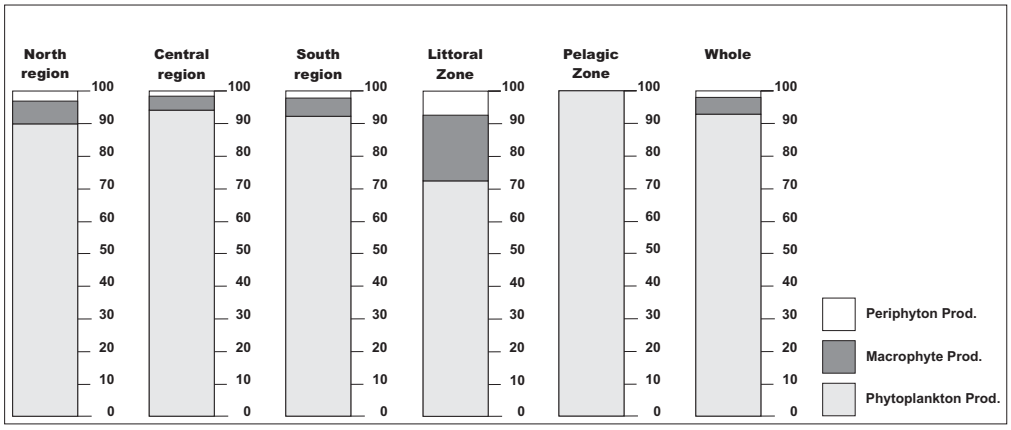

Figure 7: Individual processes comprising Gross Primary Production (GPP) through time in Lake Mangueira. The gray scale represents the results for phytoplankton, aquatic macrophytes, and periphyton primary production.

Table 4: Tukey's HSD (Honestly Significant Difference) test for GPP estimates in each individual compartment, in order to assess metabolism estimates for Lake Mangueira. The statistically significant (p<0.05) differences between the means of the pairwise component analyzed are indicated in bold.

		North			Center			South			Mangueira Lake		
		Littoral	Pelagic	Entire Region	Littoral	Pelagic	Entire Region	Littoral	Pelagic	Entire Region	Littoral	Pelagic	Entire Region
North	Littoral	-	**0.32**	**0.28**	**-0.05**	**0.34**	**0.32**	**-0.04**	**0.34**	**0.30**	**-0.03**	**0.34**	**0.31**
	Pelagic		-	**-0.05**	**-0.38**	0.02	-0.01	**-0.37**	0.01	-0.02	**-0.36**	0.01	-0.02
	Entire region			-	**-0.33**	**0.07**	**0.04**	**-0.32**	**0.06**	**0.03**	**-0.31**	**0.06**	**0.03**
Center	Littoral				-	**0.40**	**0.37**	0.01	**0.39**	**0.36**	**0.02**	**0.39**	**0.36**
	Pelagic					-	-0.03	**-0.38**	-0.01	**-0.04**	**-0.38**	0.00	**-0.04**
	Entire region						-	**-0.36**	0.02	-0.02	**-0.35**	0.02	-0.01
South	Littoral							-	**0.38**	**0.34**	0.01	**0.38**	**0.35**
	Pelagic								-	**-0.04**	**-0.37**	0.00	**-0.03**
	Entire region									-	**-0.34**	**0.04**	0.00
Mangueira Lake	Littoral										-	**0.37**	**0.34**
	Pelagic											-	**-0.03**
	Entire region												-

Similarly to GPP, the estimated R values for Lake Mangueira showed a strong spatial gradient (Fig. 6, second row, summer and winter). Higher values were found in the littoral zone and in the North area (Table 3). The spatial heterogeneity of R was lower during winter. The R estimates also showed a significant littoral-to-pelagic heterogeneity for all geographical areas (Table 5). Comparing the R estimates for pelagic zones of each compartment did not reveal any significant spatial heterogeneity (Table 5). As noted for GPP, the R estimates also showed a significant difference only when comparing the entire North area (pelagic and littoral) against the others. The estimates for respiration in the Central and South areas and the lake as a whole did not show any significant spatial heterogeneity (Table 5). The main contribution to R was associated with phytoplankton respiration. Nonetheless, other processes (e.g. zooplankton respiration) also showed a strong influence on the R composition (Fig. 8).

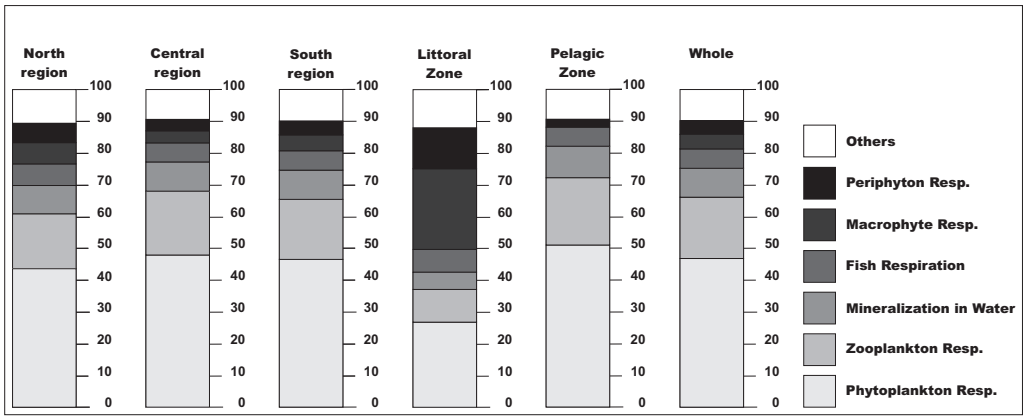

Figure 8: Individual processes comprising Ecosystem Respiration (R) through time in Lake Mangueira. The gray scale represents the results for phytoplankton respiration, zooplankton respiration, mineralization in water, fish respiration, aquatic macrophyte respiration, and periphyton respiration. The term "other processes" comprises sediment oxygen demand, nitrification in water, mineralization in water, and zoobenthos respiration.

Table 5: Tukey's HSD (Honestly Significant Difference) test for R estimates in each individual compartment in order to assess metabolism estimates for Lake Mangueira. The statistically significant (p<0.05) differences between the means of the pairwise components analyzed are indicated in bold.

		North			Center			South			Mangueira Lake		
		Littoral	Pelagic	Entire Region	Littoral	Pelagic	Entire Region	Littoral	Pelagic	Entire Region	Littoral	Pelagic	Entire Region
North	Littoral	-	**0.19**	**0.16**	**-0.02**	**0.20**	**0.18**	**-0.02**	**0.19**	**0.17**	**-0.01**	**0.19**	**0.17**
	Pelagic		-	**-0.03**	**-0.21**	0.01	-0.01	**-0.20**	0.00	-0.02	**-0.20**	0.01	-0.01
	Entire region			-	**-0.18**	**0.04**	**0.02**	**-0.18**	**0.03**	**0.01**	**-0.17**	**0.03**	**0.02**
Center	Littoral				-	**0.22**	**0.20**	0.00	**0.21**	**0.19**	**0.01**	**0.21**	**0.19**
	Pelagic					-	-0.01	**-0.21**	-0.01	**-0.02**	**-0.21**	0.00	**-0.02**
	Entire region						-	**-0.20**	0.01	-0.01	**-0.20**	0.01	-0.01
South	Littoral							-	**0.21**	**0.19**	0.00	**0.21**	**0.19**
	Pelagic								-	**-0.02**	**-0.20**	0.00	**-0.02**
	Entire region									-	**-0.18**	**0.02**	0.00
Mangueira Lake	Littoral										-	**0.21**	**0.19**
	Pelagic											-	**-0.02**
	Entire region												-

The NEP estimates also showed spatial heterogeneity, following the patterns found for GPP and R (Fig. 6, third row, summer and winter). The estimates were higher in the littoral zone and in the North area (Table 3), showing a significant spatial heterogeneity from littoral to pelagic and from north to south (entire area, Table 6). Comparing only

the pelagic zones did not reveal any significant difference, nor did comparisons of the Central and South areas and the entire lake indicate significant spatial heterogeneity (Table 6). A persistent net autotrophic condition was observed in the North area (Fig. 9), differently from the Central area, which showed a persistent net heterotrophic condition. The South area showed a nearly neutral condition (ca. 50% of the time in each condition), as did Lake Mangueira as a whole. The littoral zone showed a persistent net autotrophic condition, contrasting with the pelagic zone in all geographical areas.

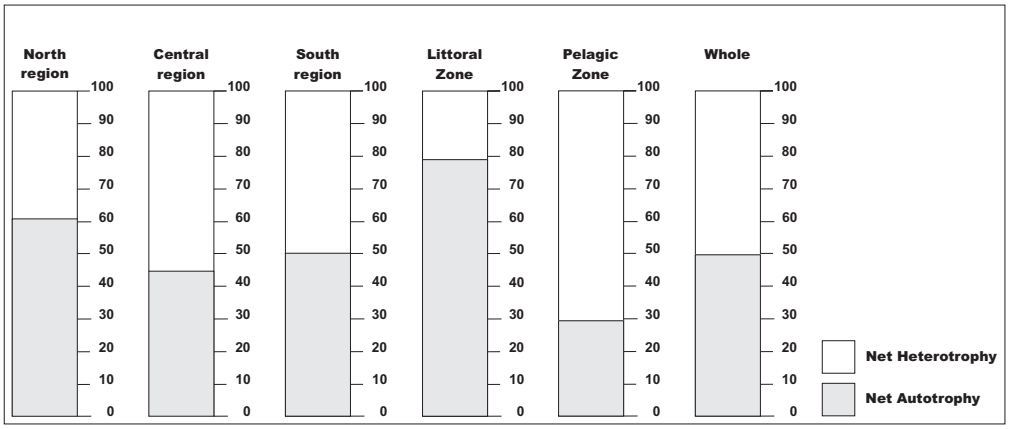

Figure 9: Percentage of time in net heterotrophic and net autotrophic conditions for Lake Mangueira. The gray scale represents the results for the net autotrophic condition and the net heterotrophic condition.

Table 6: Tukey's HSD (Honestly Significant Difference) test for NEP estimates in each individual compartment in order to assess metabolism estimates for Lake Mangueira. The statistically significant (p<0.05) differences between the means of the pairwise components analyzed are indicated in bold.

		North			Center			South			Mangueira Lake		
		Littoral	Pelagic	Entire Region	Littoral	Pelagic	Entire Region	Littoral	Pelagic	Entire Region	Littoral	Pelagic	Entire Region
North	Littoral	-	**0.14**	**0.12**	**-0.03**	**0.15**	**0.14**	**-0.02**	**0.15**	**0.13**	**-0.02**	**0.15**	**0.13**
	Pelagic		-	**-0.02**	**-0.17**	0.01	0.00	**-0.16**	0.01	-0.01	**-0.16**	0.01	-0.01
	Entire region			-	**-0.15**	**0.03**	**0.02**	**-0.14**	**0.03**	**0.01**	**-0.14**	**0.03**	**0.01**
Center	Littoral				-	**0.18**	**0.17**	0.01	**0.18**	**0.16**	**0.01**	**0.18**	**0.17**
	Pelagic					-	-0.01	**-0.17**	0.00	**-0.02**	**-0.17**	0.00	**-0.02**
	Entire region						-	**-0.16**	0.01	0.00	**-0.16**	0.01	0.00
South	Littoral							-	**0.17**	**0.16**	0.00	**0.17**	**0.16**
	Pelagic								-	**-0.02**	**-0.17**	0.00	**-0.02**
	Entire region									-	**-0.15**	**0.01**	0.00
Mangueira Lake	Littoral										-	**0.17**	**0.15**
	Pelagic											-	**-0.01**
	Entire region												-

4. Discussion

4.1. Lake Mangueira metabolism – temporal and spatial patterns

The metabolism estimates for Lake Mangueira showed a well-marked temporal and spatial pattern, in agreement with the spatial and temporal variability found previously for nutrients and phytoplankton (Fragoso Jr et al., 2011; Crossetti et al., 2013).

The GPP estimates showed hourly variations, according to light availability, and also wide day-to-day variation, which may be due to daily mixing in the water column affecting the light available for photosynthesis (Staehr and Sand-Jensen, 2007; Hanson et al., 2008). This daily variability was also apparent for NEP, reflecting the GPP variations, although the continuous estimates of R showed small daily variations, which have not been observed or taken into account in other studies (e.g. Staehr and Sand-Jensen, 2007; Coloso et al., 2011a; Sadro et al., 2011a).

In addition to the daily variations, well-marked seasonal patterns were also apparent for GPP, R, and NEP. GPP and R showed higher values during summer and lower values during winter, as also observed in some temperate lakes (Staehr and Sand-Jensen, 2007; Staehr et al., 2010; Coloso et al., 2011a; Sadro et al., 2011a; Laas et al., 2012); and agreed with the general seasonal patterns of nutrients and phytoplankton previously found for Lake Mangueira (Fragoso Jr et al., 2011; Crossetti et al., 2013). Specifically for the littoral zone, the peaks of GPP and R were shifted

to late summer and showed higher values than those found for the pelagic zone, which is likely associated with the presence of macrophytes in this zone (Lauster et al., 2006; Staehr and Sand-Jensen, 2007). The 2005 GPP peak for the littoral zone agreed with the most intense water diversion to the rice fields, leading to a decrease in water level and an increase in water temperature, and potentially increasing macrophyte production.

NEP estimates usually show wide daily variation, and daily shifts between the heterotrophic and autotrophic conditions have been reported in other systems (Staehr and Sand-Jensen, 2007; Staehr et al., 2010; Coloso et al., 2011a). The peak values found for NEP during spring and autumn can be explained by the grazing relationship between phyto- and zooplankton (Laas et al., 2012), which can influence the ecosystem respiration more than can primary production. Also, the water temperature influences the reduction of R more strongly than the reduction of GPP, causing the mid-autumn peak (Hanson et al., 2008; Holtgrieve et al., 2010). Although the autumn season could be regarded as mainly heterotrophic, positive peaks in NEP were observed. These peaks in ecosystem production might be related to cold fronts passing through the region. Autumn cold fronts followed by short-term warming periods (days to weeks) could explain the short-period positive peaks of NEP.

A spatial pattern was also apparent in the metabolism estimates. Differences between geographical areas and biological zones for phytoplankton and nutrients have been reported previously in Lake Mangueira (Fragoso Jr et al., 2008, 2011; Crossetti et al., 2013), and may be a factor controlling the spatial heterogeneity of metabolism estimates in the lake. For all seasons, GPP and R showed the same pattern, decreasing from the littoral to the pelagic zone. Submerged aquatic macrophytes tend to grow year-round in this system (Ferreira et al., 2009) and as a result the differentiation in metabolism occurs in all seasons, as also observed in temperate lakes (Lauster et al., 2006).

The metabolism estimate for winter months was lower, as was the difference between the littoral and pelagic zones, showing a tendency to homogeneity due to hydrodynamic circulation. The higher wind speeds in autumn and winter increase the lake mixing. GPP and R are positively related to water temperature (Staehr and Sand-Jensen, 2007; Hanson et al., 2008; Holtgrieve et al., 2010; Staehr et al., 2010; Coloso et al., 2011a), and in Lake Mangueira, the water temperature tends to be more homogeneous in winter (Fragoso Jr et al., 2011), which, combined with the more-pronounced hydrodynamic mixing, might explain the less-variable estimates during this season. The effect of wind on metabolism estimates was reported previously (van de Bogert et al., 2007), and in a lake where hydrodynamics plays a key role, such as in Lake Mangueira (Fragoso Jr et al., 2008, 2011), an increased effect of wind-driven hydrodynamics on the metabolism estimate can be expected during the winter.

The statistically significant (p<0.05) differences in metabolism between the biological zones and geographical areas (specifically the North area) indicate the existence of a persistent spatial separation in the metabolism of this lake. In a recent study (van de Bogert et al., 2012), an unprecedented number of dissolved-oxygen probes were used to analyze the spatial pattern in lake metabolism, and reported a well-defined spatial pattern. This spatial pattern of metabolism is commonly attributed to biomass, hydrodynamics, and/or lake morphometry (van de Bogert et al., 2007; Sadro et al., 2011a; Staehr et al., 2012a,b).

4.2. Lake Mangueira metabolism – composition of individual processes

In general, temporal and spatial patterns in lake metabolism are related to a series of metabolism drivers such as water temperature, nutrient availability, and phytoplankton chlorophyll-*a* (del Giorgio and Peters, 1994; Cole et al., 2000; Hanson et al., 2003; Lauster et al., 2006; Hanson et al., 2008; Staehr et al., 2010; Laas et al., 2012). The in-situ evaluation of these drivers is a difficult task, and in this study we focused on separating the specific processes composing GPP and R.

Phytoplankton production was the main process driving GPP estimates for each biological zone and geographical area. In temperate lakes, phytoplankton production was reported as the main driver of GPP estimates for phytoplankton-dominated lakes (Cremona et al., 2014a). However, in temperate lakes with abundant submerged macrophytes, GPP estimates increase near the macrophyte stand (Lauster et al., 2006). Lake Mangueira is a phytoplankton-dominated subtropical lake (Fragoso Jr et al., 2011; Crossetti et al., 2013) with a continuous stand of submerged macrophytes in the littoral zone (Ferreira et al., 2009; Fragoso Jr et al., 2011). Hence, the increase in the estimated GPP values in the littoral zone and the increase in the relative importance of the submerged macrophyte production were expected, indicating that distributed estimates can provide a better overview of lake metabolism and can clarify the relative importance of individual processes involved in metabolism estimations (Coloso et al., 2011a; Staehr et al., 2012b; Cremona et al., 2014a).

The estimates for R were composed mainly of the phytoplankton respiration, although the respiration of other communities was also relatively important. Other processes including fish and zoobenthos respiration and sediment oxygen demand contributed less to the R estimates (less than 10 %). Fish respiration does not play a key role in the O_2 budget for temperate lakes (Janse, 2005), and this might also be true for subtropical lakes. The small contribution of the sediments to the respiratory budget can be attributed to low organic-matter concentration in the sediment (Volkmer-Ribeiro et al., 2006). The importance of sediment organic-matter content in the overall lake nutrient dynamics and metabolism has been reported in previous studies (e.g. Smith et al., 1983; Sommaruga, 1991; Heyer and Kalff, 1998; Cowan and Boynton, 1996; Dunn et al., 2012).

Estimation of the relative importance of bacterial activity in metabolism is a new trend in research, and some recent studies have attempted to fully understand this relationship (Sadro et al., 2011b; They et al., 2013). In Lake Mangueira, bacterioplankton activity, estimated based on oxygen consumption, is low (They et al., 2010, 2013). However, these tests found a higher oxygen consumption (i.e., ecosystem respiration) than the values estimated by our process-based approach. Two main factors might explain these differences: (a) our model underestimates the levels of oxygen consumption; or (b) the optimal test conditions overestimated the oxygen consumption by submerged macrophytes. The contribution of zooplankton to respiration may be affected by the food biomass, temperature, and light, and consequently seasonal variations were expected (e.g. Devol, 1979; Gulati et al., 1982; Andrew, 1985; Ikeda, 1985; Ahrens and Peters, 1991; Berman et al., 2010; Cremona et al., 2014a). In Lake Mangueira, the estimated zooplankton biomass followed the phytoplankton biomass and showed a delay in reaching peak biomass, which indicates an asynchronous effect on the oxygen budget (Fragoso Jr et al., 2011).

NEP estimates can differ among areas in the same lake (Lauster et al., 2006; van de Bogert et al., 2007; Sadro et al., 2011a; van de Bogert et al., 2012; Staehr et al., 2012a). These differences are attributed to metabolism drivers such as chlorophyll-*a*, nutrient availabili ty, and water temperature (e.g. Hanson et al., 2003; Staehr and Sand-Jensen, 2007; Sadro et al., 2011a; Staehr et al., 2012a). As stated before, the NEP differences agreed with the biomass and nutrient patterns found.

4.3. Model capability and limitations

The IPH-ECO model proved to be suitable for representing most of the ecological and hydrodynamic processes in Lake Mangueira. The model outcomes were similar to those found previously for spatial and temporal patterns of nutrients and biomass concentration (Fragoso Jr et al., 2008, 2011). Nonetheless, the previous studies evaluated only three isolated points: three computer cells located in the North, Central, and South areas of the system. Further, Fragoso Jr et al. (2008, 2011) considered the North and South points in Lake Mangueira as littoral zones, which can lead to different interpretations since we used a depth criterion to delimit biological zones.

The process-based algorithm implemented in this study was capable of representing individual processes and their interactions, along with the spatial and temporal heterogeneity of the aquatic metabolism of Lake Mangueira. Adjusting the processes by comparing the model outcomes against nutrient concentrations and plankton biomass is standard procedure in ecological modeling studies (e.g. Hamilton and Schladow, 1997; Fragoso Jr et al., 2011; Trolle et al., 2012). However, the calibration of ecological models using specific processes (such as phytoplankton primary production or sediment oxygen demand) is a promising new line of research and might help to better represent individual processes in the future (Trolle et al., 2012). Using such a complex modeling framework, we might expect to reduce the uncertainty of parameter estimates, leading to much more reliable modeling tools.

The usual idealization of equal respiration during day and night continues to be discussed, and its role in metabolism estimations is still unknown (Hanson et al., 2008; Karakaya, 2011; Staehr et al., 2012b). Some studies indicate that continuous estimation (day- and night-time) of ecosystem respiration might improve our knowledge about different respiratory fluxes within the aquatic environment (McNair et al., 2013; Cremona et al., 2014b). Our results showed only a marginal difference (approximately 1%) between day and night respiration, indicating that the differences and relative importance may depend on the interplay of several factors within a particular lake. However, the understanding of the role of heterotrophic organisms in respiration rates is still incipient (Solomon et al., 2013; Sadro et al., 2014; Cremona et al., 2014a). Our model partially represents some trophic elements of Lake Mangueira, including fish, bacterioplankton, zooplankton, and macrophytes, due to the indirect calibration of the biomass of these elements. This limitation can be overcome by the use of better-calibrated and detailed data on trophic dynamics in Lake Mangueira.

5. Conclusion

Although shallow lakes are expected to be mostly homogeneous, the metabolism of Lake Mangueira showed spatial and seasonal variability. Continuous switching between autotrophic and heterotrophic conditions in the lake persisted over different spatial scales and even over small temporal scales. Our findings, based on process-based modeling, suggest that the usual idealization for metabolism estimation considering the use of point measurements of O2 in a lake can obscure the relative importance of the individual processes involved, and can provide only a partial picture of ecosystem functioning, leading to an incomplete conclusion about the trophic state and spatial/temporal heterogeneity. Phytoplankton production (approx. 90% in the pelagic zone and 70% in the littoral zone) was the main individual process comprising the estimated GPP values, in comparison to the epiphyton (approx. 3% in the pelagic zone and 8% in the littoral zone) and macrophytes (approx. 7% in the pelagic zone and 22% in the littoral zone). For the estimated values of R, the highest relative importance was associated with the respiration of heterotrophic organisms. The process-based modeling methodology integrating physical, chemical, and biological processes allowed estimates of ecosystem primary production and respiration in any computational time step. The model provided continuous estimates during the day and night, bringing it closer to the real ecosystem behavior, in comparison to the traditional assumption of equal respiration rates during day and night. In lakes with well-defined density layers, this approach can result in markedly different metabolism estimates in the profile, accounting more appropriately for the internal dynamics of individual physical and biological processes.

6. Acknowledgements

This study was supported by the Conselho Nacional de Desenvolvimento Científico e Tecnológico (CNPq), Brazil. We also acknowledge the assistance provided by the Instituto Chico Mendes de Conservação da Biodiversidade (ICMBio) and Estação Ecológica do TAIM (ESEC-Taim), Ministério do Meio Ambiente, Brazil. We are also grateful to the Global Lake Ecological Observatory Network (GLEON) for providing venue and resources for lake science discussions. Finally, we are grateful to Dr. Janet Reid (Trumansburg, NY, U.S.A.) for revising the final English version and two anonymous reviewers for their invaluable comments.

7. References

Ahrens, M.A., Peters, R.H., 1991. Plankton community respiration: relationships with size distribution and lake trophy. Hydrobiologia 224, 77–87.

Andrew, T., 1985. Seasonal variations in the metabolic rates of zooplankton populations in a Thames Valley reservoir. Hydrobiologia 127, 41–52.

Antenucci, J.P., Tan, K.M., Eikaas, H.S., Imberger, J., 2013. The importance of transport processes and spatial gradients on in situ estimates of lake metabolism. Hydrobiologia 700, 9–21.

Berman, T., Yacobi, Y.Z., Parparov, A., Gal, G., 2010. Estimation of long-term bacterial respiration and growth efficiency in lake Kinneret. FEMS Microbiology Ecology 71, 351–363. doi:10.1111/j.1574-6941.2009.00822.x.

Brighenti, L.S., Staehr, P.A., Gagliardi, L.M., Brandão, L.P.M., Elias, E.C., Mello, N.A.S.T., Barbosa, F.A.R., Bezerra-Neto, J.F., 2015. Seasonal changes in metabolic rates of two tropical lakes in the Atlantic forest of Brazil. Ecosystems 18, 589–604. doi:10.1007/s10021-015-9851-3.

Brookes, J.D., Antenucci, J., Hipsey, M., Burch, M.D., Ashbolt, N.J., Fergunson, C., 2004. Fate and transport of pathogens in lakes and reservoirs. Environment International 30, 741–459. doi:10.1016/j.envint.2003.11.006.

Cardoso, L.S., Fragoso Jr, C.R., Souza, R.S., Motta-Marques, D., 2012. Hydrodynamic control of plankton spatial and temporal heterogeneity in subtropical shallow lakes, in: Schulz, H.E., Simões, A.L.A., Lobosco, R.J. (Eds.), Hydrodynamics: Natural Water Bodies. InTech. chapter 2, pp. 27–48.

Cardoso, L.S., Motta-Marques, D., 2003. Rate of change of the phytoplankton community in Itapeva Lake (North Coast of Rio Grande do Sul, Brazil), based on the wind driven hydrodynamics regime. Hydrobiologia 497, 1–12.

Cardoso, L.S., Motta-Marques, D., 2004. Structure of the zooplankton community in a subtropical shallow lake (Itapeva Lake - South of Brazil) and its relationship to hydrodynamic aspects. Hydrobiologia 518, 123–134.

Cardoso, L.S., Motta-Marques, D., 2009. Hydrodynamics-driven plankton community in a shallow lake. Aquatic Ecology 43, 73–84.

Casulli, V., Cattani, E., 1994. Stability, accuracy and efficiency of a semi-implicit method for three-dimensional shallow water flow. Computers & Mathematics with Applications 27, 99–112.

Casulli, V., Cheng, R.T., 1992. Semi-implicit finite difference methods for three-dimensional shallow water flow. International Journal for Numerical Methods in Fluids 15, 629–648.

Cheng, R.T., Casulli, V., Gartner, J.W., 1993. Tidal, Residual, Intertidal Mudflat (trim) model and its applications to San Francisco Bay, california. Estuarine, Coastal and Shelf Science 36, 235–280.

Cole, J.J., Pace, M.L., Carpenter, S.R., Kitchell, J.F., 2000. Persistence of net heterotrophy in lakes during nutrient addition and food web manipulations. Limnology and Oceanography 45, 1718–1730.

Coloso, J.J., Cole, J.J., Pace, M.L., 2011a. Difficulty in discerning drivers of lake ecosystem metabolism with high-frequency data. Ecosystems 14, 935–948. doi:10.1007/s10021-011-9455-5.

Coloso, J.J., Cole, J.J., Pace, M.L., 2011b. Short-term variation in thermal stratification complicates estimation of lake metabolism. Aquatic Sciences 73, 305–315.

Cowan, J.L., Boynton, W.R., 1996. Sediment-water oxygen and nutrient exchanges along the longitudinal axis of Chesapeake Bay: Seasonal patterns, controlling factors and ecological significance. Estuaries 19, 562–580.

Cremona, F., Kõiv, T., Kisand, V., Laas, A., Zingel, P., Agasild, H., Feldmann, T.o., Jarvalt, A., Nõges, P., Nõges, T., 2014a. From bacteria to piscivorous fish: Estimates of whole-lake and component-specific metabolism with an ecosystem approach. PLoS ONE 9, e101845. doi:10.1371/journal.pone.0101845.

Cremona, F., Laas, A., Nõges, P., Nõges, T., 2014b. High-frequency data within a modeling framework: On the benefit of assessing uncertainties of lake metabolism. Ecological Modelling 294, 27–35. doi:10.1016/j.ecolmodel.2014.09.013.

Crossetti, L.O., Becker, V., Cardoso, L.S., Rodrigues, L.R., Costa, L.S., Motta-Marques, D., 2013. Is phytoplankton functional classification a suitable tool to investigate spatial heterogeneity in a subtropical shallow lake? Limnologica 43, 157–163.

del Giorgio, P.A., Peters, R.H., 1994. Patterns in planktonic P:R ratios in lakes: Influence of lake trophy and dissolved organic carbon. Limnology and Oceanography 39, 772–787.

Devol, A.H., 1979. Zooplankton respiration and its relation to plankton dynamics in two lakes of contrasting trophic state. Limnology and Oceanography 24, 893–905.

Dunn, R.J., Welsh, D.T., Jordan, M.A., Waltham, N.J., Lemckert, C.J., Teasdale, P.R., 2012. Benthic metabolism and nitrogen dynamics in a subtropical coastal lagoon: Microphytobenthos stimulate nitrification and nitrate reduction through photosynthetic oxygen evolution. Estuarine, Coastal and Shelf Science 113, 272–282. doi:10.1016/j.ecss.2012.08.016.

Ferreira, T.F., van Nes, E.H., Motta-Marques, D., 2009. Continuous growthof the giant grass *Zizaniopsis bonariensis* in subtropical wetlands. Freshwater Biology 54, 321–330. doi:10.1111/j.1365-2427.2008.02110.x.

Fragoso Jr, C.R., Janse, J.H., van Nes, E.H., Motta-Marques, D., 2009. IPH-TRIM3D-PCLake: A three-dimensional complex dynamic model for subtropical aquatic ecosystems. Ecological Modelling & Software 24, 1347–1348.

Fragoso Jr, C.R., Motta-Marques, D., Collischonn, W., Tucci, C.E., van Nes, E.H., 2008. Modelling spatial heterogeneity of phytoplankton in Lake Mangueira, a large shallow subtropical lake in South Brazil. Ecological Modelling 219, 125–137.

Fragoso Jr, C.R., Motta-Marques, D., Ferreira, T.F., Janse, J.H., van Nes, E.H., 2011. Potential effects of climate change and eutrophication on a large subtropical shallow lake. Ecological Modelling & Software 26, 1337–1348.

Giordano, J.C., Brush, M.J., Anderson, I.C., 2012. Ecosystem metabolism in shallow coastal lagoons: patterns and partitioning of planktonic, benthic, and integrated community rates. Marine Ecology Progress Series 458, 21–38. doi:10.3354/meps09719.

Gulati, R., Siewertsen, K., Postema, G., 1982. The zooplankton: its community structure, food and feeding, and role in the ecosystem Lake Vechten. Hydrobiologia 95, 127–163.

Hamilton, D.P., Schladow, S.G., 1997. Prediction of water quality in lakes and reservoirs. Part I - Model description. Ecological Modelling 96, 91–110.

Hanson, P.C., Bade, D.L., Carpenter, S.R., Kratz, T.K., 2003. Lake metabolism: Relationships with dissolved organic carbon and phosphorus. Ecological Modelling 48, 1112–1119.

Hanson, P.C., Carpenter, S.R., Armstrong, D.E., Stanley, E.H., Kratz, T.K., 2006. Lake dissolved inorganic carbon and dissolved oxygen: changing drivers from days to decades. Ecological Monographs 76, 343–363.

Hanson, P.C., Carpenter, S.R., Kimura, N., Wu, C., Cornelius, S.P., Kratz, T.K., 2008. Evaluation of metabolism models for free-water dissolved oxygen methods in lakes. Limnology and Oceanography:Methods 6, 454–465.

Heyer, C., Kalff, J., 1998. Organic matter mineralization rates in sediments: A within- and among-lake study. Limnology and Oceanography 43, 695–705.

Holtgrieve, G.W., Schindler, D.E., 2011. Marine-derived nutrients, bioturbation, and ecosystem metabolism: reconsidering the role of salmon in streams. Ecology 92, 373–385.

Holtgrieve, G.W., Schindler, D.E., Branch, T.A., A'mar, Z.T., 2010. Simultaneous quantification of aquatic ecosystem metabolism and reaeration using a bayesian statistical model of oxygen dynamics. Limnology and Oceanography 55, 1047–1063.

Ikeda, T., 1985. Metabolic rates of epipelagic marine zooplankton as a function of body mass and temperature. Marine Biology 85, 1–11.

Janse, J.H., 2005. Model studies on the eutrophication of shallow lakes and ditches. Ph.D. thesis. Wageningen University.

Ji, Z.G., 2008. Hydrodynamics and Water Quality: Modeling rivers, lakes, and estuaries. John Wiley & Sons, Inc.

Karakaya, N., 2011. Does different *versus* equal daytime and night-time respiration matter for quantification of lake metabolism using diel dissolved oxygen cycles? Annales de Limnologie - International Journal of Limnology 47, 251–257. doi:10.1051/limn/2011042.

Laas, A., Nõges, P., Kõiv, T., Nõges, T., 2012. High-frequency metabolism study in a large and shallow temperate lake reveals seasonal switching between net autotrophy and net heterotrophy. Hydrobiologia 694, 57–74. doi:10.1007/s10750-012-1131-z.

Lauster, G.H., Hanson, P.C., Kratz, T.K., 2006. Gross primary production and respiration differences among littoral and pelagic habitats in northern Wisconsin lakes. Journal of Fisheries and Aquatic Sciences 63, 1130–1141. doi:10.1139/F06-018.

McNair, J.N., Gereaux, L.C., Weinke, A.D., Sesselmann, M.R., Kendall, S.T., Biddanda, B.A., 2013. New methods for estimating components of lake metabolism based on free-water dissolved-oxygen dynamics. Ecological Modelling 263, 1130–1141. doi:10.1016/j.ecolmodel.2013.05.010.

Motta-Marques, D., Tucci, C.E., Calazans, 2002. O sistema hidrológico do TAIM (TAIM hydrological system), in: Seeliger, U., Cordazzo, C., Barbosa, F. (Eds.), Os sites e o programa brasileiro de pesquisas ecológicas de longa duração. Belo Horizonte, MG. chapter 8, pp. 125–144.

Odum, H.T., 1956. Primary production in flowing waters. Limnology and Oceanography 1, 103–119. doi:10.4319/lo.1956.1.2.0102.

Pacanowski, R., Philander, S., 1981. Parametrization of vertical mixing in numerical models of tropical oceans. Journal of Physical Oceanography 11, 1443–1451.

Sadro, S., Holtgrieve, G.W., Solomon, C.T., Koch, G.R., 2014. Widespread variability in overnight patterns of ecosystem respiration linked to gradients in dissolved organic matter, residence time, and productivity in a global set of lakes. Limnology and Oceanography 59, 1666–1678. doi:10.4319/lo.2014.59.5.1666.

Sadro, S., Melack, J.M., MacIntyre, S., 2011a. Spatial and temporal variability in the ecosystem metabolism of a high-elevation lake: integrating

benthic and pelagic habitats. Ecosystems 14, 1123–1140. doi:10.1007/s10021-011-9471-5.

Sadro, S., Nelson, C.E., Melack, J.M., 2011b. Linking diel patterns in community respiration to bacterioplankton in an oligotrophic high-elevation lake. Limnology and Oceanography 56, 540–550. doi:10.4319/lo.2011.56.2.0540.

Sand-Jensen, K., Staehr, P.A., 2007. Scaling of pelagic metabolism to size, trophy and forest cover in small Danish lakes. Ecosystems 10, 127–141. doi:10.1007/s10021-006-9001-z.

Sand-Jensen, K., Staehr, P.A., 2009. Net heterotrophy in small Danish lakes: a widespread feature over gradients in trophic status and land cover. Ecosystems 12, 336–348. doi:10.1007/s10021-008-9226-0.

Smith, K., Laver Jr., M., Brown, N., 1983. Sediment community oxygen consumption and nutrient exchange in the central and eastern North Pacific. Limnology and Oceanography 28, 882–898.

Solomon, C.T., Bruesewitz, D.A., Richardson, D.C., Rose, K.C., Van de Bogert, M.C., Hanson, P.C., Kratz, T.K., Larget, B., Adrian, R., Babin, B.L., Chiu, C.Y., Hamilton, D.P., Gaiser, E.E., Hendricks, S., Istvánovics, V., Laas, A., O'Donnel, D.M., Pace, M.L., Ryder, E., Staehr, P.A., Torgensen, T., Vanni, M.J., Weathers, K.C., Zhu, G., 2013. Ecosystem respiration: Drivers of daily variability and background respiration in lakes around the globe. Limnology and Oceanography 58, 849–866. doi:10.4319/lo.2013.58.3.0849.

Sommaruga, R., 1991. Sediment oxygen demand in man-made Lake Ton-Ton (Uruguay). Hydrobiologia 215, 215–221. doi:10.4319/lo.2013.58.3.0849.

Staehr, P.A., Baastrup-Spohr, L., Sand-Jensen, K., Stedmon, C., 2012a. Lake metabolism scales with lake morphometry and catchment conditions. Aquatic Sciences 74, 155–169. doi:10.1007/s00027-011-0207-6.

Staehr, P.A., Sand-Jensen, K., 2007. Temporal dynamics and regulation of lake metabolism. Limnology and Oceanography 52, 108–120.

Staehr, P.A., Sand-Jensen, K., Raun, A.L., Nilsson, B., Kidmose, J., 2010. Drivers of metabolism and net heterotrophy in contrasting lakes. Limnology and Oceanography 55, 817–830.

Staehr, P.A., Testa, J.M., Kemp, W.M., Cole, J.J., Sand-Jensen, K., Smith, S.V., 2012b. The metabolism of aquatic ecosystems: history, applications, and future challenges. Aquatic Sciences 74, 15–29. doi:10.1007/s00027-011-0199-2.

Straskraba, M., 1979. Natural control mechanisms in models of aquatic ecosystems. Ecological Modelling 6, 305–321.

They, N.H., Motta-Marques, D., Jeppesen, E., Søndergaard, M., 2010. Bacterioplankton in the littoral and pelagic zones of subtropical shallow lakes. Hydrobiologia 646, 311–326. doi:10.1007/s10750-010-0177-z.

They, N.H., Motta-Marques, D., Souza, R.S., 2013. Lower respiration in the littoral zone of a subtropical shallow lake. Frontiers in Microbiology 3, 1–10. doi:10.3389/fmicb.2012.00434.

Trolle, D., Hamilton, D.P., Hipsey, M.R., Bolding, K., Bruggeman, J., Mooij, W.M., Janse, J.H., Nielsen, A., Jeppensen, E., Elliot, J.A., Makler-Pick, V., Petzoldt, T., Rinke, K., Flindt, M.R., Arhonditsis, G.B., Gal, G., Bjerring, R., Tominaga, K., Hoen, J., Downing, A.S., Motta-Marques, D., Fragoso Jr., C.R., Søndergaard, M., Hanson, P.C., 2012. A community-based framework for aquatic ecosystem models. Hydrobiologia 683, 25–34. doi:10.1007/s10750-011-0957-0.

Trolle, D., Spigel, B., Hamilton, D.P., Norton, N., Sutherland, D., Plew, D., Allan, M.G., 2014. Application of a three-dimensional water quality model as a decision support tool for the management of land-use changes in the catchment of an oligotrophic lake. Environmental Management 54, 479–493. doi:10.1007/s00267-04-0306-y.

Tsai, J.W., Kratz, T.K., Hanson, P.C., Wu, J.T., Chang, W.Y., Arzberger, P.W., Lin, B.S., Lin, F.P., Chou, H.M., Chiu, C.Y., 2008. Seasonal dynamics, typhoons and the regulation of lake metabolism in a subtropical humic lake. Freshwater Biology 53, 1929–1941. doi:10.1111/j.1365-2427.2008.02017.x.

Vadeboncoeur, Y., Peterson, G., Zanden, J.V., Kalff, J., 2008. Benthic algal production across lake size gradients: interactions among morphometry, nutrients, and light. Ecology 89, 2542–2552.

van de Bogert, M.C., Bade, D.L., Carpenter, S.R., Cole, J.J., Pace, M.L., Hanson, P.C., Langman, O.C., 2012. Spatial heterogeneity strongly affects estimates of ecosystem metabolism in two north temperate lakes. Limnology and Oceanography 57, 1689–1700.

van de Bogert, M.C., Carpenter, S.R., Cole, J.J., Pace, M.L., 2007. Assessing pelagic and benthic metabolism using free water measurements. Limnology and Oceanography:Methods 5, 145–155.

Volkmer-Ribeiro, C., Motta-Marques, D., Rosa-Barbosa, R., Machado, V., 2006. Sponge spicules in sediments indicate evolution of coastal freshwater bodies, in: Proceedings of the 8th International Coastal Symposium, Itajaí, SC, Brazil, 2004, Journal of Coastal Research, (SI 39). pp. 469–472.

Zanden, M.J.V., Vadeboncoeur, Y., 2002. Fishes as integrators of benthic and pelagic food webs in lakes. Ecology 83, 2152–2161.

Capítulo 3

The role of wind-driven hydrodynamics on the process-based modeling of shallow lake metabolism

J. Rafael Cavalcanti

Artigo a ser submetido

The role of wind-driven hydrodynamics on the process-based modeling of shallow lake metabolism

J. Rafael Cavalcanti[a,*]

[a] *Universidade Federal do Rio Grande do Sul, Instituto de Pesquisas Hidráulicas, CP 15029, Porto Alegre, RS, Brazil*

Abstract

The hydrodynamics is an important factor controlling physical, chemical, and biological processes such as short-term water variations, sediment resuspension, seasonal temperature stratification, and the transport of different materials. Recently a relative importance of hydrodynamics is assumed and expected to drive the aquatic metabolism, defined as the balance between oxygen production and consumption, in different aquatic environments (NEP = GPP - R). In this study we used a process-based model capable of representing the main physical, chemical, and biological processes existing in aquatic environments (IPH-ECO model) to understand the effect of wind-driven hydrodynamic currents over aquatic metabolism estimations in Lake Mangueira, southern Brazil. The lake was divided into four different compartments (North, Center, South, and the lake as a whole) and each compartment subdivided in two biological zones (Littoral and Pelagic), a total of five different wind scenarios were used in order to assess spatial differences and the role of hydrodynamics in the metabolism estimates (GPP, R, and NEP). The simulated wind scenarios showed statistically significant (p<0.05) differences mainly in the littoral zones of each delimited compartment for GPP, R and NEP, changing the spatial separation in metabolism estimates of Lake Mangueira. The seasonal estimates showed higher values during Summer and lower values during Winter for GPP and R, whereas for NEP the higher values were observed during Spring. The simulated wind scenarios also showed variations by comparing the seasonal estimates in each wind scenario, with GPP and R showing different patterns when compared to NEP. Every season showed statistically significant variations for GPP and R and only Summer was significant for NEP in each wind scenario regarding the littoral zone. The simulated wind scenarios also affected the individual processes comprising the GPP and R estimates, consequently also affecting the NEP estimates of Lake Mangueira. The primary production of Periphyton and Aquatic Macrophytes showed more sensibility to the hydrodynamic pattern whereas microbial processes (mineralization and nitrification) were the most affected individual processes for ecosystem respiration. Our findings indicated that the spatial and temporal heterogeneity of metabolism estimations depends on the hydrodynamic pattern existent. In addition, individual processes show different effects with regard to the hydrodynamics in shallow lakes, with the sediment-related processes showing more sensibility to hydrodynamic forcing.

Keywords: Aquatic metabolism, hydrodynamics, seasonality, wind scenarios, Lake Mangueira

1. Introduction

Hydrodynamics can be an important factor controlling current induced physical, chemical, and biological processes, such as short-term water level variations, secchi depth, seasonal stratification, and the transport of materials and energy, specially at the free-surface (air-water exchange) and at the bottom (water-sediment exchange) of the aquatic ecosystem (e.g. Arfi et al., 1993; Fragoso Jr et al., 2008; Hamilton and Mitchell, 1997; Qian et al., 2011; Wu et al., 2000; Zhu et al., 2007; Fragoso Jr et al., 2011). In freshwater systems such as lakes wind can play a key-role as driver of hydrodynamics, structuring the horizontal and vertical mixing over the system (e.g. Csanady, 1968, 1973; MacIntyre and Melack, 1995). Wind-driven hydrodynamics can lead to the increase of material resuspension from bottom to the water column, structuring the spatial heterogeneity of planktonic communities, and regulating thermal

*More authors will be included before submission

structure (e.g. Chao et al., 2008; Bailey and Hamilton, 1997; Antenucci and Imberger, 2003; Gómez-Giraldo et al., 2008; Carrick et al., 1993; MacIntyre, 1993; Blukacz et al., 2010; Cardoso and Motta-Marques, 2009). Recently, a relative importance of physical processes (e.g., water circulation, turbulence) could also be noticed as driver of aquatic metabolism estimations (e.g. van de Bogert et al., 2012; Hu et al., 2015; Staehr et al., 2012c; Tonetta et al., 2016).

Lake metabolism can be depicted as a balance between Gross Primary Production (GPP) and Ecosystem Respiration (R), resulting in Net Ecosystem Production (NEP = GPP - R). Thus, the system can be defined as net autotrophic, when NEP is positive, or net heterotrophic, when NEP is negative (Staehr et al., 2012c; Cole et al., 2007). Metabolism estimates in lakes are under direct influence of different variables, driving the spatial and temporal variability of metabolic processes (Staehr et al., 2010; Coloso et al., 2011a; Hanson et al., 2006; Sadro et al., 2014; Solomon et al., 2013; Hall et al., 2015). Substrate availability, benthic substrate types, wind speed and direction, meteorological influence, macrophyte presence and watershed input can induce spatial and temporal variability of lake metabolism estimates (e.g. Lauster et al., 2006; Sadro et al., 2011; Sand-Jensen and Staehr, 2009; Staehr et al., 2012a; Hanson et al., 2003; Cole et al., 2000; del Giorgio and Peters, 1994; Obrador et al., 2014). A wide-spread methodology to estimate metabolic rates is the deploy of a high-frequency oxygen sensor usually at the pelagic zone of the lake (Alfonso et al., 2015; Brighenti et al., 2015; Cole et al., 2000; Hanson et al., 2003; Laas et al., 2012; Staehr and Sand-Jensen, 2007; Tsai et al., 2008). This approach can lead to some bias in understanding the metabolism dynamics, once the high-frequency signal might have some noise and water circulation might not be correctly taken into account (Batt and Carpenter, 2012; Cox et al., 2015; Cremona et al., 2014b; Holtgrieve et al., 2010; Rose et al., 2014; van de Bogert et al., 2012; Tonetta et al., 2016; Beck et al., 2015). Moreover, there are some processes that can alter oxygen concentrations but are not directly linked to metabolic processes, such as groundwater inflow, photo-respiration, and chemical reactions (Hanson et al., 2008).

The assessment of the physical processes as drivers of metabolic estimates is made by the use of two, or more, oxygen sensors spread over different zones, or vertical positions, of the lake (e.g. van de Bogert et al., 2007; Sadro et al., 2011; Hu et al., 2015; Staehr et al., 2012b; Tonetta et al., 2016). However, this approach is not suitable once it can be expensive and steady separation of different zones in lakes might not be the case some times (van de Bogert et al., 2012). Also, vertical stratification can play a key role structuring the vertical dynamics of lake metabolism estimations (Coloso et al., 2011b; Staehr et al., 2012b). To overcome this limitations the usage of mathematical models capable of integrating biologic and physical processes can be a promising tool to understand the complex dynamics of lake metabolism and its relations with hydrodynamics (Hanson et al., 2008; Coloso et al., 2011a; Staehr et al., 2012c; Tonetta et al., 2016). Mathematical models for estimating GPP, R, and NEP from high-frequency time series of lake and weather variables have already been developed (Hanson et al., 2008; Solomon et al., 2013; Sadro et al., 2014). These prediction models uses an Inverse Modelling Approach obtaining metabolic estimates by integrating the appropriate terms of the fitted model over the time period of interest (e.g. Staehr et al., 2012a; Brighenti et al., 2015; Obrador et al., 2014; Tonetta et al., 2016). Nevertheless, important physical processes (e.g., advection) might not be correctly accounted (Antenucci et al., 2013; McNair et al., 2013) and specific biological processes in the trophic cascate are not explicitly considered.

Process-based ecological models are important tools to understand specific individual biological processes and how they affect the ecosystem as a whole (e.g. Bonnet and Wessen, 2001; Gal et al., 2009; Jin et al., 2007; Mao et al., 2008). For water bodies where wind is the main driver of hydrodynamics, the use of hydrodynamic models coupled to complex process-based ecological models can give new insights about aquatic ecosystem functioning and potential effects over the environment (e.g. Fragoso Jr et al., 2008, 2011; You et al., 2007; Wu et al., 2013). The use of such models for estimating aquatic metabolism is a new and recent tool, in which the physical processes are accounted by the hydrodynamic model whereas lake metabolism can be estimated by the process-based model (McNair et al., 2013; Cavalcanti et al., 2016). The use of process-based models allows to understand the relative importance of individual processes, improving the knowledge about metabolism dynamics and specific biological communities driving it (Cremona et al., 2014a). In large shallow subtropical lakes, wind-driven hydrodynamics can play a key role structuring the intense vertical mixing in water column and structuring biological communities (e.g. Crossetti et al., 2013; Cardoso et al., 2012; Fragoso Jr et al., 2011). Also, the influence of hydrodynamics and its effects in metabolism estimations for subtropical lakes where suggested in previous studies (Tonetta et al., 2016; They et al., 2013). Thus, a coupled hydrodynamic and process-based approach can help understanding the influence of physical processes and the effects over metabolism estimates in lakes.

The influence of physical processes over dissolved oxygen dynamics is suggested as one of the main factor impos-

ing spatial heterogeneity in metabolism estimates. However, how the wind-driven hydrodynamics can affect specific individual processes is still non elucidated. In this study we use different wind scenarios as input data to a previous calibrated process-based complex hydrodynamic and ecological model in order to understand the metabolic processes dynamics and how it is affected by wind-driven hydrodynamics.

2. Methodology

2.1. Study area

Lake Mangueira (Fig. 1) is a large shallow lake in southern Brazil, located between 32°20'S and 33°00'S, and 052°20'W and 052°45'W. The lake surface area is approximately 820 km^2, with a mean depth of 2.6 m and maximum depth of 6.5 m, elongated, with a maximum length of 90 km and width of 10 km. The lake hydrodynamics is mainly controlled by the wind, with the northeast -southwest axis being the most important due to the wind blowing in this direction (Fragoso Jr et al., 2008). The system is polymictic with daily mixing due to strong winds and rare periods of stratification. Water inflow is negligible except for some small streams on the lake's western boundary (Fragoso Jr et al., 2008; Rodrigues et al., 2015). The trophic state varies from oligotrophic to mesotrophic, with mesotrophic conditions occuring in spring and summer. The lake is surrounded by dunes and two wetlands. This heterogeneous landscape harbors an exceptional biological diversity, which motivated the Brazilian federal authorities to protect part of the entire hydrological system as the TAIM Ecological Station in 1991 (Motta-Marques et al., 2002). The watershed (ca. 415 km^2) is used primarily for rice production.

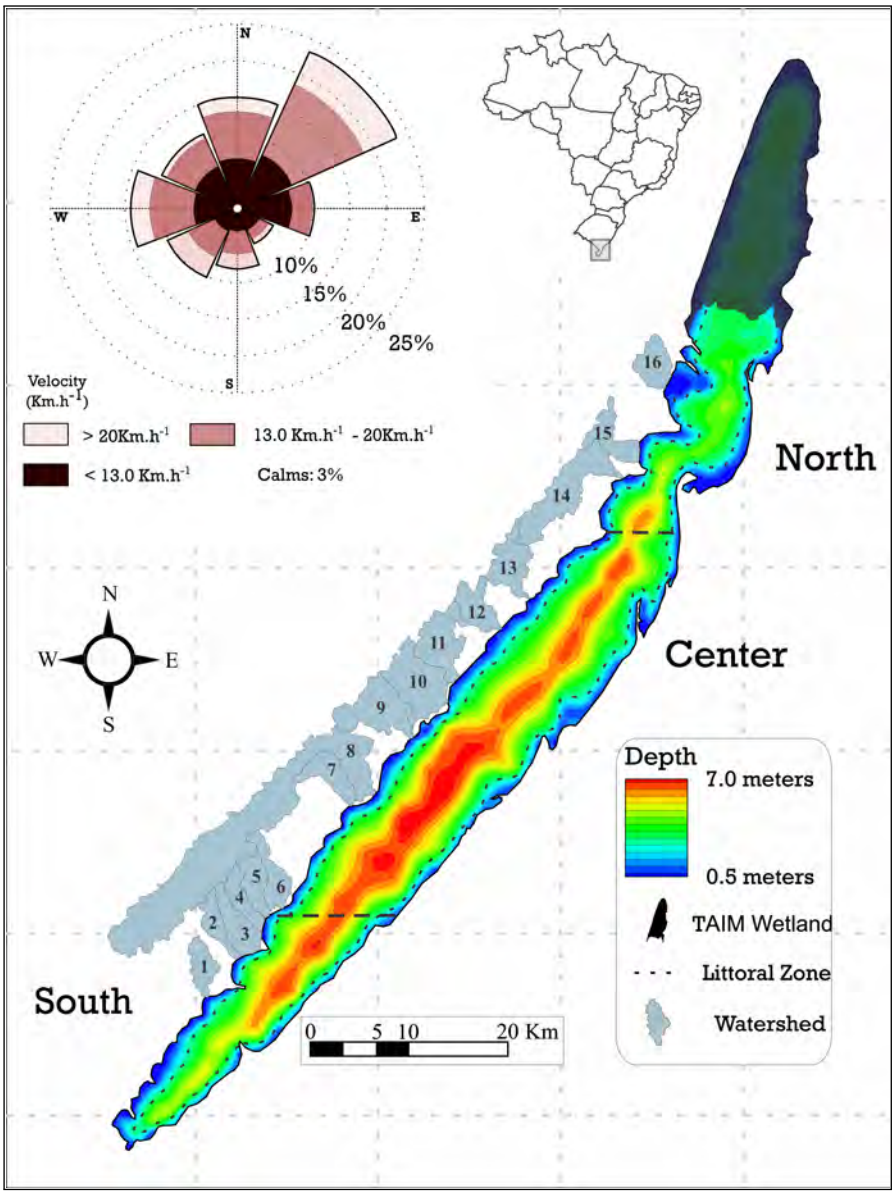

Figure 1: Lake Mangueira areas and zones. The dashed line (–) marks the estimated border between the littoral and pelagic zones. The continuous line (—) marks the limits of the North (N), Central (C), and South (S) areas. A Wind Rose shows the main wind intensity and direction from January 2001 to December 2006.

2.2. Model description

The IPH-ECO model (freely available in: `http://www.ipheco.org`), describes the main physical (water temperature and density, velocity fields, and free-water elevation), chemical and biological (e.g., nutrients and trophic structure) processes existing in the aquatic ecosystem. The model is capable of evaluating physical and water-quality processes simultaneously or separately in one, two, or three dimensions.

The IPH-ECO hydrodynamic module solves one form of the Reynolds-Averaged Navier-Stokes Equation using a semi-implicit discretization on structured staggered grids (see Casulli and Cheng, 1992; Cheng et al., 1993, for more details). The advection-diffusion solution for velocity fields is solved using an explicit Eulerian-Lagrangian finite-difference scheme. To further increase stability and accuracy, the θ-method (Casulli and Cattani, 1994) was also implemented. The parameter of horizontal eddy viscosity can be calibrated manually, and vertical eddy viscosity is

modeled as an empirical relationship (Pacanowski and Philander, 1981). To perform the coupling between physical and biological processes, IPH-ECO uses an explicit finite-difference scheme to solve an advection-diffusion-reaction type equation of the form:

$$\frac{\partial C}{\partial t} + u\frac{\partial HC}{\partial x} + v\frac{\partial HC}{\partial y} + w\frac{\partial HC}{\partial z} = \nu^h\left(\frac{\partial^2 HC}{\partial x^2} + \frac{\partial^2 HC}{\partial y^2}\right) + \frac{\partial}{\partial z}\left(\nu^v\frac{\partial HC}{\partial z}\right) + S(C) \quad (1)$$

where C is the scalar concentration being transported, which can be regarded as different ecosystem variables (e.g., nutrients, biomass, chlorophyll-a, or water temperature); H is the total water depth; $u(x, y, z, t)$, $v(x, y, z, t)$, and $w(x, y, z, t)$ are the velocity vector components in x, y, and z direction, respectively; ν^h and ν^v are the horizontal and vertical turbulent eddy viscosities; and $S(C)$ is a source/sink term that takes into account a wide variety of processes that can cause changes in the scalar concentration (e.g., settling, resuspension, and biological processes).

The limnology module of IPH-ECO is based largely on the PCLake model (Janse, 2005). Each water-quality variable has its own source/sink term, allowing IPH-ECO to describe nutrients (phosphorus, nitrogen, and silica) and dissolved-oxygen dynamics based on different processes. The model is able to describe biological biomasses such as phytoplankton, fish, aquatic macrophytes, zooplankton, and zoobenthos explicitly. Also, it describes in a simplified manner the benthic fluxes and sediment diagenesis.

2.3. Process-based algorithm for aquatic metabolism

The process-based algorithm used in this work was described in details previously Cavalcanti et al. (2016). Hence, only a brief description of the algorithm will be presented. The dissolved-oxygen (O_2) budget is related to NEP through a large variety of processes composing primary production and oxygen consumption (Odum, 1956). Accounting the effects of transport on dissolved oxygen concentration (DO) by the numerical solution of Eq. 1, the changes in DO regarding different biological processes can be depicted in terms of GPP, R, and NEP as follows:

$$\frac{\Delta O_2}{\Delta t} = NEP - F - A \quad (2)$$

where $NEP = GPP - R$ is the Net Ecosystem Production; GPP is the Gross Primary Production; and R is the Ecosystem Respiration. F is the atmospheric exchange of O_2 at the lake surface, and A represents other processes that may alter the dissolved-oxygen concentration (Table 1).

Table 1: Separation of variables representing metabolism processes. The first column shows the variables of Odum's equation; the second column shows the IPH-ECO processes used to describe lake metabolism.

Term in Odum's equation	**IPH-ECO model associated processes**
GPP	Primary Production of phytoplankton (Phyt Prod), submerged macrophytes (Macro Prod), and periphyton (Peri Prod)
R	Mineralization (Min Wat and Min Sed), nitrification (Nitr Wat and Nitr Sed) Respiration of phytoplankton (Phyt R), submerged macrophyte (Macro R), periphyton (Peri R), zooplankton (Zoop R), fish (Fish R), and zoobenthos (Bent R)
F	Atmospheric reaeration flux
A	Nitrate uptake from phytoplankton, submerged macrophyte, and periphyton

2.4. Model parameterization and simplifications

Lake Mangueira was computationally discretized using a quadrilateral grid with 500 m resolution. Due to the lake's daily mixing and brief stratification period only one vertical layer was adopted. The catchment flow was estimated using a simple rainfall-runoff model (IPH-II Model, (Tucci, 1998)) and the irrigation volume was assumed as constant through the irrigation period (summer). The meteorological data used in the simulations were collected two meteorological stations, one located at the center of the lake and another controlled by the Brazilian Institute of Meteorology (InMET) located at Santa Vitoria do Palmar (33°31'S, 53°21'W). The model was calibrated using field data obtained from 2001 to 2006, and collected at three field stations located in the North, Central, and South

areas of the lake (see Cavalcanti et al., 2016; Fragoso Jr et al., 2011, for more details about model calibration and parameterization). The model time step was set to 30s, the time weight θ was set to 0.55 and the bottom tension was parameterized using a Chezy coefficient of 45 $m^{1/2}.s^{-1}$. The output was set to 3600s, allowing us to analyze hourly estimates of lake metabolism in each wind scenario. Finally, the lake was divided into four spatial compartments to simplify the understanding of the results: North, Central and South areas, as well as Lake Mangueira as a whole (Fig. 1). In addition, each compartment was divided into two biological zones, pelagic and littoral, according to a depth criterion that relates the depth of the euphotic zone to the Secchi disk depth:

$$D = -\ln\left(\frac{I(D)}{I_s}\right).\frac{Z_s}{C_s} \tag{3}$$

where $I(D)/I_s = 0.01$ is the percentage of luminous energy that reaches the limit of the euphotic zone, C_s is a constant with typical values that range from 1.7 to 1.9 (here we adopted the mean value, 1.8), and Z_s is the Secchi disk depth, which was adopted as the mean Secchi depth observed for Lake Mangueira in the field data for the simulation period (0.89 m, see Fragoso Jr et al., 2011, for more details). The critical depth for the littoral zone was then calculated as 2.3 m.

2.5. Wind Scenarios

We evaluated lake Mangueira's metabolism estimations for different wind scenarios, which were derived from an observed wind time-series collected at tree meteorological stations within the lake. A total of five wind scenarios were explored, aiming to understand how wind direction and intensity plays its role in the lake metabolism. The control scenario took into account the observed time series of wind (scenario 0). The first scenario was composed by a simulation without wind as hydrodynamic driver (scenario 1), i.e., the currents are driven only by water Inflow (from the watershed) and Outflow (to irrigation). The second scenario was evaluated using the opposite direction of the observed wind series (scenario 2). The third scenario was composed by a constant wind, which has no seasonal feature and is consistent with the main direction (NE-SW) and mean wind intensity (4.6 $m.s^{-1}$). Finally, in the fourth scenario a 50% increase in wind velocity was used, aiming to increase horizontal homogeneity in the lake (scenario 4). The main characteristics of each scenario can be found in Table 2.

Table 2: Different wind scenarios chosen to evaluate the influence of hydrodynamics on Lake Mangueira's metabolism. Each scenario is classified with a number (first column) and a summary of its characteristics (second column).

Wind Scenario	Scenario Characteristics
Scenario 0	Control scenario using the observed wind time series
Scenario 1	Scenario without wind controlling hydrodynamics
Scenario 2	Scenario changing the observed direction with the opposite ones
Scenario 3	Constant wind, direction NE-SW and intensity 4.6 $m.s^{-1}$
Scenario 4	Scenario increasing the wind intensity in 50%

2.6. Data analysis

In order to assess the spatial differences between the wind scenarios, we use the Analysis of Variance (ANOVA) with confidence level set to 0.05. Also, a post-hoc analysis using Tukey's HSD (Honestly Significant Difference) test was performed in order to evaluate the significance of the differences between each scenario. The time series for each compartment of the lake was obtained by using all cells composing the specific compartment (geographical areas and biological zones). The metabolism time series for each compartment of the lake was obtained by using a volumetric-averaged value for all cells composing one compartment for each hourly output. Finally, the hourly output was then time-averaged using a 24-h interval (daily mean).

3. Results

The process-based metabolism estimations of Lake Mangueira showed increased values in the littoral zones of the lake regarding each geographic region delimited (Table 3, control scenario). In addition to the littoral-to-pelagic

gradient in the estimates of GPP, R and NEP, a North-to-South gradient was also observed with the northern region showing higher values while compared to the South and Center regions of the lake.

Table 3: Mean, standard deviation, minimum, and maximum calculated for Lake Mangueira metabolism estimates in each compartment (biological zones and geographical areas) regarding the Control Scenario. GPP stands for gross primary production, R for ecosystem respiration, and NEP for net ecosystem production.

		Pelagic				Littoral				Entire Region			
		Mean	Std. Dev.	Min	Max	Mean	Std. Dev.	Min	Max	Mean	Std. Dev.	Min	Max
North Region	GPP	0.17	0.07	0.01	0.33	0.50	0.24	0.02	1.41	0.22	0.08	0.01	0.42
	R	0.19	0.05	0.11	0.30	0.38	0.13	0.19	0.83	0.22	0.05	0.12	0.35
	NEP	-0.02	0.05	-0.20	0.11	0.12	0.17	-0.67	0.73	0.00	0.07	-0.24	0.16
Central Region	GPP	0.16	0.06	0.01	0.31	0.55	0.27	0.02	1.63	0.18	0.07	0.01	0.35
	R	0.18	0.05	0.11	0.30	0.40	0.14	0.19	0.91	0.20	0.05	0.11	0.32
	NEP	-0.03	0.05	-0.20	0.08	0.15	0.20	-0.73	0.87	-0.02	0.05	-0.21	0.10
South Region	GPP	0.16	0.06	0.01	0.32	0.54	0.26	0.02	1.54	0.20	0.08	0.01	0.38
	R	0.19	0.05	0.11	0.31	0.40	0.14	0.19	0.89	0.21	0.05	0.11	0.34
	NEP	-0.03	0.05	-0.21	0.09	0.14	0.19	-0.72	0.80	-0.01	0.06	-0.23	0.12
Lake Mangueira	GPP	0.16	0.06	0.01	0.31	0.53	0.26	0.02	1.54	0.19	0.07	0.01	0.37
	R	0.19	0.05	0.11	0.30	0.39	0.14	0.19	0.88	0.21	0.05	0.11	0.33
	NEP	-0.03	0.05	-0.20	0.08	0.14	0.19	-0.71	0.81	-0.01	0.06	-0.22	0.12

The comparison between different wind scenarios showed statistically significant (p<0.05) differences in the process-based metabolism estimations of Lake Mangueira. GPP estimates showed significant differences mainly for the littoral zones of the delimited compartments, regarding the majority of wind scenarios simulated (Table 4). Scenario 3 showed significant difference also regarding the entire region for each compartment. The different hydrodynamic patterns generated in each wind scenario was able to change the spatial heterogeneity of GPP estimates. Some scenarios led to a more homogeneous behavior in GPP estimates between the compartments whereas other scenarios led to a more pronounced spatial separation between the compartments (Table 4).

Table 4: Tukey's HSD (Honestly Significant Difference) test for GPP estimates in each individual compartment for different wind scenarios. The statistically significant (p<0.05) differences between the means of the pairwise component analyzed are indicated in bold. The means are calculated by comparing the control scenario against the other wind scenarios. Scenario 1 = scenario without wind, Scenario 2 = scenario with opposite wind, Scenario 3 = scenario with constant wind, and Scenario 4 = scenario with increased wind intensity.

		Scenario 1	Scenario 2	Scenario 3	Scenario 4
North	Littoral	**0.04**	**0.07**	**-0.39**	**-0.07**
	Pelagic	0.01	0.01	-0.01	<0.01
	Entire Region	0.01	0.01	**-0.06**	-0.01
Center	Littoral	**0.07**	**0.08**	**-0.38**	**-0.08**
	Pelagic	0.01	0.01	-0.01	<0.01
	Entire Region	0.01	0.01	**-0.03**	-0.01
South	Littoral	**0.05**	**0.09**	**-0.44**	**-0.09**
	Pelagic	0.01	0.01	-0.02	<0.01
	Entire Region	0.01	0.01	**-0.05**	-0.01
Mangueira	Littoral	**0.06**	**0.08**	**-0.41**	**-0.08**
	Pelagic	0.01	0.01	-0.01	<0.01
	Entire Region	0.01	0.01	**-0.04**	-0.01

Table 5: Tukey's HSD (honestly significant difference) test for GPP estimates in each individual compartment for different wind scenarios. Each number stands for the wind scenario, All stands for all the scenarios (Scenario 0 = Control Scenario, Scenario 1 = scenario without wind, Scenario 2 = scenario with opposite wind, Scenario 3 = scenario with constant wind, and Scenario 4 = scenario with increased wind intensity), and a blank space indicates no statistically significant (p>0.05) differences between the means of the pairwise component analyzed.

		North Region			Central Region			South Region			Lake Mangueira		
		Littoral	Pelagic	Entire Region	Littoral	Pelagic	Entire Region	Littoral	Pelagic	Entire Region	Littoral	Pelagic	Entire Region
North Region	Littoral	-	**All**	**All**	**All**	**All**	**All**	**All**	**All**	**All**	0,2,3,4	**All**	**All**
	Pelagic		-	**All**	**All**	0,1,2,4		**All**	2	0,1,3,4	**All**	0,1,2	3
	Entire Region			-	**All**	**All**	**All**	**All**	**All**	**All**	**All**	**All**	
Central Region	Littoral				-	**All**	**All**	2,3	**All**	**All**	0,2,4	**All**	**All**
	Pelagic					-	**All**	**All**		**All**	**All**		**All**
	Entire Region						-	**All**	**All**		**All**	**All**	
South Region	Littoral							-	**All**	**All**	3	**All**	**All**
	Pelagic								-	**All**	**All**		**All**
	Entire Region									-	**All**	0,2,3,4	
Lake Mangueira	Littoral										-	**All**	**All**
	Pelagic											-	**All**
	Entire Region												-

The simulated wind scenarios were also able to influence the process-based R estimates in Lake Mangueira. Except for the scenario without wind (Scenario 1) the R estimates in each littoral zone of the delimited compartments showed statistically significant (p<0.05) differences (Table 6). In agreement with the results found for GPP, the scenario with constant wind (Scenario 3) also showed statistically significant differences regarding the entire region of the delimited compartments. Nonetheless the scenario with opposite wind (Scenario 2) also showed a significant difference for the South entire region, which was not observed in the GPP estimates. The different hydrodynamic condition impose by each wind scenario was also able influence the spatial separation of respiration estimates, as observed for also for GPP (Table 7).

Table 6: Tukey's HSD (Honestly Significant Difference) test for R estimates in each individual compartment for different wind scenarios. The statistically significant (p<0.05) differences between the means of the pairwise component analyzed are indicated in bold. The means are calculated by comparing the control scenario against the other wind scenarios. Scenario 1 = scenario without wind, Scenario 2 = scenario with opposite wind, Scenario 3 = scenario with constant wind, and Scenario 4 = scenario with increased wind intensity.

		Scenario 1	Scenario 2	Scenario 3	Scenario 4
North	Littoral	-0.01	**0.05**	**-0.26**	**-0.04**
	Pelagic	<0.01	<0.01	-0.01	<0.01
	Entire Region	<0.01	0.01	**-0.04**	-0.01
Center	Littoral	0.01	**0.06**	**-024**	**-0.05**
	Pelagic	<0.01	<0.01	-0.01	<0.01
	Entire Region	<0.01	0.01	-0.02	<0.01
South	Littoral	<0.01	**0.06**	**-0.28**	**-0.05**
	Pelagic	<0.01	0.01	-0.01	<0.01
	Entire Region	<0.01	**0.01**	**-0.03**	-0.01
Mangueira	Littoral	<0.01	**0.05**	**-0.26**	**-0.05**
	Pelagic	<0.01	<0.01	-0.01	<0.01
	Entire Region	<0.01	0.01	**-0.03**	-0.01

Table 7: Tukey's HSD (honestly significant difference) test for R estimates in each individual compartment for different wind scenarios. Each number stands for the wind scenario, All stands for all the scenarios (Scenario 0 = Control Scenario, Scenario 1 = scenario without wind, Scenario 2 = scenario with opposite wind, Scenario 3 = scenario with constant wind, and Scenario 4 = scenario with increased wind intensity), and a blank space indicates no statistically significant (p>0.05) differences between the means of the pairwise component analyzed.

		North Region			Central Region			South Region			Lake Mangueira		
		Littoral	Pelagic	Entire Region	Littoral	Pelagic	Entire Region	Littoral	Pelagic	Entire Region	Littoral	Pelagic	Entire Region
North Region	Littoral	-	**All**	**All**	0,4	**All**	**All**	0,3,4	**All**	**All**	4	**All**	**All**
	Pelagic		-	**All**	**All**	0,1,2,4	3	**All**	2	0,1,3,4	**All**	0,1,2	3
	Entire Region			-	**All**	**All**	0,1,3,4	**All**	**All**	0,1,2,4	**All**	**All**	**All**
Central Region	Littoral				-	**All**	**All**	3	**All**	**All**	0,4	**All**	**All**
	Pelagic					-	3	**All**		**All**	**All**		**All**
	Entire Region						-	**All**	0,1,2,4	3	**All**	**All**	
South Region	Littoral							-	**All**	**All**	1,3,4	**All**	**All**
	Pelagic								-	**All**	**All**		0,1,3,4
	Entire Region									-	**All**	**All**	
Lake Mangueira	Littoral										-	**All**	**All**
	Pelagic											-	0,1,3,4
	Entire Region												-

The NEP estimations based in each wind scenario simulated showed statistically significant (p<0.05) difference mainly for the littoral zones of each compartment delimited (Table 8). Differing from GPP and R, the NEP series showed a significant difference regarding the North entire region for Scenario 1. The spatial separation in NEP estimates through each wind scenario also showed different behavior from the one observed for GPP and R with more compartments changing its spatial separation in each wind scenario (Table 9).

Table 8: Tukey's HSD (Honestly Significant Difference) test for NEP estimates in each individual compartment for different wind scenarios. The statistically significant (p<0.05) differences between the means of the pairwise component analyzed are indicated in bold. The means are calculated by comparing the control scenario against the other wind scenarios. Scenario 1 = scenario without wind, Scenario 2 = scenario with opposite wind, Scenario 3 = scenario with constant wind, and Scenario 4 = scenario with increased wind intensity.

		Scenario 1	Scenario 2	Scenario 3	Scenario 4
North	Littoral	**0.05**	**0.03**	**-0.14**	**-0.03**
	Pelagic	0.01	<0.01	-0.01	<0.01
	Entire Region	**0.02**	<0.01	-0.02	-0.01
Center	Littoral	**0.06**	**0.03**	**-0.15**	**-0.03**
	Pelagic	0.01	<0.01	-0.01	<0.01
	Entire Region	0.01	<0.01	-0.01	<0.01
South	Littoral	**0.06**	**0.03**	**-0.16**	**-0.03**
	Pelagic	0.01	<0.01	<0.01	<0.01
	Entire Region	0.01	<0.01	-0.01	<0.01
Mangueira	Littoral	**0.06**	**0.03**	**-0.15**	**-0.03**
	Pelagic	0.01	<0.01	-0.01	<0.01
	Entire Region	0.01	<0.01	-0.02	<0.01

Table 9: Tukey's HSD (honestly significant difference) test for NEP estimates in each individual compartment for different wind scenarios. Each number stands for the wind scenario, All stands for all the scenarios (Scenario 0 = Control Scenario, Scenario 1 = scenario without wind, Scenario 2 = scenario with opposite wind, Scenario 3 = scenario with constant wind, and Scenario 4 = scenario with increased wind intensity), and a blank space indicates no statistically significant (p>0.05) differences between the means of the pairwise component analyzed.

		North Region			Central Region			South Region			Lake Mangueira		
		Littoral	Pelagic	Entire Region	Littoral	Pelagic	Entire Region	Littoral	Pelagic	Entire Region	Littoral	Pelagic	Entire Region
North Region	Littoral	-	**All**	**All**	**All**	**All**	**All**	**All**	**All**	**All**	**All**	**All**	**All**
	Pelagic		-	0,2,3,4	**All**	0,2		**All**	0,2		**All**	2	
	Entire Region			-	**All**	0,2,3,4	0,2,3,4	**All**	**All**	0,1,2,4	**All**	**All**	0,1,2,4
Central Region	Littoral				-	**All**	**All**	0,1,2	**All**	**All**	0,1,2,4	**All**	**All**
	Pelagic					-		**All**		3	**All**		3
	Entire Region						-	**All**	0,1,2,4		**All**	0,1,2,4	
South Region	Littoral							-	**All**	**All**		**All**	**All**
	Pelagic								-	3	**All**		3
	Entire Region									-	**All**	0,1,2,4	
Lake Mangueira	Littoral										-	**All**	**All**
	Pelagic											-	
	Entire Region												-

The seasonal estimates of Lake Mangueira process-based ecosystem metabolism estimations showed a marked seasonality through the year, with higher values during summer and lower values during winter for GPP and R. The GPP estimates regarding each delimited compartment showed the same behavior with increased values and more amplitude (difference between the maximum and minimum values) of the estimations during summer and the opposite observed during winter (Fig. 2, Control Scenario). The seasonal time series delimited for each season (namely: Summer, Autumn, Winter, and Spring) also responded to the hydrodynamic conditions imposed by the wind scenario simulated. For the GPP estimates, each season showed statistically significant (p<0.05) differences when comparing different wind scenarios, specially for the littoral zones (Table 10). Specifically regarding the scenario without wind, the Winter series showed significant difference only in the littoral zone of the Central region. Scenario 3 showed only significant differences for Winter and Spring regarding the North and South entire regions.

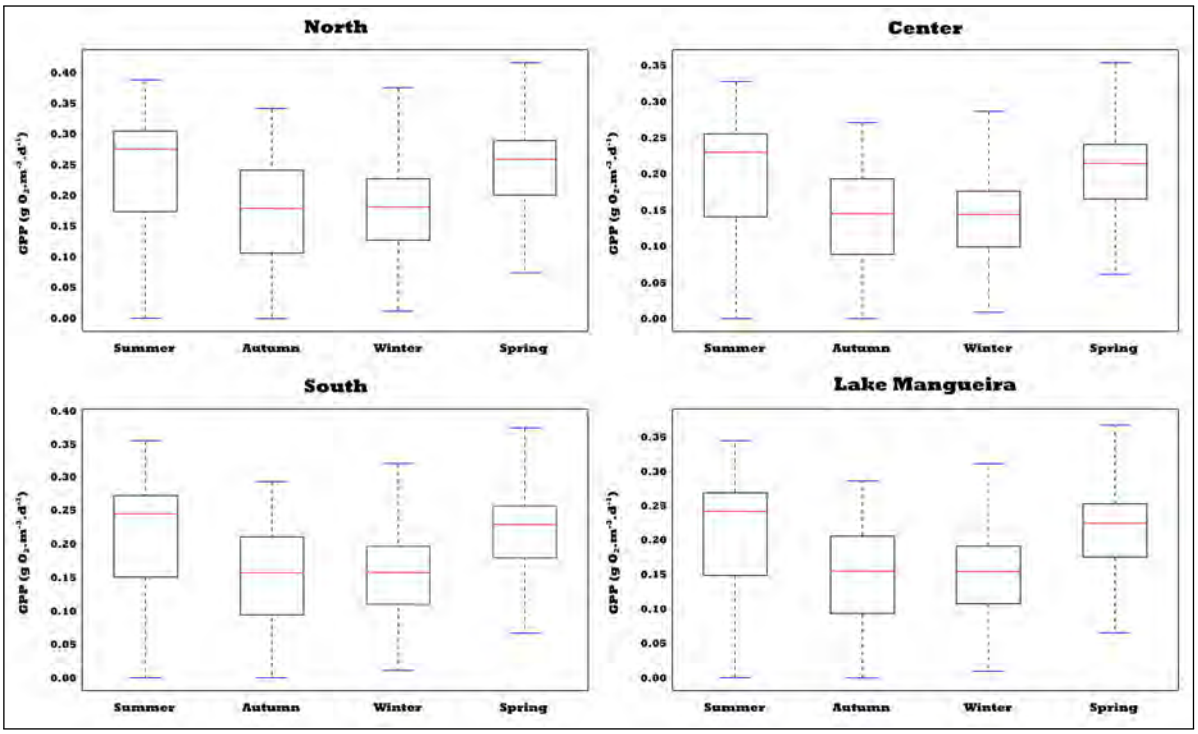

Figure 2: Box-plot of GPP Estimates in different seasons for each compartment as a whole regarding the Control Scenario. The blue line represents the minimum and maximum values observed in the series, the surrounding box represents the 75% and 25% percentile, respectively, and the red line represents the 50% percentile.

Table 10: Tukey's HSD test for GPP estimates in each individual compartment comparing the specific seasonal estimates for each wind scenario simulated. Scenario 1 = scenario without wind, Scenario 2 = scenario with opposite wind, Scenario 3 = scenario with constant wind, and Scenario 4 = scenario with increased wind intensity, S = Summer, A = Autumn, W = Winter, and Sp = Spring. Only seasons with statistically significant (p<0.05) differences between the compartments analyzed are showed.

		Scenario 1	Scenario 2	Scenario 3	Scenario 4
North	Littoral	S,A,Sp	S,A,W,Sp	S,A,W,Sp	S,A,W,Sp
	Pelagic	-	-	-	-
	Entire Region	-	-	W,Sp	-
Center	Littoral	S,A,W,Sp	S,A,W,Sp	S,A,W,Sp	S,A,W,Sp
	Pelagic	-	-	-	-
	Entire Region	-	-	-	-
South	Littoral	S,A,Sp	S,A,W,Sp	S,A,W,Sp	S,A,W,Sp
	Pelagic	-	-	-	-
	Entire Region	-	-	W,Sp	-
Mangueira	Littoral	S,A,Sp	S,A,W,Sp	S,A,W,Sp	S,A,W,Sp
	Pelagic	-	-	-	-
	Entire Region	-	-	-	-

The seasonal dynamics of the R estimates for each delimited compartment showed small amplitude with higher values observed during Summer and lower values during Winter (Fig. 3). Moreover, a much more homogeneous time series was observed during Winter when compared to other seasons. The comparison between different wind scenarios for the R estimates showed statistically significant (p<0.05) variations mainly in the littoral zones of the delimited compartments for all seasons (Table 11), except for the scenario without wind, were no significance was observed. Regarding the scenario with constant wind (Scenario 3) only Spring and Winter showed significant variations for the

entire regions.

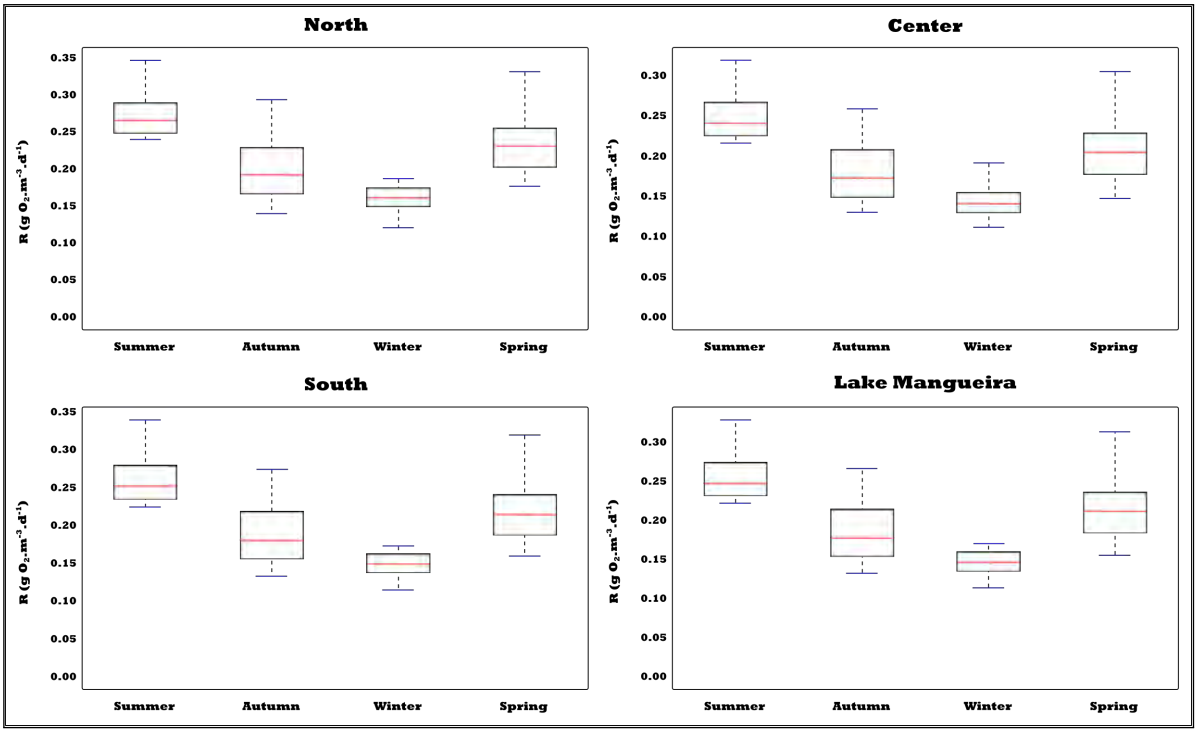

Figure 3: Box-plot of R Estimates in different seasons for each compartment as a whole regarding the Control Scenario. The blue line represents the minimum and maximum values observed in the series, the surrounding box represents the 75% and 25% percentile, respectively, and the red line represents the 50% percentile.

Table 11: Tukey's HSD test for R estimates in each individual compartment comparing the specific seasonal estimates for each wind scenario simulated. Scenario 1 = scenario without wind, Scenario 2 = scenario with opposite wind, Scenario 3 = scenario with constant wind, and Scenario 4 = scenario with increased wind intensity, S = Summer, A = Autumn, W = Winter, and Sp = Spring. Only seasons with statistically significant (p<0.05) differences between the compartments analyzed are showed.

		Scenario 1	Scenario 2	Scenario 3	Scenario 4
North	Littoral	-	S,A,W,Sp	S,A,W,Sp	S,A,W,Sp
	Pelagic	-	-	-	-
	Entire Region	-	-	W,Sp	-
Center	Littoral	-	S,A,W,Sp	S,A,W,Sp	S,A,W,Sp
	Pelagic	-	-	-	-
	Entire Region	-	-	Sp	-
South	Littoral	-	S,A,W,Sp	S,A,W,Sp	S,A,W,Sp
	Pelagic	-	-	-	-
	Entire Region	-	-	W,Sp	-
Mangueira	Littoral	-	S,A,W,Sp	S,A,W,Sp	S,A,W,Sp
	Pelagic	-	-	-	-
	Entire Region	-	-	W,Sp	-

195 The NEP estimates in each delimited compartment showed a different pattern regarding the seasonal variation when compared to GPP and R. In the NEP case, the highest values were observed during Winter, in addition to a more pronounced amplitude of the values (Fig. 4). The Summer time showed the smallest amplitude and Autumn and Spring were similar. The effect of hydrodynamics imposed by the different wind scenarios differs from the

behave observed previously for GPP and R. Only the littoral zones of each delimited compartment showed statistically
200 significant (p<0.05) differences, with Scenario 1 and Scenario 3 showing significant variations for all seasonal time series used (Table 12). The scenario with opposite wind showed significant variation only for Summer, Autumn and Spring and the scenario with increased wind intensity showed significant variations only for Summer.

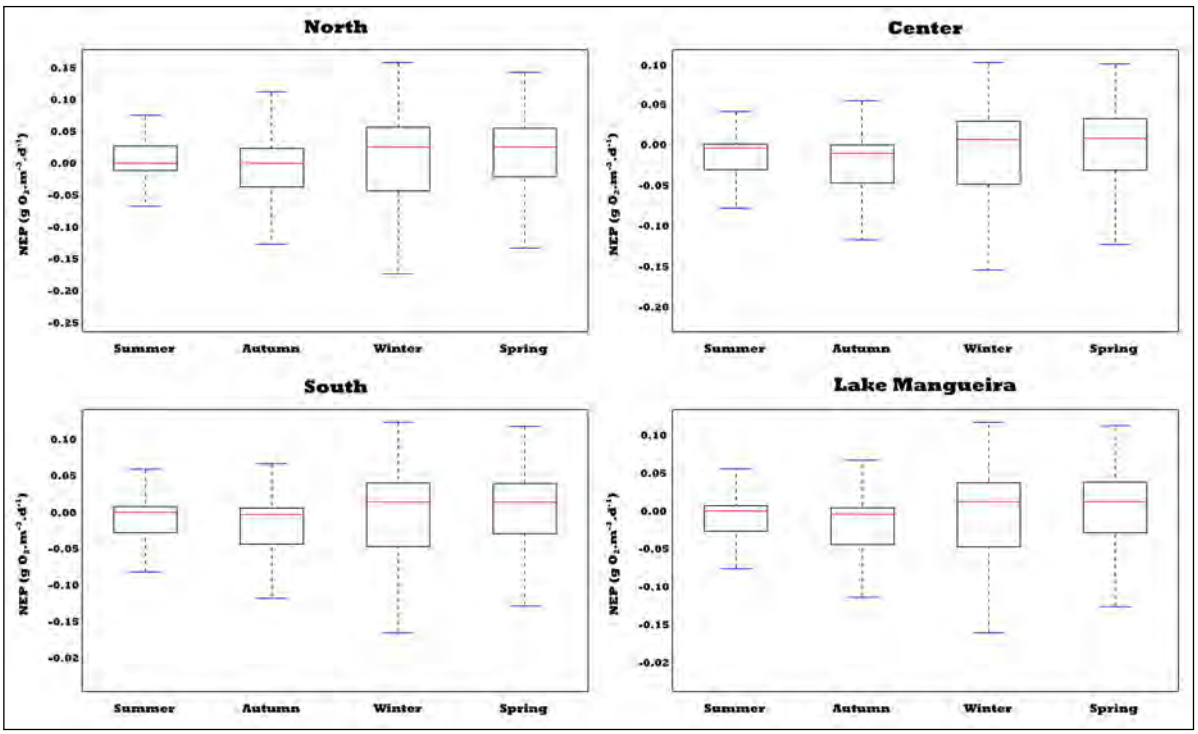

Figure 4: Box-plot of NEP Estimates in different seasons for each compartment as a whole regarding the Control Scenario. The blue line represents the minimum and maximum values observed in the series, the surrounding box represents the 75% and 25% percentile, respectively, and the red line represents the 50% percentile.

Table 12: Tukey's HSD test for NEP estimates in each individual compartment comparing the specific seasonal estimates for each wind scenario simulated. Scenario 1 = scenario without wind, Scenario 2 = scenario with opposite wind, Scenario 3 = scenario with constant wind, and Scenario 4 = scenario with increased wind intensity, S = Summer, A = Autumn, W = Winter, and Sp = Spring. Only seasons with statistically significant (p<0.05) differences between the compartments analyzed are showed.

		Scenario 1	Scenario 2	Scenario 3	Scenario 4
North	Littoral	S,A,W,Sp	S	S,A,W,Sp	S
	Pelagic	-	-	-	-
	Entire Region	-	-	-	-
Center	Littoral	S,A,W,Sp	S,A	S,A,W,Sp	S
	Pelagic	-	-	-	-
	Entire Region	-	-	-	-
South	Littoral	S,A,W,Sp	S,Sp	S,A,W,Sp	S
	Pelagic	-	-	-	-
	Entire Region	-	-	-	-
Mangueira	Littoral	S,A,W,Sp	S	S,A,W,Sp	S
	Pelagic	-	-	-	-
	Entire Region	-	-	-	-

3.1. Individual Processes

The individual processes comprising the GPP estimates (namely: Phytoplankton Production, Periphyton Production, and Macrophyte Production) showed small variations in each compartment comparing the different wind scenarios (Table 13). However, the relative changes in production for Periphyton and Macrophyte was high when comparing the different wind scenarios against the control scenario. Each compartment showed the same behavior with a decrease in production for scenarios 1 and 2, scenario 3 appears to have the most accentuated effect in this flux with an increase higher than 100% for Periphyton Production (Fig. 5, Lake Mangueira compartment).

Table 13: Differences in individual processes comprising the GPP estimates in each compartment for each wind scenario. The differences are calculated comparing the mean values of each wind scenario against the Control Scenario. A positive difference stands for an increase in the flux value and a negative difference a decrease. Lit stands for Littoral zone, Pel stands for Pelagic Zone, and Ent stands for the Entire region. Values in g $O2.m^{-3}.d^{-1}$.

Scenario 0 x Scenario 1												
	North			Center			South			Lake Mangueira		
GPP	Lit	Pel	Ent	Lit	Pel	Ent	Lit	Pel	Ent	Lit	Pel	Ent
Phyt Prod	-0.02	-0.01	-0.01	-0.02	-0.01	-0.01	-0.02	-0.01	-0.01	-0.02	-0.01	-0.01
Peri Prod	-0.02	0.00	0.00	-0.02	0.00	0.00	-0.02	0.00	0.00	-0.02	0.00	0.00
Macro Prod	-0.01	0.00	0.00	-0.03	0.00	0.00	-0.01	0.00	0.00	-0.02	0.00	0.00
Scenario 0 x Scenario 2												
	North			Center			South			Lake Mangueira		
GPP	Lit	Pel	Ent	Lit	Pel	Ent	Lit	Pel	Ent	Lit	Pel	Ent
Phyt Prod	-0.01	0.00	0.00	-0.01	0.00	0.00	-0.02	-0.01	-0.01	-0.01	0.00	-0.01
Peri Prod	-0.01	0.00	0.00	-0.02	0.00	0.00	-0.02	0.00	0.00	-0.02	0.00	0.00
Macro Prod	-0.04	0.00	-0.01	-0.04	0.00	0.00	-0.04	0.00	0.00	-0.04	0.00	0.00
Scenario 0 x Scenario 3												
	North			Center			South			Lake Mangueira		
GPP	Lit	Pel	Ent	Lit	Pel	Ent	Lit	Pel	Ent	Lit	Pel	Ent
Phyt Prod	0.03	0.01	0.01	0.04	0.01	0.01	0.05	0.01	0.01	0.04	0.01	0.01
Peri Prod	0.09	0.00	0.01	0.09	0.00	0.00	0.10	0.00	0.01	0.09	0.00	0.01
Macro Prod	0.22	0.00	0.03	0.18	0.00	0.01	0.22	0.00	0.02	0.20	0.00	0.01
Scenario 0 x Scenario 4												
	North			Center			South			Lake Mangueira		
GPP	Lit	Pel	Ent	Lit	Pel	Ent	Lit	Pel	Ent	Lit	Pel	Ent
Phyt Prod	0.01	0.00	0.00	0.01	0.00	0.00	0.01	0.00	0.00	0.01	0.00	0.00
Peri Prod	0.02	0.00	0.00	0.01	0.00	0.00	0.02	0.00	0.00	0.02	0.00	0.00
Macro Prod	0.03	0.00	0.00	0.04	0.00	0.00	0.05	0.00	0.00	0.04	0.00	0.00

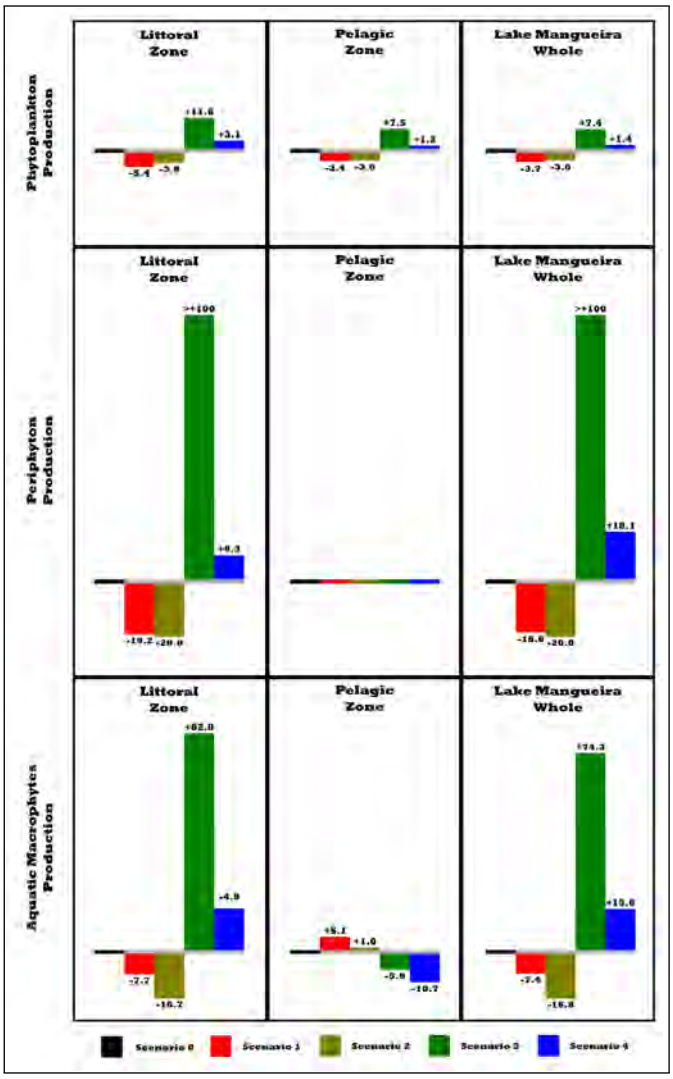

Figure 5: Percentual changes relative to the Control Scenario for individual processes comprising the GPP estimates regarding the Lake Mangueira compartment. The relative change was computed evaluating the average values between the different wind scenarios. A color bar indicates the scenario used to compare the average values and the percentual change is indicated on the top of the color bar.

210 The individual processes comprising GPP showed variations with regard to the season of the year. During summer and autumn the Periphyton and Macrophyte production showed an increase for the littoral zone (Fig. 6, Lake Mangueira as a whole). However, the phytoplankton production was the main process composing GPP regardless of the season of the year.

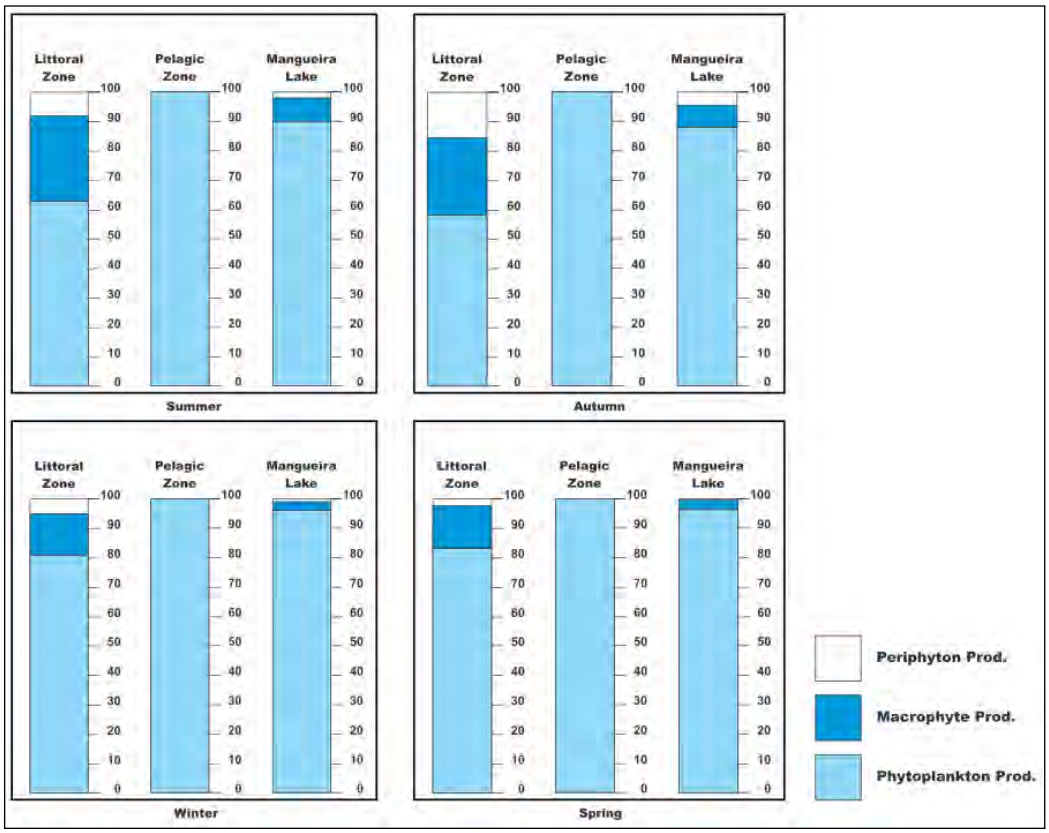

Figure 6: Individual processes comprising Gross Primary Production (GPP) through time for Lake Mangueira during Summer (top left), Autumn (top right), Winter (bottom left), and Spring (bottom right) in the Control Scenario. The blue scale represents the percentual results for phytoplankton, aquatic macrophytes, and periphyton primary production.

Regarding the individual processes comprising the R estimates, by comparing the average difference between the different wind scenarios related to the Control Scenario only Periphyton Respiration, Macrophyte Respiration, and Mineralization in the Sediment Bed showed marked variations (Table 14). The variations were mainly observed in the littoral zones with the pelagic zone showing an absence of the hydrodynamic effect for these processes comprising the R estimates. By comparing the relative changes between the control scenario and the different wind scenario, Periphyton Respiration and Macrophyte Respiration showed an increase of approx. 70 % in the littoral zones of each compartment (Fig. 7, Lake Mangueira compartment). The microbial processes (namely, mineralization and nitrification) in both, water column and sediment bed, showed the higher variations with mineralization in the sediment bed showing an increase higher than 100 % for scenario 1 (Fig. 8, Lake Mangueira compartment). The Nitrification in the water column showed marked variations also for the scenario 3.

Table 14: Differences in individual processes comprising the R estimates in each compartment for each wind scenario. The differences are calculated comparing the mean values of each wind scenario against the Control Scenario.A positive difference stands for an increase in the flux value and a negative difference a decrease. Lit stands for Littoral zone, Pel stands for Pelagic Zone, and Ent stands for the Entire region. Values in g $O2.m^{-3}.d^{-1}$.

Scenario 0 x Scenario 1												
	North			Center			South			Lake Mangueira		
R	Lit	Pel	Ent	Lit	Pel	Ent	Lit	Pel	Ent	Lit	Pel	Ent
Min Wat	0.00	0.00	0.00	0.00	0.00	0.00	0.00	0.00	0.00	0.00	0.00	0.00
Min Sed	0.02	0.00	0.01	0.02	0.00	0.00	0.02	0.00	0.00	0.02	0.00	0.00
Nitr Wat	0.00	0.00	0.00	0.00	0.00	0.00	0.00	0.00	0.00	0.00	0.00	0.00
Nitr Sed	0.00	0.00	0.00	0.00	0.00	0.00	0.00	0.00	0.00	0.00	0.00	0.00
Bent R	0.00	0.00	0.00	0.00	0.00	0.00	0.00	0.00	0.00	0.00	0.00	0.00
Fish R	0.00	0.00	0.00	0.00	0.00	0.00	0.00	0.00	0.00	0.00	0.00	0.00
Phyt R	0.00	0.00	0.00	0.00	0.00	0.00	0.00	0.00	0.00	0.00	0.00	0.00
Peri R	-0.01	0.00	0.00	-0.01	0.00	0.00	-0.01	0.00	0.00	-0.01	0.00	0.00
Macro R	-0.01	0.00	0.00	-0.02	0.00	0.00	-0.01	0.00	0.00	-0.01	0.00	0.00
Zoop R	0.00	0.00	0.00	0.00	0.00	0.00	0.00	0.00	0.00	0.00	0.00	0.00
Scenario 0 x Scenario 2												
	North			Center			South			Lake Mangueira		
R	Lit	Pel	Ent	Lit	Pel	Ent	Lit	Pel	Ent	Lit	Pel	Ent
Min Wat	0.00	0.00	0.00	0.00	0.00	0.00	0.00	0.00	0.00	0.00	0.00	0.00
Min Sed	0.00	0.00	0.00	0.00	0.00	0.00	0.00	0.00	0.00	0.00	0.00	0.00
Nitr Wat	0.00	0.00	0.00	0.00	0.00	0.00	0.00	0.00	0.00	0.00	0.00	0.00
Nitr Sed	0.00	0.00	0.00	0.00	0.00	0.00	0.00	0.00	0.00	0.00	0.00	0.00
Bent R	0.00	0.00	0.00	0.00	0.00	0.00	0.00	0.00	0.00	0.00	0.00	0.00
Fish R	0.00	0.00	0.00	0.00	0.00	0.00	0.00	0.00	0.00	0.00	0.00	0.00
Phyt R	0.00	0.00	0.00	0.00	0.00	0.00	0.00	0.00	0.00	0.00	0.00	0.00
Peri R	-0.01	0.00	0.00	-0.01	0.00	0.00	-0.01	0.00	0.00	-0.01	0.00	0.00
Macro R	-0.03	0.00	0.00	-0.03	0.00	0.00	-0.03	0.00	0.00	-0.03	0.00	0.00
Zoop R	0.00	0.00	0.00	0.00	0.00	0.00	0.00	0.00	0.00	0.00	0.00	0.00
Scenario 0 x Scenario 3												
	North			Center			South			Lake Mangueira		
R	Lit	Pel	Ent	Lit	Pel	Ent	Lit	Pel	Ent	Lit	Pel	Ent
Min Wat	0.00	0.00	0.00	0.00	0.00	0.00	0.00	0.00	0.00	0.00	0.00	0.00
Min Sed	0.01	0.00	0.00	0.01	0.00	0.00	0.01	0.00	0.00	0.01	0.00	0.00
Nitr Wat	0.00	0.00	0.00	0.00	0.00	0.00	0.01	0.00	0.00	0.00	0.00	0.00
Nitr Sed	0.00	0.00	0.00	0.00	0.00	0.00	0.00	0.00	0.00	0.00	0.00	0.00
Bent R	0.00	0.00	0.00	0.00	0.00	0.00	0.00	0.00	0.00	0.00	0.00	0.00
Fish R	0.01	0.00	0.00	0.00	0.00	0.00	0.00	0.00	0.00	0.00	0.00	0.00
Phyt R	0.00	0.00	0.00	0.00	0.00	0.00	0.00	0.00	0.00	0.00	0.00	0.00
Peri R	0.04	0.00	0.01	0.04	0.00	0.00	0.04	0.00	0.00	0.04	0.00	0.00
Macro R	0.16	0.00	0.02	0.13	0.00	0.01	0.15	0.00	0.01	0.14	0.00	0.01
Zoop R	0.00	0.00	0.00	0.00	0.00	0.00	0.00	0.00	0.00	0.00	0.00	0.00
Scenario 0 x Scenario 4												
	North			Center			South			Lake Mangueira		
R	Lit	Pel	Ent	Lit	Pel	Ent	Lit	Pel	Ent	Lit	Pel	Ent
Min Wat	0.00	0.00	0.00	0.00	0.00	0.00	0.00	0.00	0.00	0.00	0.00	0.00
Min Sed	0.00	0.00	0.00	0.00	0.00	0.00	0.00	0.00	0.00	0.00	0.00	0.00
Nitr Wat	0.00	0.00	0.00	0.00	0.00	0.00	0.00	0.00	0.00	0.00	0.00	0.00
Nitr Sed	0.00	0.00	0.00	0.00	0.00	0.00	0.00	0.00	0.00	0.00	0.00	0.00
Bent R	0.00	0.00	0.00	0.00	0.00	0.00	0.00	0.00	0.00	0.00	0.00	0.00
Fish R	0.00	0.00	0.00	0.00	0.00	0.00	0.00	0.00	0.00	0.00	0.00	0.00
Phyt R	0.00	0.00	0.00	0.00	0.00	0.00	0.00	0.00	0.00	0.00	0.00	0.00
Peri R	0.01	0.00	0.00	0.01	0.00	0.00	0.01	0.00	0.00	0.01	0.00	0.00
Macro R	0.02	0.00	0.00	0.03	0.00	0.00	0.03	0.00	0.00	0.03	0.00	0.00
Zoop R	0.00	0.00	0.00	0.00	0.00	0.00	0.00	0.00	0.00	0.00	0.00	0.00

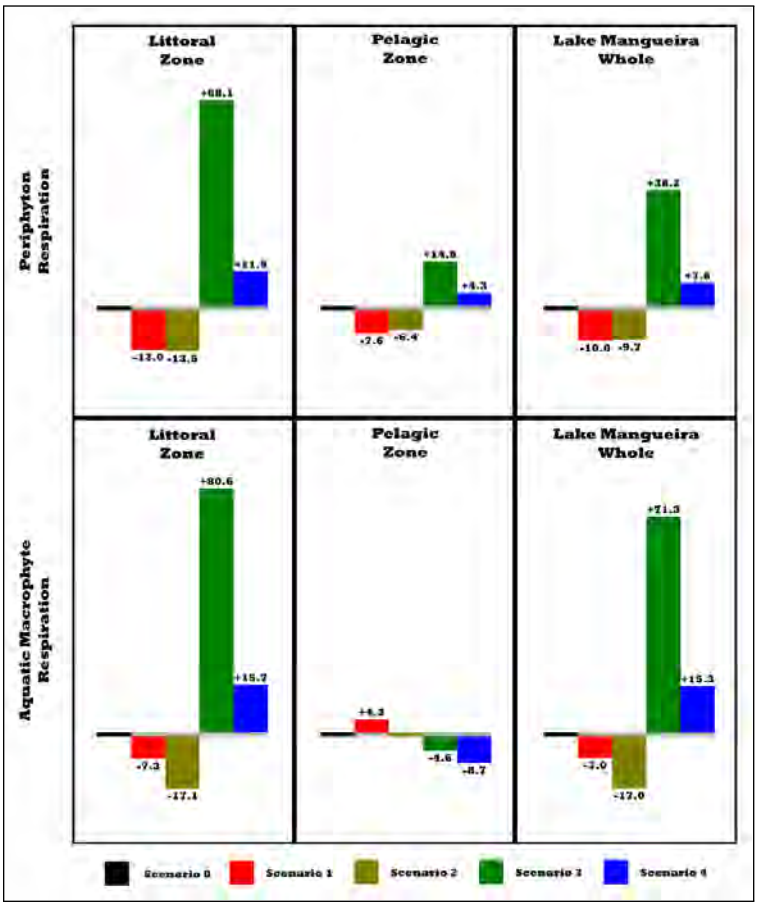

Figure 7: Percentual changes relative to the Control Scenario for Periphyton Respiration and Macrophyte Respiration estimates regarding the Lake Mangueira compartment. The relative change was computed evaluating the average values between the different wind scenarios. A color bar indicates the scenario used to compare the average values and the percentual change is indicated on the top of the color bar.

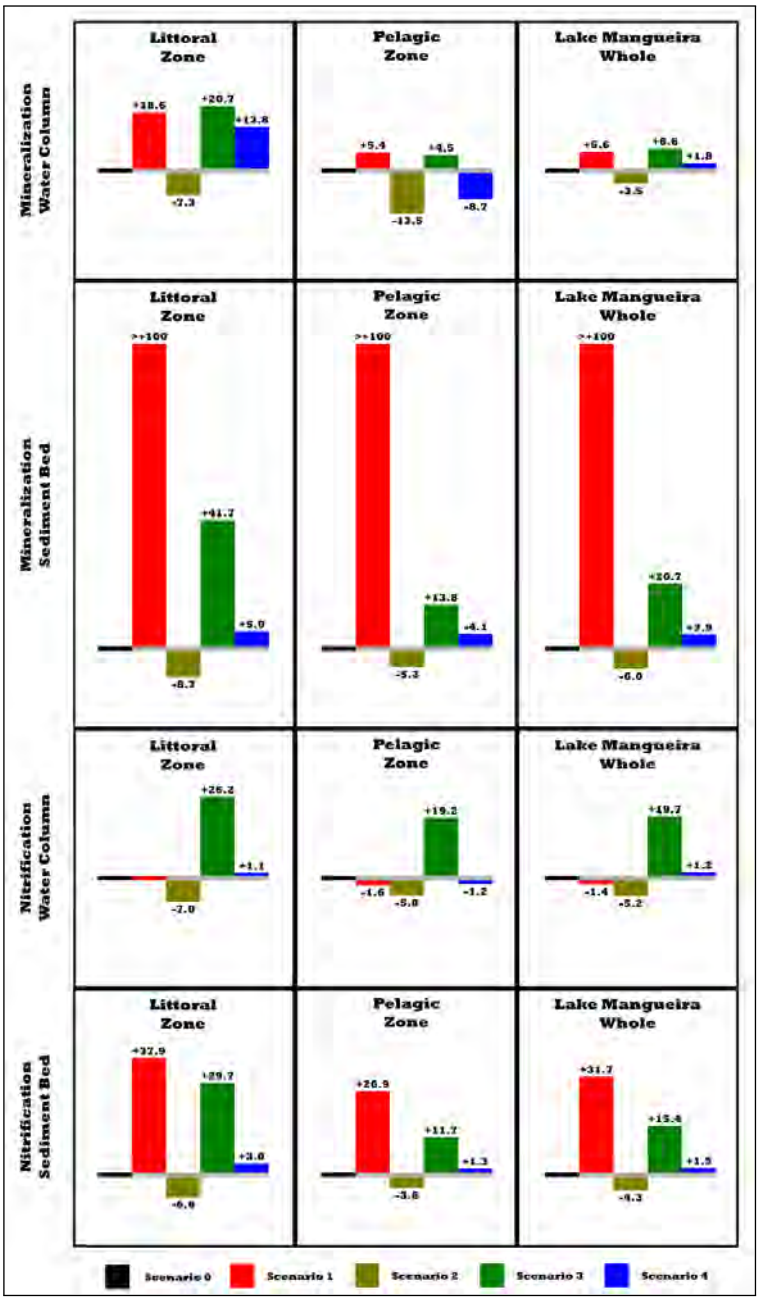

Figure 8: Percentual changes relative to the Control Scenario for Mineralization and Nitrification in Water Column and Sediment Bed estimates regarding the Lake Mangueira compartment. The relative change was computed evaluating the average values between the different wind scenarios. A color bar indicates the scenario used to compare the average values and the percentual change is indicated on the top of the color bar.

The individual processes comprising R also showed variations with regard to the season of the year. The littoral zone showed an increase in Macrophyte respiration and the pelagic zone an increase in zooplankton respiration for each season (Fig. 9, Lake Mangueira as a whole). Phytoplankton respiration was was the main process composing R estimates regardless of the season of the year.

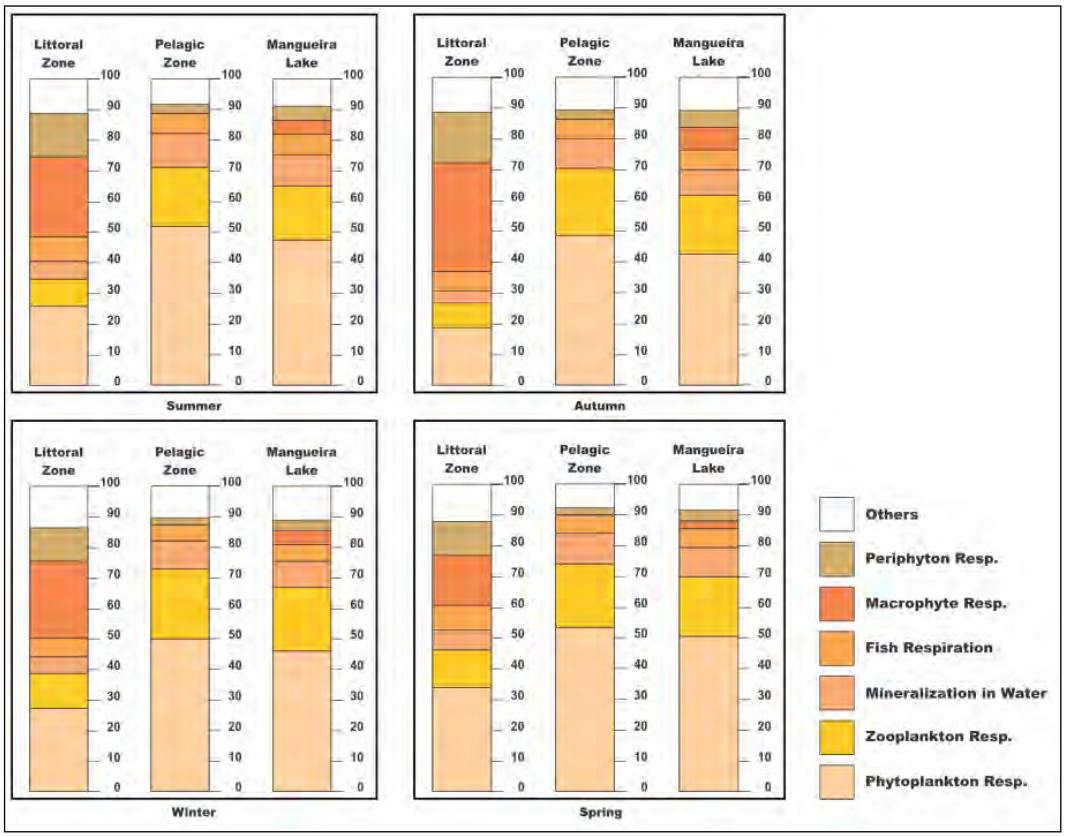

Figure 9: Individual processes comprising Ecosystem Respiration (R) through time for Lake Mangueira during Summer (top left), Autumn (top right), Winter (bottom left), and Spring (bottom right) in the Control Scenario. The brown scale represents the percentual results for phytoplankton respiration, zooplankton respiration, mineralization in water, fish respiration, aquatic macrophyte respiration, and periphyton respiration. The term "other processes" comprises sediment oxygen demand, nitrification in water, mineralization in water, and zoobenthos respiration.

The average differences in NEP estimates comparing each wind scenario against the Control Scenario showed higher values for the littoral zones of each compartment analyzed (Table 15). However, regarding the mean net autotrophic and mean net heterotrophic conditions the variations are more pronounced in the pelagic zone of each compartment (Fig. 10, Lake Mangueira compartment), with the scenario without wind and the scenario with constant wind affecting the most.

Table 15: Differences and percentual changes for NEP estimates in each compartment for each wind scenario. The differences are calculated comparing the mean values of each wind scenario against the Control Scenario and the percentual changes are computed related to the Control Scenario. A positive difference stands for an increase in the flux value and a negative difference a decrease. Lit stands for Littoral zone, Pel stands for Pelagic Zone, and Ent stands for the Entire region. Net Aut stands for Net Autotrophic and Net Het stands for Net Heterotrophic. Values in g $O2.m^{-3}.d^{-1}$.

Scenario 0 x Scenario 1												
	North			Center			South			Lake Mangueira		
	Lit	Pel	Ent	Lit	Pel	Ent	Lit	Pel	Ent	Lit	Pel	Ent
NEP	-0.05	-0.01	-0.02	-0.06	-0.01	-0.01	-0.06	-0.01	-0.01	-0.06	-0.01	-0.01
Net Aut (%)	-5.2	-25.2	-18.1	-4.1	-19.4	-22.5	-4.9	-22.5	-24.5	-4.6	-21.6	-22.7
Net Het (%)	18.7	15.2	28.8	16.8	8.9	22.7	18.8	9.3	26.4	18.2	10.1	26.4
Scenario 0 x Scenario 2												
	North			Center			South			Lake Mangueira		
	Lit	Pel	Ent	Lit	Pel	Ent	Lit	Pel	Ent	Lit	Pel	Ent
NEP	-0.02	0.00	0.00	-0.03	0.00	0.00	-0.03	0.00	0.00	-0.03	0.00	0.00
Net Aut (%)	0.0	-3.7	-2.1	0.4	-5.4	-6.0	0.0	-3.8	-3.9	0.0	-3.4	-5.6
Net Het (%)	0.0	2.2	3.4	-1.5	2.5	6.0	0.0	1.6	4.2	0.0	1.6	6.5
Scenario 0 x Scenario 3												
	North			Center			South			Lake Mangueira		
	Lit	Pel	Ent	Lit	Pel	Ent	Lit	Pel	Ent	Lit	Pel	Ent
NEP	0.13	0.01	0.02	0.13	0.01	0.01	0.14	0.00	0.01	0.13	0.01	0.01
Net Aut (%)	1.9	24.4	14.8	1.6	25.7	20.3	1.6	16.4	17.0	1.3	24.8	18.0
Net Het (%)	-6.8	-14.8	-23.6	-6.6	-11.8	-20.5	-6.3	-6.8	-18.3	-4.9	-11.6	-21.0
Scenario 0 x Scenario 4												
	North			Center			South			Lake Mangueira		
	Lit	Pel	Ent	Lit	Pel	Ent	Lit	Pel	Ent	Lit	Pel	Ent
NEP	0.03	0.00	0.00	0.03	0.00	0.00	0.03	0.00	0.00	0.03	0.00	0.00
Net Aut (%)	0.8	5.3	2.3	0.1	3.8	4.8	0.4	7.8	5.8	0.0	3.1	3.7
Net Het (%)	-2.7	-3.2	-3.6	-0.5	-1.8	-4.8	-1.4	-3.3	-6.2	0.0	-1.5	-4.3

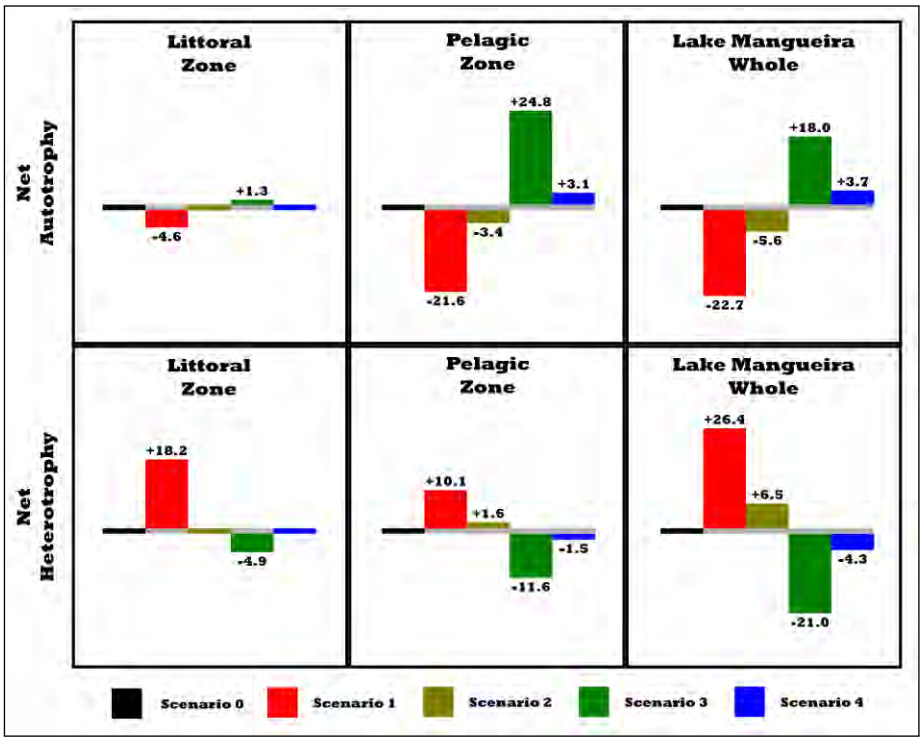

Figure 10: Percentual changes relative to the Control Scenario for Net Autotrophy and Net Heterotrophy conditions for the Lake Mangueira compartment. The relative change was computed evaluating the average values between the different wind scenarios. A color bar indicates the scenario used to compare the average values and the percentual change is indicated on the top of the color bar.

The trophic condition (autotrophic or heterotrophic) in Lake Mangueira showed marked variations with regard to the season of the year, specially in the pelagic zone of the lake (Fig. 11, Lake Mangueira as a whole). This constantly change in the mean condition in the pelagic zone also influenced the net autotrophy and net heterotrophy in the compartment as a whole, depending on the season of the year.

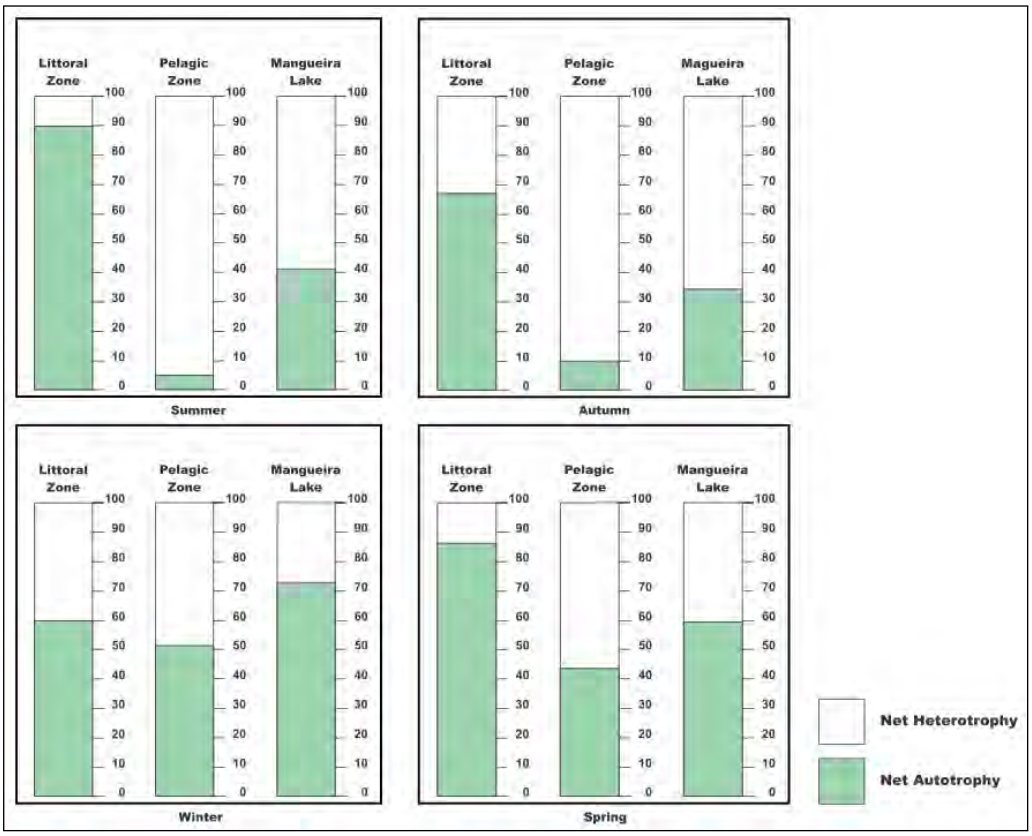

Figure 11: Percentage of time in net heterotrophic and net autotrophic conditions for Lake Mangueira during Summer (top left), Autumn (top right), Winter (bottom left), and Spring (bottom right) in the Control Scenario. The green color represents the percentual results for the net autotrophic condition and the blue color net heterotrophic condition.

4. Discussion

The role of hydrodynamics over metabolism estimates is a recent field of research and the majority of studies compute only partially the physical processes leading to mixing and transport of substances in water. The use of a process-based computational model capable of integrating hydrodynamics and biological processes allowed to evaluate physical processes interacting simultaneously with the biological processes comprising the metabolism estimates (GPP, R, and NEP). By changing the main driver of Lake Mangueira hydrodynamics (i.e., the wind) the effect of wind-driven currents was evaluated and the potential changes in aquatic metabolism was estimated. This approach can be an important way to complement the studies performed by using only punctual estimates of lake metabolism, difficulting the correct estimation of hydrodynamics and its role structuring the aquatic metabolism estimates (Hanson et al., 2008; van de Bogert et al., 2012).

The wind-driven hydrodynamic scenarios simulated here were able to change the GPP, R, and consequently NEP estimates in Lake Mangueira, mainly for the littoral zone of the lake (Tables 4, 6, and 8). Due to the lower depths and wave circulation such as gyres and seiches existing in Lake Mangueira (Fragoso Jr et al., 2011), the metabolism estimation sensibility to wind patterns in the littoral zone of each compartment agrees with the results found recently in other lakes (Idrizaj et al., 2016; Tonetta et al., 2016), were a relative importance of benthic processes was observed. Our findings indicated an increase in benthic-littoral processes specially the periphyton and macrophyte production and respiration for GPP (Fig. 5) and R (Fig. 7), respectively, and also microbial processes (mineralization and nitrification) for R (Fig. 8). The works of Obrador and Petrus (2013); Lauster et al. (2006); Idrizaj et al. (2016) show the importance of a correct description of littoral and benthic metabolism estimations, with spatial heterogeneity in the metabolism estimations being observed comparing littoral and pelagic zones using punctual estimations. The wind-

driven current can transport benthic material and oxygen from littoral zone to pelagic zone, influencing the estimates of primary production, whereas the resuspension of material due to wind and organic matter from the catchment can increase the consumption of oxygen in the littoral zone (van de Bogert et al., 2007, 2012), leading to a more heterogeneous metabolism estimate. Interestingly, the scenario without wind showed no significant variation in the respiration estimates however an increase up to 100 % was observed in the mineralization process in this wind scenario. Despite the high increase in this oxygen consumption process, the phytoplankton respiration is the main process controlling the R estimates in Lake Mangueira (Cavalcanti et al., 2016), showing the importance of estimating correctly the vast majority of biological processes contributing to the metabolism estimations in aquatic environments. As suggested in different works, the hydrodynamics plays a key-role structuring the spatial heterogeneity of metabolism estimations in aquatic environments (Hanson et al., 2008; van de Bogert et al., 2012; Staehr et al., 2012c; Tonetta et al., 2016). For Lake Mangueira the changing of wind patterns changed the heterogeneity in metabolism estimations (Tables 5, 7, and 9) by increasing or decreasing the homogeneity between the lake compartments (North, Center, and South) and biological zones (littoral and pelagic).

The aquatic metabolism seasonal dynamics in Lake Mangueira showed a marked variation, with higher values during summer and lower values during winter for GGP and R. This elevated variation in GPP and R estimates is driven by the phytoplankton growth during summer and decay during winter (Fragoso Jr et al., 2011; Crossetti et al., 2013), since the phytoplankton production and respiration is the main process composing GPP and R estimates (Cavalcanti et al., 2016). The seasonal variation in GPP and R estimates is also observed in different lakes in many regions, often well correlated with chlorophyll-*a* and water transparency (e.g., Staehr et al., 2012c; Tonetta et al., 2016; Hanson et al., 2008; Sand-Jensen and Staehr, 2009). The NEP variation showed an increase in amplitude during winter (Fig. 4), which could be a combined effect of the increase in water depth due to the stop in irrigation and the less incoming organic matter and nutrients from the catchment, which can subsidize larger respiration values during summer in Lake Mangueira (Fragoso Jr et al., 2011). Moreover, the reduction in water temperature tend to show a negative effect on ecosystem respiration for many lakes Staehr et al. (2010); Sadro et al. (2011); Laas et al. (2012); Staehr et al. (2012c). The combined effect of catchment load and water temperature is also observed in the percentual trophic condition of Lake Mangueira (Fig. 11) where the summmer showed a tendency to be net heterotrophic. Hydrodynamics had an interesting effect on seasonal metabolic rates for Lake Mangueira, with GPP and R showing a significant change in the littoral zone for each season (Tables 10 and 11). The scenario without wind showed significant variations only for GPP and the majority of compartments showed no variation for Winter time. In this particular case, the biological condition such as water temperature ans transparency shows more importance than hydrodynamics, which is also observed in lakes with small effect of the wind Laas et al. (2012).

5. Conclusion

The use of computational models capable of integrating hydrodynamic and biological processes simultaneously has proven to be an important complement in regard to investigating ecosystem metabolism heterogeneity in shallow lakes. The process-based model was capable to represent the main features and differences between biological zones of Lake Mangueira (namely: littoral, pelagic and benthic zones), which is only partially described by common methodologies using oxygen probes or bottles located at only one point of the lake. The role of hydrodynamics in the spatial explicit ecosystem metabolism estimations was evaluated by changing the wind pattern using a total of five different wind scenarios. Each scenario affected mainly the littoral zone estimates of GPP, R, and NEP whereas the pelagic zone showed no statistical significant differences. The seasonal estimates also showed a partial influence by hydrodynamics, with some season-specific series showing statistical significant differences mainly in the littoral zone of each compartment. Finally, the individual processes also showed sensibility to the wind pattern with the benthic-littoral processes being affected the most. For GPP, periphyton and macrophyte production reached an increase up to 80 % depending upon the wind scenario whereas for R the microbial processes reached an increase up to 100 % in some cases. The importance of individual processes is clear in this last result, once if we estimated only benthic processes and neglected the entire trophic chain the final conclusion could be entirely different. Hydrodynamics played a key-role structuring the process-based metabolism estimations in Lake Mangueira. The physical mixing can be an important factor structuring the metabolism estimations in different water environments, such as estuaries and deep lakes, where the density currents are more highlighted.

6. References

Alfonso, M.B., Vitale, A.J., Menéndez, M.C., Perillo, V.L., Piccolo, M.C., Perillo, G.M.E., 2015. Estimation of ecosystem metabolism from diel oxygen technique in a saline shallow lake: La Salada (Argentina). Hydrobiologia 752, 223–237. doi:10.1007/s10750-014-2092-1.

Antenucci, J.P., Imberger, J., 2003. The seasonal evolution of wind/internal wave resonance in lake kinneret. Limnology and Oceanography 48, 2055–2061. doi:10.4319/lo.2003.48.5.2055.

Antenucci, J.P., Tan, K.M., Eikaas, H.S., Imberger, J., 2013. The importance of transport processes and spatial gradients on in situ estimates of lake metabolism. Hydrobiologia 700, 9–21.

Arfi, R., Guiral, D., Bouvy, M., 1993. Wind induced resuspension in a shallow subtropical lagoon. Estuarine, Coastal and Shelf Science 36, 587–604.

Bailey, M.C., Hamilton, D.P., 1997. Wind induced resuspension: a lake-wide model. Ecological Modelling 99, 217–228. doi:10.1016/S0304-3800(97)01955-8.

Batt, R.D., Carpenter, S.R., 2012. Free-water lake metabolism: addressing noisy time series with a kalman filter. Limnology and Oceanography: Methods 10, 20–30. doi:10.4319/lom.2012.10.20.

Beck, M.W., Hagy III, J.D., Murrell, M.C., 2015. Improving estimates of ecosystem metabolism by reducing effects of tidal advection on dissolved oxygen time series. Limnology and Oceanography: Methods 13, 731–745. doi:10.1002/lom3.10062.

Blukacz, E., Sprules, W., Shuter, B., Richards, J., 2010. Evaluating the effect of wind-driven patchiness on trophic interactions between zooplankton and phytoplankton. Limnology and Oceanography 55, 1590–1600. doi:10.4319/lo.2010.55.4.1590.

Bonnet, M., Wessen, K., 2001. Elmo, a 3-d water quality model for nutrients and chlorophyll: first application on a lacustrine ecosystem. Ecological Modelling 141, 19–33. doi:10.1016/S0304-3800(00)00434-8.

Brighenti, L.S., Staehr, P.A., Gagliardi, L.M., Brandão, L.P.M., Elias, E.C., Mello, N.A.S.T., Barbosa, F.A.R., Bezerra-Neto, J.F., 2015. Seasonal changes in metabolic rates of two tropical lakes in the Atlantic forest of Brazil. Ecosystems 18, 589–604. doi:10.1007/s10021-015-9851-3.

Cardoso, L.S., Fragoso Jr, C.R., Souza, R.S., Motta-Marques, D., 2012. Hydrodynamic control of plankton spatial and temporal heterogeneity in subtropical shallow lakes, in: Schulz, H.E., Simões, A.L.A., Lobosco, R.J. (Eds.), Hydrodynamics: Natural Water Bodies. InTech. chapter 2, pp. 27–48.

Cardoso, L.S., Motta-Marques, D., 2009. Hydrodynamics-driven plankton community in a shallow lake. Aquatic Ecology 43, 73–84.

Carrick, H.J., Aldridge, F.J., Schelske, C.L., 1993. Wind influences phytoplankton biomass and composition in a shallow, productive lake. Limnology and Oceanography 38, 1179–1192. doi:10.4319/lo.1993.38.6.1179.

Casulli, V., Cattani, E., 1994. Stability, accuracy and efficiency of a semi-implicit method for three-dimensional shallow water flow. Computers & Mathematics with Applications 27, 99–112.

Casulli, V., Cheng, R.T., 1992. Semi-implicit finite difference methods for three-dimensional shallow water flow. International Journal for Numerical Methods in Fluids 15, 629–648.

Cavalcanti, J.R., Motta-Marques, D., Fragoso Jr, C.R., 2016. Process-based modeling of shallow lake metabolism: Spatial-temporal variability and relative importance of single processes. Ecological Modelling 323, 28–40. doi:10.1016/j.ecolmodel.2015.11.010.

Chao, X., Jia, Y., Shields Jr., F.D., Wang, S.S., Cooper, C.M., 2008. Three-dimensional numerical modeling of cohesive sediment transport and wind wave impact in a shallow oxbow lake. Advances in Water Resources 31, 1004–1014.

Cheng, R.T., Casulli, V., Gartner, J.W., 1993. Tidal, residual, intertidal mudflat (trim) model and its applications to san francisco bay, california. Estuarine, Coastal and Shelf Science 36, 235–280.

Cole, J., Prairie, Y., Caraco, N., McDowell, W., Tranvik, T., Striegl, R., Duarte, C., Kortelainen, P., Downing, J., Middelburg, J., Melack, J., 2007. Plumbing the global carbon cycle: Integrating inland waters into the terrestrial carbon budget. Ecosystems 10, 171–184. doi:10.1007/s10021-006-9013-8.

Cole, J.J., Pace, M.L., Carpenter, S.R., Kitchell, J.F., 2000. Persistence of net heterotrophy in lakes during nutrient addition and food web manipulations. Limnology and Oceanography 45, 1718–1730.

Coloso, J.J., Cole, J.J., Pace, M.L., 2011a. Difficulty in discerning drivers of lake ecosystem metabolism with high-frequency data. Ecosystems 14, 935–948. doi:10.1007/s10021-011-9455-5.

Coloso, J.J., Cole, J.J., Pace, M.L., 2011b. Short-term variation in thermal stratification complicates estimation of lake metabolism. Aquatic Sciences 73, 305–315. doi:10.1007/s00027-010-0177-0.

Cox, T.J., Maris, T., Soetaert, K., Kromkamp, J.C., Meire, P., Meysman, F., 2015. Estimating primary production from oxygen time series: A novel approach in the frequency domain. Limnology and Oceanography: Methods 13, 529–552. doi:10.1002/lom3.10046.

Cremona, F., Kõiv, T., Kisand, V., Laas, A., Zingel, P., Agasild, H., Feldmann, T.o., Jarvalt, A., Nõges, P., Nõges, T., 2014a. From bacteria to piscivorous fish: Estimates of whole-lake and component-specific metabolism with an ecosystem approach. PLoS ONE 9, e101845. doi:10.1371/journal.pone.0101845.

Cremona, F., Laas, A., Nõges, P., Nõges, T., 2014b. High-frequency data within a modeling framework: On the benefit of assessing uncertainties of lake metabolism. Ecological Modelling 294, 27–35. doi:10.1016/j.ecolmodel.2014.09.013.

Crossetti, L.O., Becker, V., Cardoso, L.S., Rodrigues, L.R., Costa, L.S., Motta-Marques, D., 2013. Is phytoplankton functional classification a suitable tool to investigate spatial heterogeneity in a subtropical shallow lake? Limnologica 43, 157–163.

Csanady, G., 1968. Motions in a model great lake due to a suddenly imposed wind. Journal of Geophysical Research 73, 6435–6447. doi:10.1029/JB073i020p06435.

Csanady, G., 1973. Wind-induced barotropic motions in long lakes. Journal of Physical Oceanography 3, 429–438. doi:10.1175/1520-0485(1973)003<0429:WIBMIL>2.0.CO;2.

del Giorgio, P.A., Peters, R.H., 1994. Patterns in planktonic P:R ratios in lakes: Influence of lake trophy and dissolved organic carbon. Limnology and Oceanography 39, 772–787.

Fragoso Jr, C.R., Motta-Marques, D., Collischonn, W., Tucci, C.E., van Nes, E.H., 2008. Modelling spatial heterogeneity of phytoplankton in lake mangueira, a large shallow subtropical lake in south brazil. Ecological Modelling 219, 125–137.

Fragoso Jr, C.R., Motta-Marques, D., Ferreira, T.F., Janse, J.H., van Nes, E.H., 2011. Potential effects of climate change and eutrophication on a large subtropical shallow lake. Ecological Modelling & Software 26, 1337–1348.

Gal, G., Hipsey, M., Parparov, A., Wagner, U., Makler, V., Zohary, T., 2009. Implementation of ecological modeling as an effective management and investigation tool: Lake kinneret as a case study. Ecological Modelling 220, 1697–1718. doi:10.1016/j.ecolmodel.2009.04.010.

Gómez-Giraldo, A., Imberger, J., Antenucci, J.P., Yeates, P.S., 2008. Wind-shear–generated high-frequency internal waves as precursors to mixing in a stratified lake. Limnology and Oceanography 53, 354–367. doi:10.4319/lo.2008.53.1.0354.

Hall, E., Schoolmaster Jr., D., Amado, A., Stets, E., Lennon, J., Domine, L., Cotner, J., 2015. Scaling relationships among drivers of aquatic respiration in temperate lakes: from the smallest to the largest freshwater ecosystems. Inland Waters 6, 1–10. doi:10.5268/IW-6.1.839.

Hamilton, D.P., Mitchell, S.F., 1997. Wave-induced shear stresses, plant nutrients and chlorophyll in seven shallow lakes. Freshwater Biology 38, 159–168.

Hanson, P.C., Bade, D.L., Carpenter, S.R., Kratz, T.K., 2003. Lake metabolism: Relationships with dissolved organic carbon and phosphorus. Ecological Modelling 48, 1112–1119.

Hanson, P.C., Carpenter, S.R., Armstrong, D.E., Stanley, E.H., Kratz, T.K., 2006. Lake dissolved inorganic carbon and dissolved oxygen: changing drivers from days to decades. Ecological Monographs 76, 343–363.

Hanson, P.C., Carpenter, S.R., Kimura, N., Wu, C., Cornelius, S.P., Kratz, T.K., 2008. Evaluation of metabolism models for free-water dissolved oxygen methods in lakes. Limnology and Oceanography:Methods 6, 454–465.

Holtgrieve, G.W., Schindler, D.E., Branch, T.A., A'mar, Z.T., 2010. Simultaneous quantification of aquatic ecosystem metabolism and reaeration using a bayesian statistical model of oxygen dynamics. Limnology and Oceanography 55, 1047–1063.

Hu, Z., Xiao, Q., Yang, J., Xiao, W., Wang, W., Liu, S., Lee, X., 2015. Temporal dynamics and drivers of ecosystem metabolism in a large subtropical shallow lake (lake taihu). International Journal of Environmental Research and Public Health 12, 3691–3706. doi:10.3390/ijerph120403691.

Idrizaj, A., Laas, A., Anijalg, U., Noges, P., 2016. Horizontal differences in ecosystem metabolism of a large shallow lake. Journal of Hydrology 535, 93–100. doi:10.1016/j.jhydrol.2016.01.037.

Janse, J.H., 2005. Model studies on the eutrophication of shallow lakes and ditches. Ph.D. thesis. Wageningen University.

Jin, K.R., Ji, Z.G., James, R.T., 2007. Three-dimensional water quality and SAV modeling of a large shallow lake. Journal of Great Lakes Research 33, 28–45. doi:10.3394/0380-1330(2007)33[28:TWQASM]2.0.CO;2.

Laas, A., Nõges, P., Kõiv, T., Nõges, T., 2012. High-frequency metabolism study in a large and shallow temperate lake reveals seasonal switching between bet autotrophy and net heterotrophy. Hydrobiologia 694, 57–74. doi:10.1007/s10750-012-1131-z.

Lauster, G.H., Hanson, P.C., Kratz, T.K., 2006. Gross primary production and respiration differences among littoral and pelagic habitats in northern wisconsin lakes. Journal of Fisheries and Aquatic Sciences 63, 1130–1141. doi:10.1139/F06-018.

MacIntyre, S., 1993. Vertical mixing in a shallow, eutrophic lake: Possible consequences for the light climate of phytoplankton. Limnology and Oceanography 38, 798–817. doi:10.4319/lo.1993.38.4.0798.

MacIntyre, S., Melack, J.M., 1995. Vertical and horizontal transport in lakes: Linking littoral, benthic, and pelagic habitats. Journal of the North American Benthological Society 14, 599–615.

Mao, J., Chen, Q., Chen, Y., 2008. Three-dimensional eutrophication model and application to taihu lake, china. Journal of Environmental Sciences 20, 278–284. doi:10.1016/S1001-0742(08)60044-3.

McNair, J.N., Gereaux, L.C., Weinke, A.D., Sesselmann, M.R., Kendall, S.T., Biddanda, B.A., 2013. New methods for estimating components of lake metabolism based on free-water dissolved-oxygen dynamics. Ecological Modelling 263, 1130–1141. doi:10.1016/j.ecolmodel.2013.05.010.

Motta-Marques, D., Tucci, C.E., Calazans, 2002. O sistema hidrológico do TAIM (TAIM hydrological system), in: Seeliger, U., Cordazzo, C., Barbosa, F. (Eds.), Os sites e o programa brasileiro de pesquisas ecológicas de longa duração. Belo Horizonte, MG. chapter 8, pp. 125–144.

Obrador, B., Petrus, J.L., 2013. Carbon and oxygen metabolism in a densely vegetated lagoon: implications of spatial heterogeneity. Limnetica 32, 321–336.

Obrador, B., Staehr, P.A., Christensen, J.P., 2014. Vertical patterns of metabolism in three contrasting stratified lakes. Limnology and Oceanography 59, 1228–1240. doi:10.4319/lo.2014.59.4.1228.

Odum, H.T., 1956. Primary production in flowing waters. Limnology and Oceanography 1, 103–119.

Pacanowski, R., Philander, S., 1981. Parametrization of vertical mixing in numerical models of tropical oceans. Journal of Physical Oceanography 11, 1443–1451.

Qian, J., ZHENG, S.s., Wang, P.f., Wang, C., 2011. Experimental study on sediment resuspension in taihu lake under different hydrodynamic disturbances. Journal of Hydrodynamics 23, 826–833.

Rodrigues, L.R., Motta-Marques, D., Fontoura, N.F., 2015. Fish community in a large coastal subtropical lake: how an environmental gradient may affect the structure of trophic guilds. Limnetica 34, 495–506.

Rose, K.C., Winslow, L.A., Read, J.S., Read, E.K., Solomon, C.T., Adrian, R., Hanson, P.C., 2014. Improving the precision of lake ecosystem metabolism estimates by identifying predictors of model uncertainty. Limnology and Oceanography: Methods 12, 303–312. doi:10.4319/lom.2014.12.303.

Sadro, S., Holtgrieve, G.W., Solomon, C.T., Koch, G.R., 2014. Widespread variability in overnight patterns of ecosystem respiration linked to gradients in dissolved organic matter, residence time, and productivity in a global set of lakes. Limnology and Oceanography 59, 1666–1678. doi:10.4319/lo.2014.59.5.1666.

Sadro, S., Melack, J.M., MacIntyre, S., 2011. Spatial and temporal variability in the ecosystem metabolism of a high-elevation lake: integrating benthic and pelagic habitats. Ecosystems 14, 1123–1140. doi:10.1007/s10021-011-9471-5.

Sand-Jensen, K., Staehr, P.A., 2009. Net heterotrophy in small danish lakes: a widespread feature over gradients in trophic status and land cover. Ecosystems 12, 336–348. doi:10.1007/s10021-008-9226-0.

Solomon, C.T., Bruesewitz, D.A., Richardson, D.C., Rose, K.C., Van de Bogert, M.C., Hanson, P.C., Kratz, T.K., Larget, B., Adrian, R., Babin, B.L., Chiu, C.Y., Hamilton, D.P., Gaiser, E.E., Hendricks, S., Istvánovics, V., Laas, A., O'Donnel, D.M., Pace, M.L., Ryder, E., Staehr, P.A., Torgensen, T., Vanni, M.J., Weathers, K.C., Zhu, G., 2013. Ecosystem respiration: Drivers of daily variability and background respiration in

lakes around the globe. Limnology and Oceanography 58, 849–866. doi:10.4319/lo.2013.58.3.0849.

Staehr, P.A., Baastrup-Spohr, L., Sand-Jensen, K., Stedmon, C., 2012a. Lake metabolism scales with lake morphometry and catchment conditions. Aquatic Sciences 74, 155–169. doi:10.1007/s00027-011-0207-6.

Staehr, P.A., Christensen, J.P., Batt, R.D., Read, J.S., 2012b. Ecosystem metabolism in a stratified lake. Limnology and Oceanography 57, 1317–1330. doi:10.4319/lo.2012.57.5.1317.

Staehr, P.A., Sand-Jensen, K., 2007. Temporal dynamics and regulation of lake metabolism. Limnology and Oceanography 52, 108–120.

Staehr, P.A., Sand-Jensen, K., Raun, A.L., Nilsson, B., Kidmose, J., 2010. Drivers of metabolism and net heterotrophy in constrasting lakes. Limnology and Oceanography 55, 817–830.

Staehr, P.A., Testa, J.M., Kemp, W.M., Cole, J.J., Sand-Jensen, K., Smith, S.V., 2012c. The metabolism of aquatic ecosystems: history, applications, and future challenges. Aquatic Sciences 74, 15–29. doi:10.1007/s00027-011-0199-2.

They, N.H., Motta-Marques, D., Souza, R.S., 2013. Lower respiration in the littoral zone of a subtropical shallow lake. Frontiers in microbiology 3, 1–10. doi:10.3389/fmicb.2012.00434.

Tonetta, D., Staehr, P.A., Schmitt, R., Petrucio, M.M., 2016. Physical conditions driving the spatial and temporal variability in aquatic metabolism of a subtropical coastal lake. Limnologica 58, 30–40. doi:10.1016/j.limno.2016.01.006.

Tsai, J.W., Kratz, T.K., Hanson, P.C., Wu, J.T., Chang, W.Y., Arzberger, P.W., Lin, B.S., Lin, F.P., Chou, H.M., Chiu, C.Y., 2008. Seasonal dynamics, typhoons and the regulation of lake metabolism in a subtropical humic lake. Freshwater Biology 53, 1929–1941. doi:10.1111/j.1365-2427.2008.02017.x.

Tucci, C., 1998. Modelos Hidrológicos (*In Portuguese*). ABRH/UFRGS.

van de Bogert, M.C., Bade, D.L., Carpenter, S.R., Cole, J.J., Pace, M.L., Hanson, P.C., Langman, O.C., 2012. Spatial heterogeneity strongly affects estimates of ecosystem metabolism in two north temperate lakes. Limnology and Oceanography 57, 1689–1700.

van de Bogert, M.C., Carpenter, S.R., Cole, J.J., Pace, M.L., 2007. Assessing pelagic and benthic metabolism using free water measurements. Limnology and Oceanography:Methods 5, 145–155.

Wu, T.F., Qin, B.Q., Zhu, G.W., Zhu, M.Y., Li, W., Luan, C.M., 2013. Modeling of turbidity dynamics caused by wind-induced waves and current in the taihu lake. International Journal of Sediment Research 28, 139–148. doi:10.1016/S1001-6279(13)60026-8.

Wu, X., Kong, F., Chen, Y., Qian, X., Zhang, L., Yu, Y., Zhang, M., Xing, P., 2000. Horizontal distribution and transport processes of bloom-forming *Microcystis* in a large shallow lake (taihu, china). Limnologica 40, 8–15.

You, B.S., Zhong, J.C., Fan, C.X., Wang, T.C., Zhang, L., Ding, S.M., 2007. Effects of hydrodynamics processes on phosphorus fluxes from sediment in large, shallow Taihu Lake. Journal of Environmental Sciences 19, 1055–1060. doi:10.1016/S1001-0742(07)60172-7.

Zhu, G., Qin, B., Gao, G., Zhang, L., Luo, L., Zhang, Y., 2007. Effects of hydrodynamics on phosphorus concentrations in water of lake taihu, a large, shallow, eutrophic lake of china. Hydrobiologia 581, 53–61.

Capítulo 4

A Conservative Finite Volume Scheme with Time-Accurate Local Time Stepping for Scalar Transport on Unstructured Grids

J. Rafael Cavalcanti
Michael Dumbser
David da Motta-Marques
Carlos Ruberto Fragoso Júnior

Artigo publicado ao periódico "*Advances in Water Resources*", Fator de Impacto (ISI): 3.417, Qualis CAPES: Engenharias I - A2.

A Conservative Finite Volume Scheme with Time-Accurate Local Time Stepping for Scalar Transport on Unstructured Grids

J. Rafael Cavalcanti[a,*], Michael Dumbser[b], David da Motta-Marques[a], Carlos Ruberto Fragoso Junior[c]

[a] *Universidade Federal do Rio Grande do Sul, Instituto de Pesquisas Hidráulicas, CP 15029, Porto Alegre, RS, Brazil*
[b] *Laboratory of Applied Mathematics, Department of Civil, Environmental and Mechanical Engineering, University of Trento, Via Mesiano 77, 38123 Trento, Italy*
[c] *Centro de Tecnologia, Universidade Federal de Alagoas, Maceió, AL, Brazil*

Abstract

In this article we propose a new conservative high resolution TVD finite volume scheme with time-accurate local time stepping (LTS) on unstructured grids for the solution of scalar transport problems, which are typical in the context of water quality simulations. To keep the presentation of the new method as simple as possible, the algorithm is only derived in two space dimensions and for purely convective transport problems, hence neglecting diffusion and reaction terms. The new numerical method for the solution of the scalar transport is directly coupled to the hydrodynamic model of Casulli and Walters [1] that provides the dynamics of the free surface and the velocity vector field based on a semi-implicit discretization of the shallow water equations. Wetting and drying is handled rigorously by the nonlinear algorithm proposed by Casulli [2]. The new time-accurate local time stepping algorithm allows a *different time step size* for *each* element of the unstructured grid, based on an *element-local* CFL stability condition. The proposed method does not need any synchronization between different time steps of different elements and is by construction locally and globally conservative. The LTS scheme is based on a piecewise linear polynomial reconstruction in space-time using the MUSCL-Hancock method, to obtain second order of accuracy in both space and time.

The new algorithm is first validated on some classical test cases for pure advection problems, for which exact solutions are known. In all cases we obtain a very good level of accuracy, showing also numerical convergence results; we furthermore confirm mass conservation up to machine precision and observe an improved computational efficiency compared to a standard second order TVD scheme for scalar transport with global time stepping (GTS). Then, the new LTS method is applied to some more complex problems, where the new scalar transport scheme has also been coupled to a semi-implicit model for the simulation of the free surface hydrodynamics, including nonlinear wetting and drying. The last application shown in this paper is carried out on a real geometry, for which we have taken available DTM data of the lake Guaiba in Brazil. Comparisons have been made in all cases with a second order TVD scheme based on global time stepping. For the new local time stepping algorithm we report a significant reduction in computational effort, with a savings of CPU time of the order of up to **95 %**.

Keywords: fully asynchronous time-accurate local time stepping (LTS), high resolution finite volume schemes, scalar transport, semi-implicit schemes for free surface hydrodynamics, unstructured mesh, Lake Guaiba

1. Introduction

The problem of water quality modeling can be divided into two main sub-tasks: (1) the hydrodynamical model, which provides the time-dependent information about the free-surface elevation, the wet area and circulation patterns (velocity field); for a survey of explicit schemes that provide a valid hydrodynamic model see, for example, [3, 4, 5, 6, 7, 8, 9, 10, 11, 12, 13, 14, 15, 16]; for semi-implicit hydrodynamic models see, for example, [17, 18, 1, 2, 19, 20, 21, 22, 23, 24]. (2) the water quality model, which gives the time-dependent information about important scalar

*Corresponding author
Email addresses: rafaelcavalcantii@gmail.com (J. Rafael Cavalcanti), michael.dumbser@unitn.it (Michael Dumbser)

quantities, such as, *e.g.*, water temperature, salinity, phytoplankton biomass, and the concentration of nutrients or toxics. The interface between those two models can play a key-role in environments where physical processes, such as internal circulation and mixing, can affect the scalar distribution [25, 26, 27, 28, 29].

Several hydrodynamic and water quality models are available, some of them with hydrodynamical and water quality model interface already implemented [1, 30, 31, 32, 33]. However, in many *real-world* applications the time step used in the hydrodynamic model is *less restrictive* than the time step required for the simulation of the scalar transport problem, see [30]. This results in a common shortcoming in the use of global time stepping algorithms, where the smallest elements, or the elements with the highest velocities, usually dictate the time step of all other elements in the computational domain. A global time step restriction can lead to very large computational times for the water quality model, in particular when many scalars are being considered simultaneously [34]. But even in the case where only one passive scalar is present, a transport algorithm based on a global time step may significantly slow down the simulation. This discussion is of course only true when an *unconditionally stable* implicit or semi-implicit scheme, like the one of Casulli et al. [17, 18, 1, 2], is used for the hydrodynamics, since any explicit Godunov-type finite volume scheme with global time stepping [16] would require a time step restricted by the largest eigenvalue of the PDE system governing the hydrodynamics, $\lambda_{\max} = |\mathbf{u}| + \sqrt{gH}$, which is more restrictive than the maximum eigenvalue of the pure scalar transport $\lambda_{\max} = |\mathbf{u}|$. As a matter of fact, the LTS algorithm presented in this paper is particularly well-suited for being used with a hydrodynamics model that uses the semi-implicit discretization [17, 18, 1, 2].

The use of local time stepping (LTS) algorithms in finite volume and DG finite element methods is increasing and it is based on the ideas of [35, 36]. These methods usually involve separating different regions according to a CFL-type condition, where small time steps are used only when locally necessary. The use of a local time stepping algorithm in finite element schemes requires identifying and treating the interface between regions with different time steps, thus the number of such regions affects the efficiency of the solver [34]. Finite volume schemes using local time stepping can also be found, but mostly in the context of adaptive mesh refinement (AMR), or block-clustered local time stepping [37, 38, 39, 40, 41, 42, 43, 44]. Recently, new finite element based local time stepping algorithms were presented in the context of so-called ADER-DG schemes [45, 46, 47, 48, 49, 50], with the main advantage of using a really local time step for each element of the computational mesh, without any synchronization and without clustering sub-regions of the domain based on a similar CFL condition. Such LTS algorithms without the need of synchronization between elements have been recently also extended to high order Arbitrary-Lagrangian-Eulerian (ALE) finite volume schemes with local time stepping for nonlinear hyperbolic conservation laws, see [51, 52]. For scalar transport problems, [34] reported the efficiency of the local time stepping procedure using structured grids, but the method used there was only first order accurate. For alternative LTS algorithms see [53, 54, 50], but the main advantage of the present LTS formulation lies in its simplicity and in its generality, which allows to handle fully asynchronous time steps that can be different in each element and which do not need to be integer multiples of each other.

In this paper a new second order accurate MUSCL-type TVD finite volume method with time-accurate local time-stepping is developed along the ideas of [45, 49, 51, 52], in order to solve scalar transport problems on unstructured grids. The aim is to significantly reduce the total CPU time needed for the solution of scalar transport problems within the framework of a water quality model. The LTS scheme proposed in this paper is very *simple* to implement and can be directly coupled to the semi-implicit hydrodynamic model of Casulli and Walters [1] on unstructured grids, including the recent nonlinear wetting and drying algorithm of Casulli [2]. We would like to stress here that standard second order MUSCL-type finite volume schemes with global time stepping are currently much more widespread in application codes than high order DG schemes. There has been little work so far on LTS algorithms for second order finite volume schemes on unstructured meshes. This makes the design of an LTS algorithm for MUSCL-type finite volume schemes on unstructured grids, like the one proposed in this paper, interesting for the implementation into existing application codes if the expected gains in CPU time are high enough. As shown at the end of this paper, there is indeed the potential to get a speed-up of about one order of magnitude for a real-world prototype application. Furthermore, the issue of slope limiting in the DG context is still an ongoing topic of research, see [55, 56, 57, 58, 59, 60, 61, 62, 63, 64] for some recent developments on this topic, also in the context of synchronized LTS within high order AMR algorithms.

We would also like to point out why we prefer the use of an explicit LTS algorithm over the use of a higher order implicit time discretization for the scalar transport equation: 1. The nonlinear slope-limiting of higher order implicit schemes is not straightforward. It makes the final system to be solved for the unknown concentration at the new time level nonlinear, hence in general rather difficult and expensive to solve. Note that one is usually interested

in maintaining positivity of concentration values, hence nonlinear slope limiting like the one used in our paper is indeed necessary, also in the implicit case. Therefore, the presented explicit LTS algorithm is in our opinion easier to implement into an existing standard explicit second order MUSCL-type finite volume code than a higher order nonlinear implicit discretization [1] of the transport equation, where typically an (inexact) Newton-Krylov solver [66, 67] with preconditioning and appropriate globalization strategies are needed. 2. Implicit upwind schemes are in general more diffusive than explicit upwind schemes of the same order of accuracy. For example, the first order implicit upwind method applied to the linear scalar transport equation in 1D has a leading diffusion error that scales with (1+CFL), where CFL is the Courant number, while the explicit upwind scheme has a leading diffusion error that scales only with (1-CFL), see [68] for a detailed error analysis based on the method of differential approximation. Since our LTS approach allows the user to run the simulation with an almost *constant CFL number* throughout the computational domain, instead of using a *constant time step* that is necessary in global time stepping algorithms, it is possible to choose a large value for the CFL number, close to the maximum admissible stability limit, and hence *reducing* the numerical diffusion errors.

The new LTS algorithm is tested and validated on different benchmark problems, comparing with existing analytical solutions or with the numerical results obtained with a standard global time stepping algorithm. The rest of the paper is organized as follows: in Section 2 the new algorithm is presented and explained in detail for the case of a purely convective transport, without diffusion and reaction terms; in Section 3 the computational results obtained for several benchmark problems are presented and discussed. Some concluding remarks and an outlook to further developments is given in the concluding Section 4. A detailed pseudo-code of the new LTS algorithm is given in the appendix, in order to facilitate the reader with the practical implementation.

2. Scalar Transport Scheme with LTS

The transport of a scalar quantity in the context of water quality simulations can be described as an advection-diffusion-reaction equation written in conservation form, where the time evolution of the volume concentration of a dissolved quantity $C = C(\mathbf{x}, t)$ is typically written as:

$$\frac{\partial CH}{\partial t} + \nabla \cdot (CH\,\mathbf{u}) = \nabla \cdot (H\,\Gamma\,\nabla(C)) + S_C, \qquad \mathbf{x} \in \Omega \subset \mathbb{R}^2, \quad t \in \mathbb{R}_0^+. \tag{1}$$

Here, $\mathbf{u} = \mathbf{u}(\mathbf{x}, t)$ is the velocity vector and $H = H(\mathbf{x}, t)$ is the total water depth, which are both provided by a hydrodynamical model, see [1]; Γ is the diffusivity tensor and S_C is a net source/sink term. Discarding the diffusion and reaction terms, we have a simple linear advection equation

$$\frac{\partial CH}{\partial t} + \nabla \cdot (CH\,\mathbf{u}) = 0. \tag{2}$$

In the following, the computational domain Ω is discretized by triangular control volumes denoted by T_i. Integrating the PDE over a spatial control volume T_i and over the time interval $[t^n, t^{n+1}]$ yields after the use of Gauss' theorem the following integral form of the conservation law (2):

$$\int_{t^n}^{t^{n+1}} \int_{T_i} \frac{\partial CH}{\partial t}\, d\mathbf{x}\, dt + \int_{t^n}^{t^{n+1}} \int_{\partial T_i} (CH\,\mathbf{u}) \cdot \mathbf{n}\, dS\, dt = 0, \tag{3}$$

where ∂T_i denotes the boundary of the control volume T_i and $\mathbf{n}$ is the outward-pointing unit normal vector on the boundary. Using the definitions

$$V_i^n = \int_{T_i} H(\mathbf{x}, t^n)\, d\mathbf{x}, \qquad C_i^n = \frac{1}{V_i^n} \int_{T_i} C(\mathbf{x}, t^n)\, H(\mathbf{x}, t^n)\, d\mathbf{x}, \qquad \text{and} \qquad F_{ij} = \frac{1}{\Delta t} \int_{t^n}^{t^{n+1}} \int_{\partial T_{ij}} (CH\,\mathbf{u}) \cdot \mathbf{n}_{ij}\, dS\, dt, \tag{4}$$

[1] The nonlinearity in a higher order discretization of the linear transport equation arises from the necessity of introducing nonlinear slope limiters, according to Godunov's theorem, which states that linear monotone schemes are at most of order one, see [65].

where ∂T_{ij} denotes the segment of the boundary of element T_i that is in common with the neighbor element T_j, and where $\mathbf{n}_{ij}$ is the associated unit normal vector pointing from T_i to T_j, a Finite Volume discretization of (3) with *global time step* reads

$$V_i^{n+1} C_i^{n+1} = V_i^n C_i^n - \Delta t \sum_{j \in \mathcal{N}_i} \lambda_{ij} F_{ij}. \tag{5}$$

Here, $\mathcal{N}_i$ is the set of neighbors of element T_i and, as already stated above, the subscripts i and j indicate the element and its neighbor on the common edge ∂T_{ij}, respectively. The length of edge ∂T_{ij} is denoted by λ_{ij}, the superscript n indicates the time level, $\Delta t = t^{n+1} - t^n$ is a *global* time step and F_{ij} is the numerical flux which is specified below. Different methods can be used to evaluate the numerical flux at an element interface face in finite volume schemes. In this work we choose an upwind formulation, that reads as follows:

$$F_{ij} = F_{ij}(C_{ij}^-, C_{ij}^+) = \frac{1}{2}(H_{ij}^{n+1} u_{ij}^{n+1}) \left(C_{ij}^+ + C_{ij}^-\right) - \frac{1}{2} \left|H_{ij}^{n+1} u_{ij}^{n+1}\right| \left(C_{ij}^+ - C_{ij}^-\right), \tag{6}$$

where H_{ij}^{n+1} is the water depth and $u_{ij}^{n+1} = \mathbf{u}_{ij}^{n+1} \cdot \mathbf{n}_{ij}$ denotes the normal velocity at the interface, respectively. Note that H_{ij}^{n+1} and u_{ij}^{n+1} are directly provided by the flow solver [1]. C_{ij}^+ and C_{ij}^- are the *reconstructed interface values* at the common edge ∂T_{ij} from the left and the right, respectively. These values can be approximated using *piece-wise constant* cell averages, i.e. taking simply $C_{ij}^+ = C_j^n$ and $C_{ij}^- = C_i^n$, resulting in a classical first order *Godunov*-type scheme. Another approach is to approximate those values using a piecewise linear reconstruction in space and time within each element, resulting in a second order *MUSCL*-type scheme.

2.1. Second order MUSCL-type method on unstructured meshes with global time stepping

To simplify the description of the algorithm, we first present the second order MUSCL reconstruction in a *global* time stepping framework, where the global time step size is denoted by $\Delta t = t^{n+1} - t^n$. The MUSCL method of van Leer [69] provides an accurate and robust numerical solution of conservation laws, even in cases where the solution exhibit shocks, discontinuites, or large gradients [70]. The main idea is to improve the piece-wise constant data of the first-order Godunov scheme by a piece-wise linear data reconstruction, in order to achieve higher order of accuracy.

Instead of a simple cell averaged value, the data within each cell is approximated using a piecewise linear reconstruction in space and time, also known as the MUSCL-Hancock Method [71, 70], that reads as follows:

$$C_i(\mathbf{x}, t) = C_i^n + \nabla C_i^n \cdot (\mathbf{x} - \mathbf{x}_i) + \partial_t C_i^n \, (t - t^n), \tag{7}$$

where the barycenter of cell T_i is denoted with $\mathbf{x}_i$, C_i^n is the cell-averaged value at time t^n, ∇C_i^n is the spatial gradient of the passive scalar, which still needs to be determined, and $\partial_t C_i^n$ is its first time derivative, which can be directly computed from the PDE in primitive form once the slope ∇C_i^n is known as follows:

$$\partial_t C_i^n = -\mathbf{u}_i^n \cdot \nabla C_i^n. \tag{8}$$

Here, $\mathbf{u}_i^n$ denotes the velocity vector at the barycenter of cell T_i, which is provided by the flow solver.

According to Godunov's theorem [70, 72], there are no better than first order accurate *linear* monotone schemes for advection equations, hence high order accurate linear schemes will inevitably produce spurious oscillations in the vicinity of large gradients and discontinuities. In order to avoid these oscillations, a higher order scheme must therefore be *nonlinear*. For that purpose, we use a non-linear *slope limiter* function Φ_i that is applied to the unlimited gradient $\tilde{\nabla} C_i^n$ following the procedure outlined by Barth and Jespersen in their pioneering work [73]. In more detail, one first computes an *unlimited* slope $\tilde{\nabla} C_i^n$ by simply evaluating

$$\tilde{\nabla} C_i^n = \frac{1}{|T_i|} \sum_{j \in \mathcal{N}_i} \frac{1}{2} \left(C_i^n + C_j^n\right) \mathbf{n}_{ij}, \qquad \text{with} \qquad |T_i| = \int_{T_i} d\mathbf{x}. \tag{9}$$

From this unlimited slope, a *preliminary* spatial reconstruction reads

$$\tilde{C}_i(\mathbf{x}, t^n) = C_i^n + \tilde{\nabla} C_i^n \cdot (\mathbf{x} - \mathbf{x}_i). \tag{10}$$

We would like to point out that an *alternative slope computation* is based on integral conservation of the preliminary spatial reconstruction polynomial $\tilde{C}_i(\mathbf{x},t)$ on a *reconstruction stencil* $\mathcal{S}_i$ that consists of element T_i and its direct side neighbors. The corresponding reconstruction equations read

$$\frac{1}{|T_j|}\int_{T_j}\tilde{C}_i(\mathbf{x},t)d\mathbf{x} = C_j^n, \qquad \forall T_j \in \mathcal{S}_i. \tag{11}$$

The resulting overdetermined linear system (11) can be solved with a *constrained* least-squares algorithm [74], where the constraint is given by the requirement that the conservation principle (11) is exactly satisfied for element T_i.

The main idea of the Barth and Jespersen [73] slope limiter is to satisfy a discrete maximum principle, i.e. to find the largest admissible value for Φ_i for which the values of the reconstructed variables do not exceed the maximum and the minimum values of the cell averages in the set $\mathcal{S}_i = T_i \cup \mathcal{N}_i$. Hence, in a second step, one needs to calculate the maximum and minimum values of C_i^n in the set $\mathcal{S}_i$ as

$$C_i^{\min} = \min_{j\in\mathcal{S}_i}\left(C_j^n\right) \qquad \text{and} \qquad C_i^{\max} = \max_{j\in\mathcal{S}_i}\left(C_j^n\right). \tag{12}$$

Since the reconstruction polynomial is required to remain within the upper and lower bounds

$$C_i^{\min} \le C_i(\mathbf{x},t^n) \le C_i^{\max}, \tag{13}$$

the slope $\tilde{\nabla}C_i^n$ is modified so that (13) is satisfied. For piecewise linear polynomial reconstruction, the extreme values inside a triangular element occur at the vertices of the triangle, see [73]. In the following, we will denote the set of vertices of element T_i with $\mathcal{V}_i$. Hence, for each vertex coordinate $\mathbf{X}_k$ of the element T_i with $k \in \mathcal{V}_i$, compute the node values $\tilde{C}_i(\mathbf{X}_k,t^n)$ from (10) using the *unlimited* slope $\tilde{\nabla}C_i^n$ to determine a value $\bar{\Phi}_{i,k}$ as follows:

$$\bar{\Phi}_{i,k} = \begin{cases} \min\left(1, \frac{C_i^{\max}-C_i^n}{\tilde{C}_i(\mathbf{X}_k,t^n)-C_i^n}\right), & \text{if } \tilde{C}_i(\mathbf{X}_k,t^n)-C_i^n > 0, \\ \min\left(1, \frac{C_i^{\min}-C_i^n}{\tilde{C}_i(\mathbf{X}_k,t^n)-C_i^n}\right), & \text{if } \tilde{C}_i(\mathbf{X}_k,t^n)-C_i^n < 0, \\ 1, & \text{if } \tilde{C}_i(\mathbf{X}_k,t^n)-C_i^n = 0. \end{cases} \tag{14}$$

From these values $\bar{\Phi}_{i,k}$ the value of the slope limiter is obtained as $\Phi_i = \min_{k\in\mathcal{V}_i}\left(\bar{\Phi}_{i,k}\right)$. After the calculation of Φ_i, one obtains the final limited slope as

$$\nabla C_i^n = \Phi_i \tilde{\nabla} C_i^n, \tag{15}$$

from which also the time derivative $\partial_t C_i^n$ can be calculated according to (8). The reconstructed values C_{ij}^- and C_{ij}^+ used for the flux calculation (6) are then given by

$$C_{ij}^- = C_i(\mathbf{x}_{ij}, t^{n+\frac{1}{2}}), \qquad C_{ij}^+ = C_j(\mathbf{x}_{ij}, t^{n+\frac{1}{2}}), \tag{16}$$

where $\mathbf{x}_{ij}$ denotes the coordinate of the midpoint of the common edge ∂T_{ij} shared by elements T_i and T_j and the half-time step is denoted by $t^{n+\frac{1}{2}} = t^n + \frac{1}{2}\Delta t$. In the presence of viscous terms, one can take them into account inside the slope limiter following the ideas of Toro [75] and Casulli and Zanolli [30] in the context of viscous flux limiters. To guarantee monotonicity of the fully discrete solution, the limiter (14) and (15) should be applied in a second step in an analogous way at time t^{n+1} also to the temporal slope $\partial_t C_i^n$.

2.2. Local Time Stepping (LTS)

In this section the details of our new Local Time Stepping (LTS) algorithm for scalar transport are presented. In a classical GTS algorithm for pure advection, the global time step Δt is chosen according to a *global* CFL stability condition related to the element size h_i and the advection velocity $\mathbf{u}_i$ on each element,

$$\Delta t^n = \text{CFL} \min_{T_j\in\Omega}\left(\frac{h_j}{\left\|\mathbf{u}_j\right\|}\right), \tag{17}$$

where Δt^n is the global time step, CFL $< 1/d$ is the Courant-Friedrichs-Lewy number, d is the number of space dimensions and h_j is the characteristic mesh size of each element, which in our case is taken as the incircle diameter of triangle T_j; $\mathbf{u}_j$ is the velocity vector in T_j. Note that in (17) a global minimum is taken over all elements in the domain. When coupling different models with each other, like a hydrodynamic and a water quality model, for example, this global time step restriction may become too severe and the time step of the explicit scheme for the scalar transport could even limit the time step of the hydrodynamic model. In such cases, a *sub-cycling* approach should be used [30, 76], to decouple the time step of the explicit scalar transport scheme from the time step used in the semi-implicit hydrodynamic model [1].

The LTS procedure implemented here follows ideas presented for the first time in the discontinuous Galerkin (DG) finite element context [45, 46, 47, 49]. In the aforementioned references, the LTS algorithm was shown to converge with high order of accuracy in both space and time. The main difference between the LTS algorithm presented in this paper is the use of the nonlinear reconstruction operator, which requires information from the neighbor cells. In an *unlimited* DG framework like the one used in [45, 49], a reconstruction step was not necessary. Note, however, that the DG method *does* need a reconstruction step if a nonlinear slope or moment limiter is required to satisfy a discrete maximum principle. Instead of one global time step (17) each element will now compute a *local time step* following a *local CFL stability condition*, based on the set $\mathcal{S}_i$, i.e. the element and its direct neighbors:

$$\Delta t_i^n = \text{CFL} \min_{T_j \in \mathcal{S}_i} \left(\frac{h_j}{\left\| \mathbf{u}_j \right\|} \right), \tag{18}$$

where Δt_i^n is now the *local time step*. Accordingly, each element will also have associated a *local time* t_i^n. To be precise, even the superscript depends on the element number, hence $n = n(i)$, but to simplify notation, we will drop the explicit dependence of n on the element number i.

A local time stepping algorithm is not organized in time steps, but in so-called cycles. In each cycle, one loops over all elements in the domain and verifies the so-called *update criterion* or *evolve condition* [45, 46], i.e. an element is only updated if and only if the following condition holds:

$$t_i^n + \Delta t_i^n \leq t_j^n + \Delta t_j^n, \qquad \forall\, j \in \mathcal{N}_i. \tag{19}$$

This condition means that the future time of an element must be less or equal than the future times of the neighbor elements and is a direct result of the causality principle. Note that the method presented in this paper is a *fully asynchronous* local time stepping method, where *no synchronization* between elements is needed, apart from the update criterion (19) above.

Furthermore, the time intervals in which numerical fluxes are computed across element boundaries are defined as

$$[t_{ij}^n, t_{ij}^{n+1}] = [\max(t_i^n, t_j^n), \min(t_i^{n+1}, t_j^{n+1}], \qquad \Delta t_{ij} = t_{ij}^{n+1} - t_{ij}^n, \qquad t_{ij}^{n+\frac{1}{2}} = \frac{1}{2}\left(t_{ij}^n + t_{ij}^{n+1} \right). \tag{20}$$

The finite volume scheme with LTS then reads for those elements T_i that satisfy (19):

$$V_i^{n+1} C_i^{n+1} = V_i^n C_i^n + M_i - \sum_{j \in \mathcal{N}_i} \Delta t_{ij}\, \lambda_{ij}\, F_{ij}\left(C_{ij}^-, C_{ij}^+ \right), \qquad t_i^{n+1} = t_i^n + \Delta t_i^n. \tag{21}$$

The boundary extrapolated values C_{ij}^- and C_{ij}^+ used in (21) are computed from the local space-time reconstruction (7) simply as

$$\begin{aligned} C_{ij}^- &= C_i^n + \nabla C_i^n \left(\mathbf{x}_{ij} - \mathbf{x}_i \right) + \partial_t C_i^n \left(t_{ij}^{n+\frac{1}{2}} - t_i^n \right), \\ C_{ij}^+ &= C_j^n + \nabla C_j^n \left(\mathbf{x}_{ij} - \mathbf{x}_j \right) + \partial_t C_j^n \left(t_{ij}^{n+\frac{1}{2}} - t_j^n \right). \end{aligned} \tag{22}$$

The term M_i in (21) is the so-called *memory variable*, which takes into account past fluxes through the element interfaces, i.e. from time t_i^n to t_{ij}^n. In practice, this memory variable is simply updated by the *neighbors* of an element, to assure that the scheme is exactly conservative and simple to implement. Once an element has been updated by Eqn.

(21), its own memory variable is reset to zero, and the fluxes across the element boundary are added to the memory variables of the neighbor elements, i.e.

$$M_i := 0, \qquad M_j := M_j + \Delta t_{ij}\, \lambda_{ij}\, F_{ij}\left(C_{ij}^-, C_{ij}^+\right). \tag{23}$$

The last open problem is how to perform the *reconstruction* for element T_i after its update in an LTS context, since the neighbor cells in general are at a different time $t_j^n \neq t_i^n$. Since the space-time reconstruction (7) is valid inside the entire space-time control volume $T_j \times [t_j^n, t_j^{n+1}]$, we simply proceed as follows: instead of using (9), we compute the unlimited gradient $\tilde{\nabla} C_i^n$ at the aid of the predictor (7) in the neighbor cells using the *virtual* cell averages $\bar{C}_j^n$:

$$\tilde{\nabla} C_i^n = \frac{1}{|T_i|} \sum_{j \in \mathcal{N}_i} \frac{1}{2}\left(C_i^n + \bar{C}_j^n\right) \mathbf{n}_{ij}, \qquad \text{with} \qquad \bar{C}_j^n = C_j^n + \partial_t C_j^n (t_i^n - t_j^n). \tag{24}$$

Note that a valid predictor is always available in the neighbor cells due to the update criterion (19). After the computation of the unlimited slope from Eqn. (24), the limited slope and the computation of the time derivative $\partial_t C_i^n$ are obtained as described in Section 2.1.

The LTS algorithm can be summarized in 4 main steps. From the known initial condition C_i^0, perform the nonlinear reconstruction and time evolution according to Section 2.1. Then, in each subsequent cycle, loop over all elements and do:

Step 1. **Computation of the local time step**:
A local time step is calculated for each element using Equation (18).

Step 2. **Update criterion**:
An element T_i is scheduled for updating and flux calculation if and only if the update criterion (19) is satisfied. This means that only those elements can perform an update, whose future time t_i^{n+1} is less or equal than the future times t_j^{n+1} of the neighbor elements $T_j \in \mathcal{S}_i$.

Step 3. **Flux calculation and quantity update**:
Once an element is allowed to perform the update, the numerical fluxes across the element boundaries are calculated as follows:

(a) Calculation of the flux time interval:
The different time levels and time steps in each element require the definition of the flux time interval $[t_{ij}^n, t_{ij}^{n+1}]$ on the element boundary ∂T_{ij} according to (20).

(b) Computation of the boundary extrapolated values:
As in a GTS algorithm, the numerical flux F_{ij} needs boundary extrapolated values C_{ij}^- and C_{ij}^+ as input. In the LTS algorithm presented here, the boundary extrapolated values C_{ij}^- and C_{ij}^+ are easily computed from the element-local space-time reconstruction according to (22). At the end of steps (a) and (b) the numerical flux F_{ij} can be calculated using (6).

(c) Quantity Update:
The concentration is updated according to Eqn. (21). In order to maintain conservation, the finite volume scheme (21) is supplemented by a *memory variable* M_i, which takes into account the past fluxes through element boundaries. The memory variable is always updated by the *neighbors* of an element. In practice, one simply sets the memory variable M_i to zero after the update of element T_i, and adds the fluxes through the element boundaries to the memory variables M_j of the neighbor elements $T_j \in \mathcal{N}_i$.

Step 4. **Reconstruction, slope limiting and time evolution**: The last step in the finite volume LTS algorithm consists in computing again a valid space-time reconstruction polynomial (7) for the next time step of element T_i. For that purpose, *virtual* cell averages $\bar{C}_j^n$ are used in the neighbors of an updated element T_i, see Eqn. (24), since in general $t_i^n \neq t_j^n$. The slope limiter and the time derivative are then computed as usual, based on the Barth and Jespersen reconstruction algorithm [73] summarized in Section 2.1.

For the sake of clarity, and to facilitate the reader in the practical implementation of the present algorithm, these five steps are described again in detail in a schematic pseudo-code presented in Appendix A. For further details about LTS and different applications see [45, 49, 46, 47, 51, 52].

3. Numerical Results

The scalar transport algorithm with LTS proposed in this work was coupled to an unstructured hydrodynamic model based on the semi-implicit discretization of the shallow water equations on unstructured grids [77, 1, 78, 2, 19, 24] including nonlinear wetting and drying (UnTRIM^2). Despite the model complexity that could be used in such an advanced scheme for 3D free surface flows, which allows to account for nonlinear wetting and drying, nonhydrostatic pressure distribution or even for a complex multi-valued free surface, here we limit ourselves to the two-dimensional hydrostatic case with wetting and drying, for the sake of clarity and simplicity, in order to prevent the other more advanced features of the hydrodynamical model from complicating the results obtained with the new transport scheme.

To validate our new LTS algorithm we first use three rather simple but classic benchmark problems that consist in the pure advection of a scalar quantity C within a given velocity field $\mathbf{u}$. In all cases, an exact solution is known. One is the rotating slotted cylinder problem of Zalesak [79], the other one is a kinematic frontogenesis problem as described, for example, in [80, 81, 82, 74]. In the third test problem, we advect a smooth function in a known velocity field and compute the numerical convergence rates on a sequence of successively refined meshes, confirming that the presented LTS method is indeed second order accurate in space and time.

In order to compare the advantages using the LTS algorithm coupled to a hydrodynamic model, three additional test cases were solved: i) the transport of a constant scalar in a 1D Riemann problem and in an oscillating lake with wetting and drying, in order to check the consistency with continuity (CWC) property, ii) the scalar transport occurring in a steady flow within a curved channel, iii) the scalar transport occurring in a realistic lake-river system based on the available DTM data of the lake Guaiba in Brazil.

If not stated otherwise, the default slope reconstruction algorithm is given by the discrete form of Gauss' theorem, Eqn. (9).

3.1. Rotating slotted cylinder problem

The rotating slotted cylinder problem is solved on a two-dimensional square domain $\Omega = [-0.5; 0.5]^2$ with a prescribed fixed divergence-free velocity field given by $\mathbf{u} = \mathbf{\Omega} \times \mathbf{x}$, with $\mathbf{\Omega} = (0, 0, \omega)$ and $\mathbf{x} = (x, y, 0)$. Initially the center of the slotted cylinder is placed at $\mathbf{x}_c = (0.25, 0, 0)$, while the cylinder radius is $r_c = 0.15$ and the slot width is $s = 0.05$. The value of the concentration C inside the cylinder is $C = 1$ and outside the cylinder it is $C = 0$. With the given angular frequency $\omega = 2\pi$ the period of one entire rotation is $T = 1$. The problem is solved on an unstructured triangular mesh with 46,030 triangular elements using a characteristic mesh size of $h = 0.007$, approximating the resolution used in [79]. The evolution of the slotted cylinder is reported in Fig. (1), where the results of the new local time stepping algorithm are compared with the classical global time stepping approach. Overall we can observe an excellent agreement between the two solutions, which are both affected by numerical diffusion that can be noticed during the temporal evolution. In both simulations the total mass was conserved up to machine precision and the discrete maximum principle was satisfied during the entire simulation. Differences in terms of element updates and CPU time between the LTS and the GTS algorithm are reported in Table 3. For this test case the use of a local time stepping scheme led to a savings of $\approx 14\%$ of CPU time.

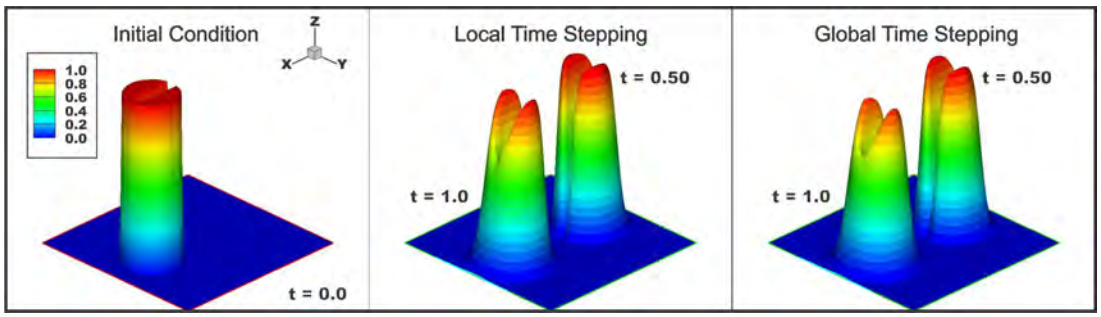

Figure 1: Evolution of the rotating slotted cylinder problem of Zalesak at times $t = 0$, $t = 0.50$, and $t = 1.0$ using a second order MUSCL-Hancock finite volume scheme using LTS and GTS.

3.2. Kinematic frontogenesis problem

The kinematic frontogenesis problem is a benchmark arising from the field of computational meteorology [80, 81, 82]. We solve it using the most refined unstructured triangular mesh presented in [74], resulting in 231,188 triangular elements (characteristic mesh length $h = 0.01$). The velocity field $\mathbf{u} = (u_0, v_0)$ used in the simulation is given by

$$u_0 = -y\omega(r), \qquad v_0 = x\omega(r), \qquad \omega(r) = \frac{1}{r}U_t(r), \; r = \sqrt{x^2 + y^2}, \qquad U_t(r) = U_{\max}\mathrm{sech}^2(r)\tanh(r), \tag{25}$$

where u_0 and v_0 are the prescribed velocities in the $x - y$ plane and $U_{\max} = 2.5980762$. The discontinuous initial condition depends only on y and reads as follows:

$$C(\mathbf{x}, 0) = \begin{cases} 0, & \text{if } y < 0, \\ 1, & \text{if } y \geq 0. \end{cases} \tag{26}$$

The exact solution of the problem is reported, for example, in [82, 74] and develops smaller and smaller length scales as time increases. The numerical results obtained with the local and the global time stepping algorithm are shown in Fig. 2. We note an excellent agreement between LTS and GTS. Also in this test case total mass was conserved up to machine precision during the entire simulation. A comparison between GTS and LTS for this test case (Table 3) reports a CPU time savings of $\approx 68\%$.

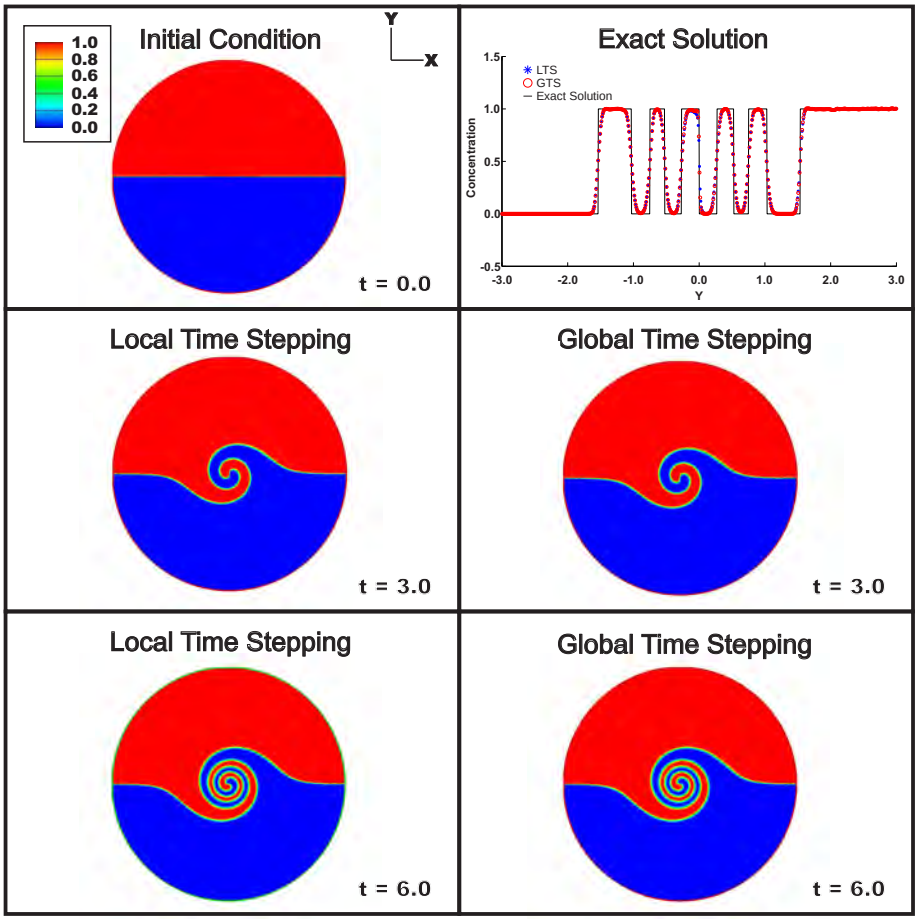

Figure 2: Numerical solution of the kinematic frontogenesis problem solved with a second order MUSCL-Hancock finite volume scheme using LTS and GTS (triangular mesh with characteristic mesh length $h = 0.01$).

3.3. Numerical convergence study on a smooth advection problem

Here we solve a similar but smooth advection problem on the circular domain $\Omega = \{\mathbf{x} : \|\mathbf{x}\| \leq 1\}$ with the same velocity field as in the slotted cylinder problem, i.e. $\mathbf{u} = \boldsymbol{\Omega} \times \mathbf{x}$ with $\boldsymbol{\Omega} = (0, 0, \omega)$, $\omega = 2\pi$ and $\mathbf{x} = (x, y, 0)$. The initial condition for the scalar concentration is given by

$$C(\mathbf{x}, 0) = \exp\left(-\frac{1}{2}((x - 0.25)^2 + y^2)/0.05^2\right). \tag{27}$$

Simulations are performed until $t = 0.25$, which corresponds to a quarter of a rotation period, hence the exact solution of the problem then reads

$$C(\mathbf{x}, 0.25) = \exp\left(-\frac{1}{2}(x^2 + (y - 0.25)^2)/0.05^2\right). \tag{28}$$

The numerical convergence results obtained with the global and local time stepping algorithm on a sequence of successively refined meshes are reported in Table 1, showing that both schemes reach their designed second order of accuracy. We furthermore provide a detailed CPU time comparison, as well as a comparison of the necessary total number of element updates (EU). We also compare the two alternative slope reconstruction algorithms with each other, i.e. the one based on the discrete form of Gauss' theorem (9) according to [73] and the one based on integral conservation (11) and constrained least squares [74].

3.4. Consistency with continuity test (CWC)

Here, we run two numerical test problems to check the consistency with continuity (CWC) property of the new LTS algorithm for scalar transport. Briefly, the CWC condition requires that the scalar transport equation (1) is discretized numerically in a way that is *compatible* with the continuity equation of the discrete hydrodynamics model

Global time stepping (GTS) with gradient reconstruction based on Gauss' theorem (9)						
h	L^1 error	L^2 error	L^1 order	L^2 order	CPU time	total EU
1/20	3.5802E-03	1.5905E-02			0.17	4.4950E+05
1/40	6.8186E-04	3.3112E-03	2.4	2.3	1.36	3.5045E+06
1/80	1.6913E-04	7.6704E-04	2.0	2.1	13.81	2.8516E+07
1/160	4.3280E-05	1.9674E-04	2.0	2.0	129.20	2.4947E+08
Local time stepping (LTS) with gradient reconstruction based on Gauss' theorem (9)						
h	L^1 error	L^2 error	L^1 order	L^2 order	CPU time	total EU
1/20	3.5723E-03	1.6063E-02			0.12	2.5710E+05
1/40	7.8525E-04	3.6766E-03	2.2	2.1	0.96	1.9600E+06
1/80	2.1774E-04	9.6602E-04	1.9	1.9	11.56	1.5246E+07
1/160	5.8858E-05	2.8442E-04	1.9	1.8	95.43	1.2102E+08
h	L^1 error	L^2 error	L^1 order	L^2 order	CPU time	total EU
Global time stepping (GTS) with gradient reconstruction based on integral conservation (11)						
1/20	3.5478E-03	1.5687E-02			0.14	4.4950E+05
1/40	6.8448E-04	3.3010E-03	2.4	2.2	1.08	3.5045E+06
1/80	1.6912E-04	7.6839E-04	2.0	2.1	11.67	2.8516E+07
1/160	4.3280E-05	1.9667E-04	2.0	2.0	110.38	2.4947E+08
Local time stepping (LTS) with gradient reconstruction based on integral conservation (11)						
1/20	3.5412E-03	1.5886E-02			0.10	2.5710E+05
1/40	7.8659E-04	3.6716E-03	2.2	2.1	0.79	1.9600E+06
1/80	2.1778E-04	9.6609E-04	1.9	1.9	10.36	1.5246E+07
1/160	5.8838E-05	2.8406E-04	1.9	1.8	85.18	1.2102E+08

Table 1: Numerical convergence results for two different gradient reconstruction methods for the smooth advection test case at time $t = 0.25$. Comparison of global time stepping (GTS) with local time stepping (LTS) in terms of errors, total element updates (EU) and CPU time. The characteristic mesh size is denoted by h.

[1, 2]. In particular, no new extrema must be generated in the discrete solution of the scalar concentration C. For a more detailed discussion on this topic, see the papers of Gross et al. [83] and Casulli and Zanolli [30].

We first solve a 1D Riemann problem for the hydrodynamics equations on the two-dimensional computational domain $\Omega = [-1, 1] \times [-0.1, 0.1]$, which is discretized using a rather coarse mesh of only 2226 triangular elements. The free surface elevation for $x < 0$ is given by $\eta_L = 1$, while it is $\eta_R = 0.5$ for $x \geq 0$. The fluid is initially at rest $\mathbf{u} = 0$ and the bottom is flat $h = 0$. The initial concentration is globally constant $C(\mathbf{x}, 0) = 1$. No-flux boundary conditions ($\mathbf{u} \cdot \mathbf{n} = 0$) are imposed on all domain boundaries, and the simulation is run up to a final time of $t = 2$ with a constant time step of $\Delta t = 0.01$. The exact solution for the scalar concentration is a constant $C(\mathbf{x}, t) = 1$ for all times. The numerical results for the error between exact and numerical solution in L_1, L_2 and L_∞ norm are reported in Fig. 3. The errors are close to machine zero during the entire simulation for both, the local time stepping algorithm (LTS) and the conventional global time stepping algorithm (GTS).

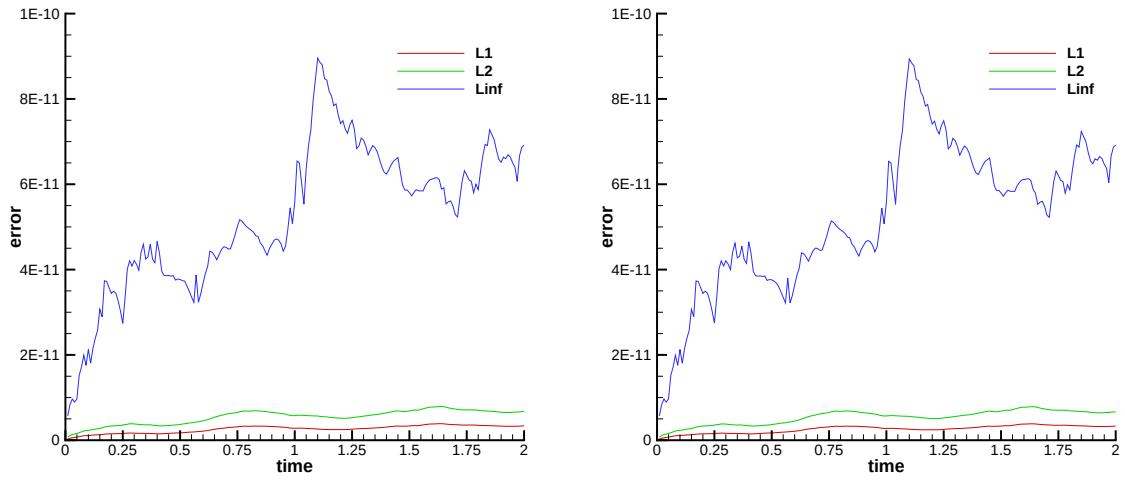

Figure 3: Error norms for the CWC test advecting a globally constant scalar quantity $C = 1$ in a 1D Riemann problem on a 2D rectangular domain. Left: local time stepping (LTS) algorithm. Right: global time stepping (GTS) algorithm.

The second CWC test problem is solved with the LTS algorithm on the same computational domain $\Omega = [-1, 1] \times [-0.1, 0.1]$ and on the same mesh as the 1D Riemann problem before. It consists in an initial free surface given by $\eta(\mathbf{x}, 0) = \max(-h, 0.5 + 0.25x)$ and a parabolic bottom $h = -x^2$, while the velocity is at rest $\mathbf{u}(\mathbf{x}, 0) = 0$. The initial concentration of the scalar is $C(\mathbf{x}, 0) = 1$ and should remain constant everywhere and for all times. We stress that this test problem involves *wetting and drying*,which is handled by the new nonlinear wetting and drying algorithm introduced by Casulli in [2] and analyzed theoretically by Brugnano and Casulli in [84, 85]. We stress that in this nonlinear wetting and drying algorithm, no small tolerance or thin water film is needed to deal with dry cells, since the method [2] is designed to handle also perfectly dry cells with zero volume. The computational results are depicted in Fig. 4, where we show the free surface at times $t = 0$ and $t = 0.8$, as well as the temporal evolution of the ratio of total scalar mass and initial scalar mass, which should remain constant in time. We furthermore plot the scalar concentration C at the final time $t = 2$. From the numerical results it can be clearly observed that the proposed local time stepping (LTS) algorithm for scalar transport is consistent with the continuity equation in the sense of [83, 30] and perfectly mass conservative even in the case of nonlinear wetting and drying.

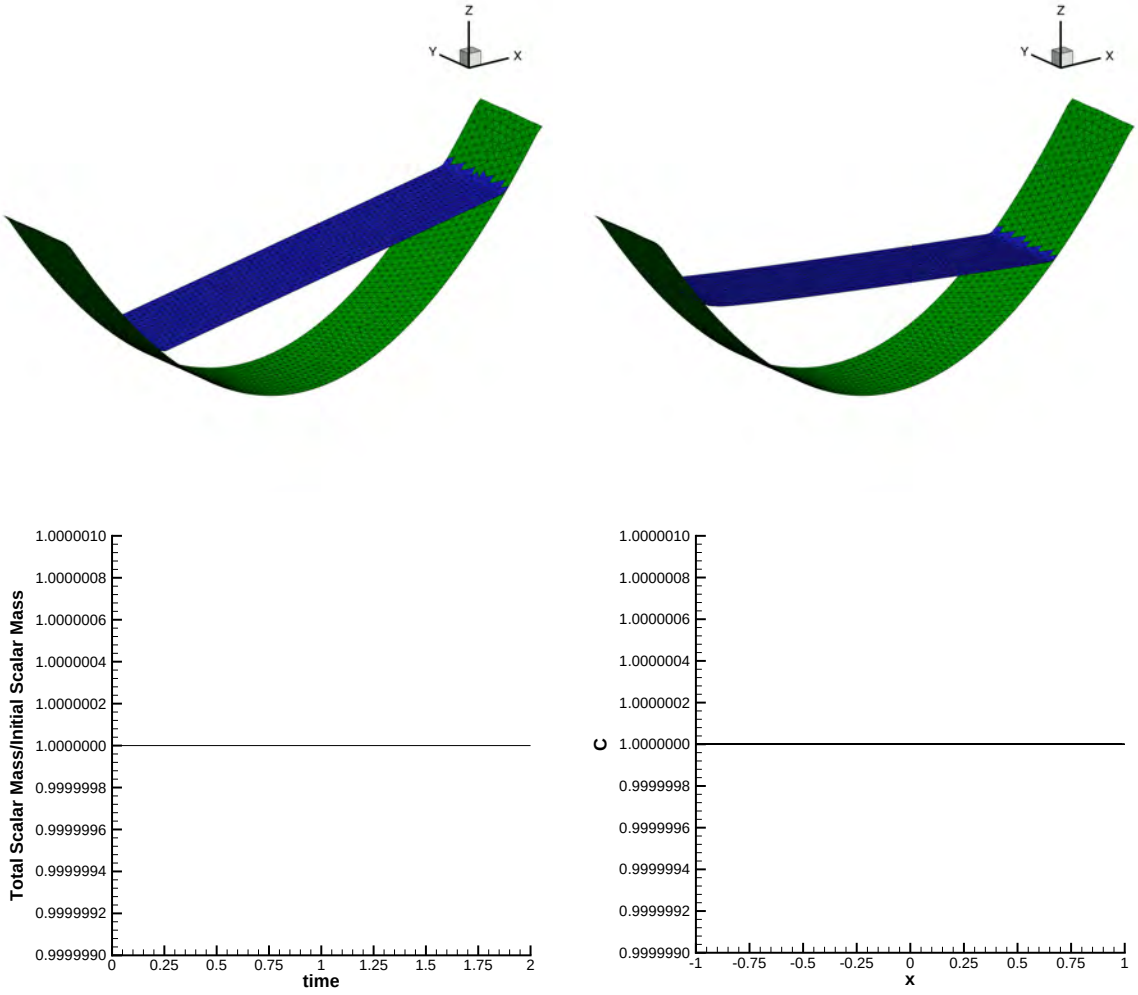

Figure 4: CWC test on an oscillating lake with wetting and drying. Top row: bottom (green) and free surface (blue) at $t = 0$ (left) and $t = 0.8$ (right). Bottom row: time evolution of the ratio of the total scalar mass w.r.t. the initial scalar mass (left) and scalar concentration at the final time $t = 2.0$ (right).

3.5. Curved Channel

This test case consists in the advection of a scalar quantity through a curved "U" channel. The same test case is presented in [30], where a comparison between the flow alignment and the use of flux limiters is discussed. The channel used here has length $L = 8570$ m, width $W = 120$ m and constant depth $h = 10$ m. The channel is open at both ends where a different water surface elevation $\eta_1 = 9$ cm and $\eta_2 = -9$ cm is specified in order to drive a steady flow. The channel is then covered with an unstructured grid with characteristic length of $\lambda = 20$ m (Fig. 5).

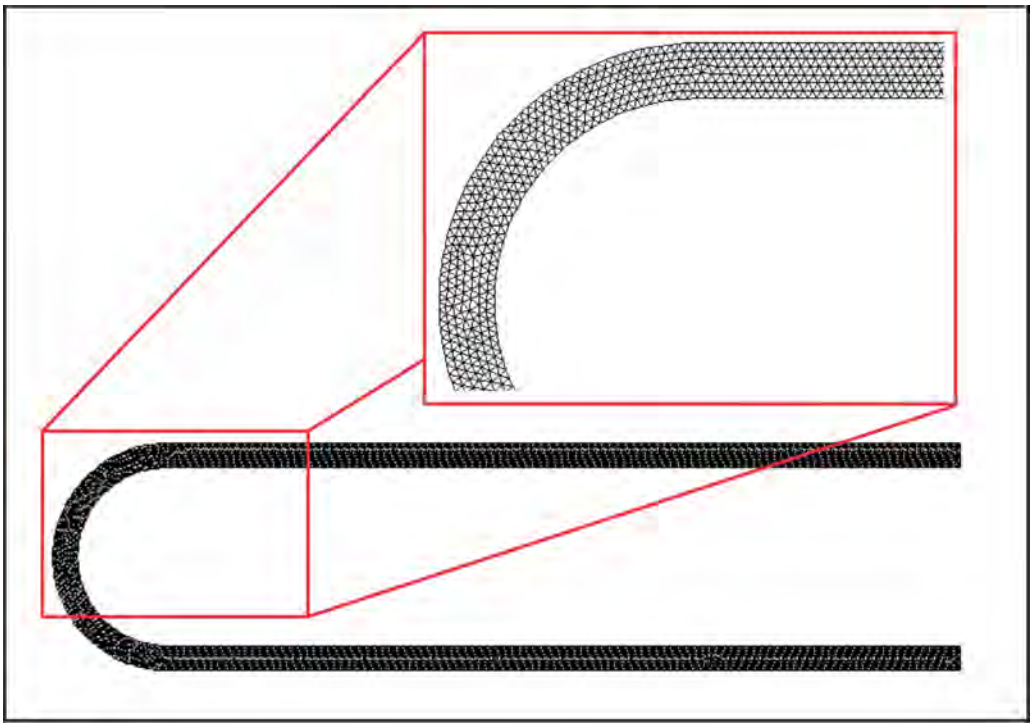

Figure 5: Unstructured triangular mesh used in the curved channel test case. Characteristic mesh length $\lambda = 20$ m.

A uniform flow is assumed after 3h of simulation, then a passive scalar of concentration $C = 1$ is released into the system at the lower right end of the channel and the simulation is performed up to a final time of 8 hours. In both cases, using LTS and GTS, we have achieved exact mass conservation up to machine precision and the maximum principle for the scalar was satisfied, i.e. $0 \leq C \leq 1$ was satisfied for all times. The concentration profiles obtained with the LTS algorithm match those of the global time stepping approach, see (Fig. 6). In this test case, the CPU time savings were only of $\approx 3\%$. Nonetheless, the LTS algorithm still represented a marginal gain in simulation time, showing the applicability of the algorithm even in applications where the velocity field and the element size are rather homogeneous.

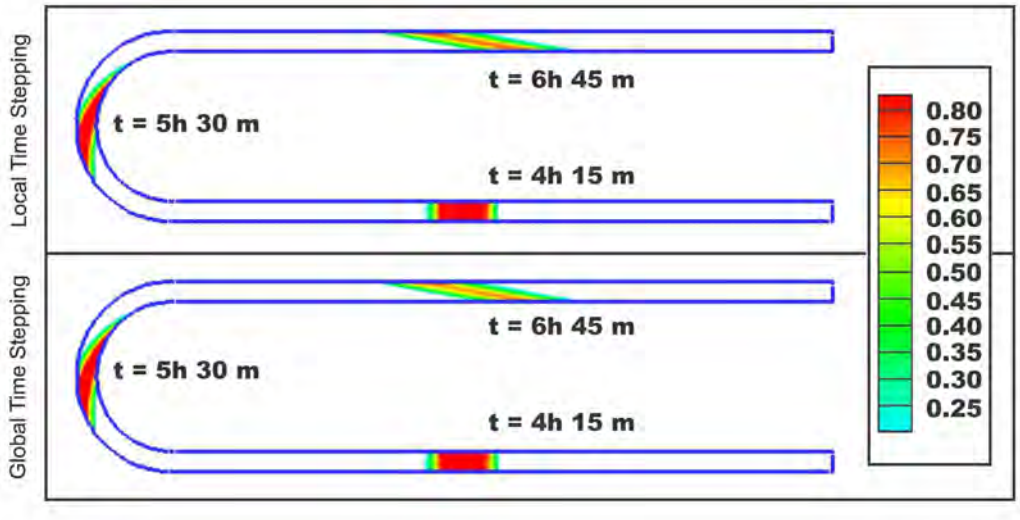

Figure 6: Numerical results for the curved channel test case using a second order MUSCL-Hancock finite volume scheme using LTS and GTS at times $t = 4h15m$, $t = 5h30m$, and $t = 6h45m$.

3.6. Guaiba lake-river system

This test case aims at showing the performance of the local time stepping algorithm in a more realistic real-world scenario that considers the interface between rivers and a lake. The chosen domain was the Lake Guaiba interface, near Porto Alegre, Rio Grande do Sul, Brazil. It is a large (surface area ca. 436 km^2) and shallow (mean depth 6.0 m at full pool) water body and plays a fundamental role in transport, irrigation, drinking water supply and wastewater discharge for the region. Its length measures 50 km, whereas its width at certain points has a cross section of up to 15 km. Moreover, the Guaiba Lake comprises one of the most important freshwater systems in Rio Grande do Sul.

The domain was covered using an unstructured triangular mesh with refinements at the lake islands, inside the river and at the lake-river connection, resulting in 31,734 triangular elements. The mesh features were rather heterogeneous, with element area ranging from 8.06 m^2 to 134,717.03 m^2 and edge length ranging from 1.24 m to 794.05 m (Fig. 7). A bathymetric survey of the Guaiba lake was carried out by the Diretoria de Hidrografia e Navegação do Ministério da Marinha in 1964. Therefore, average depths at each element were estimated by interpolation using a simplified Inverse Distance Weighting algorithm [86]. Daily water level and discharge data (obtained for 2006 due to their consistency over the entire year) were freely provided by Agência Nacional de Águas (Table 2). The discharge stations at the Jacuí, Sinos, Caí and Gravataí rivers were used as upstream boundary conditions, whereas the water level station at Ponta dos Coatis was assumed as the downstream boundary condition (Fig. 7). Since there are no discharge stations at the interface of the Jacuí and Guaiba rivers, continuous discharge values for the Jacuí River were estimated based on a regionalization method [e.g. 87] using the discharge data available. This approach has proven itself suitable to simulate Lake Guaiba hydrodynamics in a previous study [88].

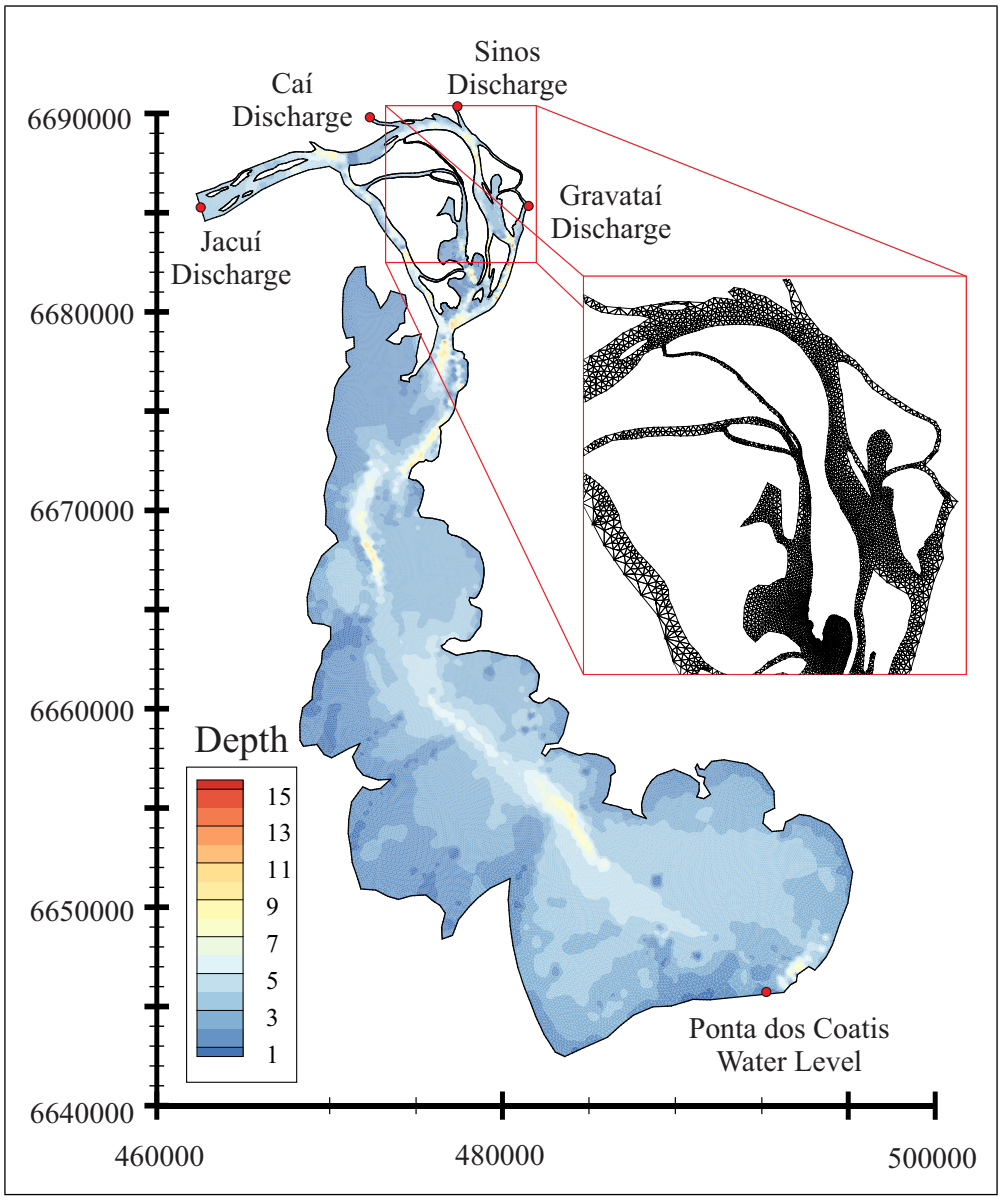

Figure 7: Lake Guaiba bathymetric information and boundary conditions. The boundary conditions used in Jacuí, Caí, Sinos and Gravataí were discharge data whereas the boundary condition used in Ponta dos Coatis was a prescribed water level. A snapshot shows the unstructured triangular mesh used in the test case for the most refined section of the domain.

Table 2: Streamflow and water level gauging stations of the Guaiba Lake and its tributaries used in this study.

Boundary Conditions	Station Number	Latitude	Longitude	Station Name	River	Available Data
	86720000	29°14′04” S	51°51′18” W	Encantado	Jacuí	Discharge
	85900000	29°59′41” S	51°22′38” W	Rio Pardo	Taquari	Discharge
Upstream	87382000	29°45′32” S	52°09′02” W	São Leopoldo	Sinos	Discharge
	87170000	29°35′19” S	51°22′56” W	Barca do Caí	Caí	Discharge
	87399000	29°57′52” S	50°58′40” W	Passo das Canoas	Gravataí	Discharge
Downstream	87500020	30°15′32” S	51°09′20” W	Ponta dos Coatis	Guaiba	Water Level

The semi-implicit discretization of the hydrodynamics equations together with an Eulerian-Lagrangian scheme for the nonlinear convective terms [1] leads to an unconditionally stable scheme, hence the CFL-type time step restriction on the transport equation [30] leads to smaller time steps in the transport model than in the hydrodynamkcs. Consistency with continuity is achieved by a proper flux calculation taking into account the updated normal velocity and face height at a proper intermediate time via linear interpolation, see [83, 30]. Thus, the coupling between hydrodynamics and transport proposed here allows for asynchronous time steps during the simulation. The scalar transport is computed *online* with the simulation of the hydrodynamics.

The bottom roughness in this complex system was simply modeled by using a constant Chezy coefficient set to 44.7 $m^{1/2}.s^{-1}$ over the entire domain. The horizontal eddy viscosity was chosen to be constant and equal to 5 $m^2.s^{-1}$. The θ parameter in the time discretization of the hydrodynamic model was chosen to be equal to $\theta = 0.6$ [89, 83]. The numerical simulation was performed for 5 *days* using a time step of 1 *hour* for the hydrodynamical model. After 1 day of hydrodynamical simulation, a passive scalar substance with concentration $C = 1$ was injected into the system at the Jacuí River inflow boundary condition. The results for both LTS and GTS algorithms agreed well with each other, even in such a rather complex case, see (Fig. 8). The CPU time saved in this test case was $\approx 95\%$, which is an enormous gain.

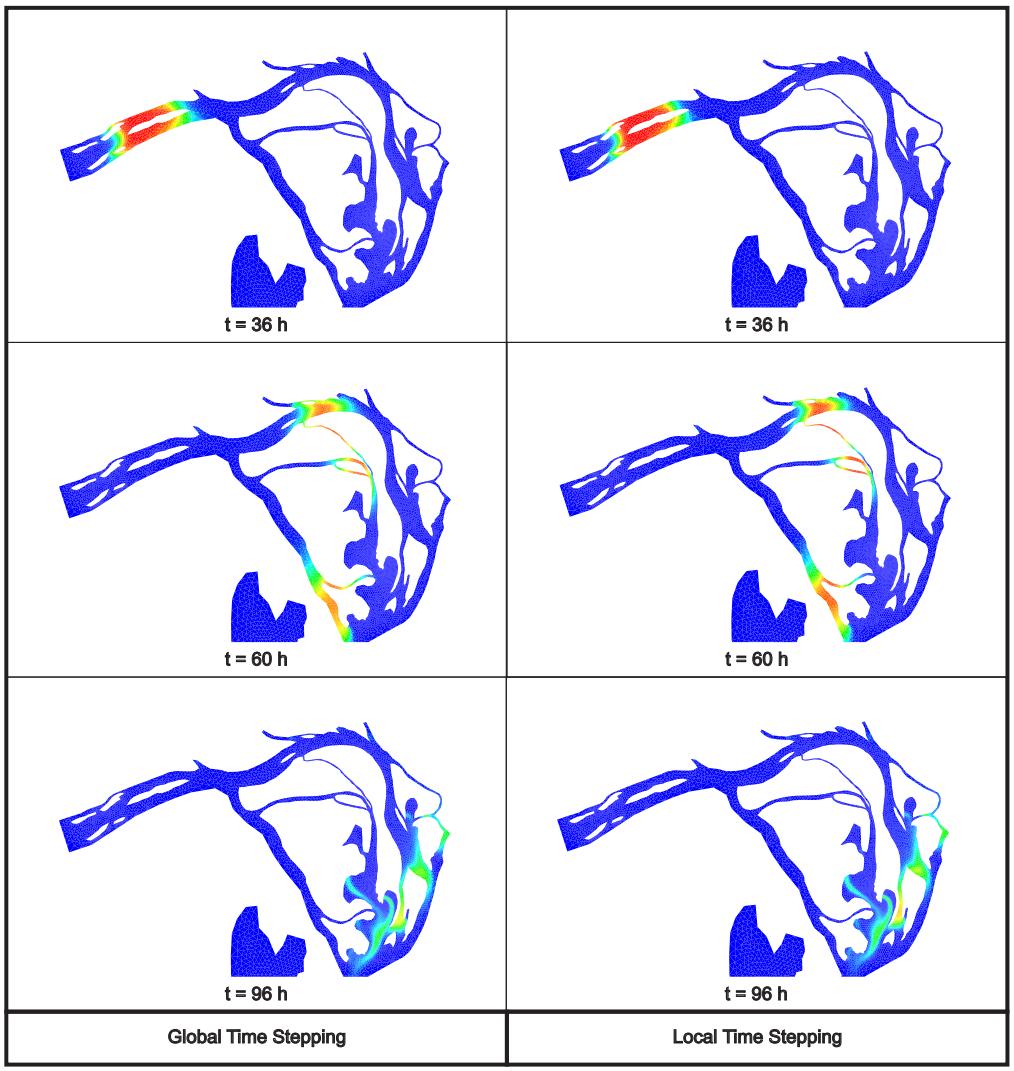

Figure 8: Numerical results for the lake-river interface test case using a second order MUSCL-Hancock finite volume scheme using LTS and GTS at times $t = 36h$, $t = 60h$, and $t = 96h$.

Lake and river systems are well known for the necessity of fine meshes inside the river and the use of a coarse mesh in the lake region. However, since the domain covered by the lake is typically very large compared to the one of the river, still many elements of the computational domain are necessary to discretize the lake. Furthermore, flow velocities are typically much higher in the river than in the lake. The use of a GTS-type algorithm requires all elements of the mesh to be penalized using the small time step that is dictated by the stability condition of the small high velocity elements inside the river. Hence, this situation is almost ideal for the use of a local time stepping algorithm like the one presented here, where the small elements with high flow velocity in the river can be updated with very small time steps, while the large elements with low fluid velocity in the lake can proceed with much larger time steps. This result is reported in Table 3, where the GTS algorithm needed a total CPU time of 418.12 seconds, while the new LTS algorithm presented in this paper was able to produce the same results in only 17.38 seconds. This corresponds to a CPU time reduction by **one order of magnitude**. Note that the CPU times reported here refer to the pure cost of the scalar transport and not to the hydrodynamical model. The gain in computational effort can also be noticed on the total number of element updates (TEU) necessary for the simulation of the scalar transport in both algorithms. Comparing GTS with LTS we can notice a reduction of $\approx 98\%$ on the total number of elements updated

in favor of LTS.

Table 3: Comparison between GTS and LTS for the numerical test cases reported.

Test Case	Algorithm	CPU time (s)	$\frac{t_{LTS}}{t_{GTS}}$	Total Element Updates (TEU)	$\frac{TEU_{LTS}}{TEU_{GTS}}$
Slotted Cylinder	GTS	40.81	**0.86**	168285680	**0.39**
	LTS	35.27		66188996	
Frontogenesis	GTS	144.47	**0.32**	553464072	**0.11**
	LTS	46.45		58184514	
Curved Channel	GTS	14.09	**0.97**	28185564	**0.65**
	LTS	13.70		18262412	
Guaiba Lake	GTS	418.12	**0.04**	1066611474	**0.02**
	LTS	17.38		19800511	

4. Conclusion

In this paper we have presented a novel conservative, two-dimensional unstructured finite volume scheme that is capable of solving advection-dominated scalar transport problems with time-accurate local time stepping. The numerical scheme is robust, conservative and nominally second order accurate in space and time by using a classical MUSCL-Hancock method. The new local time stepping algorithm for scalar transport was coupled to a 2D hydrodynamic model based on the semi-implicit discretization of the shallow water equations. This allows to simulate the hydrodynamics and the resulting scalar transport simultaneously. The problem of small time steps, which arises very often in water quality modeling, was overcome by the use of a novel, but simple to implement local time stepping algorithm, which uses asynchronous information between different time steps amongst the element neighbors. The LTS algorithm presented lower CPU times for all test cases shown here. With the Guaiba lake-river test problem we have also shown that the method is capable of significantly reducing the necessary CPU time for large scale and long-time simulations, specially when discretizing highly irregular domains like estuaries, lakes or rivers, for example. Also, the algorithm reported a lower number of total element updates when compared to a global time stepping algorithm.

The real gain in computational effort using the novel LTS algorithm in a true *real-world* application of water quality modeling is yet unknown. Further improvements on the numerical scheme presented here are the extension to three space dimensions. We furthermore plan the extension of the present LTS framework to the discretization of diffusion terms and (stiff) reaction source terms, as well as the extension to the transport of multiple scalars that can interact with each other, for example, by chemical reactions or chemotaxis.

5. Acknowledgments

The authors are grateful to CAPES/BR, the Brazilian Federal Agency for the Support and Evaluation of Graduate Education, for the scholarship awarded to R.C. during the first semester of 2014, process no. BEX 11698/13-6. M.D. was funded by the European Research Council (ERC) under the European Union's Seventh Framework Programme (FP7/2007-2013) within the research project *STiMulUs*, ERC Grant agreement no. 278267

The authors would also like to thank Prof. Vincenzo Casulli for the inspiring discussions on the subject.

Last but not least, the authors would like to thank the three anonymous referees, who helped to significantly improve the quality and the clarity of this manuscript.

References

[1] V. Casulli, R. Walters, An unstructured grid, three-dimensional model based on shallow water equations, International Journal for Numerical Methods in Fluids 32 (2000) 331–348.

[2] V. Casulli, A high-resolution wetting and drying algorithm for free-surface hydrodynamics, International Journal for Numerical Methods in Fluids 60 (2009) 391–408.

[3] A. Bermudez, M. Vázquez-Cendón, Upwind methods for hyperbolic conservation laws with source terms, Computers and Fluids 23 (1994) 1049–1071.

[4] R. J. LeVeque, Balancing source terms and flux gradients in high-resolution godunov methods: The quasi-steady wavepropagation algorithm, Journal of Computational Physics 146 (1998) 346–365.
[5] M. Vázquez-Cendón, Improved treatment of source terms in upwind schemes for the shallow water equations in channels with irregular geometry, Journal of Computational Physics 148 (1999) 497–526.
[6] P. Garcia-Navarro, M. Vázquez-Cendón, On numerical treatment of the source terms in the shallow water equations, Computers & Fluids 29 (2000) 951–979.
[7] P. Brufau, M. Vazquez-Cendon, P. Garcia-Navarro, A numerical model for the flooding and drying of irregular domains, International Journal for Numerical Methods in Fluids 39 (2002) 247–275.
[8] S. Noelle, N. Pankratz, G. Puppo, J. Natvig, Well-balanced finite volume schemes of arbitrary order of accuracy for shallow water flows, Journal of Computational Physics 213 (2006) 474–499.
[9] S. Noelle, Y. Xing, C. Shu, High-order well-balanced finite volume WENO schemes for shallow water equation with moving water, Journal of Computational Physics 226 (2007) 29–58.
[10] E. Audusse, F. Bouchut, M. Bristeau, R. Klein, B. Perthame, A fast and stable well-balanced scheme with hydrostatic reconstruction for shallow water flows, SIAM Journal on Scientific Computing 25 (2004) 2050–2065.
[11] M. Castro, J. Gallardo, C. Parés, High-order finite volume schemes based on reconstruction of states for solving hyperbolic systems with nonconservative products. applications to shallow-water systems, Mathematics of Computation 75 (2006) 1103–1134.
[12] C. Parés, Numerical methods for nonconservative hyperbolic systems: a theoretical framework, SIAM Journal on Numerical Analysis 44 (2006) 300–321.
[13] M. Castro, A. Pardo, C. Parés, E. Toro, On some fast well-balanced first order solvers for nonconservative systems, Mathematics of Computation 79 (2010) 1427–1472.
[14] A. Canestrelli, M. Dumbser, A. Siviglia, E. Toro, Well-balanced high-order centered schemes on unstructured meshes for shallow water equations with fixed and mobile bed, Advances in Water Resources 33 (2010) 291–303.
[15] Y. Xing, C. Shu, High-order well-balanced finite difference WENO schemes for a class of hyperbolic systems with source terms, Journal of Scientific Computing 27 (1-3) (2006) 477–494.
[16] E. Toro, Shock-Capturing Methods for Free-Surface Shallow Flows, John Wiley & Sons, 2001.
[17] V. Casulli, Semi-implicit finite difference methods for the two-dimensional shallow water equations, Journal of Computational Physics 86 (1990) 56–74.
[18] V. Casulli, R. Cheng, Semi-implicit finite difference methods for three-dimensional shallow water flow, International Journal of Numerical Methods in Fluids 15 (1992) 629–648.
[19] V. Casulli, G. S. Stelling, Semi-implicit subgrid modelling of three-dimensional free-surface flows, International Journal for Numerical Methods in Fluids 67 (2011) 441–449.
[20] G. Stelling, S. P. A. Duynmeyer, A staggered conservative scheme for every froude number in rapidly varied shallow water flows, International Journal for Numerical Methods in Fluids 43 (2003) 1329–1354.
[21] S. Kramer, G. Stelling, A conservative unstructured scheme for rapidly varied flows, International Journal for Numerical Methods in Fluids 58 (2008) 183–212.
[22] M. Dumbser, V. Casulli, A staggered semi-implicit spectral discontinuous galerkin scheme for the shallow water equations, Applied Mathematics and Computation 219 (15) (2013) 8057–8077.
[23] M. Tavelli, M. Dumbser, A high order semi–implicit discontinuous Galerkin method for the two dimensional shallow water equations on staggered unstructured meshes, Applied Mathematics and Computation 234 (2014) 623–644.
[24] V. Casulli, A semi-implicit numerical method for the free–surface Navier–Stokes equations, International Journal for Numerical Methods in Fluids 74 (2014) 605–622.
[25] B. R. Hodges, J. Imberger, A. Saggio, K. Winters, Modeling basin-scale internal waves in a stratified lake, Limnology and Oceanography 45 (2000) 1603–1620.
[26] C. R. Fragoso Jr, D. Motta-Marques, W. Collischonn, C. E. Tucci, E. H. van Nes, Modelling spatial heterogeneity of phytoplankton in lake mangueira, a large shallow subtropical lake in south brazil, Ecological Modelling 219 (2008) 125–137.
[27] C. R. Fragoso Jr, D. Motta-Marques, T. F. Ferreira, J. H. Janse, E. H. van Nes, Potential effects of climate change and eutrophication on a large subtropical shallow lake, Ecological Modelling & Software 26 (2011) 1337–1348.
[28] K. Park, H. Wang, S.-C. Kim, J.-H. Oh, A model study of the estuarine turbidity maximum along the main channel of the upper chesapeake bay, Estuaries and Coasts 31 (1) (2008) 115–133.
[29] J. Shen, H. Wang, Determining the age of water and long-term transport timescale of the chesapeake bay, Estuarine, Coastal and Shelf Science 74 (4) (2007) 750–763.
[30] V. Casulli, P. Zanolli, High resolution methods for multidimensional advection–diffusion problems in free-surface hydrodynamics, Ocean Modelling 10 (2005) 137–151.
[31] Y. Zhang, A. Baptista, A semi-implicit Eulerian-Lagragian finite-element model for cross-scale ocean circulation, Ocean Modelling 21 (2008) 71–96.
[32] C. R. Fragoso Jr, J. H. Janse, E. H. van Nes, D. Motta-Marques, IPH-TRIM3D-PCLake: A three-dimensional complex dynamic model for subtropical aquatic ecosystems, Ecological Modelling & Software 24 (2009) 1347–1348.
[33] O. Fringer, M. Gerritsen, R. L. Street, An unstructured-grid, finite-volume, nonhydrostatic, parallel coastal ocean simulator, Ocean Modelling 14 (2006) 139–173.
[34] B. Hodges, A new approach to the local time stepping problem for scalar transport, Ocean Modelling 77 (2014) 1–19.
[35] S. Osher, R. Sanders, Numerical approximations to non-linear conservation laws with locally varying time and space grids, Mathematics of Computation 41 (1983) 321–336.
[36] J. Flaherty, R. Loy, M. Shephard, B. Szymanski, J. Teresco, L. Ziantz, Adaptive local refinement with octree load–balancing for the parallel solution of three–dimensional conservation laws, Journal of Parallel and Distributed Computing 47 (1997) 139–152.
[37] M. J. Berger, J. Oliger, Adaptive Mesh Refinement for Hyperbolic Partial Differential Equations, Journal of Computational Physics 53 (1984)

484.
[38] M. J. Berger, P. Colella, Local adaptive mesh refinement for shock hydrodynamics, Journal of Computational Physics 82 (1989) 64–84.
[39] M. Berger, D. George, R. LeVeque, K. Mandli, The GeoClaw software for depth-averaged flows with adaptive refinement, Advances in Water Resources 34 (9) (2011) 1195–1206.
[40] A. Baeza, P. Mulet, Adaptive mesh refinement techniques for high-order shock capturing schemes for multi-dimensional hydrodynamic simulations, International Journal for Numerical Methods in Fluids 52 (2006) 455–471.
[41] A. Baeza, A. Martínez-Gavara, P. Mulet, Adaptation based on interpolation errors for high order mesh refinement methods applied to conservation laws , Applied Numerical Mathematics 62 (2012) 278–296.
[42] M. Dumbser, O. Zanotti, A. Hidalgo, D. Balsara, ADER-WENO Finite Volume Schemes with Space-Time Adaptive Mesh Refinement, Journal of Computational Physics 248 (2013) 257–286.
[43] J. Utzmann, T. Schwartzkopff, M. Dumbser, C. Munz, Heterogeneous Domain Decomposition for Computational Aeroacoustics, AIAA Journal 44 (2006) 2231–2250.
[44] C. Castro, M. Käser, E. Toro, Space–time adaptive numerical methods for geophysical applications, Philosophical Transactions of the Royal Society A: Mathematical, Physical and Engineering Sciences 367 (2009) 4613–4631.
[45] M. Dumbser, M. Käser, E. F. Toro, An arbitrary high order discontinuous Galerkin method for elastic waves on unstructured meshes V: Local time stepping and p-adaptivity, Geophysical Journal International 171 (2007) 695–717.
[46] F. Lörcher, G. Gassner, C. D. Munz, A discontinuous Galerkin scheme based on a space-time expansion. I. inviscid compressible flow in one space dimension, Journal of Scientific Computing 32 (2007) 175–199.
[47] G. Gassner, F. Lörcher, C. D. Munz, A discontinuous Galerkin scheme based on a space-time expansion II. viscous flow equations in multi dimensions., Journal of Scientific Computing 34 (2008) 260–286.
[48] G. Gassner, M. Dumbser, F. Hindenlang, C. Munz, Explicit one–step time discretizations for discontinuous Galerkin and finite volume schemes based on local predictors, Journal of Computational Physics 230 (2011) 4232–4247.
[49] A. Taube, M. Dumbser, C. Munz, R. Schneider, A High Order Discontinuous Galerkin Method with Local Time Stepping for the Maxwell Equations, International Journal Of Numerical Modelling: Electronic Networks, Devices And Fields 22 (2009) 77–103.
[50] L. Krivodonova, An efficient local time–stepping scheme for solution of nonlinear conservation laws, Journal of Computational Physics 229 (2010) 8537–8551.
[51] M. Dumbser, Arbitrary–Lagrangian–Eulerian ADER–WENO finite volume schemes with time–accurate local time stepping for hyperbolic conservation laws, Computer Methods in Applied Mechanics and Engineering 280 (2014) 57–83.
[52] W. Boscheri, M. Dumbser, O. Zanotti, High Order Cell-Centered Lagrangian-Type Finite Volume Schemes with Time-Accurate Local Time Stepping on Unstructured Triangular Meshes, Journal of Computational Physics 291 (2015) 120–150.
[53] M. Grote, T. Mitkova, High-order explicit local time-stepping methods for damped wave equations, Journal of Computational and Applied Mathematics 239 (2013) 270–289.
[54] M. Grote, T. Mitkova, Explicit local time-stepping methods for Maxwell's equations, Journal of Computational and Applied Mathematics 234 (2010) 3283–3302.
[55] L. Krivodonova, J. Xin, J.-F. Remacle, N. Chevaugeon, J. Flaherty, Shock detection and limiting with discontinuous Galerkin methods for hyperbolic conservation laws, Applied Numerical Mathematics 48 (34) (2004) 323 – 338.
[56] H.Luo, J.D.Baum, R.Löhner, A Hermite WENO-based limiter for discontinuous Galerkin method on unstructured grids, J. Comput. Phys. 225 (2007) 686–713.
[57] J.Zhu, J. Qiu, C.W.Shu, M. Dumbser, Runge–Kutta discontinuous Galerkin method using WENO limiters II: Unstructured meshes, J. Comput. Phys. 227 (9) (2008) 4330–4353.
[58] D.Kuzmin, Slope limiting for discontinuous Galerkin approximations with a possibly non-orthogonal Taylor basis, International Journal for Numerical Methods in Fluids 71 (9) (2013) 1178–1190.
[59] D.Kuzmin, Hierarchical slope limiting in explicit and implicit discontinuous Galerkin methods, Journal of Computational Physics 257 (2014) 1140 – 1162.
[60] J. Zhu, X. Zhong, C. Shu, J. Qiu, Runge–Kutta discontinuous Galerkin method using a new type of WENO limiters on unstructured meshes, J. Comp. Phys. 248 (2013) 200–220.
[61] M. Sonntag, C. Munz, Shock capturing for discontinuous galerkin methods using finite volume subcells, in: J. Fuhrmann, M. Ohlberger, C. Rohde (Eds.), Finite Volumes for Complex Applications VII, Springer, 2014, pp. 945–953.
[62] M. Dumbser, O. Zanotti, R. Loubère, S. Diot, A posteriori subcell limiting of the discontinuous Galerkin finite element method for hyperbolic conservation laws, Journal of Computational Physics 278 (2014) 47–75.
[63] O. Zanotti, F. Fambri, M. Dumbser, A. Hidalgo, Space-time adaptive ADER discontinuous Galerkin finite element schemes with a posteriori subcell finite volume limiting, Computers and Fluids 118 (2015) 204–224.
[64] O. Zanotti, F. Fambri, M. Dumbser, Solving the relativistic magnetohydrodynamics equations with ADER discontinuous Galerkin methods, a posteriori subcell limiting and adaptive mesh refinement, Monthly Notices of the Royal Astronomical Society (MNRAS) 452 (2015) 3010–3029.
[65] E. F. Toro, Riemann Solvers and Numerical Methods for Fluid Dynamics, Second Edition, Springer–Verlag, 1999.
[66] S. Bellavia, S. Berrone, Globalization strategies for Newton–Krylov methods for stabilized FEM discretization of Navier–Stokes equations, Journal of Computational Physics 226 (2) (2007) 2317–2340.
[67] S. Bellavia, M. Macconi, B. Morini, An affine scaling trust–region approach to bound–constrained nonlinear systems, Applied Numerical Mathematics 44 (3) (2003) 257–280.
[68] Y. Shokin, The method of differential approximation, Springer, Heidelberg, New York, 1983.
[69] B. van Leer, Towards the ultimate conservative difference scheme V: A second order sequel to Godunov's method, Journal of Computational Physics 32 (1979) 101–136.
[70] E. Toro, Riemann Solvers and Numerical Methods for Fluid Dynamics, 3rd Edition, Springer, 2009.
[71] B. van Leer, On the relation between the upwind-differencing schemes of Godunov, Enguist-Osher and Roe, J. Sci. Stat. Comput. 5 (1985)

1–20.
[72] S. Godunov, Finite difference methods for the computation of discontinuous solutions of the equations of fluid dynamics, Mathematics of the USSR: Sbornik 47 (1959) 271–306.
[73] T. Barth, D. Jespersen, The design and application of upwind schemes on unstructured meshes, AIAA Paper 89-0366 (1989) 1–12.
[74] M. Dumbser, M. Käser, Arbitrary high order non-oscillatory finite volume schemes on unstructured meshes for linear hyperbolic systems, Journal of Computational Physics 221 (2007) 693–723.
[75] E. Toro, Viscous flux limiters, in: Vos, Rizzi, Rhyming (Eds.), Notes on Numerical Fluid Mechanics, Vol. 35, Vieweg, 1992, pp. 592–600.
[76] M. Tavelli, M. Dumbser, V. Casulli, High resolution methods for scalar transport problems in compliant systems of arteries, Applied Numerical Mathematics 74 (2013) 62–82.
[77] V. Casulli, A semi-implicit finite difference method for non-hydrostatic free-surface flows, International Journal for Numerical Methods in Fluids 30 (1999) 425–440.
[78] V. Casulli, P. Zanolli, Semi-implicit numerical modeling of nonhydrostatic free-surface flows for environmental problems, Mathematical and Computer Modelling 36 (2002) 1131–1149.
[79] S. Zalesak, Fully multidimensional flux-corrected transport algorithms for fluids, Journal of Computational Physics 31 (1979) 335–362.
[80] C. Doswell, A kinematic analysis of frontogenesis associated with a non-divergent vortex, Journal of Atmospheric Sciences 41 (1984) 1242–1248.
[81] R. Davies-Jones, Comments on 'A kinematic analysis of frontogenesis associated with a non-divergent vortex', Journal of Atmospheric Sciences 42 (1985) 2073–2075.
[82] E. Toro, V. Titarev, ADER schemes for scalar hyperbolic conservation laws with source terms in three space dimensions, Journal of Computational Physics 202 (2005) 196–215.
[83] E. S. Gross, L. Bonaventura, G. Rosatti, Consistency with continuity in conservative advection schemes for free-surface models, International Journal for Numerical Methods in Fluids 38 (2002) 307–327.
[84] L. Brugnano, V. Casulli, Iterative solution of piecewise linear systems, SIAM Journal on Scientific Computing 30 (2007) 463–472.
[85] L. Brugnano, V. Casulli, Iterative solution of piecewise linear systems and applications to flows in porous media, SIAM Journal on Scientific Computing 31 (2009) 1858–1873.
[86] D. Shepard, A two-dimensional interpolation function for irregularly spaced data, Proceedings of the 23rd National Conference, ACM, New York (1968) 517–523.
[87] J. Samuel, P. Coulibaly, R. Metcalfe, Estimation of continuous streamflow in Ontario ungauged basins: Comparison of regionalization methods, Journal of Hydrologic Engineering 16 (2011) 447–459.
[88] F. Pereira, C. Fragoso Jr., C. Uvo, W. Collischonn, D. Motta-Marques, Assessment of numerical schemes for solving the advection-diffusion equation on unstructured grids: case study of Guaba River, Brazil, Nonlinear Processes in Geophysics 20 (2013) 1113–1125. doi:10.5194/npg-20-1113-2013.
[89] V. Casulli, E. Cattani, Stability, accuracy and efficiency of a semi-implicit method for three-dimensional shallow water flow, Computers and Mathematics with Applications 27 (1994) 99–112.

AppendixA. LTS Pseudo-code

To facilitate the reader with the practical implementation of the LTS algorithm presented in this paper, we show the associated pseudo-code in the following. The code refers to the scalar transport of a quantity C in a given vector field $\mathbf{u}$ for one time step of the hydrodynamical model Δt_H.

Algorithm 1 Scalar Transport with Local Time Stepping

procedure LTS(**u**,C,dtH)
  1.Initialize variables:
  $Done$ = **false** ▷ Updated Element Control Vector
  $t = 0.$ ▷ Initial local time
  $MV = 0.$ ▷ Set memory variable to zero
  2.Find the initial local time step:
  for $i \leftarrow 1, nElem$ **do** ▷ Loop over all elements
    Calculate $dt(i)$ using (18)
  end for
  3.Initial Linear Reconstruction:
  for $i \leftarrow 1, nElem$ **do** ▷ Loop over all elements
    Calculate spatial and temporal gradients ∇C_i^n and $\partial_t C_i^n$ using (15) and (8)
  end for
  for $iCycle \leftarrow 1, nCycle$ **do** ▷ Loop over a maximum number of cycles
    for $i \leftarrow 1, nElem$ **do** ▷ Loop over the elements
      if ($Done(i)$ ==**true**) **then** ▷ Check if the element is up-to-date
        skip element i
      end if
      4.Update Criteria:
      $stencilmin = t(i) + dt(i)$
      for $j \in \mathcal{N}_i$ **do** ▷ Loop over the set of neighbors
        $stencilmin = \min(stencilmin, t(j) + dt(j))$ ▷ Minimum Future Time
      end for
      if ($t(i) + dt(i) \leq stencilmin$) **then** ▷ Update criterion (19)
        $sumflux = 0$
        for $j \in \mathcal{N}_i$ **do** ▷ Loop over the set of neighbors
          5.Flux Time Interval: ▷ Computing the flux through the element faces
          $t1 = \max(t(i), t(j))$ ▷ Compute t_{ij}^n from (20)
          $t2 = \min(t(i) + dt(i), t(j) + dt(j))$ ▷ Compute t_{ij}^{n+1} from (20)
          if ($t2 - t1 > 0$) **then** ▷ Compute flux only for positive interval lengths
            $t05 = 0.5 \cdot (t1 + t2)$ ▷ Compute the half time level of the flux interval
            $CL = C(i) + \nabla C_i^n \cdot (\mathbf{x}_{ij} - \mathbf{x}_i) + \partial_t C_i^n \cdot (t05 - t(i))$ ▷ Reconstruct the left interface state
            $CR = C(j) + \nabla C_j^n \cdot (\mathbf{x}_{ij} - \mathbf{x}_j) + \partial_t C_j^n \cdot (t05 - t(j))$ ▷ Reconstruct the right interface state
            $F_{ij} = F_{ij}(CL, CR)$ ▷ Compute the flux according to (6)
          else
            $F_{ij} = 0$
          end if
          $sumflux = sumflux - (t2 - t1) \cdot F_{ij} \cdot \lambda_{ij}$ ▷ Compute the sum of the edge fluxes
          $MV(j) = MV(j) + (t2 - t1) \cdot F_{ij} \cdot \lambda_{ij}$ ▷ Store flux in the neighbor's memory variable
        end for
        $C(i) = \frac{1}{V_i^{n+1}} \left(V_i^n C(i) + MV(i) + sumflux \right)$ ▷ Update the concentration according to (21)
        $MV(i) = 0$ ▷ Set the memory variable of element i to zero

Algorithm 2 Scalar Transport with Local Time Stepping - Cont.

```
            6. Update Local Time:
            t(i) = t(i) + dt(i)
            7. Compute the virtual cell averages of the neighbors:
            for j ∈ N_i do                                   ▷ Loop over the set of neighbors
                Cbar(j) = C(j) + ∂_t C_j^n · (t(i) − t(j))   ▷ Compute the virtual cell averages (24)
            end for
            Calculate spatial and temporal gradients ∇C_i^n and ∂_t C_i^n using (24), (15) and (8)
            Calculate dt(i) using (18)
            if (t(i) + dt(i) > dtH) then
                dt(i) = dtH - t(i)                           ▷ Reduce last local time step, to reach dtH exactly
            end if
            if (t(i) ≥ dtH) then
                Done(i) =true                                ▷ If time dtH is reached, element is done
            end if
        end if
    end for                                                  ▷ Elements Loop
    if (ALL(Done) ==true) then                               ▷ Check if all elements have reached the final time
        Exit the Cycle Loop
    end if
  end for                                                    ▷ Cycle Loop return C
end procedure
```

Capítulo 5

A Conservative Three-Dimensional Finite Volume Scheme with Time-Accurate Local Time Stepping for Water Quality Applications on Unstructured Grids

J. Rafael Cavalcanti

Artigo a ser submetido

A Conservative Three-Dimensional Finite Volume Scheme with Time-Accurate Local Time Stepping for Water Quality Applications on Unstructured Grids

J. Rafael Cavalcanti[a,*]

[a]*Instituto de Pesquisas Hidráulicas, Universidade Federal do Rio Grande do Sul, CP 15029, Porto Alegre, RS, Brazil*

Abstract

In this study we developed a new three-dimensional, conservative, high resolution, TVD finite volume scheme with local time stepping (LTS) on unstructured grids for the numerical solution of advection-diffusion-reaction type of equations, typical in water quality applications. The new numerical algorithm is directly coupled to semi-implicit hydrodynamic models with free-surface and nonlinear wetting and drying (UnTRIM type of models). The new three-dimensional time-accurate local time stepping scheme derived here allows a different time step size for each triangular element of the unstructured computational mesh, based on an element-local CFL stability condition. The LTS scheme is based on a piecewise linear polynomial reconstruction using the MUSCL-Hancock method, hence being second order accurate in both space and time. The three-dimensional algorithm developed here is first validated on some classical test cases for convection, diffusion, and reaction problems, for which the solutions are known. In all classical cases we obtain a good level of accuracy and confirm mass conservation up to machine precision. Furthermore we observe an improved computational efficiency compared to a standard second order TVD scheme for scalar transport with global time stepping (GTS). The new three-dimensional LTS method was then applied to coupled free-surface and transport problems, showing its advantages in wind-driven hydrodynamics cases, heterogeneous bathymetry and mesh discretization, and the capability to simulate the transport of substances undergoing transformations. The last test was an application to simulate water temperature dynamics in a deep reservoir, for which real data is available (Faxinal Reservoir, south Brazil). In every test case the comparison with a second order TVD scheme based on global time stepping was performed, with savings of CPU time up to **99 %**.

Keywords: Local time stepping (LTS), finite volume schemes, water quality modelling, unstructured mesh, Faxinal Reservoir

1. Introduction

Physical processes (e.g., water mixing, thermal stratification, tides, and seiches) are important drivers of many lakes, estuaries, and rivers hydrodynamics, being utterly linked to biological processes (e.g., phytoplankton biomass distribution, primary production, and organic matter decomposition) in some cases [e.g. 5, 40, 51, 31, 57]. The numerical simulation of aquatic environments has become an useful manner to assess water quality and biological community dynamics laying within these environments [45, 43, 22, 41]. In this context, the link between physical and biological processes is usually achieved by coupled numerical solutions, simulating hydrodynamics, solute transport (e.g., salt and nutrients), and specific processes capable of transforming a desired scalar substance (e.g., thermal balance, phytoplankton metabolism, and dissolved oxygen balance). Hence, a vital part of coupled hydrodynamic and water quality simulations relays on the numerical schemes used for both, hydrodynamic and scalar transport solutions, which guarantees the water volume conservation and exact mass transport through the domain of interest [12, 29, 30, 36].

The numerical simulation of free-surface hydrodynamics is achieved by solving some form of the 3D Navier-Stokes equations, combined with some conservation equation for water volume [10]. Presently, a new generation

*More authors will be included before submission

of unstructured hydrodynamic models is under development, with the advantage of using an unstructured mesh to simulate real systems with complex morphometry [15, 39, 11, 58, 24]. These type of models are robust enough to perform accurate hydrodynamic simulations using time steps, in some cases, only limited by horizontal viscosity and mesh aspects [e.g. 11, 58]. In a water quality modelling context, once the velocity field and free-surface elevation are computed, the transport of different passive scalars can be performed independently. The coupling between both solutions, hydrodynamic and scalar transport, might not be straightforward, specially if high resolution and mass conservation is expected [12]. It is a requirement of the numerical scheme used to compute the transport of scalar quantities to be monotonic and mass conservative while coupled to the hydrodynamic solution. This condition, also referred to as *consistency with continuity* [see 28, for more details], is necessary in order to prevent instability in transport solutions, specially in applications where the cell volumes are not constant in time (which is the case for coupled hydrodynamic and water quality modelling).

The scalar/solute transport (only mentioned as scalar transport hereafter) is described by an depth-averaged advection-diffusion-reaction type of equation. Advection can be regarded as the predominant factor in most practical scalar transport problems, with diffusion being responsible for local mixing [37, 36]. The reactive terms (stiff or non-stiff) can change scalar concentrations by transforming mass or internal energy, accounting for specific processes altering, for example, phytoplankton biomass, nutrient concentration and water temperature [32, 23, 4]. The numerical solution of scalar transport equations might increase considerably the mathematical complexity of the coupled (hydrodynamic and water quality) simulations [44]. There are many numerical methods which can be used to solve scalar transport problems, such as finite difference, finite volume, and finite element methods [37, 12, 56, 7, 29]. The use of finite volume schemes, such as the first-order upwind scheme, has the advantage of dealing with large scalar gradients (e.g., concentration and water temperature) including discontinuities [52]. Nevertheless, the poor accuracy due to high numerical diffusion in the first-order schemes [52] is a drawback for scalar transport simulations. In order to reduce the inherent numerical diffusion of first-order upwind methods, high-resolution finite volume schemes have been developed [e.g. 27, 54, 42, 33]. Higher order of accuracy is usually achieved by using some form of TVD limiter, preventing undesired unphysical oscillations in the solution [34]. One commonly used approach is the Monotone Upstream-centered Scheme for Conservation Laws [MUSCL, 54] consisting in a slope limiting technique, in which the limiter is applied in a geometric manner to the gradients of a piecewise linear reconstruction of the solution thus creating a monotone scheme.

A common shortcoming for coupled hydrodynamic and water quality simulations is the simulation time step, usually when localized high velocity conditions or heterogeneous element-size (common in unstructured or adaptive-mesh grids) are observed. This is the case in many water quality applications, such as the simulation of: (i) estuaries, (ii) domains where river and lakes (or floodplains) connect, (iii) reservoirs with specific energy production operations, (iv) and environments where wind can play a key-role on water surface. The simulation time step used with the semi-implicit discretization of the continuity equation [TRIM/UnTRIM, 10, 11] is often less restrictive than the time step required for the simulation of the scalar transport problem. This holds due to the Eulerian-Lagrangian Method (ELM) used to compute the non-linear convective terms appearing in the momentum equations discretization which has the ability to deal with Courant numbers greater than unity, enabling the use of relatively large time steps. In order to overcome this mismatch between hydrodynamic and scalar transport problems one can use a subcycling approach, where the time step of the scalar transport numerical solution is bounded by either a global CFL-restriction or the hydrodynamic solution time step [50, 56, 12]. Therefore, the *global time step* used in the subcycling approach is dictated by the smallest (or the one with the highest velocities) control volume in the entire computational domain. Currently, a new class of numerical methods that allow for time-accurate local time stepping (LTS) under finite volume architecture is under developed [e.g., 18, 20, 21, 2, 6], where each element can be updated by its own optimal time step, given by a local CFL stability condition. To the best of the author's knowledge, this kind of finite volume scheme with Local Time Stepping to solve scalar transport problems has only been proposed recently in [13], where the scheme is implemented to a linear advection scalar transport case in two space dimensions. Here, we extend the algorithm presented in [13] to three space dimensions and new transport mechanisms, namely diffusion and reactive terms.

In this study, we present a time accurate Local Time Stepping algorithm which can be used in three-dimensional numerical simulations of scalar transport on unstructured triangular meshes. The newly developed transport solution can be promptly integrated to hydrodynamic models using a semi-implicit solution [e.g. 10, 11, 58]. The new algorithm is tested and validated on different benchmark problems, comparing with existing analytical solutions or with

the numerical results obtained with a standard global time stepping algorithm. Also, a complete lake thermodynamic simulation, in which hydrodynamics thermal balance plays a key-role, is performed using *in-situ* data and both algorithms (global and local time stepping) are compared. The remainder of the paper is organized as follows: in Section 2 the new algorithm is presented and explained in detail accounting for advection, diffusion, and reaction mechanisms; in Section 3 the computational results obtained for two benchmark problems involving separated and combined advection and diffusion processes, and coupled simulations with hydrodynamics, including wet- and dry-ing problems and non-conservative substance simulations, are presented and discussed; in Section 4 the presently developed algorithm is applied to simulate the thermal structure of a shallow lake subjected to *wind-driven* hydrodynamics and the results compared to a global time stepping algorithm. Some concluding remarks and an outlook to further developments is given in the concluding Section 5.

2. Three-Dimensional Scalar Transport Solution with LTS

The transport of a scalar quantity in the context of water quality simulations can be described as an advection-diffusion-reaction equation written in conservation form, where the time evolution of the volume concentration of a dissolved quantity $C = C(\mathbf{x}, t)$ is typically written as:

$$\frac{\partial \mathrm{HC}}{\partial t} + \nabla \cdot (\mathbf{u}\,\mathrm{HC}) = \nabla(\mathbf{\Gamma}\,\nabla(\mathrm{HC})) + S_C, \qquad \mathbf{x} \in \Omega \subset \mathbb{R}^2, \quad t \in \mathbb{R}_0^+. \tag{1}$$

Here, $\mathbf{u} = \mathbf{u}(\mathbf{x}, t)$ is the velocity vector and $H = H(\mathbf{x}, t)$ is the total water depth, which are both provided by a hydrodynamical model; Γ is the diffusivity tensor and S_C is a net source/sink term. Eq. (1) can conveniently be written as:

$$\frac{\partial \mathrm{HC}}{\partial t} + \nabla \cdot \mathbf{f} = S_C \tag{2}$$

where $\mathbf{f} = \mathrm{HC}\,\mathbf{u} - \mathbf{\Gamma}\,\nabla(\mathrm{HC})$ is a flux vector. In the following the computational domain Ω is discretized by triangular control volumes denoted by T_i. Integrating the PDE over a spatial control volume T_i and over the time interval $[t^n, t^{n+1}]$ yields after the use of Gauss' theorem the following integral form of the conservation law (2):

$$\int_{t^n}^{t^{n+1}} \int_{T_i} \frac{\partial \mathrm{HC}}{\partial t}\, d\mathbf{x}\, dt + \int_{t^n}^{t^{n+1}} \int_{\partial T_i} \mathbf{f} \cdot \mathbf{n}\, dS\, dt = \int_{t^n}^{t^{n+1}} \int_{T_i} S_C\, d\mathbf{x}\, dt, \tag{3}$$

where ∂T_i denotes the boundary of the control volume T_i and $\mathbf{n}$ is the outward-pointing unit normal vector on the boundary. Using the definitions

$$V_i^n = \int_{T_i} H(\mathbf{x}, t^n)\, d\mathbf{x}, \quad C_i^n = \frac{1}{V_i^n} \int_{T_i} C(\mathbf{x}, t^n)\, H(\mathbf{x}, t^n)\, d\mathbf{x},$$

$$S_i = \frac{1}{\Delta t \cdot V_i^n} \int_{t^n}^{t^{n+1}} \int_{T_i} S_C\, d\mathbf{x}\, dt \quad \text{and} \quad F_{ij} = \frac{1}{\Delta t} \int_{t^n}^{t^{n+1}} \int_{\partial T_{ij}} \mathbf{f} \cdot \mathbf{n}_{ij}\, dS\, dt, \tag{4}$$

where ∂T_{ij} denotes the segment of the boundary of element T_i that is in common with the neighbor element T_j, and where $\mathbf{n}_{ij}$ is the associated unit normal vector pointing from T_i to T_j, a three-dimensional Finite Volume discretization of (3) with *global time step* reads

$$V_{k,i}^{n+1} C_{k,i}^{n+1} = V_{k,i}^n C_{k,i}^n - \Delta t \sum_{j \in \mathcal{N}_i} \lambda_j F_{k,j} + \Delta t\, S_{k,i}. \tag{5}$$

Here, $\mathcal{N}_i$ is the set of neighbors of element T_i (including vertical and horizontal computational cells) and, as already stated above, the subscripts i and j indicate the element and its neighbor on the common edge ∂T_{ij}, respectively. The subscript k denotes the vertical layer, the length of edge ∂T_{ij} is denoted by λ_j, the superscript n indicates the time

level, $\Delta t = t^{n+1} - t^n$ is a *global* time step. $V^n_{k,i} = \Delta z^n_{k,i}\, A_i$ is the cell volume at layer k and time step n, where A_i is the element area and $F_{k,j}$ is the numerical flux. Different schemes can be used to compute the numerical flux at an element interface face. In this work we choose an upwind formulation, that reads as follows:

$$\begin{aligned} F_{k,j} = F_{k,j}((C^-_{k,j}, \nabla\, C^-_{k,j}), (C^+_{k,j}, \nabla\, C^+_{k,j})) \quad &= \quad \frac{1}{2}(\Delta z^{n+1}_{k,j} u^{n+1}_{k,j} - \Delta z^{n+1}_{k,j} \Gamma^{n+1}_{k,j}) \left(C^+_{k,j} + C^-_{k,j}\right) \\ &- \quad \frac{1}{2} \left|\Delta z^{n+1}_{k,j} u^{n+1}_{k,j} + 2\,\eta\, \Delta z^{n+1}_{k,j} \Gamma^{n+1}_{k,j}\right| \left(C^+_{k,j} - C^-_{k,j}\right), \end{aligned} \tag{6}$$

where $\Delta z^{n+1}_{k,j}$ is the layer thickness at edge j, $u^{n+1}_{k,j} = \mathbf{u}^{n+1}_{k,j} \cdot \mathbf{n}_{ij}$ denotes the normal velocity at the interface, and $\Gamma^{n+1}_{k,j} = \mathbf{\Gamma}^{n+1}_{k,j} \cdot \mathbf{n}_{ij}$ is the diffusion coefficient at edge j. Note that $\Delta z^{n+1}_{k,j}$, $u^{n+1}_{k,j}$, and $\Gamma^{n+1}_{k,j}$ are directly provided by the flow solver [11]. $C^+_{k,j}$ and $C^-_{k,j}$ are the *reconstructed interface values* at the common edge ∂T_{ij} from the left and the right, respectively. These values can be approximated using *piece-wise constant* cell averages, i.e. taking simply $C^+_{k,j} = C^n_{k,right}$ and $C^-_{k,j} = C^n_{k,left}$, resulting in a classical first order *Godunov*-type scheme. In this work we use a piecewise linear reconstruction in space and time within each element, resulting in a second order *MUSCL*-type scheme. According to [17, 26, 25], η in (6) can be computed from the solution of the generalized diffusive Riemann problem as

$$\eta = \frac{2N+1}{h\,\sqrt{\frac{1}{2}\pi}} \tag{7}$$

where the characteristic size h is taken to be circumcenter distance between two elements sharing edge j for which the flux is being computed; and for second order accurate Finite-Volume MUSCL schemes, $N = 0$ [17].

In the case of vertical faces the numerical flux is calculated for $k \pm \frac{1}{2}$ as follows:

$$\begin{aligned} F_{k\pm\frac{1}{2},i} = F_{k\pm\frac{1}{2},i}\left((C^-_{k\pm\frac{1}{2},i}, \nabla\, C^-_{k\pm\frac{1}{2},i}), (C^+_{k\pm\frac{1}{2},i}, \nabla\, C^+_{k\pm\frac{1}{2},i})\right) \quad &= \quad \frac{1}{2}(w^{n+1}_{k\pm\frac{1}{2},i} - \Gamma^{n+1}_{k\pm\frac{1}{2},i}) \left(C^+_{k\pm\frac{1}{2},i} + C^-_{k\pm\frac{1}{2},i}\right) \\ &- \quad \frac{1}{2} \left|w^{n+1}_{k\pm\frac{1}{2},i} + 2\,\eta\, \Gamma^{n+1}_{k\pm\frac{1}{2},i}\right| \left(C^+_{k\pm\frac{1}{2},i} - C^-_{k\pm\frac{1}{2},i}\right), \end{aligned} \tag{8}$$

where $w^{n+1}_{k\pm\frac{1}{2}}$ is the vertical velocity component at the interface $k \pm \frac{1}{2}$, which is also provided by the flow solver. Here we assume the positive direction as an outward pointing vector from bottom to top in each layer.

2.1. Three dimensional MUSCL method on unstructured triangular meshes

The MUSCL method [54] is an accurate and robust *second*-order finite volume numerical scheme that can be used in the solution of conservation laws, even when the solution exhibit shocks, discontinuities, and large gradients [52]. The high-order accuracy on MUSCL-type schemes is achieved by a piece-wise linear reconstruction of cell averaged data to the interfaces where the numerical flux is to be computed.

Instead of a simple cell averaged value, the data within each cell is approximated using a piecewise linear reconstruction in space and time that reads as follows:

$$C_{k,i}(\mathbf{x}, t) = C^n_{k,i} + \nabla C^n_{k,i} \cdot (\mathbf{x} - \mathbf{x}_{k,i}) + \partial_t C^n_{k,i}\,(t - t^n), \tag{9}$$

where the barycenter of the computational cell $T_{k,i}$ is denoted with $\mathbf{x}_{k,i}$, $C^n_{k,i}$ is the cell-averaged value at time t^n, $\nabla C^n_{k,i}$ is the spatial gradient of the passive scalar, which still needs to be determined, and $\partial_t C^n_{k,i}$ is its first time derivative, which can be directly computed from the PDE in primitive form once the slope $\nabla C^n_{k,i}$ is known as follows:

$$\partial_t C^n_{k,i} = -\mathbf{u}^n_{k,i} \cdot \nabla C^n_{k,i} + \mathbf{\Gamma}^n_{k,i} \cdot \nabla^2 C^n_{k,i}. \tag{10}$$

Here, $\mathbf{u}^n_{k,i}$ denotes the velocity vector at the barycenter of the computational cell $T_{k,i}$, which is provided by the flow solver.

In order to avoid spurious oscillations common to linear high order schemes [27], we use a non-linear *slope limiter* function $\Phi_{k,i}$ that is applied to the unlimited gradient $\tilde{\nabla} C^n_{k,i}$ following the procedure outlined in [3]. First one compute

an *unlimited* slope $\tilde{\nabla} C^n_{k,i}$ by simply evaluating

$$\tilde{\nabla} C^n_{k,i} = \frac{1}{|T_{k,i}|} \sum_{j \in \mathcal{N}_{k,i}} \frac{1}{2} \left(C^n_{k,i} + C^n_{k,j} \right) \mathbf{n}_{ij}. \tag{11}$$

From this unlimited slope, a *preliminary* spatial reconstruction reads

$$\tilde{C}_{k,i}(\mathbf{x}, t^n) = C^n_{k,i} + \tilde{\nabla} C^n_{k,i} \cdot (\mathbf{x} - \mathbf{x}_{k,i}), \tag{12}$$

The main idea of the non-linear slope limiter is to satisfy a discrete maximum principle, i.e., to find the largest admissible value for $\Phi_{k,i}$ for which the values of the reconstructed variables do not exceed the maximum and the minimum values of the cell averages in the set $\mathcal{S}_{k,i} = T_{k,i} \cup \mathcal{N}_{k,i}$. Hence, one needs to compute the maximum and minimum values of $C^n_{k,i}$ in the set $\mathcal{S}_{k,i}$ as

$$C^{\min}_{k,i} = \min_{j \in \mathcal{S}_{k,i}} \left(C^n_{k,j} \right) \qquad \text{and} \qquad C^{\max}_{k,i} = \max_{j \in \mathcal{S}_{k,i}} \left(C^n_{k,j} \right). \tag{13}$$

Since the reconstruction polynomial is required to remain within the upper and lower bounds

$$C^{\min}_{k,i} \leq C_{k,i}(\mathbf{x}, t^n) \leq C^{\max}_{k,i}, \tag{14}$$

the slope $\tilde{\nabla} C^n_{k,i}$ is modified so that (14) is satisfied. According to [3] while using a piece-wise linear polynomial reconstruction, the extreme values inside a triangular element will occur at the vertices of the triangle. In the following, we will denote the set of vertices of element $T_{k,i}$ with $\mathcal{V}_{k,i}$. Hence, for each vertex coordinate $\mathbf{X}_v$ of the element $T_{k,i}$ with $v \in \mathcal{V}_{k,i}$, compute the node values $\tilde{C}_{k,i}(\mathbf{X}_v, t^n)$ from (12) using the *unlimited* slope $\tilde{\nabla} C^n_{k,i}$ to determine a value $\bar{\Phi}_{i,v}$ as follows:

$$\bar{\Phi}_{i,v} = \begin{cases} \min\left(1, \frac{C^{\max}_{k,i} - C^n_{k,i}}{\tilde{C}_{k,i}(\mathbf{X}_v, t^n) - C^n_{k,i}}\right), & \text{if } \tilde{C}_{k,i}(\mathbf{X}_v, t^n) - C^n_{k,i} > 0, \\ \min\left(1, \frac{C^{\min}_{k,i} - C^n_{k,i}}{\tilde{C}_{k,i}(\mathbf{X}_v, t^n) - C^n_{k,i}}\right), & \text{if } \tilde{C}_{k,i}(\mathbf{X}_v, t^n) - C^n_{k,i} < 0, \\ 1, & \text{if } \tilde{C}_{k,i}(\mathbf{X}_v, t^n) - C^n_{k,i} = 0. \end{cases} \tag{15}$$

From these values $\bar{\Phi}_{i,v}$ the final value of the slope limiter is obtained as $\Phi_{k,i} = \min_{v \in \mathcal{V}_{k,i}} \left(\bar{\Phi}_{i,v} \right)$. After the calculation of $\Phi_{k,i}$, one obtains the final limited slope as

$$\nabla C^n_{k,i} = \Phi_{k,i} \tilde{\nabla} C^n_{k,i}, \tag{16}$$

from which also the time derivative $\partial_t C^n_{k,i}$ can be calculated according to (10). The reconstructed values $C^-_{k,j}$ and $C^+_{k,j}$ used for the flux calculation (6) are then given by

$$C^-_{k,j} = C_{k,left}(\mathbf{x}_{k,j}, t^{n+\frac{1}{2}}), \qquad C^+_{k,j} = C_{k,right}(\mathbf{x}_{k,j}, t^{n+\frac{1}{2}}), \tag{17}$$

where $\mathbf{x}_{k,j}$ denotes the coordinate of the midpoint of the common edge ∂T_{ij} shared by elements T_{left} and T_{right} and the half-time step used in a global time step context is denoted by $t^{n+\frac{1}{2}} = t^n + \frac{1}{2}\Delta t$.

The vertical reconstruction is performed similar to an one-dimensional MUSCL schemes. Here we choose to use the MINMOD slope limiter to compute the vertical reconstructed values $C^-_{k\pm\frac{1}{2},i}$ and $C^+_{k\pm\frac{1}{2},i}$ as follows:

$$\nabla C^n_{k,i} = \text{MinMod}\left(C^n_{k,i} - C^n_{k-1,i},\ C^n_{k+1,i} - C^n_{k,i} \right) \tag{18}$$

where

$$\text{MinMod}(a, b) = \begin{cases} a & \text{if } |a| < |b| \text{ and } ab > 0 \\ b & \text{if } |a| > |b| \text{ and } ab > 0 \\ 0 & \text{if } ab \leq 0 \end{cases} \tag{19}$$

2.1.1. Local Time Stepping (LTS)

The LTS procedure showed here is an extension of the ideas presented for the first time in [13]. In the mentioned reference, the LTS algorithm was shown to converge with high order of accuracy in both space and time for simple advection problems in two dimensional unstructured triangular meshes. The main difference in the LTS algorithm presented in this paper is the use of advection, diffusion, and reaction mechanisms to perform scalar transport in three dimensional unstructured triangular meshes using an high-order scheme.

In a classical global time stepping (GTS) Finite Volume numerical scheme, the time step Δt is chosen according to a *global* CFL stability condition related to the element size h_i and thickness Δz_i, consequently the advection-diffusion constraints in each element can be depicted as follows

$$\Delta t^n \leq \text{CFL} \cdot \min_{T_i \in \Omega} \left(\frac{1}{\frac{\left\|\mathbf{u}_{\max k,j}\right\|}{h_i} + 2\frac{\left\|\mathbf{\Gamma}_{\max k,j}\right\|}{h_i^2} + \frac{\left\|\mathbf{w}_{\max k\pm\frac{1}{2},i}\right\|}{\Delta z_{k,i}} + 2\frac{\left\|\mathbf{\Gamma}_{\max k\pm\frac{1}{2},i}\right\|}{\Delta z_{k,i}^2}} \right), \tag{20}$$

where Δt^n is the global time step, CFL $< 1/d$ is the Courant-Friedrichs-Lewy number, d is the number of space dimensions and h_j is the characteristic mesh size of each element, which in this case is taken as the maximum diameter of a circle inscribed in triangle T_i; $\mathbf{u}_{k,j}$ and $\mathbf{\Gamma}_{k,j}$ are the velocity vector and diffusion coefficient in the edges of T_i, respectively. $\Delta z_{k,i}$ is the thickness of layer k of the element i.

Note that (20) refers to a global minimum taken over all computational cells in the domain. In out new LTS scheme, instead of one global time step (20) each computational cell will now compute a *local time step* following a *local* CFL stability condition based on the set $\mathcal{S}_{k,i}$, i.e., the element and its direct neighbors

$$\Delta t_{k,i}^n = \text{CFL} \min_{T_j \in \mathcal{S}_{k,i}} \left(\frac{1}{\frac{\left\|\mathbf{u}_{\max k,j}\right\|}{h_j} + 2\frac{\left\|\mathbf{\Gamma}_{\max k,j}\right\|}{h_j^2} + \frac{\left\|\mathbf{w}_{\max k\pm\frac{1}{2},j}\right\|}{\Delta z_{k,j}} + 2\frac{\left\|\mathbf{\Gamma}_{\max k\pm\frac{1}{2},j}\right\|}{\Delta z_{k,j}^2}} \right), \tag{21}$$

where $\Delta t_{k,i}^n$ is now the *local time step*. Accordingly, each computational cell will now have an associated *local time* $t_{k,i}^n$.

In each temporal iteration (named here as *cycles*), one loops over all computational cells in the domain and verifies the *update criterion* [19, 38], i.e., an computational cell is only updated if and only if the following condition holds:

$$t_{k,i}^n + \Delta t_{k,i}^n \leq t_{k,j}^n + \Delta t_{k,j}^n, \qquad \forall j \in \mathcal{N}_{k,i}. \tag{22}$$

This condition means that the future time of an element must be less or equal than the future times of the neighbor computational cells and is a direct result of the causality principle. Furthermore, the time intervals in which numerical fluxes are computed across element boundaries are defined as

$$[t_{k,ij}^n, t_{k,ij}^{n+1}] = [\max(t_{k,i}^n, t_{k,j}^n), \min(t_{k,i}^{n+1}, t_{k,j}^{n+1}], \qquad \Delta t_{k,ij} = t_{k,ij}^{n+1} - t_{k,ij}^n, \qquad t_{k,ij}^{n+\frac{1}{2}} = \frac{1}{2}\left(t_{k,ij}^n + t_{k,ij}^{n+1}\right). \tag{23}$$

The finite volume scheme with LTS then reads for those elements $T_{k,i}$ that satisfy (22):

$$V_{k,i}^{n+1} C_{k,i}^{n+1} = V_{k,i}^n C_{k,i}^n + M_{k,i} - \sum_{j \in \mathcal{N}_i} \Delta t_{k,ij}\, \lambda_{ij}\, F_{k,ij}\left((C_{k,ij}^-, \nabla\, C_{k,ij}^-), (C_{k,ij}^+, \nabla\, C_{k,ij}^+)\right) + \Delta t_{k,i}\, S_{k,i}, \qquad t_{k,i}^{n+1} = t_{k,i}^n + \Delta t_{k,i}^n. \tag{24}$$

The boundary extrapolated values $C_{k,j}^-$ and $C_{k,j}^+$ used in (24) are computed from the local space-time reconstruction (9) simply as

$$\begin{aligned} C_{k,j}^- &= C_{k,i}^n + \nabla C_{k,i}^n \left(\mathbf{x}_j - \mathbf{x}_{k,i}\right) + \partial_t C_{k,i}^n \left(t_{k,ij}^{n+\frac{1}{2}} - t_{k,i}^n\right), \\ C_{k,j}^+ &= C_{k,j}^n + \nabla C_{k,j}^n \left(\mathbf{x}_j - \mathbf{x}_{k,j}\right) + \partial_t C_{k,j}^n \left(t_{k,ij}^{n+\frac{1}{2}} - t_{k,j}^n\right). \end{aligned} \tag{25}$$

Finally, the term $M_{k,i}$ in (24) is a *memory variable*, which takes into account past fluxes through the computational cell interfaces, i.e., from time $t^n_{k,i}$ to $t^n_{k,ij}$. In practice, this memory variable is simply updated by the *neighbors* of a computational cell, to assure that the scheme is exactly conservative and simple to implement. Once a computational cell has been updated by Eqn. (24), its own memory variable is reset to zero, and the fluxes across the element boundary are added to the memory variables of the neighbor elements, i.e.

$$M_{k,i} := 0, \qquad M_{k,j} := M_{k,j} + \Delta t_{k,ij}\, \lambda_j\, F_{k,j}\left((C^-_{k,j}, \nabla\, C^-_{k,j}), (C^+_{k,j}, \nabla\, C^+_{k,j})\right). \tag{26}$$

At the end of the cycle, one still need to perform the *reconstruction* for element $T_{k,i}$ after its update in an LTS context, once the neighbor cells in general are at a different time $t^n_{k,j} \neq t^n_{k,i}$. Since the space-time reconstruction (9) is valid inside the entire space-time control volume $T_j \times [t^n_{k,j}, t^{n+1}_{k,j}]$, we simply proceed as follows: instead of using (11), we compute the unlimited gradient $\tilde{\nabla} C^n_{k,i}$ at the aid of the predictor (9) in the neighbor cells using the *virtual* cell averages $\bar{C}^n_{k,j}$:

$$\tilde{\nabla} C^n_{k,i} = \frac{1}{|T_i|} \sum_{j \in \mathcal{N}_i} \frac{1}{2} \left(C^n_{k,i} + \bar{C}^n_{k,j}\right) \mathbf{n}_{ij}, \qquad \text{with} \qquad \bar{C}^n_{k,j} = C^n_{k,j} + \partial_t C^n_{k,j} (t^n_{k,i} - t^n_{k,j}). \tag{27}$$

Note that a valid predictor is always available in the neighbor cells due to the update criterion (22). After the computation of the unlimited slope from Eqn. (27), the limited slope and the computation of the time derivative $\partial_t C^n_{k,i}$ are obtained as described in Section 2.

3. Numerical Tests

The three-dimensional scalar transport algorithm with LTS proposed in this work was coupled to an unstructured hydrodynamic model based on the semi-implicit discretization of the shallow water equations on unstructured grids [e.g., 11, 8, 9] including nonlinear wetting and drying (UnTRIM^2). Despite the model complexity that could be used in such an advanced scheme for 3D free surface flows, here we limit ourselves to the three-dimensional hydrostatic case with non-linear wetting and drying, in order to prevent the other more advanced features of the hydrodynamical model from complicating the results obtained with the new transport scheme. Since the 2D version of this numerical scheme has already been validated [13], here we focus on the 3D version only.

To validate our 3D LTS algorithm we first use two classic benchmark problems that consist in the advection and diffusion of a scalar quantity C within a given velocity field $\mathbf{u}$. In all cases, an exact solution is known. One is the rotating sphere problem [47, 55, 1], the other is an advection-diffusion problem of a 3D Gaussian concentration field [55, 16]. In order to compare the advantages of using the 3D LTS algorithm coupled to a hydrodynamic model, two additional test cases were solved: i) the transport of a passive scalar in a round lake with wind-driven hydrodynamic forcing, in order to check the mass conservation when the free-surface dynamic changes, and ii) a rectangular channel with flow and tidal boundaries where the scalar is going through linear changes, in order to check the mass conservation when there are reaction terms being computed. The last numerical test is an application of the current LTS scheme to simulate thermodynamics at a deep reservoir located in southern Brazil (Faxinal Reservoir). In this last case a robust wet-and dry-ing algorithm must be used due to the heterogeneous topography and the requirement of a precise heat balance performed at the free-surface.

The coupling of different numerical solutions such as the case of hydrodynamic models coupled to water quality models [e.g., 23, 43, 35] must respect a condition known as Consistency with Continuity (CWC, [28, 12]). The CWC condition requires the scalar transport equation (1) to be numerically solved in such a fashion that is *compatible* with the continuity equation numerically solved by the hydrodynamic model. Furthermore, no new extrema is to be generated in the numerical solution of the scalar concentration being transported [12]. The use of an Eulerian-Lagrangian solution to compute the velocity advection and horizontal friction terms in semi-implicit hydrodynamic models leads to a mild limitation on the hydrodynamic time step, depending upon the horizontal viscosity coefficient and on the smallest element size [11]. In addition, when baroclinic flows are being simulated a mild numerical stability constraint is introduced depending upon the maximum internal wave speed [29]. As the transport equation showed in (1) is computed explicitly in a Finite Volume context, the time steps of the hydrodynamic model may bee too

large, requiring additional stability criterion. The time step used to compute scalar transport turns into the following criterion:

$$\Delta t = \min\left(\Delta t_{LTS/GTS}, \Delta t_{hydro}\right) \tag{28}$$

where $\Delta t_{LTS/GTS}$ is the time step calculated by the numerical approach used (eqs. (20) or (21)); Δt_{hydro} is the time step of the hydrodynamic model. Hence, the computation of scalar transport is accomplished using a time step that is automatically adjusted to be equal or smaller than that of the hydrodynamic model [56, 12]. To be consistent with the discretized continuity equation the velocities used in the transport solution are kept constant for all subcycles in the same hydrodynamic time step.

3.1. Three-dimensional advection of a sphere

The test case consists in a cubic region of dimensions $x \in [0, 1]$, $y \in [0, 1]$, and $z \in [0, 1]$ covered with triangular elements with characteristic length $h = 0.01$ m and 100 vertical layers, totalizing 2253400 prismatic elements. The sphere has 0.3 m diameter, centered about the point (0.5, 0.5, 0.75), with C being assigned as 1 inside the sphere and 0 outside. The velocity field is a solid-body rotation flow field around the cube diagonal, defined by ($x = y = z$):

$$u = \frac{\Omega}{\sqrt{3}}(y - z); \qquad v = \frac{\Omega}{\sqrt{3}}(z - x); \qquad w = \frac{\Omega}{\sqrt{3}}(x - y) \tag{29}$$

where $u, v,$ and w are the components of the velocity vector in x-, y-, and z-directions, respectively; Ω is the angular velocity, chosen such that one full revolution occurs within 628 time steps. Using $\Delta t = 1$ s yields $\Omega = 2.\pi$ rad/s.

The concentration profile computed by the LTS and the GTS schemes after one full revolution are show in (Fig. 1), and in both, LTS and GTS, the total mass was conserved with an error remaining smaller than $1x10^{-15}$ through the entire simulation. Is can be noticed that the field remains symmetrical, though with a slight tendency to elongate toward the center of rotation. The error in the simulated peak concentration is around 0.05% for the LTS scheme and around 0.1% for the GTS scheme. The front extend over 30 cells for the exact solution and around 40 cells for the numerical schemes used. Thus, the scheme with Local Time Stepping presented the same capability of simulating 3D scalar transport than the Global Time Stepping scheme. Also, the inherent numerical diffusion observed in the 2nd Order MUSCL Method here implemented is similar to other works [1]. In addition, in this pure advection test case the LTS scheme was able to reduce in around 20 % the total time elapsed to perform the entire simulation (Table 1). Moreover, the total number of elements updated by the LTS scheme was only 9% of the total number of elements updated by the GTS scheme.

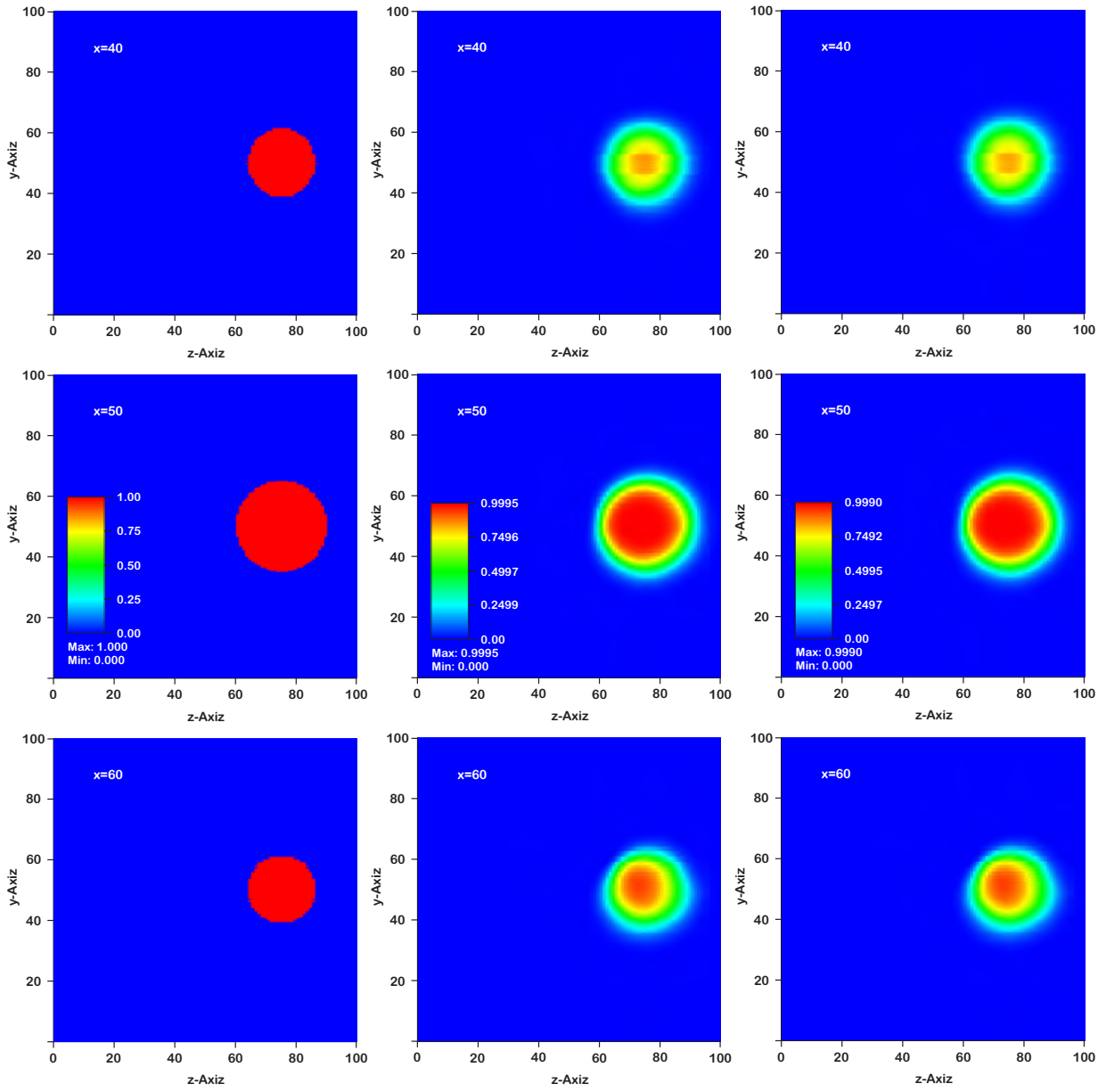

Figure 1: Evolution of the rotating sphere problem at the beginning and after one full revolution of the simulation using a three-dimensional second order MUSCL-Hancock finite volume scheme using LTS and GTS algorithms.

3.2. Three-dimensional advection-diffusion of a Gaussian sphere

For evaluating advection-diffusion using the three-dimensional numerical scheme proposed here we take our test problem from the following function:

$$C(x,y,z,t) = \frac{M}{(2\pi)^{(3/2)}\delta_x\delta_y\delta_z}\exp\left[-\frac{1}{2}\left(\frac{(x-ut-x_0)^2}{\delta_x^2}+\frac{(y-vt-y_0)^2}{\delta_y^2}+\frac{(z-wt-z_0)^2}{\delta_z^2}\right)\right] \tag{30}$$

which by assuming $\delta_x = \delta_y = \delta_z = \delta = \sqrt{2(Dt + L_0^2)}$ as the standard deviation one has:

$$C(x, y, z, t) = \frac{M}{(4\pi(Dt + L_0^2))^{(3/2)}} \exp\left[-\frac{1}{4(Dt + L_0^2)}\left((x - ut - x_0)^2 + (y - vt - y_0)^2 + (z - wt - z_0)^2\right)\right] \tag{31}$$

The domain is consistent with the previous test case and the initial Gaussian concentration field is written as:

$$C(x, y, z) = \frac{M}{(4\pi L_0^2)^{(3/2)}} \exp\left[-\frac{1}{4L_0^2}\left((x - x_0)^2 + (y - y_0)^2 + (z - z_0)^2\right)\right] \tag{32}$$

where the characteristic dimension of the Gaussian profile is set to $L_0 = 0.05$ m and the total mass is set to $M = 5.5$ g. This combination results in an initial peak of around $C_{max} = 0.98$ g.m^{-3}. The problem is then simulated by setting a constant velocity field $u = v = w = 0.2$ m/s, and the Gaussian profile center of gravity is set to $(x_0, y_0, z_0) = (0.5, 0.5, 0.5)$. The time step is chosen as $\Delta t = 0.01$ s and the simulation is performed through 100 time steps.

First the performance of the schemes are tested with a uniform velocity field, i.e., $D = 0.0$ m^2/s. Then, the diffusion coefficient is added by setting $D = 0.001$ m^2/s and increased by a factor of ten by setting $D = 0.01$ m^2/s (Fig. 2). After 100 computational steps the center of gravity is correctly advected in all cases and therefore is not shown. For the case with zero diffusion, $D = 0.0$ m^2/s, the peak attenuates from 0.98 to 0.81 ($\approx 18\%$) for the LTS scheme and to 0.80 ($\approx 19\%$) for the GTS over 100 time steps (Fig. 2, top row). Adding a diffusion coefficient as defined by setting $D = 0.001$ m^2/s reduces the errors between the MUSCL scheme and the analytical solution (0.59 g.m^{-3}). The peak attenuates from 0.98 to 0.53 ($\approx 10\%$ difference against the analytical solution) for the LTS scheme and to 0.52 ($\approx 12\%$ difference against the analytical solution) for the GTS over 100 time steps (Fig. 2, middle row). Increasing the diffusion coefficient further by a factor of ten leads to exact agreement with the exact solution (Fig. 2, bottom row).

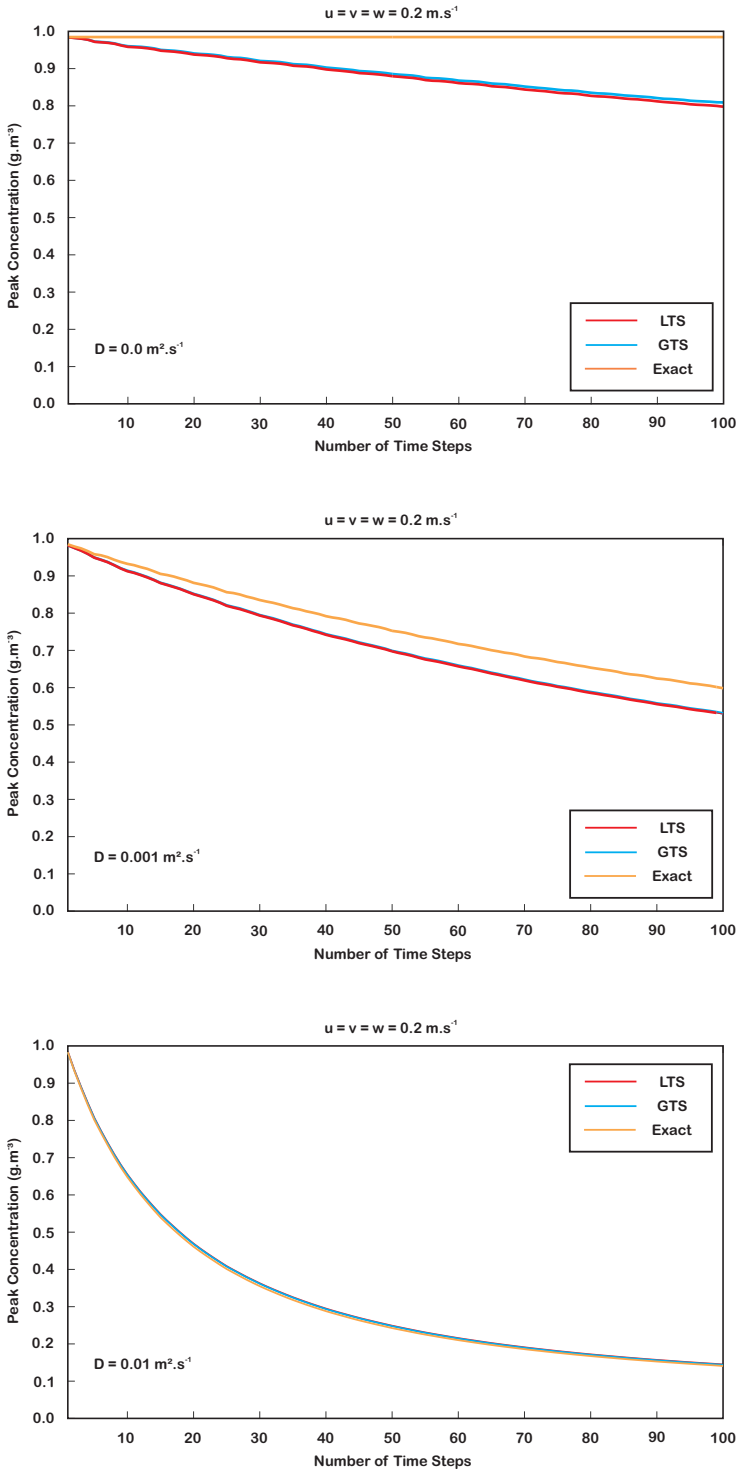

Figure 2: Advection-diffusion of a Gaussian sphere in a three-dimensional velocity field. Comparison between analytical calculated peak concentration and simulation using a three-dimensional second order MUSCL-Hancock finite volume scheme using LTS and GTS algorithms. Top row: No diffusion; Middle row: $D_x = D_y = D_z = 0.001$ m^2.s^{-1}; Bottom row: $D_x = D_y = D_z = 0.01$ m^2.s^{-1}.

3.3. Coupled hydrodynamic and transport simulation I: Wind-driven hydrodynamics

Wind blowing over a lake surface leads to circulation patterns of remarkable ecological relevance, specially when intense vertical mixing is observed. In order to evaluate the mass conservation and the respect to a local max-min principle for our new three-dimensional local time stepping solution we consider an idealized round lake with wind blowing from a constant direction. We expect an intense vertical mixing to occur near the surface of the lake, with a decay in the velocity profile from surface to bottom. Also, the solution must be mass conservative and since we do not consider inflows or outflows with different scalar concentrations, the initial concentration field must remain the same. We chose a round domain with 100 km diameter and flat bottom (h = 50 m). The domain is then covered with 5626 non-overlaping triangular elements with characteristic length h = 2 Km and 10 vertical layers with thickness varying from 1.0 m to 10 m. The wind stress at the lake surface is parameterized by using an air-density based formulation [46], and the bottom friction at the lake bottom is parameterized by a Manning-Chézy formulation, with Manning's Coefficient set as 0.012. The horizontal non-linear convective terms in the momentum equations are neglected. The wind magnitude is set at 10 $m.s^{-1}$ blowing from the east and a constant vertical eddy viscosity/diffusivity is set at 10^{-4} $m^2.s^{-1}$. The time step used is 300 s and the simulation is performed through 5 days. The initial concentration field is constant and set at 1 $g.m^{-3}$.

After 5 days of simulation the velocity field presents a decaying profile from top to bottom and the concentration field remains constant and equal to the initial condition (Fig. 3). The velocity magnitude increases up to 3 $m.s^{-1}$ in the first layer decreasing to values near zero at the bottom. This heterogeneous velocity field leads to an intense vertical mixing near the surface and horizontal mixing near the boundaries of the domain. The three-dimensional finite volume devised here was capable of maintaining the initial concentration field in both cases (GTS and LTS). Also, the total mass was conserved up to machine precision through the entire simulation. In this rather heterogeneous environment, the LTS scheme showed itself more efficient regarding the CPU time elapsed (Table 1), saving up to 24 % of simulation time and reducing the number of elements to be updated (only 16% when compared to the GTS scheme).

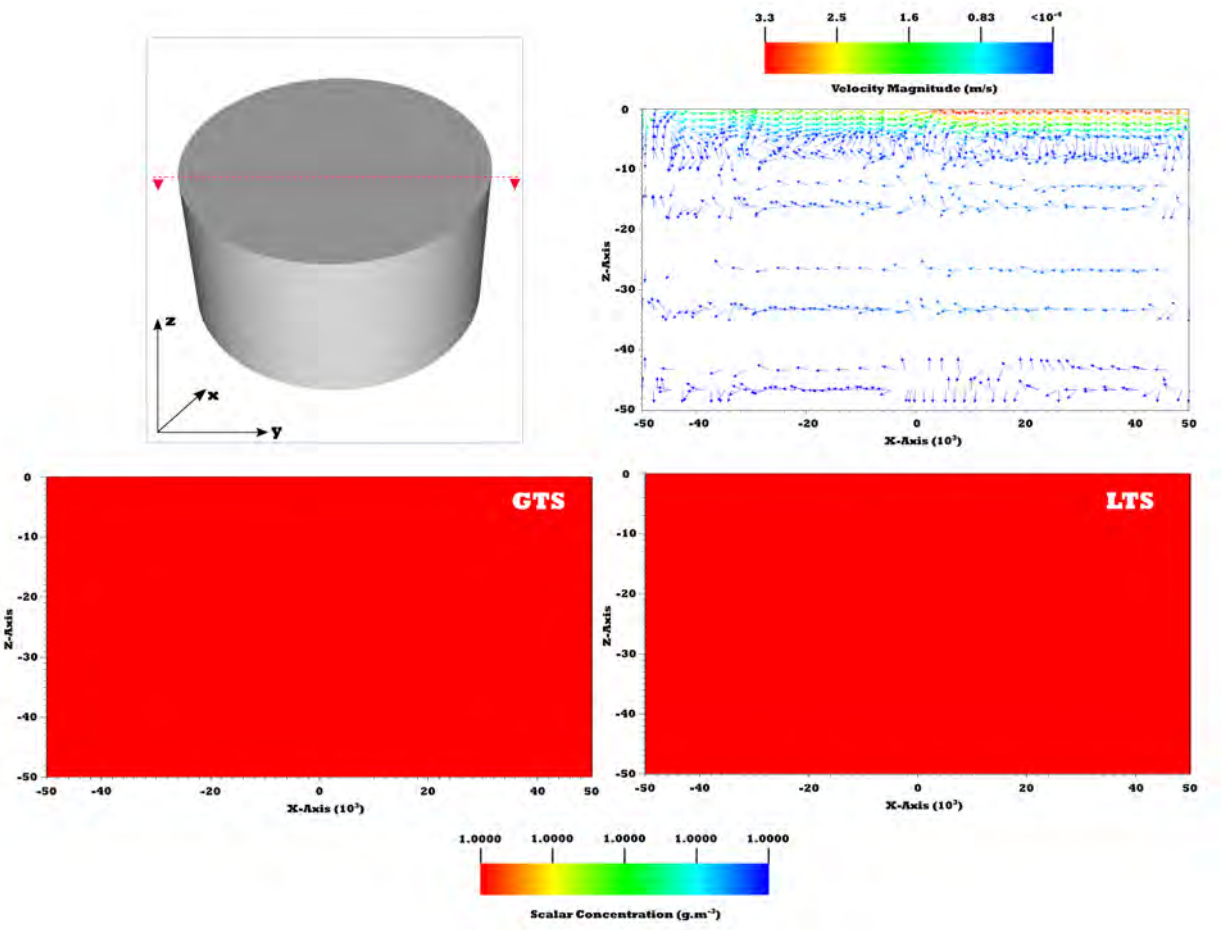

Figure 3: Numerical results of the wind-driven hydrodynamics test case for $t = 5$ days considering a flat bottom. The results are extracted from a vertical cur through the y-axis (top, to the left). The velocity field magnitude and direction are shown in the top, to the right. The concentration field if show at the bottom, for both GTS (left) and LTS (right) schemes.

The same test case was further evaluated considering a parabolic bottom given by:

$$h(x, y) = H_{cen} \cdot \left[1 - \frac{x_b(x, y)^2 + y_b(x, y)^2}{L^2}\right] \tag{33}$$

where h(x,y) is the element bathymetry; $H_{cen} = 50m$ is the maximum depth at the center of the domain; $x_b(x, y)$ and $y_b(x, y)$ are the element barycenter x- and y-coordinates; and L = 55 Km is the length of the parabolic profile. In this case, the thickness of some prismatic elements were small, specially near the boundary of the domain, which lead to a severe CFL restriction on time step. This case is very interesting to analyze our LTS scheme, once there will be intense mixing in the vertical and near the border of the domain, where it has a shallow area (Fig. 4). In fact, the LTS scheme performed the simulation in approximately 1 ***hour***, which is higher than the previous test case with flat bottom (around 0.1 hour). Interestingly, the GTS scheme required far more CPU time to finish the entire simulation. The traditional scheme required approximately 106 hours (around 4-5 ***days***) to perform the total of 5 days of computational simulation (Table 1). In this case, it can be shown the enhance performance regarding the CPU time required to simulate complex systems, as those where localized velocity is observed and/or severe grid refinement is necessary.

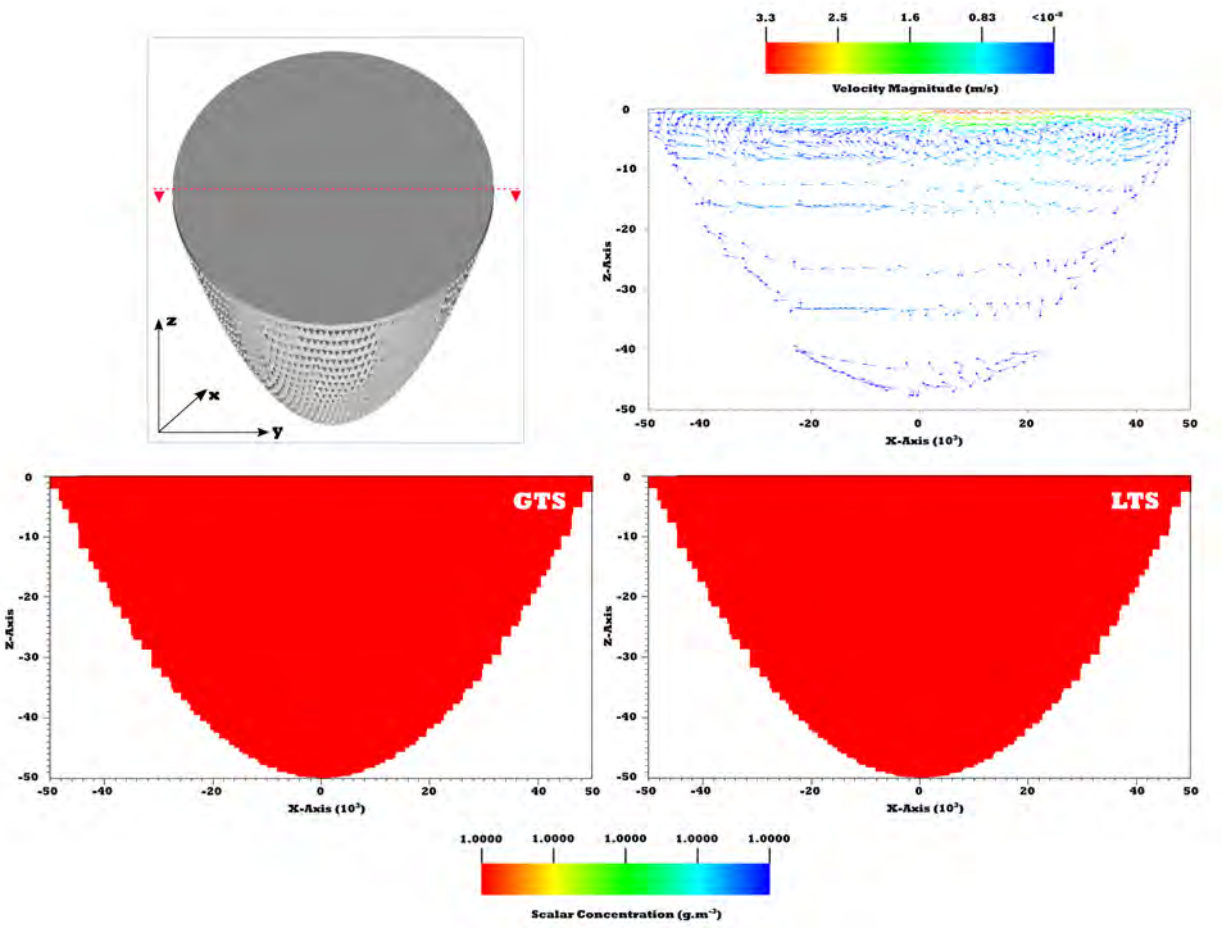

Figure 4: Numerical results of the wind-driven hydrodynamics test case for $t = 5$ days considering a parabolic bottom. The results are extracted from a vertical cur through the y-axis (top, to the left). The velocity field magnitude and direction are shown in the top, to the right. The concentration field if show at the bottom, for both GTS (left) and LTS (right) schemes.

3.4. Coupled hydrodynamic and transport simulation II: Nonconservative substance

The mass conservation under forcing (inflow and outflow) and transformations (reaction) is evaluated by using the test case presented in [56]. We set a rectangular channel of 170 km length, 6 km width, and 10 m depth. The domain is covered with 3806 triangular elements of characteristic length varying from 0.5 to 1.0 km and 10 equally spaced vertical layers totalizing 38060 prismatic elements. A constant discharge rate (inflow) of 300 $m^3.s^{-1}$ is imposed at one end while a M_2 tide of 0.4 m amplitude is specified at the other end. After 6 *days* of hydrodynamic simulation we insert two kinds of passive scalars, one being conservative (S0) and the other being nonconservative (S1). The nonconservative scalar substance is subjected to a linear transformation into S2, which is further transformed into S3 also at a linear rate. The injection occurs through 5 *days* with a constant rate of 30 kg/s. The time step is set at 20 *min* and the simulation is performed through an entire *year*. Opposite to the last test case, the nonlinear convective terms in the hydrodynamic solution are turned on. The bottom friction is parameterized by a Manning-Chézy formulation with n = 0.012. The constant horizontal eddy viscosity/diffusivity is set at 0.05 $m^2.s^{-1}$ and the constant vertical eddy viscosity/diffusivity at 10^{-4} $m^2.s^{-1}$.

The total scalar mass introduced in the channel is conserved from the moment it is introduced to the moment it reaches the open end of the channel (Fig. 5). After the non-passive scalar is introduced, the total mass of S1 follows the same pattern as S0 but rapidly begin to turn into S2. After the insertion period, the total mass of S1 starts to decline, and both S2 and S3 continues to increase. The total mass of S3 begins to decline only when the loss through the open end of the channel exceeds the supplement from S2. At each time step, the combined masses of S1, S2, and

S3 is equal to the total mass of the conservative scalar S0. As expected, even when reactive processes are present, such as the one transforming S1 into S2 and further into S3, the numerical scheme neither creates nor destroys mass artificially. In addition, the numerical solution matches the one found using the traditional GTS scheme and the CPU time save is close to 5 %.

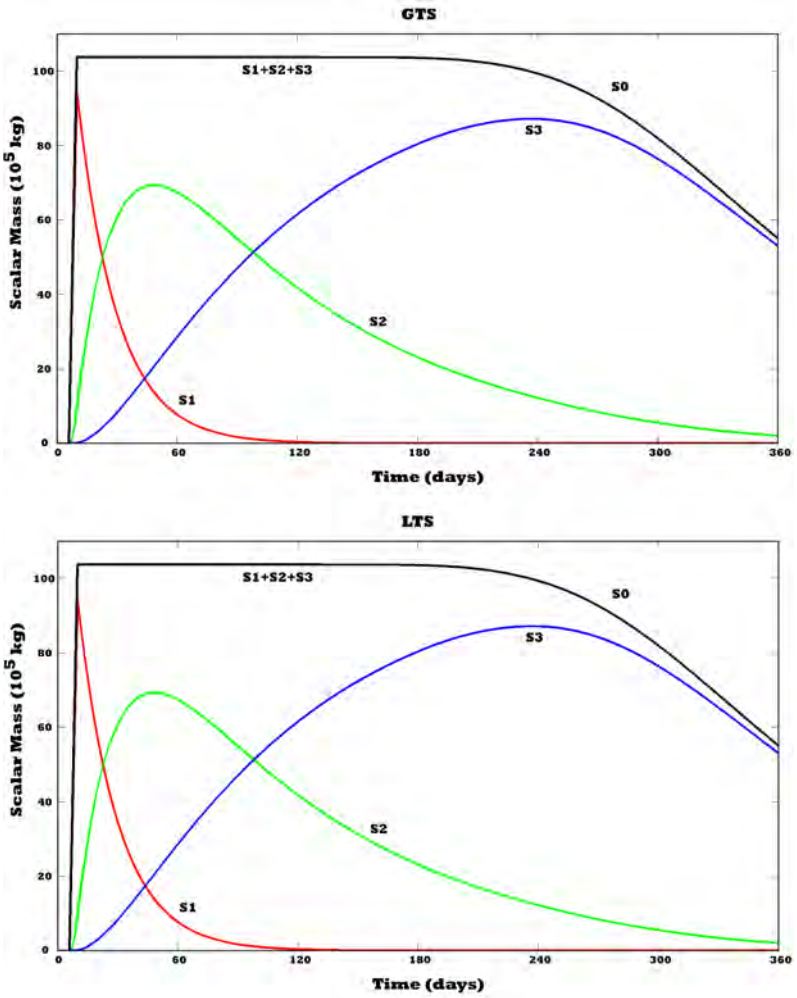

Figure 5: Simulated total mass of the conservative (S0) and nonconservative (S1, S2, and S3) tracers in the coupled hydrodynamic and transport test using a three-dimensional second order MUSCL-Hancock finite volume scheme using GTS (top) and LTS (bottom).

Table 1: Comparison between GTS and LTS for the main numerical test cases reported.

Test Case	Algorithm	CPU time (s)	$\frac{t_{LTS}}{t_{GTS}}$	Total Element Updates (TEU)	$\frac{TEU_{LTS}}{TEU_{GTS}}$
Sphere Advection	GTS	203.07	**0.80**	624191800	**0.29**
	LTS	163.22		184353647	
Gaussian Plume Advection	GTS	260.33	**1.22**	676020000	**0.67**
	LTS	317.58		450660000	
Gaussian Plume Advection + Diffusion (D = 0.001)	GTS	547.02	**0.90**	1577380000	**0.50**
	LTS	494.01		788660000	
Gaussian Plume Advection + Diffusion (D = 0.01)	GTS	3524.80	**0.75**	2001045408	**0.27**
	LTS	2655.98		536882704	
Wind-driven hydrodynamics (flat bottom)	GTS	500.60	**0.76**	512327600	**0.16**
	LTS	381.50		83291327	
Wind-driven hydrodynamics (parabolic bottom)	GTS	384536.95	**0.01**	1247439441600	**<0.01**
	LTS	4214.88		243880244	
Non-Conservative Substance	GTS	10210.00	**0.95**	15857318400	**0.40**
	LTS	9729.20		6317388388	

4. Application: Thermodynamics Simulation in Deep Reservoir

4.1. Study Site

The Faxinal reservoir (Fig. 6) is a deep, subtropical, reservoir in southern Brazil, located between 29°06 S and 29°04 S, and 51°04 W and 51°01 W. The reservoir surface area is c.a. 3.1 km and has mean elevation of 698 m measured from the sea surface. The reservoir is 30m deep at the deepest point, eutrophic (epilimnion annual mean: Total Phosphorous = 29,4 μg.L^{-1}, and Chlorophyll-a = 15 μg.L^{-1}), and stratified through 7 months with vertical mixing during winter. The reservoir has a catchment area of c.a. 57.7 km and presents three main tributary streams, namely: Alegre Stream, Herval Stream, and Faxinal Stream. The reservoir is mainly used for water supply to the city of Caxias do Sul, Rio Grande do Sul, Brazil.

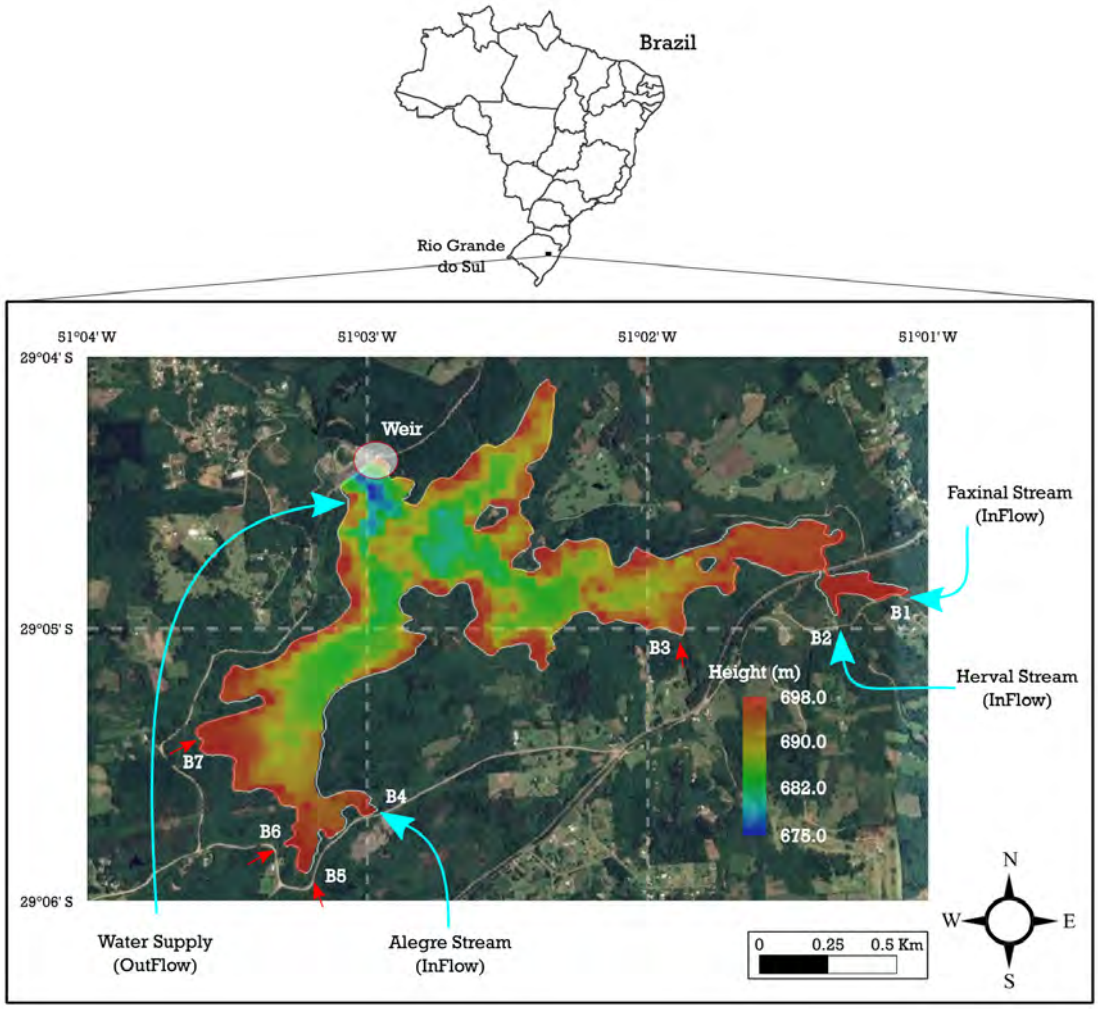

Figure 6: Faxinal Reservoir location. The white circle indicates the weir location, the cyan arrow shows the affluent streams and the water supply outflow, and the small red arrows indicates four small creeks reaching the reservoir.

4.2. In-situ measurements

The field campaigns in the Faxinal Reservoir were carried out from November 2011 to December 2012 in monthly basis (13 in total). Near the deepest point, a vertical profile of water temperature was collected with a multi-parameter probe (Yellow Spring Model 6920, YSI, Ohio, USA). The vertical data was gathered for each 1 meter depth measured from the surface until a depth of 10 m where the collection was more sparse raging from 2 to 5 meters until reaches the bottom. The surface water temperature at the reservoir ranged from 25°C during spring/summer to 13°C during autumn/winter whereas the bottom water temperature remained close to 13°C all year (Fig. 7). The water level was also collected during the period in a gauge station near the weir. A total variation of 1.5m was observed mainly during the winter time (Fig. 7). A detailed discussion about the main limnological features of the Faxinal Reservoir can be found in [48].

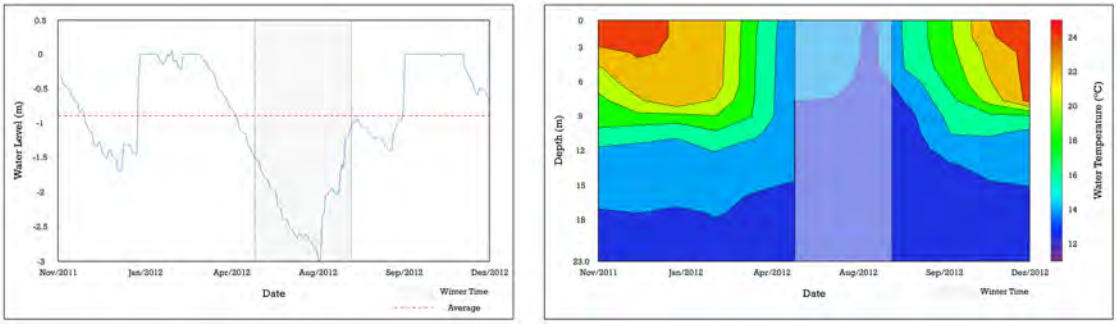

Figure 7: Water level (left) and vertical profile of Water Temperature from November 2011 to December 2012 collected in the deepest point of the reservoir (right). A gray box indicates de winter time and a red dashed line the average value of water level.

4.3. Catchment and Water Supply Flow

The catchment modeling was performed in a previous work [49] and will be briefly explained here. The flow analysis was conducted using a simple rainfall-runoff model (IPH-II). The model mathematical basis is the continuity equation composed of three main algorithms: a) losses by evapotranspiration and interception by leaves or stems of plants; b) evaluation of infiltration and percolation; and c) evaluation of surface and groundwater flows [53]. The model was calibrated by fitting the observed water levels (Fig. 7) computed from a balance of volume in a single cell. The water balance accounted direct Precipitation and Catchment Flow as ingoing flux and Water Supply and direct Evaporation as outgoing flux. The total watershed flow entering the Faxinal Reservoir presented an average value of 1.74 $m.s^{-1}$ while the water supply varied during the year with an increase near the winter (Fig. 8). Through manual calibration of the IPH-II model parameters, [49] was able to estimate the flow reaching the reservoir using a total of seven basins, three related to the main streams and the other four related to small creeks reaching the reservoir. The location of the nine total boundary conditions used in the simulation can be regarded in Fig. 6. More details about the seven basins can be found in Table 2.

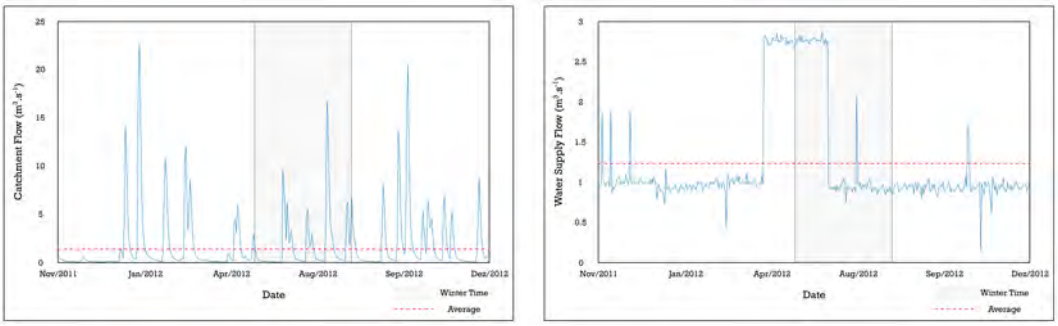

Figure 8: Catchment flow (left) and water supply flow (right) estimated through the simulation period. A gray box indicates de winter time and a dashed red line the average flow.

Table 2: Area, main river length, slope, and average runoff of the main basins used to estimate catchment flow reaching the Faxinal Reservoir.

Basin	Area (km^2)	River Length (km)	Slope (m/m)	Ave. Runoff ($m^3.s^{-1}$)
B1 (Faxinal)	29.44	11.8	0.01	0.93
B2 (Herval)	11.75	6.72	0.02	0.36
B3	2.03	2.85	0.04	0.07
B4 (Alegre)	7.38	4.67	0.02	0.07
B5	2.92	1.99	0.02	0.10
B6	2.58	2.68	0.03	0.10
B7	1.50	1.65	0.05	0.11

4.4. Environmental conditions

The Environmental data required to perform the thermodynamic simulation at the Faxinal Reservoir were collected at two meteorological stations near the reservoir (namely: Caxias do Sul and Bento Gonçalves). The stations are operated by the Brazilian Institute for Meteorology (InMET) and the data is available on line (`http://www.inmet.gov.br`). A total of six time series were collected (Fig. 9): Air Temperature (°C), Solar Radiation (W.m^{-2}), Humidity (%), Precipitation (mm.d^{-1}), Evaporation (mm.d^{-1}), and Wind Intensity (m.s^{-1}).

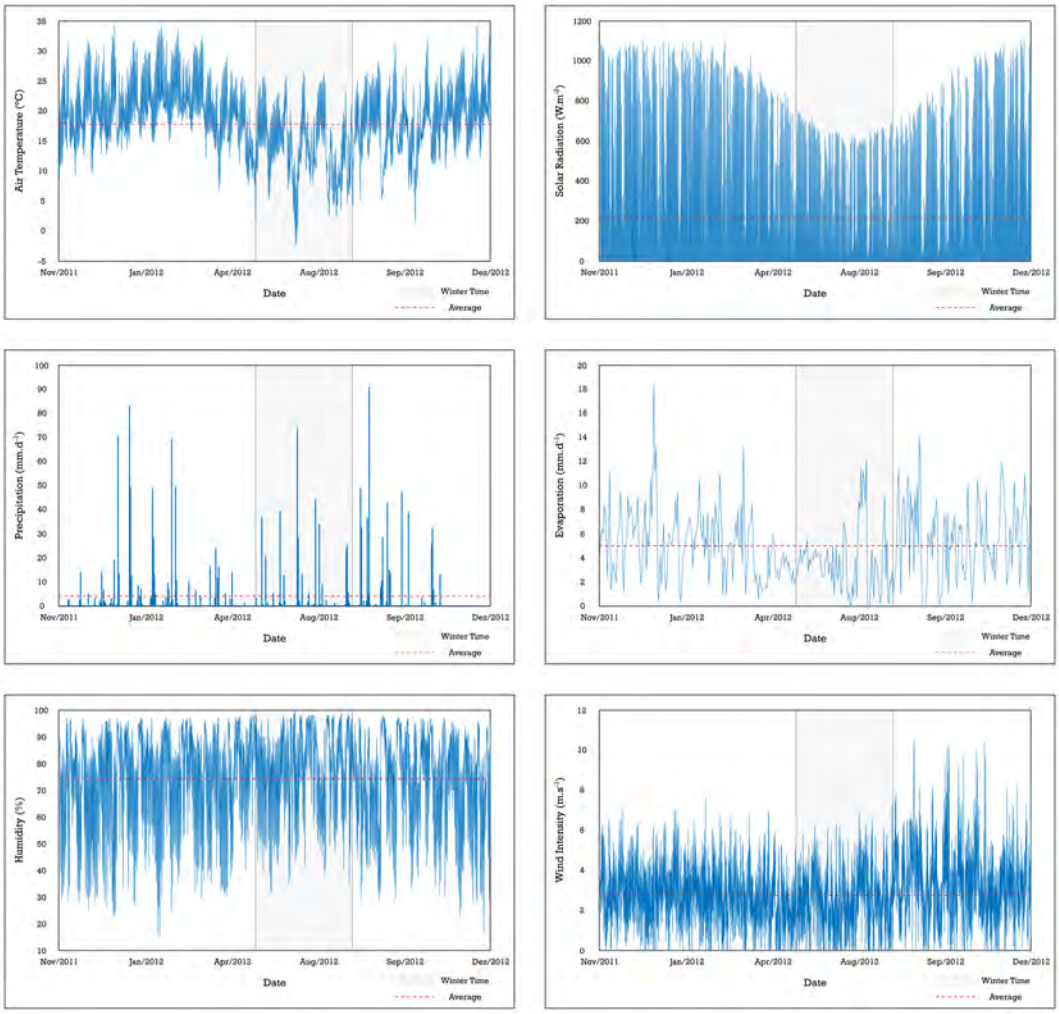

Figure 9: Environmental data collected near the Faxinal Reservoir: Air Temperature (top, left), Solar Radiation (top, right), Precipitation (middle, left), Evaporation (middle, right), Humidity (bottom, left), and Wind Intensity (bottom, right). A gray box indicates de winter time and a dashed red line the average values.

4.5. Model Parameterization and Simplifications

The model simulation was performed using a 1D vertical model, i.e., only one triangular element was taken into consideration with 20 vertical layers of 1.0m thickness in each layer except the last layer which has 3.0 m thickness. The triangular element has 3.8 Km^2 of surface area and is 24 m deep. The θ parameter was set to 0.55, the wind drag was parameterized as described in [46], and the bottom friction was described by the Manning-Chezy formulation, with Manning's coefficient equal to 0.035. The time step was set to 30 s, respecting the limitation imposed by the baroclinic pressure discretization [29]. The spilled flow was described as a rectangular weir with 20m in length and the elevation set to the reference depth (0 m). The heat budget is computed as described by [14] with a constant vertical

attenuation coefficient of 3.84, allowing the water surface energy budget to penetrate 1.0m in the water column. The Longwave atmospheric attenuation coefficient was set to 0.75 and the water surface emissivity to 0.97 in the heat budget model.

4.6. Results

Using the catchment Inflow estimated and the meteorological data available the volume was reasonably conserved and the water depth in the reservoir matched with an adjustment coefficient of $R^2 = 0.89$ (Fig. 10). The water temperature was poor adjusted using this one dimensional approach. We believe that a dynamic update of the attenuation coefficient can improve the result and a spatially explicit simulation of incoming water from the catchment with different temperatures can improve the seasonality and vertical stratification. As suggested in [43], the spatial discretization can change the final result and the complexity of the simulations, affecting the natural dynamics being represented by the model. Nevertheless, the LTS scheme devised here was able to represent (partially) the temperature dynamics in the Faxinal Reservoir.

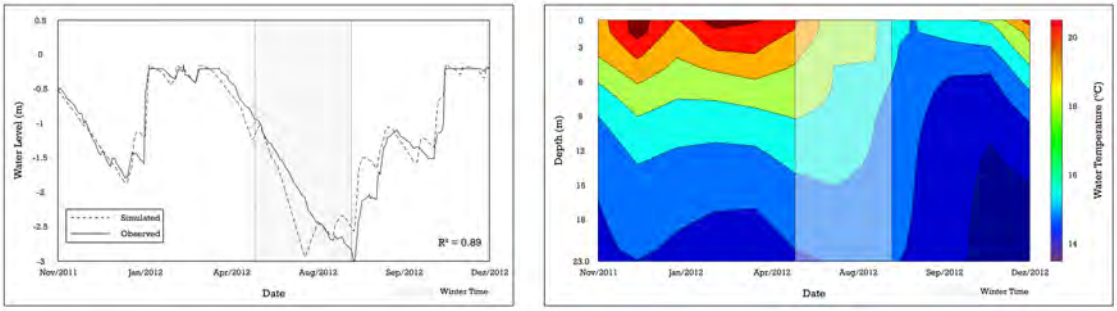

Figure 10: Simulation results for water depth (right) and seasonal stratification (left). A gray box indicates de winter time.

5. Conclusion

The new three-dimensional, conservative, unstructured finite volume scheme developed here was capable of simulating advection-diffusion-reaction scalar transport problems with time-accurate local time stepping. The numerical scheme has proven to be robust, conservative and capable of dealing with free-surface dynamics and wetting and drying problems. In almost all test cases the LTS algorithm improved here was more efficient than a traditional GTS algorithm, specially in applications with heterogeneous convection and mesh size are observed. In a representative three-dimensional round, deep lake with wind blowing in the water surface an heterogeneous bottom the 3D LTS solution showed up to 99 % of time save compared to the common GTS solution. The new algorithm was also able to describe smooth solutions such as the transport of a three-dimensional Gaussian plume where convection and diffusion were both dominant. Water quality problems were different substances interact with each other was testes by an idealized straight channel were a pollutant is injected and is subject to linar transformations in different substances. The LTS algorithm was capable to transform the substances without loosing mass along the simulation. Finally, a real application was performed were the new LTS algorithm was able to represent reasonably the thermodynamics of a deep reservoir in the south of Brazil. Furthermore we plan to apply our new improved three-dimensional model in spatially explicit water quality application in different water environments, in order to simulate water temperature, sediment dynamics and ecological processes.

6. References

[1] Badrot-Nico, F., Brissaud, F., Guinot, V., 2007. A finite volume upwind scheme for the solution of the linear advection-diffusion equation with sharp gradients in multiple dimensions. Advances in Water Resources 30, 2002–2025.

[2] Baeza, A., Martnez-Gavara, A., Mulet, P., 2012. Adaptation based on interpolation errors for high order mesh refinement methods applied to conservation laws. Applied Numerical Mathematics 62, 278–296. doi:10.1016/j.apnum.2011.09.008.

[3] Barth, T., Jespersen, D., 1989. The design and application of upwind schemes on unstructured meshes. AIAA Paper 89-0366 , 1–12.

[4] Bocaniov, S.A., Smith, R.E., Spillman, C.M., Hipsey, M.R., Leon, L.F., 2014. The nearshore shunt and the decline of the phytoplankton spring bloom in the Laurentian Great Lakes: insights from a three-dimensional lake model. Hydrobiologia 731, 151–172. doi:10.1007/s10750-013-1642-2.

[5] Carrick, H., Aldridge, F., Schelske, C., 1993. Wind influences phytoplankton biomass and composition in a shallow, productive lake. Limnology and Oceanography 38, 1179–1192.

[6] Castro, C., Käser, M., Toro, E., 2009. Spacetime adaptive numerical methods for geophysical applications. Philosophical Transactions of The Royal Society A 367, 4613–4631. doi:10.1098/rsta.2009.0158.

[7] Casulli, V., 1990. Semi-implicit finite difference methods for the two-dimensional shallow water equations. Journal of Computational Physics 86, 56–74.

[8] Casulli, V., 2009. A high-resolution wetting and drying algorithm for free-surface hydrodynamics. International Journal for Numerical Methods in Fluids 60, 391–408.

[9] Casulli, V., 2014. A semi–implicit numerical method for the free–surface Navier–Stokes equations. International Journal for Numerical Methods in Fluids 74, 605–622.

[10] Casulli, V., Cheng, R.T., 1992. Semi-implicit finite difference methods for three-dimensional shallow water flow. International Journal for Numerical Methods in Fluids 15, 629–648.

[11] Casulli, V., Walters, R.A., 2000. An unstructured grid, three-dimensional model based on the shallow water equations. International Journal for Numerical Methods in Fluids 32, 331–348.

[12] Casulli, V., Zanolli, P., 2005. High resolution methods for multidimensional advection–diffusion problems in free-surface hydrodynamics. Ocean Modelling 10, 137–151.

[13] Cavalcanti, J., Dumbser, M., Motta-Marques, D., Fragoso Junior, C.R., 2015. A conservative finite volume scheme with time-accurate local time stepping for scalar transport on unstructured grids. Advances in Water Resources 86, 217–230. doi:10.1016/j.advwatres.2015.10.002.

[14] Chapra, S.C., 2008. Surface Water-Quality Modeling. 4th ed., Waveland Press, Inc.

[15] Chen, C., Liu, H., Beardsley, R., 2003. An unstructured grid, finitevolume, three-dimensional, primitive equations ocean model: application to coastal ocean and estuaries. Journal of Atmospheric and Oceanic Technology 20, 159–186.

[16] Dehghan, M., 2004. Numerical solution of the three-dimensional advection-diffusion equation. Applied Mathematics and Computation 150, 5–19.

[17] Dumbser, M., 2010. Arbitrary high order $P_N P_M$ schemes on unstructured meshes for the compressible Navier-Stokes equations. Computers & Fluids 39, 60–76. doi:10.1016/j.compfluid.2009.07.003.

[18] Dumbser, M., Hidalgo, A., Zanotti, O., 2014. High order spacetime adaptive ADER-WENO finite volume schemes for non-conservative hyperbolic systems. Computer Methods in Applied Mechanics and Engineering 268, 359–387. doi:10.1016/j.cma.2013.09.022.

[19] Dumbser, M., Käser, M., Toro, E., 2007. An arbitrary high order discontinuous Galerkin method for elastic waves on unstructured meshes V: Local time stepping and p-adaptivity. Geophysical Journal International 171, 695–717. doi:10.1111/j.1365-246X.2007.03427.x.

[20] Dumbser, M., Zanotti, O., Hidalgo, A., Balsara, D.S., 2013. ADER-WENO finite volume schemes with spacetime adaptive mesh refinement. Journal of Computational Physics 248, 257–286. doi:10.1016/j.jcp.2013.04.017.

[21] Ferrari, A., Munz, C.D., Weigand, B., 2011. A high order sharp-interface method with local time stepping for compressible multiphase flows. Communications in Computational Physics 9, 205–230. doi:10.4208/cicp.090310.050510a.

[22] Fragoso Jr, C.R., Motta-Marques, D., Collischonn, W., Tucci, C.E., van Nes, E.H., 2008. Modelling spatial heterogeneity of phytoplankton in Lake Mangueira, a large shallow subtropical lake in South Brazil. Ecological Modelling 219, 125–137.

[23] Fragoso Jr, C.R., Motta-Marques, D., Ferreira, T.F., Janse, J.H., van Nes, E.H., 2011. Potential effects of climate change and eutrophication on a large subtropical shallow lake. Ecological Modelling & Software 26, 1337–1348.

[24] Fringer, O.B., Gerritsen, M., Street, R., 2006. An unstructured-grid, finite-volume,nonhydrostatic, parallel coastal ocean simulator. Ocean Modelling 14, 139–173. doi:10.1016/j.ocemod.2006.03.006.

[25] Gassner, G., Lorcher, F., Munz, C., 2007. A contribution to the construction of diffusion fluxes for finite volume and discontinuous galerkin schemes. Journal of Computational Physics 224, 1049–1063. doi:10.1016/j.jcp.2006.11.004.

[26] Gassner, G., Lorcher, F., Munz, C., 2008. Discontinuous galerkin scheme based on a space-time expansion ii. viscous flow equations in multi dimensions. Journal of Scientific Computing 34, 260–286. doi:10.1007/s10915-007-9169-1.

[27] Godunov, S., 1959. Finite difference methods for the computation of discontinuous solutions of the equations of fluid dynamics. Mathematics of the USSR: Sbornik 47, 271–306.

[28] Gross, E.S., Bonaventura, L., Rosatti, G., 2002. Consistency with continuity in conservative advection schemes for free-surface models. International Journal for Numerical Methods in Fluids 38, 307–327. doi:10.1002/fld.222.

[29] Gross, E.S., Casulli, V., Bonaventura, L., Koseff, J.R., 1998. A semi-implicit method for vertical transport in multidimensional models. International Journal for Numerical Methods in Fluids 28, 157–186. doi:10.1002/(SICI)1097-0363(19980715)28:1<157::AID-FLD144>3.0.CO;2-U.

[30] Gross, E.S., Koseff, J.R., Monismith, S.G., 1999. Evaluation of advective schemes for estuarine salinity simulations. Journal of Hydraulic Engineering 125, 32–46. doi:10.1061/(ASCE)0733-9429(1999)125:1(32).

[31] Guangwei, Z., Qin, B., Gao, G., Zhang, L., Luo, L., Zhang, Y., 2007. Effects of hydrodynamics on phosphorus concentrations in water of Lake Taihu, a large, shallow, eutrophic lake of China. Hydrobiologia 581, 53–61. doi:10.1007/s10750-006-0519-z.

[32] Hamilton, D.P., Schladow, S.G., 1997. Prediction of water quality in lakes and reservoirs. Part I - Model description. Ecological Modelling 96, 91–110. doi:10.1016/S0304-3800(96)00062-2.

[33] Harten, A., 1983. High resolution schemes for hyperbolic conservation laws. Journal of Computational Physics 49, 357–393.

[34] Hubbard, M.E., 1999. Multidimensional slope limiters for MUSCL-type finite volume schemes on unstructured grids. Journal of Computational Physics 155, 54–74.

[35] Jin, K.R., Ji, Z.G., James, R.T., 2007. Three-dimensional water quality and sav modeling of a large shallow lake. Journal of Great Lakes Research 33, 28–45. doi:10.3394/0380-1330(2007)33[28:TWQASM]2.0.CO;2.

[36] Kong, J., Xin, P., Shen, C.J., Song, Z.Y., Li, L., 2013. A high-resolution method for the depth-integrated solute transport equation based on an unstructured mesh. Environmental Modelling & Software 40, 109–127. doi:10.1016/j.envsoft.2012.08.009.

[37] Liang, D., Wang, X., Falconer, R.A., Bockelmann-Evans, B.N., 2010. Solving the depth-integrated solute transport equation with a tvd-maccormack scheme. Enviromental Modelling & Software 25, 1619–1629. doi:10.1016/j.envsoft.2010.06.008.

[38] Lörcher, F., Gassner, G., Munz, C.D., 2007. A discontinuous Galerkin scheme based on a space-time expansion. I. inviscid compressible flow in one space dimension. Journal of Scientific Computing 32, 175–199.

[39] Lynch, D., Werner, F., 1991. Three-dimensional hydrodynamics on finite elements. part II: non-linear time-stepping model. International Journal for Numerical Methods in Fluids 12, 5077–533.

[40] MacIntyre, S., Melack, J.M., 1995. Vertical and horizontal transport in lakes: linking littoral, benthic, and pelagic habitats. Journal of the North American Benthological Society 14, 599–615.

[41] Mooij, W.M., Trolle, D., Jeppesen, E., Arhonditsis, G., Belolipetsky, Pavel, V., Chitamwebwa, D.B., Degermendzhy, A.G., DeAngelis, D.L., Domis, L.N.d.S., Downing, A.S., Elliott, A., Fragoso Jr., C.R., Gaedke, U., Genova, S.N., Gulati, R.D., Hakanson, L., Hamilton, D.P., Hipsey, M.R., Hoen, J., Hulsmann, Los, F.H., Makler-Pick, V., Petzoldt, T., Prokopkin, I.G., Rinke, K., Schep, S.A., Tominaga, K., Van Dam, A.A., Van Nes, E.H., Wells, S.A., Janse, J.H., 2010. Challenges and opportunities for integrating lake ecosystem modelling approaches. Aquatic Ecology 44, 633–667. doi:10.1007/s10452-010-9339-3.

[42] Roe, P., 1981. Approximate Riemann solvers, parameter vectors, and difference schemes. Journal of Computational Physics 43, 357–372.

[43] Romero, J., Antenucci, J., Imberger, J., 2004. One- and three-dimensional biogeochemical simulations of two differing reservoirs. Ecological Modelling 174, 143–160. doi:10.1016/j.ecolmodel.2004.01.005.

[44] Rubio, A., Zalts, A., El Hasi, C., 2008. Numerical solution of the advection-reaction-diffusion equation at different scales. Environmental Modelling & Software 23, 90–95. doi:10.1016/j.envsoft.2007.05.009.

[45] Sahlberg, J., 2003. Physical modelling of the Akkajaure reservoir. Hydrology and Earth System Sciences 7, 268–282. doi:10.5194/hess-7-268-2003.

[46] Smith, S., Banke, E., 1975. Variation of the sea surface drag coefficient with wind speed. Quartely Journal of the Royal Meteorological Society 101, 665–673. doi:10.1002/qj.49710142920.

[47] Smolarkiewicz, P.K., 1984. A fully multidimensional positive definite advection transport algorithm with small implicit diffusion. Journal of Computational Physics 54, 325–362.

[48] Souza, R., 2014. Emissão de gases de carbono em ecossistemas aquáticos subtropicais continentais: de padrões locais a mudanças climáticas. Phd thesis. Instituto de Pesquisas Hidráulicas, Universidade Federal do Rio Grande do Sul. (*In Portuguese*).

[49] Tambara, V.T., Fragoso Jr, C., Motta-Marques, D., 2017. Modeling metabolism in an integrated subtropical watershed-reservoir system. Brazilian Journal of Water Resources 22, 1–13. doi:10.1590/2318-0331.011716048.

[50] Tavelli, M., Dumbser, M., Casulli, V., 2013. High resolution methods for scalar transport problems in compliant systems of arteries. Applied Numerical Mathematics 74, 62–82.

[51] Teeter, A.M., Johnson, B.H., Berger, C., Stelling, G., Scheffner, N.W., Garcia, M.H., Parchure, T., 2001. Hydrodynamic and sediment transport modeling with emphasis on shallow-water, vegetated areas (lakes, reservoirs, estuaries and lagoons). Hydrobiologia 444, 1–23. doi:10.1023/A:1017524430610.

[52] Toro, E., 2009. Riemann Solvers and Numerical Methods for Fluid Dynamics. third ed., Springer.

[53] Tucci, C., 1998. Modelos Hidrológicos (*In Portuguese*). ABRH/UFRGS.

[54] van Leer, B., 1979. Towards the ultimate conservative difference scheme V: A second order sequel to Godunov's method. Journal of Computational Physics 32, 101–136.

[55] Vested, H.J., Justesen, P., Ekebjaerg, L., 1992. Advection-dispersion modelling in three dimensions. Applied Mathematical Modelling 16, 506–519.

[56] Wang, C.F., Wang, H.V., Kuo, A.Y., 2008. Mass conservative transport scheme for the application of the ELCIRC model to water quality computation. Journal of Hydraulic Engineering 134, 1166–1171.

[57] Wu, T., Qin, B., Zhu, G., Luo, L., Ding, Y., Bian, G., 2013. Dynamics of cyanobacterial bloom formation during short-term hydrodynamic fluctuation in a large shallow, eutrophic, and wind-exposed Lake Taihu, China. Environmental Science and Pollution Research 20, 8546–8556. doi:10.1007/s11356-013-1812-9.

[58] Zhang, Y., Baptista, A.M., Meyers III, E.P., 2004. A cross-scale model for 3d baroclinic circulation in estuary-plume-shelf systems: I. Formulation and skill assessment. Continental Shelf Research 24, 2187–2214.

Capítulo 6

Conclusão

Este trabalho foi desenvolvido com base em duas grandes áreas de estudo: a influência da hidrodinâmica sobre o metabolismo aquático em lagos rasos; e o desenvolvimento de novos métodos numéricos buscando melhorar os esquemas tradicionais utilizados em modelos de qualidade da água.

O metabolismo aquático da Lagoa Mangueira foi avaliado utilizando um novo algoritmo computacional, desenvolvido neste trabalho, baseado em processos biológicos e implementado no Modelo IPH-ECO. O algoritmo utiliza os principais processos individuais envolvidos no balanço de oxigênio dissolvido (e.g., produção primária do fitoplâncton, mineralização de matéria orgânica), separando-os em diferentes componentes seguindo a Equação de Odum (GPP, R e NEP). O uso de um modelo matemático complexo como o IPH-ECO permitiu a integração de processos biológicos e físicos, sendo possível estimar de maneira dinâmica e espacialmente explícita os principais componentes utilizados para estimar o metabolismo em ambientes aquáticos (GGP, R e NEP). Apesar de lagos rasos serem considerados sistemas homogêneos, o metabolismo aquático da Lagoa Mangueira demonstrou variabilidade espacial e temporal. Nossos resultados mostraram uma contínua alteração entre condições autotróficas (NEP>0) e heterotróficas (NEP<0) levando em conta diferentes escalas espaciais e mesmo em escalas temporais curtas. A produção primária do fitoplâncton foi o principal processo individual formando as estimativas de GPP (aprox. 90% na zona pelágica e 70% na zona litorânea) enquanto a respiração, R, foi principalmente formada pelo processo de respiração de organismos heterotróficos. Por meio do uso de diferentes cenários de vento, foi possível avaliar a influência da hidrodinâmica sobre as estimativas de metabolismo aquático na Lagoa Mangueira. A hidrodinâmica foi capaz de influenciar as estimativas de metabolismo aquático, sendo possível observar diferenças significativas ($p<0.05$) entre as estimativas em diferentes cenários hidrodinâmicos. Sem circulação hidrodinâmica ocorre um aumento na importância dos processos ocorrendo próximo a camada de sedimentos, no fundo da lagoa. Quanto maior a intensidade da

circulação hidrodinâmica, mais as macrófitas aquáticas foram capazes de dominar os processos de GPP, R e NEP na lagoa. Nossos resultados, obtidos a partir de uma modelagem baseada em processos, sugerem que a hidrodinâmica é um fator-chave na composição das estimativas de metabolismo aquático em lagos. Além disso, o uso de coletas pontuais apresenta apenas uma parte do funcionamento do sistema, levando a uma conclusão parcial sobre o estado trófico do sistema e sua heterogeneidade espacial e temporal.

Ao longo deste trabalho foi desenvolvido também um novo método numérico que pode ser utilizado na solução da Equação de Transporte de Escalares em grades não-estruturadas. O novo esquema numérico é baseado no método dos Volumes Finitos utilizando uma aproximação de MUSCL de 2ª ordem (no espaço e no tempo) para interpolar os valores na interface entre elementos. A integração numérica é realizada utilizando um novo esquema de passo de tempo *localizado* (LTS), permitindo a redução do tempo total de simulação quando comparado a esquemas tradicionais baseados em passo de tempo *global* (GTS). Além disso, o método é diretamente acoplado a modelos hidrodinâmicos tridimensionais que utilizam soluções numéricas semi-implícitas em grades não-estruturadas (UnTRIM). O novo esquema foi testado em diferentes problemas clássicos (*benchmark*) e idealizados, sendo aplicado em dois ambientes aquáticos distintos (Lago Guaíba e Reservatório do Faxinal). A solução numérica foi considerada robusta e eficiente quando utilizada em problemas clássicos para testar métodos numéricos, levando em conta diferentes mecanismos de transporte (advecção, difusão e reação). O mesmo pode ser observado ao testar a nova solução em problemas idealizados levando em conta variações na superfície livre, i.e., acoplado a um modelo hidrodinâmico em grade não-estruturada. Nestes casos, a combinação entre características da circulação (campo de velocidades e difusão) e características da discretização computacional (elementos com diferentes tamanhos) levam a maior eficiência no uso da nova solução localizada, chegando a reduzir até 90% no tempo total gasto com simulações. Os resultados obtidos a partir das aplicações do novo método numérico em sistemas reais mostram uma ferramenta promissora e flexível, capaz de ser estendida para grades estruturadas e soluções de Equações de Transporte para grandezas vetoriais. Em modelos hidrodinâmicos semi-implícitos, utilizar esta nova solução no lugar da tradicional solução Euleriana-Lagrageana poderia remover as tradicionais restrições no passo de tempo devido a viscosidade horizontal e máxima velocidade das ondas internas não-lineares no caso de escoamento baroclínicos.

Capítulo 7

Anexo A: Modelo IPH-ECO

O modelo computacional IPH-ECO é uma ferramenta capaz de simular ecossistemas aquáticos (*e.g.*, lagos, reservatórios e estuários) de forma dinâmica, levando em conta processos físicos, químicos e biológicos. O modelo vem sendo desenvolvido pelo Grupo de Pesquisa em Ecotecnologia, do Instituto de Pesquisas Hidráulicas da Universidade Federal do Rio Grande do Sul (GPE-IPH/UFRGS), consistindo em diversas equações diferenciais parciais sendo dividido em dois módulos principais: (a) um módulo hidrodinâmico detalhado, descrevendo fluxos quantitativos (*e.g.*,padrões de circulação, campos de velocidade) e níveis de água; e (b) um módulo de qualidade da água, que lida com o mecanismos de transporte de nutrientes e todas as interações entre a cadeia trófica aquática. As equações diferenciais do módulo hidrodinâmico são solucionadas numericamente aplicando um esquema semi-implícito de diferenças finitas em domínios estruturados (Casulli & Cheng, 1992) ou não-estruturados (Casulli & Walters, 2000). As equações diferenciais para o transporte de substâncias é solucionada com um esquema conservativo baseado em volumes finitos, com os termos fontes nestas equações (*i.e.*, processos capazes de gerar/consumir substâncias) baseados em grande parte no modelo PC-Lake (Janse, 2005).

7.1 Capacidades do Modelo

O modelo IPH-ECO é capaz de simular escoamentos e variáveis de qualidade de água (*e.g.*, nutrientes, biomassa de fitoplâncton) em domínios tri-dimensionais, sendo possível adaptar a resolução do modelo para aplicações bi-dimensionais, uni-dimensionais e modelos concentrados. É possível utilizar o modelo em diversas áreas, como segue:

- Escoamentos derivados por maré, vento e fluviais;

- Escoamentos sobre estruturas hidráulicas (vertedores);
- Simulação de Estratificação em lagos, reservatórios e estuários;
- Entrada de sal em sistemas aquáticos;
- Simulação com diferentes temperaturas de água e entrada de esgotos;
- Avaliação de transporte de material dissolvido e poluentes;
- Transporte de sedimentos e morfologia;
- Simulação das interações na cadeia trófica aquática;

7.2 Modelo Hidrodinâmico

7.2.1 Malhas Não-Estruturadas

A fim de resolver as equações matemáticas utilizadas pelo IPH-ECO, o domínio horizontal é coberto por um conjunto de polígonos convexos não sobrepostos entre si. Cada face de um polígono é um segmento que o liga a outro polígono ou um contorno do domínio. Dentro de cada polígono existe um ponto, definido como centro, de forma que o segmento ligando os centros de dois polígonos vizinhos é não-nulo e ortogonal ao segmento que forma a face separando estes dois vizinhos. Nesta condição, a malha é chamada de ortogonal (Casulli & Walters, 2000). O centro do polígono não necessariamente coincide com o centro geométrico (ou centróide). Exemplos de grades ortogonais estruturadas são malhas formadas por elementos quadrados assim como malhas formadas por triângulos equiláteros uniformes (Fig. 7.1). Nestes casos em particular o centro de cada polígono pode ser identificado como o centroide destes polígonos.

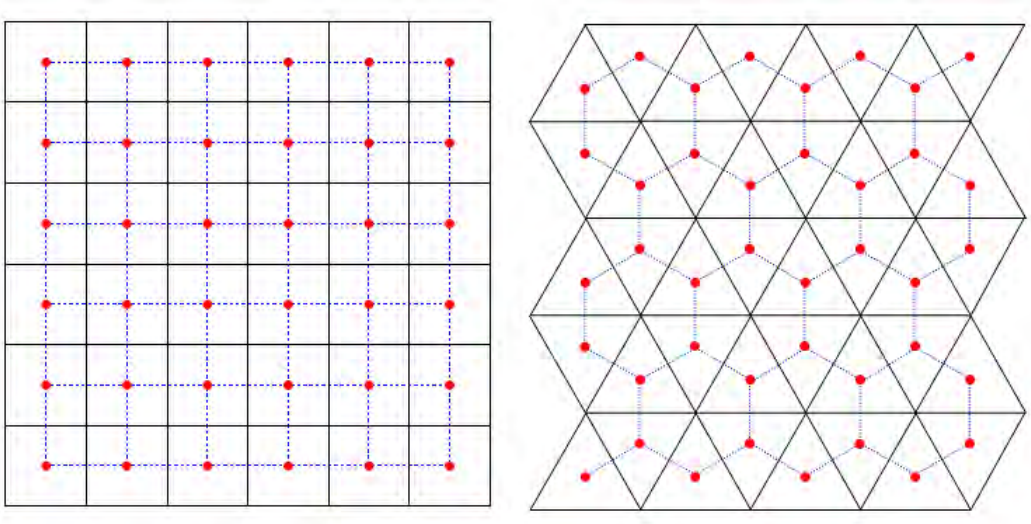

Figura 7.1: Duas malhas estruturadas ortogonais. Malha utilizando quadriláteros (esquerda) e malha utilizando triângulos equiláteros (direita). Pontos vermelhos indicam o centro do polígono e as linhas finas indicam os segmentos ligando dois centros.

Atualmente, o modelo IPH-ECO é capaz de simular domínios cobertos por elementos quadrangulares (versão estruturada) ou triangulares (versão não-estruturada). A geração destas malhas computacionais pode ser simples, como no caso estruturado, ou complexo, como no caso não-estruturado. O uso de malhas triangulares visa alinhar a malha computacional ao contorno do domínio. No entanto, triângulos que não respeitam as condições de ortogonalidade podem ser gerados (Fig. 7.2). Esta restrição passa a ser respeitada caso seja utilizada a construção da malha utilizando a chamada triangulação de Delaunay, desde que os triângulos gerados tenham ângulos menores que 90°.

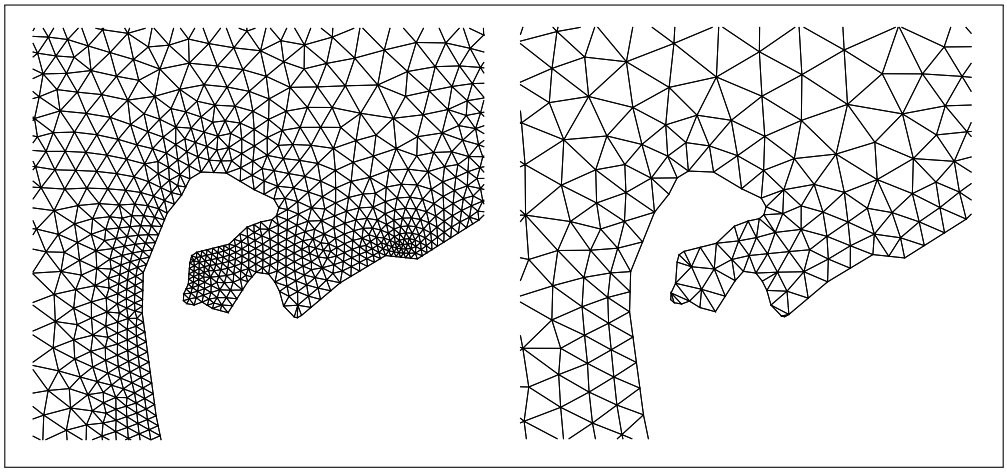

Figura 7.2: Malhas não-estruturadas geradas levando em conta o critério de ortogonalidade (esquerda) e sem levar em conta o critério de ortogonalidade (direita). Triângulos "esguios" ou com ângulos obtusos podem gerar instabilidades na solução numérica.

Uma vez que o domínio *(X, Y)* foi coberto com uma malha não-estruturada ortogonal, temos N_p polígonos, cada um com um número conhecido de faces ($S_i = 3$ ou $S_i = 4$). Tomando como N_s o número total de faces da malha, definimos como λ_j, com $j = 1, 2, ..., N_s$ o comprimento de cada face de um elemento. As faces de um polígono "i" qualquer são identificadas por um índice $j(i, l)$, com $l = 1, 2, ..., S_i$, de forma que $1 \leq j(i, l) \leq N_s$. De maneira similar, os dois polígonos que dividem a face "j" são identificados como $p(j, 1)$ e $p(j, 2)$ de forma que $1 \leq p(j, 1) \leq N_p$ e $1 \leq p(j, 2) \leq N_p$. A distância não-nula entre os centros de dois polígonos que dividem a face "j" é denotado por δ_j. Ao longo da direção vertical uma discretização simples, baseada em diferenças finitas, não necessariamente uniforme, é adotada. Denotando por $z_{k+\frac{1}{2}}$, um dado nível da superfície, a discretização vertical é dada por $\Delta z_k = z_{k+\frac{1}{2}} - z_{k-\frac{1}{2}}$, com $k = 1, 2, ..., N_z$. A discretização espacial em três dimensões consiste em prismas dos quais as faces horizontais são os polígonos de uma dada malha ortogonal e as alturas são dadas por Δz_k. (Fig. 7.3).

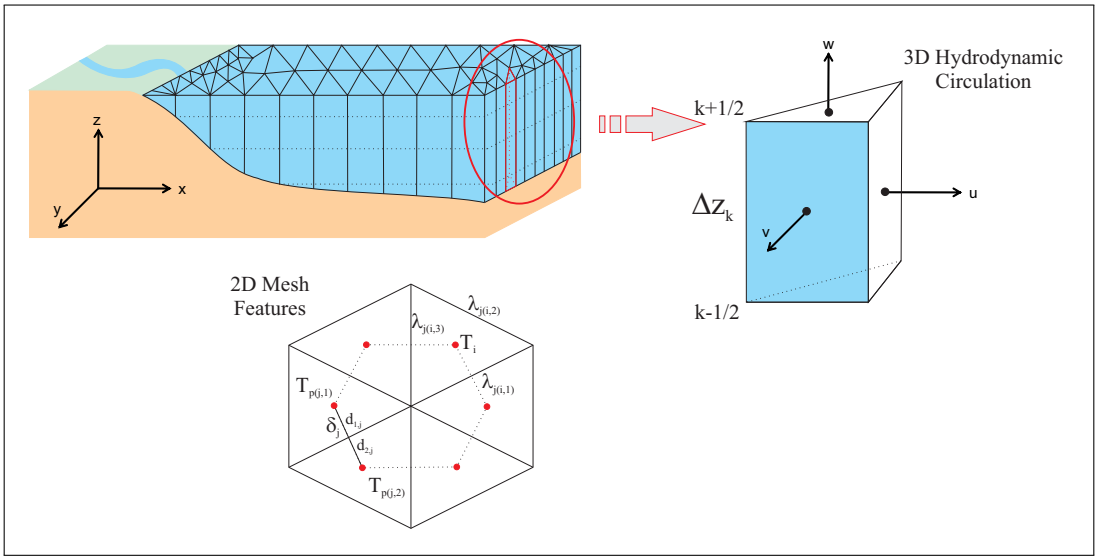

Figura 7.3: Discretização tridimensional não-estruturada. Os elementos são compostos por prismas triangulares definidos por uma espessura Δz em cada camada vertical "k". Cada triângulo T_i possue três faces com comprimento λ_j. Em cada face "j", os triângulos adjacentes $T_{p(j,1)}$ e $T_{p(j,2)}$ são separados por uma distância não-nula δ_j, onde $d_{1,j}$ e $d_{2,j}$ são as respectivas distâncias do centro de $T_{p(j,1)}$ e $T_{p(j,2)}$ ao centro da face "j".

As velocidades e a elevação da superfície da água são definidos em pontos diferentes da malha (*staggered grid*). A elevação da superfície da água, assumida constante em cada polígono, é localizada no centro do polígono "i"; o componente da velocidade normal a cada face do prisma, assumido constante ao longo da face, é definido no ponto de intersecção entre a face e o segmento unindo os centros dos dois prismas que dividem a face "j"; As concentrações simuladas são localizadas no centro dos prismas, numa posição intermediária entre $z_{k+\frac{1}{2}}$ e $z_{k-\frac{1}{2}}$. Finalmente, a profundidade da água em cada face é definida e assumida como constante ao longo de cada face do polígono.

7.2.2 Equações Governantes

As equações tridimensionais descrevendo escoamento com superfície livre pode ser derivado a partir das Equações de Navier-Stokes após ponderar sob escalas de tempo turbulentas (*Reynolds Averaged Navier-Stokes Equations*). Estas equações expressam os princípios físicos da conservação do volume, da massa e de quantidade de movimento (ou momento). As equações de quantidade de movimento para um

fluido incompressível possuem a seguinte forma:

$$\frac{\partial u}{\partial t} + u\frac{\partial u}{\partial t} + v\frac{\partial u}{\partial t} + w\frac{\partial u}{\partial t} - fv = -g\frac{\partial p}{\partial x} + \nu^h\left(\frac{\partial^2 u}{\partial x^2} + \frac{\partial^2 u}{\partial y^2}\right) + \frac{\partial}{\partial z}\left(\nu^v\frac{\partial u}{\partial z}\right) \quad (7.1)$$

$$\frac{\partial v}{\partial t} + u\frac{\partial v}{\partial t} + v\frac{\partial v}{\partial t} + w\frac{\partial v}{\partial t} + fu = -g\frac{\partial p}{\partial y} + \nu^h\left(\frac{\partial^2 v}{\partial x^2} + \frac{\partial^2 v}{\partial y^2}\right) + \frac{\partial}{\partial z}\left(\nu^v\frac{\partial v}{\partial z}\right) \quad (7.2)$$

$$\frac{\partial w}{\partial t} + u\frac{\partial w}{\partial t} + v\frac{\partial w}{\partial t} + w\frac{\partial w}{\partial t} = -g\frac{\partial p}{\partial z} + \nu^h\left(\frac{\partial^2 w}{\partial x^2} + \frac{\partial^2 w}{\partial y^2}\right) + \frac{\partial}{\partial z}\left(\nu^v\frac{\partial w}{\partial z}\right) - \frac{\rho}{\rho_0}g \quad (7.3)$$

onde $u(x, y, z, t)$, $v(x, y, z, t)$ e $w(x, y, z, t)$ são as componentes do vetor velocidade nas direções X, Y e Z, respectivamente; t é o tempo; $p(x, y, z, t)$ é a pressão normalizada definida como a pressão dividida por uma densidade de referência constante ρ_0; f é o parâmetro de Coriolis; g é a aceleração da gravidade e ν^h e ν^v são os coeficientes de viscosidade turbulenta (*eddy viscosity*) na horizontal e vertical, respectivamente. Por último, ρ é a densidade da água e ρ_0 é a densidade de referência da água (constante).

A conservação do volume é expressa a partir da condição de incompressibilidade:

$$\frac{\partial u}{\partial t} + \frac{\partial v}{\partial t} + \frac{\partial w}{\partial t} = 0 \quad (7.4)$$

Integrando a equação da continuidade (Eq. 7.4) ao longo da profundidade e assumindo uma condição cinemática na superfície obtemos a seguinte relação (Casulli & Cheng, 1992):

$$\frac{\partial \eta}{\partial t} + \frac{\partial}{\partial x}\left[\int_{-h}^{\eta} u dz\right] + \frac{\partial}{\partial y}\left[\int_{-h}^{\eta} v dz\right] = 0 \quad (7.5)$$

onde $h(x, y)$ é a batimetria e $\eta(x, y, t)$ é a elevação da superfície livre. Desta forma, definimos $H(x, y, t) = h(x, y) + \eta(x, y, t)$ como a profundidade total da água (Fig. 7.4).

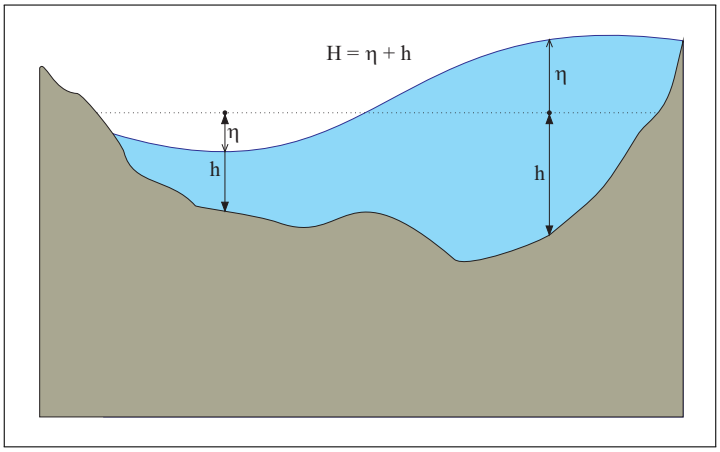

Figura 7.4: Relação entre elevação da superfície livre η, batimetria h e profundidade total H. A batimetria é positiva num plano apontando para baixo, o contrário sendo adotado para a elevação da superfície livre. A elevação da superfície livre pode assumir valores positivos e negativos.

A conservação da massa de uma variável escalar é expressa pela seguinte forma diferencial:

$$\frac{\partial C}{\partial t} + \frac{\partial (uC)}{\partial x} + \frac{\partial (vC)}{\partial y} + \frac{\partial (wC)}{\partial z} = \frac{\partial}{\partial x}\left(K^h \frac{\partial C}{\partial x}\right) + \frac{\partial}{\partial y}\left(K^h \frac{\partial C}{\partial y}\right) + \frac{\partial}{\partial z}\left(K^v \frac{\partial C}{\partial z}\right) + S(C) \tag{7.6}$$

onde $C(x, y, z, t)$ denota a concentração de uma dada quantidade escalar sendo transportada (e.g., Salinidade, temperatura, sólidos suspensos, ou nutrientes); K^h e K^v são as difusividades horizontais e vertical, respectivamente; o termo $S(C)$ engloba os principais processos capazes de produzir ou consumir o escalar sendo transportado.

A densidade da água é um parâmetro importante para estudos de qualidade da água e hidrodinâmica. A densidade da água pode ser calculada levando em conta a temperatura da água e a concentração de sal pela seguinte equação (Read et al., 2011):

$$\begin{aligned}\rho = {} & 999.842594 + 6.793952x10^{-2}T - 9.095290x10^{-3}T^2 \\ & + 1.001685x10^{-4}T^3 - 1.120083x10^{-6}T^4 + 6.536332x10^{-9}T^5 \\ & + (0.824493 - 4.0899x10^{-3}T + 7.6438x10^{-5}T^2 - 8.2467x10^{-7}T^3 \\ & + 5.3875x10^{-9}T^4)S + (-5.72466x10^{-3} + 1.0227x10^{-4}T \\ & - 1.6546x10^{-6}T^2)S^{\frac{3}{2}} + 4.8314x10^{-4}S^2\end{aligned} \tag{7.7}$$

A pressão $p(x, y, z, t)$ nas equações (7.1)-(7.3) pode ser decomposta na soma de parcelas hidrostáticas e não-hidrostáticas. A componente hidrostática da pressão

é determinada pela equação de quantidade de movimento na vertical (Eq. 7.3), desprezando os termos convectivos e viscosos. Logo, a pressão $p(x, y, z, t)$ pode ser expressa por:

$$p(x, y, z, t) = p_a(x, y, t) + g[\eta(x, y, t) - z] + g \int_z^\eta \frac{\rho - \rho_0}{\rho_0} d\xi + q(x, y, z, t) \quad (7.8)$$

onde o primeiro termo do lado direito $p_a(x, y, t)$ corresponde a pressão atmosférica na superfície, e o segundo e terceiro termos correspondem as contribuições barotrópicas e baroclínicas à pressão hidrostática e $q(x, y, z, t)$ corresponde a componente não-hidrostática da pressão. Consequentemente, as equações de quantidade de movimento (7.1)-(7.3) podem ser reescritas como:

$$\frac{du}{dt} - fv = -\frac{\partial p_a}{\partial x} - g\frac{\partial \eta}{\partial x} - g\frac{\partial}{\partial x}\left[\int_z^\eta \frac{\rho - \rho_0}{\rho_0} d\xi\right] - \frac{\partial q}{\partial x} + \nu^h \left(\frac{\partial^2 u}{\partial x^2} + \frac{\partial^2 u}{\partial y^2}\right) + \frac{\partial}{\partial z}\left(\nu^v \frac{\partial u}{\partial z}\right) \quad (7.9)$$

$$\frac{dv}{dt} + fu = -\frac{\partial p_a}{\partial y} - g\frac{\partial \eta}{\partial y} - g\frac{\partial}{\partial x}\left[\int_z^\eta \frac{\rho - \rho_0}{\rho_0} d\xi\right] - \frac{\partial q}{\partial y} + \nu^h \left(\frac{\partial^2 v}{\partial x^2} + \frac{\partial^2 v}{\partial y^2}\right) + \frac{\partial}{\partial z}\left(\nu^v \frac{\partial v}{\partial z}\right) \quad (7.10)$$

$$\frac{dw}{dt} = -\frac{\partial q}{\partial z} + \nu^h \left(\frac{\partial^2 w}{\partial x^2} + \frac{\partial^2 w}{\partial y^2}\right) + \frac{\partial}{\partial z}\left(\nu^v \frac{\partial w}{\partial z}\right) \quad (7.11)$$

Assumindo a pressão como hidrostática, a Equação (7.11) é desprezada e $q(x, y, z, t) = 0$. Neste caso, é assumido que a componente não-hidrostática da pressão não causa grandes variações no escoamento. Desta forma, o conjunto de equações (7.9)-(7.11) se reduz a forma tridimensional das equações de águas rasas (Casulli & Walters, 2000), onde agora a velocidade vertical $w(x, y, z, t)$ é computada a partir da equação da continuidade em sua forma diferencial (Eq. 7.4).

As condições de contorno para as equações de quantidade de movimento na superfície são dadas pelas tensões de arraste do vento:

$$\nu^v \frac{\partial u}{\partial z} = \gamma_T(u_a - u), \quad \nu^v \frac{\partial v}{\partial z} = \gamma_T(v_a - v) \quad \text{em} \quad z = \eta \quad (7.12)$$

onde u_a e v_a são os componentes da velocidade do vento nas direções X e Y, respectivamente, e γ_T é definido de acordo com

$$\gamma_T = r_T \sqrt{(u_a - u)^2 + (v_a - v)^2} \quad (7.13)$$

onde r_T é um coeficiente de arraste do vento, que pode ser calculado utilizando (Smith & Banke, 1975):

$$r_T = \frac{\rho_{air}}{\rho}\left(0.63 + 0.066\sqrt{{u_a}^2 + {v_a}^2}\right) 10^{-3} \quad (7.14)$$

A densidade do ar (ρ_{air}) pode ser adotada como constante dentro do intervalo $1.2 \leq \rho_{air} \leq 1.3$.

Na interface entre sedimento e a coluna d'água uma condição similar é especificada:

$$\nu^v \frac{\partial u}{\partial z} = \gamma_B u, \quad \nu^v \frac{\partial v}{\partial z} = \gamma_B v, \quad \text{em} \quad z = -h \tag{7.15}$$

onde γ_B é definido como:

$$\gamma_T = r_B \sqrt{u^2 + v^2} \tag{7.16}$$

e r_B é um coeficiente de fricção com o fundo, que pode ser calculado utilizando um modelo de turbulência ou pela formula de Chezy:

$$r_B = \frac{g}{{C_z}^2} \tag{7.17}$$

7.2.3 Esquema Semi-Implícito de Diferenças Finitas

Um esquema semi-implícito para a solução das equações (7.9)-(7.11), o qual a estabilidade independe da velocidade de propagação das ondas de superfície, viscosidade vertical e coeficiente de fricção com o fundo foi descrito por Casulli & Walters (2000) para a forma tridimensional das equações de águas rasas. Este método é eficiente e capaz de resolver também a forma bidimensional das equações de águas rasas no caso particular onde apenas uma camada vertical é especificada. Neste esquema, a elevação da superfície da água nas equações (7.9)-(7.11), e a velocidade na forma integral da equação da continuidade (Eq. 7.5), são discretizados utilizando o método θ (Casulli & Cattani, 1994). Além disto, o termo de fricção com o fundo é discretizado implicitamente por motivos de estabilidade.

Uma vez que as equações (7.9)-(7.11) são invariáveis sob rotação ao longo dos eixos x e y no plano horizontal, uma discretização semi-implícita em diferenças finitas

$$\begin{aligned} u_{j,k}^{n+1} =& \mathbf{F} u_{j,k}^n - g \frac{\Delta t}{\delta_j} \left[\theta(\eta_{p(j,2)}^n - \eta_{p(j,1)}^n) + (1-\theta)(\eta_{p(j,2)}^{n+1} - \eta_{p(j,1)}^{n+1}) \right] \\ &+ \frac{\Delta t}{\Delta z_{j,k}^n} \left[\nu_{j,k+1/2}^v \frac{u_{j,k+1}^{n+1} - u_{j,k}^{n+1}}{\Delta z_{j,k+1/2}^n} - \nu_{j,k-1/2}^v \frac{u_{j,k}^{n+1} - u_{j,k-1}^{n+1}}{\Delta z_{j,k-1/2}^n} \right], \\ k = m_j, m_{j+1}, ..., M_j^n & \end{aligned} \tag{7.18}$$

onde $u_{j,k}^n$ é a componente horizontal da velocidade normal à face "j" da malha, na camada vertical k e no passo de tempo n. A direção positiva de $u_{j,k}^n$ é adotada de $p(j,1)$ para $p(j,2)$. $\mathbf{F}$ é um operador explícito que leva em conta as discretizações da pressão atmosférica, Coriolis, pressão baroclínica, advecção e termos viscosos horizontais. Este operador pode ser discretizado utilizando diferentes esquemas

numéricos, dos quais o esquema Euleriano-Lagrangiana vem sendo mais utilizado devido a menor restrição no passo de tempo (Casulli & Cheng, 1992; Casulli & Walters, 2000). A única restrição ao operador **F** é que ao se desprezar os termos de Coriolis, pressão baroclínica, advecção e viscosidade horizontal, **F** se reduza ao operador identidade, i.e., $\mathbf{F}u^n_{j,k} = u^n_{j,k}$. θ é um ponderador temporal a ser tomado no intervalo $1/2 \leq \theta \leq 1$ (Casulli & Cattani, 1994).

O incremento vertical $\Delta z^n_{j,k}$ é definido como a distância entre duas camadas verticais consecutivas, exceto próximo ao fundo e próximo à superfície livre, onde $\Delta z^n_{j,k}$ é a distância da camada vertical até o fundo ou até a superfície livre. De maneira geral, $\Delta z^n_{j,k}$ depende da localização espacial e próximo à superfície livre depende também do passo de tempo. O incremento espacial $\Delta z^n_{j,k}$ pode exibir valores nulos, levando em conta a secagem e inundação de células computacionais. Neste caso, as equações (7.18) não estão definidas para pontos onde $\Delta z^n_{j,k} = 0$ e $u^{n+1}_{j,k}$ é assumido. Finalmente, m_j e M^n_j, $1 \leq m_j \leq M^n_j \leq N_z$, são as os limites inferiores e superiores das camadas verticais. Como indicado, m e M dependem da posição espacial e M também depende do passo de tempo, para levar em conta a dinâmica da superfície livre. Em células inundadas, a Equação (7.18) é uma equação linear que envolve as variáveis desconhecidas $u^{n+1}_{j,k}$, $\eta^{n+1}_{p(j,1)}$ e $\eta^{n+1}_{p(j,2)}$.

Os valores de $u^{n+1}_{j,k}$ acima da superfície livre e abaixo do fundo na Equação (7.18) são eliminadas pelo uso das condições de contorno (7.12) e (7.15) que geram as seguintes equações:

$$\nu^v_{j,M+1/2} \frac{u^{n+1}_{j,M+1} - u^{n+1}_{j,M}}{\Delta z^n_{j,M+1/2}} = \gamma^{n+1}_{T,j}(u^{n+1}_{a,j} - u^{n+1}_{j,M}) \tag{7.19}$$

e

$$\nu^v_{j,m-1/2} \frac{u^{n+1}_{j,m} - u^{n+1}_{j,m-1}}{\Delta z^n_{j,m-1/2}} = \gamma^{n+1}_{B,j} u^{n+1}_{j,m} \tag{7.20}$$

Assumindo uma elevação da superfície livre constante em cada coluna d'água, uma discretização semi-implícita em *volumes finitos* da Equação (7.5) em cada polígono é dada por (Casulli, 2009):

$$V_i(\eta^{n+1}_i) = V_i(\eta^n_i) - \Delta t \sum_{l=1}^{N_s} s_{i,l} \lambda_{j(i,l)} [\theta \sum_{m_{j(i,l)}}^{M^n_{j(i,l)}} \Delta z^n_{j(i,l),k} u^{n+1}_{j(i,l),k} - (1-\theta) \sum_{m_{j(i,l)}}^{M^n_{j(i,l)}} \Delta z^n_{j(i,l),k} u^n_{j(i,l),k}] \tag{7.21}$$

onde $V_i(\eta^n_i)$ é o volume de água num prisma "i" delimitado pela elevação da superfície livre η^n_i; $s_{i,j}$ é uma função sinal associada com a orientação da velocidade normal associada a face "j" do polígono "i". Especificamente, $s_{i,j} = 1$ se uma

velocidade positiva na face "j" corresponde a um fluxo de saída, $s_{i,j} = -1$ se a uma velocidade positiva na face "j" corresponde a um fluxo de entrada no polígono "i". Logo, uma vez que $p[j(i,l),1] = i$ ou $p[j(i,l),2] = i$, i.e., o elemento de interesse deve ser um dos vizinhos, $s_{i,j}$ pode ser escrito como:

$$s_{i,j} = \frac{p[j(i,l),2] - 2i + p[j(i,l),1]}{p[j(i,l),2] - p[j(i,l),1]} \tag{7.22}$$

Os novos campos de velocidade ($u_{j,k}^{n+1}$) e elevação da superfície livre (η_i^{n+1}) e o correspondente domínio molhado (Ω_i^{n+1}) são determinados a partir da solução das equações (7.18) e (7.21) em cada passo de tempo. Esta solução leva em conta as equações em forma de matrizes, após a incluir as condições de contorno (7.20) e (7.19):

$$\mathbf{A}_j^n \mathbf{U}_j^{n+1} = \mathbf{G}_j^n - \theta g \frac{\Delta t}{\delta_j} [\eta_{p(j,2)}^{n+1} - \eta_{p(j,1)}^{n+1}] \Delta \mathbf{Z}_j^n \tag{7.23}$$

$$\begin{aligned} V_i(\eta_i^{n+1}) = V_i(\eta_i^n) &- \theta \Delta t \sum_{l=1}^{N_s} s_{i,l} \lambda_{j(i,l)} [\Delta \mathbf{Z}_{j(i,l)}^n]^T \mathbf{U}_{j(i,l)}^{n+1} \\ &- (1-\theta) \Delta t \sum_{l=1}^{N_s} s_{i,l} \lambda_{j(i,l)} [\Delta \mathbf{Z}_{j(i,l)}^n]^T \mathbf{U}_{j(i,l)}^n \end{aligned} \tag{7.24}$$

onde $\mathbf{U}$, $\Delta\mathbf{Z}$, $\mathbf{G}$ e $\mathbf{A}$ são definidos como:

$$\mathbf{U}_j^{n+1} = \begin{bmatrix} u_{j,M}^{n+1} \\ u_{j,M-1}^{n+1} \\ \vdots \\ u_{j,m}^{n+1} \end{bmatrix}, \quad \mathbf{\Delta Z}_j^n = \begin{bmatrix} \Delta z_{j,M}^n \\ \Delta z_{j,M-1}^n \\ \vdots \\ \Delta z_{j,m}^n \end{bmatrix},$$

$$\mathbf{G}_j^n = \begin{bmatrix} \Delta z_{j,M}^n \mathbf{F} u_{j,M}^n - \frac{\Delta t}{\delta_j}(1-\theta) g (\eta_{p(j,2)}^n - \eta_{p(j,1)}^n) + \Delta t \gamma_{T,j}^{n+1} u_{a,j}^{n+1} \\ \Delta z_{j,M-1}^n \mathbf{F} u_{j,M-1}^n - \frac{\Delta t}{\delta_j}(1-\theta) g (\eta_{p(j,2)}^n - \eta_{p(j,1)}^n) \\ \vdots \\ \Delta z_{j,m}^n \mathbf{F} u_{j,m}^n - \frac{\Delta t}{\delta_j}(1-\theta) g (\eta_{p(j,2)}^n - \eta_{p(j,1)}^n) \end{bmatrix},$$

$$\mathbf{A}_j^n = \begin{bmatrix} \Delta z_{j,M}^n + a_{j,M-1/2}^n + \Delta t \gamma_{T,j}^{n+1} & -a_{j,M-1/2}^n & \cdots & 0 \\ -a_{j,M-1/2}^n & \Delta z_{j,M-1}^n + a_{j,M-1/2}^n + a_{j,M-3/2}^n & -a_{j,M-3/2}^n & \\ \vdots & \vdots & \vdots & \vdots \\ 0 & & -a_{j,m+1/2}^n & \Delta z_{j,m}^n + a_{j,m+1/2}^n + \Delta t \gamma_{B,j}^{n+1} \end{bmatrix},$$

com $a_{j,k\pm1/2}^n = \nu_{j,k\pm1/2}^v \frac{\Delta t}{\Delta z_{j,k\pm1/2}^n}$.

Substituindo a Equação (7.23) na Equação (7.24) gera a seguinte expressão para η_i^{n+1}:

$$V_i(\eta_i^{n+1}) - g\theta^2\Delta t^2 \sum_{l=1}^{N_s} \frac{s_{i,l}\lambda_{j(i,j)}}{\delta_{j(i,l)}} \left[(\mathbf{\Delta Z})^T \mathbf{A}^{-1} \mathbf{\Delta Z}\right]_{j(i,l)}^n (\eta_{p(j(i,l),2)}^{n+1} - \eta_{p(j(i,l),1)}^{n+1})$$
$$= V_i(\eta_i^n) - (1-\theta)\Delta t \sum_{l=1}^{N_s} s_{i,l}\lambda_{j(i,l)} \left[(\mathbf{\Delta Z})^T \mathbf{U}\right]_{j(i,l)}^n$$
$$- \theta\Delta t \sum_{l=1}^{N_s} \left[(\mathbf{\Delta Z})^T \mathbf{A}^{-1} \mathbf{G}\right]_{j(i,l)}^n \tag{7.25}$$

Nos polígonos "i", onde $H_{j(i,l)}^n = 0$ para $l = 1, 2, ..., N_s$, a Equação (7.25) se reduz a $V_i(\eta_i^{n+1}) = V_i(\eta_i^n)$, logo $\eta_i^{n+1} = \eta_i^n$. Neste caso, a Equação (7.25) não contribui para o sistema que será formulado. O restante das equações (onde ao menos um $H_{j(i,l)}^n$ é maior que zero) pode ser reunido num sistema *moderadamente* não-linear, esparso, de N_η equações para η_i^{n+1}, com $N_\eta \leq N_p$. Detalhes da solução deste sistema será apresentado na próxima seção.

Uma vez que a nova elevação da superfície livre η_i^{n+1} é computada, as velocidades discretizadas $u_{j,k}^{n+1}$ são prontamente obtidas por meio da Equação (7.18) ao longo de todo o domínio. Uma discretização em volumes finitos da Equação (7.4) permite computar o campo de velocidades verticais no novo intervalo de tempo. Especificamente, ao assumir $w_{i,m-1/2}^{n+1} = 0$, a componente vertical da velocidade em cada coluna d'água é calculada como:

$$w_{i,k+1/2}^{n+1} = w_{i,k-1/2}^{n+1} - \frac{1}{A_i} \sum_{l=1}^{N_s} s_{i,l}\lambda_{j(i,l)}\Delta z_{j(i,l),k}^n u_{j(i,l),k}^{n+1}, \quad k = m_i, m_i+1, ..., M_i^n - 1 \tag{7.26}$$

onde A_i é a área do polígono "i".

Finalmente, a elevação da superfície livre nas faces dos polígonos η_j^{n+1} pode ser computada a partir de $\eta_{p(j,1)}^{n+1}$ e $\eta_{p(j,2)}^{n+1}$ por diferentes critérios (máximo, mínimo, *upwind*):

$$H_j^{n+1} = max[0, h_j + \eta_{p(j,1)}^{n+1}, h_j + \eta_{p(j,2)}^{n+1}] \tag{7.27}$$

7.2.4 Método de Newton para Solução dos Níveis

O algoritmo de secagem e inundação proposto por Casulli (2009) leva à formação de um sistema moderadamente não-linear (Eq. 7.25) para a elevação da superfície livre η^{n+1}. A não-linearidade reside na definição da volume $V(\eta^{n+1})$. Este sistema deve ser solucionado a cada passo de tempo de maneira eficiente e que garanta a existência de uma solução única e fisicamente compatível, i.e., $V(\eta^{n+1}) > 0 \quad \forall i \in \Omega$. Para tanto, a Equação (7.25) deve ser primeiro escrita na forma matricial:

$$\mathbf{V}(\zeta) + \mathbf{T}\zeta = \mathbf{b} \tag{7.28}$$

onde:

$$\zeta = \begin{bmatrix} \eta_1^{n+1} \\ \eta_2^{n+1} \\ \vdots \\ \eta_{N_\eta}^{n+1} \end{bmatrix}, \quad \mathbf{V}(\zeta) = \begin{bmatrix} V_1(\zeta_1) \\ V_2(\zeta_2) \\ \vdots \\ V_{N_\eta}(\zeta_{N_\zeta}) \end{bmatrix},$$

A matriz $\mathbf{T}$ é esparsa e simétrica, com dimensão $N_\eta x N_\eta$, e surge a partir do segundo termo do lado esquerdo da Equação (7.25) e o vetor $\mathbf{b}$, com N_η elementos dado pelo lado direito da Equação (7.25). Podemos assumir que $N_\eta = N_p$ e que a matriz $\mathbf{T}$ é irredutível. Isto pode não ser o caso quando, a qualquer passo de tempo, dois ou mais sub-domínios, não-conectados, estejam inundados. Nesta circunstância, as considerações a seguir são válidas para cada sub-domínio em separado, onde a respectiva matriz $\mathbf{T}$ é irredutível.

O i-ésimo elemento da diagonal principal da matriz $\mathbf{T}$ é o coeficiente de η_i^{n+1} na Equação (7.25) dado por:

$$t_{i,i} = g\theta^2 \Delta t^2 \sum_{l=1}^{N_s} \frac{s_{i,l}\lambda_{j(i,j)}}{\delta_{j(i,l)}} \left[(\mathbf{\Delta Z})^T \mathbf{A}^{-1} \mathbf{\Delta Z} \right]_{j(i,l)}^n \tag{7.29}$$

Os possíveis elementos não-nulos fora da diagonal principal, em cada linha da matriz $\mathbf{T}$, são os coeficientes de $\eta_{n(i,j)}^{n+1}$ na Equação (7.25) dados por:

$$t_{i,n(i,l)} = -g\theta^2 \Delta t^2 \frac{s_{i,l}\lambda_{j(i,j)}}{\delta_{j(i,l)}} \left[(\mathbf{\Delta Z})^T \mathbf{A}^{-1} \mathbf{\Delta Z} \right]_{j(i,l)}^n \tag{7.30}$$

Desta forma, desde que $H \geq 0$, temos que $t_{i,n(i,l)} \leq 0$, para todo $l = 1, 2, ..., N_s$. Além disso, como $\mathbf{T}$ é irredutível para cada $i = 1, 2, ..., N_p$, ao menos um $t_{i,n(i,l)}$ é não-nulo. Consequentemente, $t_{i,i} > 0$.

A partir das considerações acima, podemos concluir que $\mathbf{T}$ é uma matriz irredutível, simétrica e positiva semi-definida de forma que $t_{i,i} > 0$ para cada "i" e $t_{i,j} \leq 0$ sempre que $i \neq j$. Além disso, $\sum_{j=1}^{N_p} t_{i,j} = 0$, com $i = 1, 2, ..., N_p$, e $\sum_{i=1}^{N_p} (T\zeta)_i = 0$ para qualquer vetor ζ. Finalmente, para qualquer matriz diagonal não-nula $\mathbf{P}$, com $\mathbf{P} \geq 0$, temos que $\mathbf{P} + \mathbf{T}$ é uma matriz irredutível e simétrica. Logo, $\mathbf{P} + \mathbf{T}$ é positiva definida e $(\mathbf{P} + \mathbf{T})^{-1} > 0$.

A Equação (7.21) implica na conservação do volume total de água, i.e., $\sum_{i=1}^{N_p} V_i(\eta_i^{n+1}) = \sum_{i=1}^{N_p} V_i(\eta_i^n)$. Contudo, quando nos deparamos com situações onde perdas e ganhos são considerados e/ou na presença de contornos abertos, onde o fluxo é especificado como uma condição de contorno, o novo volume total é dado por $\sum_{i=1}^{N_p} V_i(\eta_i^{n+1}) = \sum_{i=1}^{N_p} b_i$, e inclui o volume de água no passo de tempo anterior mais ou menos o volume total de água entrando ou saindo de Ω durante o passo de tempo Δt. Neste caso $\sum_{i=1}^{N_p} b_i = 0$ é um requerimento para que o sistema (7.28) seja

fisicamente e matematicamente compatível. Logo, uma solução única é garantida de existir quando o problema é corretamente proposto (Brugnano & Casulli, 2008, 2009; Casulli, 2009).

No caso onde a elevação da superfície livre é especificada como condição de contorno, a correspondente Equação (7.25) são removidas do sistema e a correspondente matriz $\mathbf{T}$ é positiva definida. Consequentemente, a inequalidade $\sum_{i=1}^{N_p} b_i > 0$ não é necessária para demonstrar a existência e unicidade da solução do sistema (7.28).

Um algoritmo eficiente, baseado no método de Newton, para a solução do sistema (7.28) é dado por:

$$\zeta^{m+1} = \zeta^m - [\mathbf{P}(\zeta^m) + \mathbf{T}]^{-1}[\mathbf{V}(\zeta^m) + \mathbf{T}\zeta^m - \mathbf{b}], \quad m = 0, 1, 2, ... \tag{7.31}$$

onde m denota agora o índice da iteração (não confundir com passo de tempo) e $\mathbf{P}(\zeta^m)$ é uma matriz diagonal cujos elementos da diagonal são as áreas molhadas de cada elemento.

Sempre que $\mathbf{P}(\eta^n) \neq 0$, a idealização $\mathbf{P}(\zeta^0)$ é trivialmente satisfeita ao se escolher $\zeta^0 = \eta^n$ como chute inicial. Neste caso, apenas um, ou um finito número de iterações, será suficiente para resolver o sistema (7.28). No caso onde não ocorra secagem e inundação no domínio Ω entre os passos de tempo n e $n+1$, usando $\zeta^0 = \eta^n$ como chute inicial, temos $\mathbf{P}(\zeta) = \mathbf{P}(\zeta^0)$, e a solução exata do sistema (7.28) é encontrada com apenas uma iteração (Casulli, 2009). Uma vez que $\mathbf{P}(\zeta^m) + \mathbf{T}$ é uma matriz simétrica, a solução em cada iteração em (7.31) pode ser realizada utilizando um algoritmo de gradientes conjugados precondicionado.

No caso onde a elevação da superfície livre é dada como condição de contorno, a matriz $\mathbf{T}$ resultante é positiva definida. Neste caso a idealização $\sum_{i=1}^{N_p} b_i > 0$ pode ser removida e a convergência do esquema iterativo (7.31) é garantida com qualquer condição inicial. Além disto, com a simplificação que a batimetria em cada célula é constante, os volumes de água são dados por $V_i(\zeta_i) = A_i \max(0, h_i + \zeta_i)$ e o sistema (7.28) se torna linear. Neste caso, é comprovado que o algoritmo de Newton irá convergir em um número finito de iterações (Brugnano & Casulli, 2008, 2009).

7.3 Esquema Euleriano-Lagrangiano

A partir da discretização semi-implicita em diferenças finitas das Equações (7.9)-(7.11), um operador explícito $\mathbf{F}u^n_{j,k}$ foi definido. Este termo leva em conta a aceleração de Coriolis, as componentes atmosférica e baroclínica da pressão, e os termos advectivos e viscosos. Nesta seção, será descrita a solução numérica utilizada para este operador.

De uma maneira geral, podemos escrever os termos componentes do operador

F da seguinte maneira:

$$\mathbf{F}u = \frac{D\mathbf{u}_h}{Dt} = \mathbf{R}_h \tag{7.32}$$

onde $D/Dt = \partial/\partial t + \mathbf{u}_h.\nabla$ é a derivada total que leva em conta apenas os fluxos advectivos e $\mathbf{R}_h$ é um operador de reação levando em conta o efeito de Coriolis, as componentes atmosférica e baroclínica da pressão e os termos viscosos da equação de quantidade de movimento. Uma discretização semi-Lagrangiana em diferenças finitas de (7.32) para computar a evolução da velocidade normal, $u_{j,k}$, na face "j" é dada por:

$$u_{j,k}^{n+1} = u_{j,k}^{-} + \Delta t R_j \tag{7.33}$$

onde $R_j = \mathbf{n}_j.\mathbf{R}_h$ e $\mathbf{n}_j$ é o vetor normal à face "j". O segundo termo do lado direito da Equação (7.33) é discretizado no baricentro da face "j", configurando uma simplificação Euleriana-Lagrangiana do tradicional método semi-Lagrangiano. Para cada passo de tempo, a componente normal do vetor velocidade ao final da trajetória, $u_{j,k}^{-}$, é obtido via interpolação na localização espacial $\mathbf{x}_j^{-}$, que é definido como o ponto final da trajetória Lagrangiana obtida pela integração para trás no tempo:

$$\mathbf{x}_j^{-} = \mathbf{x}_j - \int_{t^n}^{t^{n+1}} \mathbf{u}^n(\mathbf{x}(t))dt \tag{7.34}$$

onde o índice de passo de tempo em $\mathbf{x}_j$ foi ignorado uma vez que esta localização é fixa no tempo. Empregando uma integração de primeira ordem baseada no método de Euler resulta em:

$$\mathbf{x}_j^{-} = \mathbf{x}_j - \Delta t \mathbf{u}_j^n \tag{7.35}$$

onde $\mathbf{u}_j^n = \mathbf{u}^n(\mathbf{x}_j)$ é o vetor velocidade na face "j" e no tempo n. Portanto, o campo de velocidades no passo de tempo n é necessário tanto para o cálculo de $\mathbf{x}_j^{-}$ quanto para interpolar $\mathbf{u}_j^n$ na localização $\mathbf{x}_j^n$, e a discretização usada em (7.35) é de primeira ordem. A integração, ou cálculo da trajetória, necessita de uma interpolação para encontrar $\mathbf{u}^n(\mathbf{x})$ independente do método numérico.

Casos onde o Número de Courant é estimado como maior que um, a integração pode ser dividida em N sub-intervalos, desde que $\Delta t' = \Delta t/N$. O valor de N é escolhido de forma que $\Delta t'|U^n|$ seja sempre menor que um. Esta condição garante que consistência, uma vez que as linhas de trajetória não irão atravessar fronteiras sólidas (Casulli, 1990; Cheng et al., 1993). Caso o valor de N seja maior que um, se faz necessário interpolar $\mathbf{u}^n(\mathbf{x})$ a cada sub-intervalo de integração.

A interpolação vertical pode ser realizada utilizando uma interpolação linear simples (de primeira ou segunda ordem) no plano z, o que não limita a precisão ou a estabilidade do método. Em resumo, os passos necessários para se determinar a velocidade ao final da trajetória de integração, $u_{j,k}^*$ e $v_{j,k}^*$, são (Wang et al., 2011):

1. aproximar o vetor velocidade na face "j" para obter $\mathbf{u}_j^n$. Uma vez que a Equação (7.18) computa apenas $u_{j,k}^n$, a componente tangencial da velocidade

na face "j", $v^n_{j,k}$, deve ser estimada para se obter $\mathbf{u}^n_j = v^n_{j,k}.\mathbf{n}_j + u^n_{j,k}.\mathbf{t}_j$ (ver Fig. 7.5);

2. Computar a localização da trajetória, $\mathbf{x}^-_j$. Caso apenas um sub-intervalo de integração seja utilizado, a localização pode ser computada de maneira direta usando a Equação (7.35). Caso mais de um sub-intervalo de integração seja utilizado, o vetor velocidade deve ser interpolado a cada passo de integração;

3. Interpolar para obter as componentes do vetor velocidade na localização $\mathbf{x}^-_j$, i.e., $\mathbf{u}^-_j$. A componente normal para utilizar na Equação (7.33) é então obtida utilizando $u^-_{j,k} = \mathbf{n}_j.\mathbf{u}^-_j$

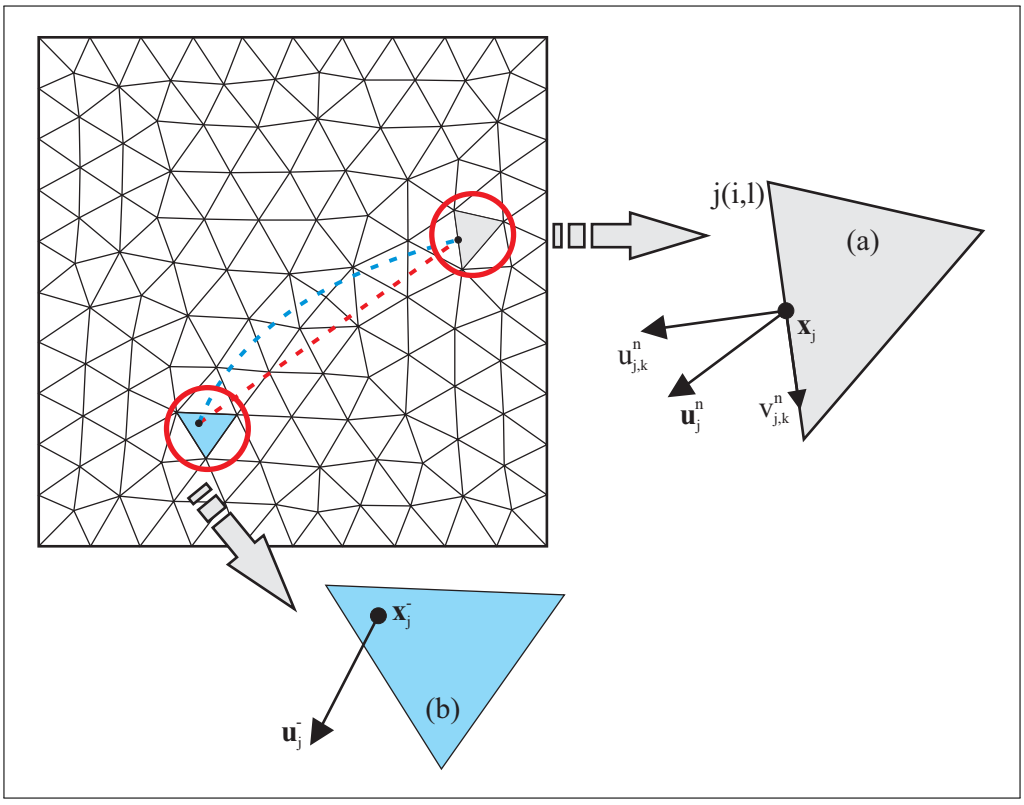

Figura 7.5: Ilustração de duas trajetória Lagrangianas. Em vermelho, trajetória com apenas um intervalo de integração. Em azul, trajetória com mais de um sub-intervalo de integração. No polígono (a) é mostrado o vetor velocidade $\mathbf{u}^n_j$ com suas componentes normal $u^n_{j,k}$ e tangencial $u^n_{j,k}$ na localização de partida $\mathbf{x}_j$ para a face $j(i,l)$. O polígono (b) mostra o vetor velocidade $\mathbf{u}^-_j$ na localização de chegada $\mathbf{x}^-_j$, após a integração da trajetória.

7.3.1 Métodos de Interpolação

Existem diversas formas de se estimar as velocidades nodais ($\mathbf{u}_p$) e tangenciais (v_j) a partir das velocidades normais (u_j). A velocidade nodal (ou seja, nos vértices) é estimada utilizado um método baseado na média ponderada pela área de cada elemento na vizinhança de Voronoi do vértice, i.e., elementos $T_1, T_2, ...T_6$ (Fig. 7.6-(a)). Para cada vizinho de Voronoi, a velocidade nodal é computada utilizando o método de baixa ordem de Raviart-Thomas (ver Walters et al., 2009; Wang et al., 2011, para maiores detalhes). De posse das velocidades nodais em cada vértice do domínio Ω, a componente tangencial pode ser computada a partir de uma média ponderada pela área usando as velocidades nodais nos dois vértices da face "j" (Fig. 7.6-(b)). O vetor velocidade é então computado utilizando $\mathbf{u}_j^n = v_{j,k}^n.\mathbf{n}_j + u_{j,k}^n.\mathbf{t}_j$. De posse das velocidades nas faces e vértices do polígono, a velocidade numa localização qualquer, dentro do polígono, é computada utilizando uma interpolação quadrática (Fig. 7.6-(c)), dada por (Huebner et al., 2011):

$$\begin{aligned}\mathbf{u}(x,y) = (2A_{23}-1)A_{23}\mathbf{u}_{p,1} + (2A_{13}-1)A_{13}\mathbf{u}_{p,2} + (2A_{12}-1)A_{12}\mathbf{u}_{p,3} \\ + 4A_{13}A_{23}\mathbf{u}_{e,4} + 4A_{12}A_{13}\mathbf{u}_{e,5} + 4A_{12}A_{23}\mathbf{u}_{e,6}\end{aligned} \tag{7.36}$$

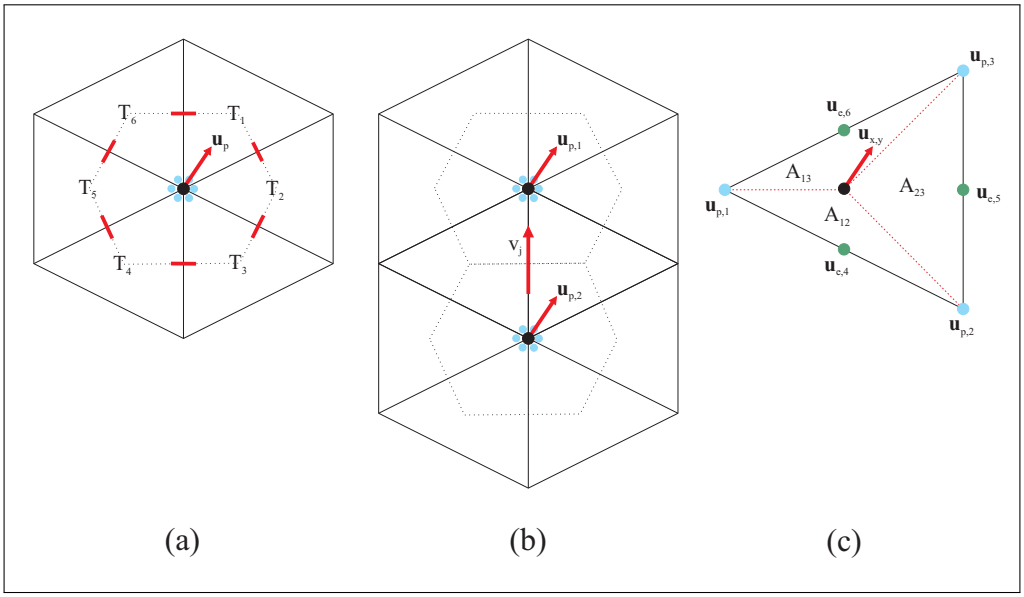

Figura 7.6: Conjunto de elementos utilizados ao computar as velocidades nos vértices (a), nas faces (b) e numa localização aleatória dentro do elemento (c). Pequenas linhas vermelhas indicam as velocidades normais utilizadas e linhas tracejadas pretas indicam os vizinhos de Voronoi. Linhas tracejadas vermelhas indicam os sub-elementos utilizados para a interpolação quadrática.

7.3.2 Solução dos termos Reativos

Os termos reativos da Eq. 7.33 (a saber: fluxos viscosos, efeito de Coriolis e componente baroclínica da pressão) são computados utilizando um esquema explícito de diferenças finitas. A solução numérica destes termos é a fonte das restrições ao passo de tempo na solução hidrodinâmica dos modelos TRIM (grade estruturada) e UnTRIM (grade não-estruturada). O efeito de Coriolis é computado utilizando uma solução baseada em diferenças finitas e levando em conta o ponderador temporal θ. O valor de $\mathbf{F}u_{j,k}$ calculado a partir da solução Euleriana-Lagrangiana (ELM) é então atualizado como:

$$\mathbf{F}u_{j,k} = \overbrace{u^*_{j,k}}^{\text{ELM}} + \underbrace{\frac{\left[1-\theta\left(1-\theta\right)f^2\Delta t^2\right]u^*_{j,k} + f\Delta t v^*_{j,k}}{1+\left(\theta f\Delta t\right)^2}}_{\text{Coriolis}} \tag{7.37}$$

onde $f = 2\Omega\sin(\Phi)$ é o efeito de Coriolis, Ω é a velocidade angular da Terra sobre seu eixo e Φ é a latitude; $u^*_{j,k}$ é a componente horizontal da velocidade normal a j-ésima face da malha computacional e $v^*_{j,k}$ é a velocidade tangencial na mesma face. Estas componentes (normal e tangencial) são computadas ao final da trajetória Lagrangiana a partir dos valores de velocidades adjacentes.

A componente baroclínica da pressão é discretizada utilizando uma solução explícita de diferenças finitas em cada face da malha computacional, sendo o operador $\mathbf{F}u_{j,k}$ atualizado da seguinte forma:

$$\mathbf{F}u_{j,k} = \overbrace{\mathbf{F}u^*_{j,k}}^{\text{ELM + Coriolis}} \underbrace{- g\frac{\Delta t}{\delta_j\rho_0}\sum_{l=k}^{M_j}\omega_l\left[\rho^n_{p(j,2),l} - \rho^n_{p(j,1),l}\right]\Delta z^n_{j,l}}_{\text{Pressão Baroclínica}} \tag{7.38}$$

O fluxo viscoso na solução do operador $\mathbf{F}u_{j,k}$ é computado seguindo as definições propostas em Cheng et al. (1984). Considerando um forma geral da equação de transporte sem termos reativos, temos:

$$\frac{\partial\varphi}{\partial t} + \mathbf{u}\cdot\nabla\varphi = \nabla\cdot\left(D\nabla\varphi\right) \tag{7.39}$$

onde φ é uma substância sendo transportada; D é um coeficiente de dispersão/difusão; e $\mathbf{u}$ é um campo de velocidades conhecido. Eq. 7.39 pode ser escrita numa forma Lagrangiana similar a Eq. 7.33 como:

$$\frac{D\varphi}{Dt} = \nabla\cdot\left(D\nabla\varphi\right) \tag{7.40}$$

Considerando agora um sistema de "coordenadas naturais" baseadas na linha de corrente, ou trajetória, da partícula e sua componente normal num dado ponto 0 (Fig. 7.7).

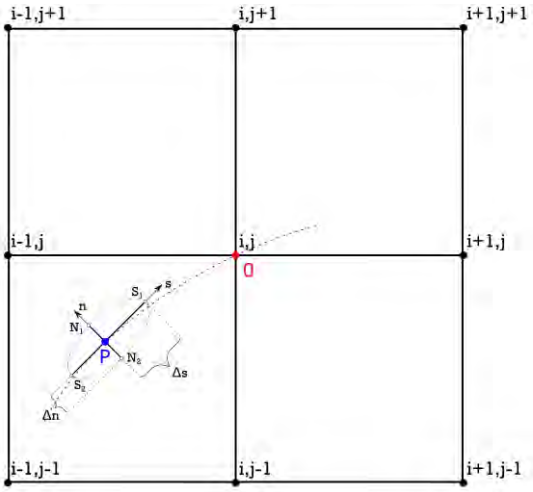

Figura 7.7: Relação entre as coordenadas naturais (s,n) e as coordenadas cartesianas (x,y). Adaptado de Cheng et al. (1984).

Por definição, um ponto P localizado nesta trajetória irá passar pelo ponto 0 com o passar do tempo. Se assumirmos também que o eixo principal do tensor dispersão está alinhado com os eixos da trajetória e normal, em cada ponto da trajetória a Eq. 7.40 pode ser escrita como:

$$\frac{D\varphi}{Dt} = \frac{\partial}{\partial s}\left(D_s \frac{\partial \varphi}{\partial s}\right) + \frac{\partial}{\partial n}\left(D_n \frac{\partial \varphi}{\partial n}\right) \tag{7.41}$$

onde s e n são as coordenadas na direção normal e na direção da trajetória; D_s e D_n são os coeficientes de dispersão na direção normal e na direção da linha de corrente. A solução dos fluxos advectivos foi mostrada em detalhes anteriormente, logo não será considerada aqui. Levando em conta apenas os termos de dispersão na Eq. 7.41, considerando D_s e D_n constantes e utilizando uma discretização explícita a partir do método das diferenças finitas centradas, temos:

$$D_s \frac{\varphi^*(S_1) - 2\varphi^*(P) + \varphi^*(S_2)}{(\Delta s)^2} + D_n \frac{\varphi^*(N_1) - 2\varphi^*(P) + \varphi^*(N_2)}{(\Delta n)^2} \tag{7.42}$$

onde Δs e Δn são os espaçamentos nas direções s e n, respectivamente; e S_1, S_2, N_1 e N_2 são os pontos definidos pela Fig. 7.7. Combinando a Eq. 7.42 com a Eq. 7.38, resulta na forma final do operador $\mathbf{F}$ utilizado na solução hidrodinâmica do modelo TRIM/UnTRIM:

$$\begin{aligned} \mathbf{F}u_{j,k} = \mathbf{F}u^*_{j,k} + & \quad \left[\frac{\Delta t D_s}{\delta_j^2}\right]\left[u^*_{j,k}(S_1) - 2u^*_{j,k}(P) + u^*_{j,k}(S_2)\right] \\ + & \quad \left[\frac{\Delta t D_n}{\lambda_j^2}\right]\left[u^*_{j,k}(N_1) - 2u^*_{j,k}(P) + u^*_{j,k}(N_2)\right] \end{aligned} \tag{7.43}$$

onde $\mathbf{F}u^*_{j,k}$ leva em conta o fluxo advectivo (ELM), o efeito de Coriolis, e a componente Baroclínica da pressão. Ainda, os pontos S_1, S_2, N_1 e N_2 são agora definidos como o baricentro dos elementos dividindo a j-ésima face (S_1 e S_2) e os vértices desta mesma face (N_1 e N_2), como mostrado na Fig. 7.8.

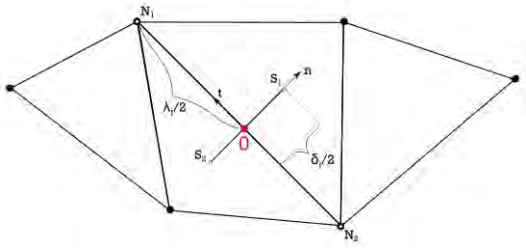

Figura 7.8: Calculo dos pontos S_1, S_2, N_1 e N_2 utilizando um sistema alinhado com a "j-ésima" face da malha computacional.

7.4 Transporte de Escalares

O transporte de substâncias escalares (e.g., temperatura, salinidade, biomassa) é realizado utilizando uma versão modificada da Equação (7.6). Esta alteração é necessária uma vez que o modelo hidrodinâmico altera as espessuras das células, $\Delta z^n_{i,k}$, para levar em conta a dinâmica da superfície livre η^n_i (Gross et al., 1998). A Equação de transporte de escalares, ponderada pela profundidade, é dada de maneira compacta da seguinte forma:

$$\frac{\partial HC}{\partial t} + \nabla \cdot (\mathbf{u}HC - \mathbf{\Gamma}\nabla(HC)) = S_C \tag{7.44}$$

onde $\mathbf{u} = \mathbf{u}(\mathbf{x}, t)$ é o vetor velocidade e $H = H(\mathbf{x}, t)$ é a profundidade total da água, ambos oriundos do modelo hidrodinâmico (Casulli & Walters, 2000); Γ é o tensor difusividade, aqui dado como uma matriz diagonal $\mathbf{\Gamma} = (K^h_x, K^h_y, K^v_z)$ e S_C é um termo de perdas e ganhos, capaz de englobar processos específicos de geração/consumo da substância transportada.

Assumindo que a Equação (7.44) é computada *off-line*, ou seja, após o cálculo do campo de velocidades e níveis, e integrando a mesma sobre um domínio computacional Ω formado por triângulos T_i, num intervalo de tempo $[t^n, t^{n+1}]$, e utilizando o Teorema de Gauss, resulta a seguinte equação:

$$\int_{t^n}^{t^{n+1}} \int_{T_i} \frac{\partial HC}{\partial t}\, d\mathbf{x}\, dt + \int_{t^n}^{t^{n+1}} \int_{\partial T_i} (\mathbf{u}HC - \mathbf{\Gamma}\nabla(HC)) \cdot \mathbf{n}\, dS\, dt = \int_{t^n}^{t^{n+1}} \int_{T_i} S_C\, d\mathbf{x}\, dt \tag{7.45}$$

onde ∂T_i é o contorno do volume de controle T_i e $\mathbf{n}$ é o vetor unitário normal no contorno (direção de dentro para fora do contorno). Usando as definições:

$$V_i^n = \int_{T_i} H(\mathbf{x}, t^n)\, d\mathbf{x},$$
$$C_i^n = \frac{1}{V_i^n} \int_{T_i} C(\mathbf{x}, t^n)\, H(\mathbf{x}, t^n)\, d\mathbf{x}, \qquad \text{e}$$
$$F_{ij} = \frac{1}{\Delta t} \int_{t^n}^{t^{n+1}} \int_{\partial T_{ij}} (\mathbf{u} HC - \mathbf{\Gamma} \nabla (HC)) \cdot \mathbf{n}_{ij}\, dS\, dt,$$

onde ∂T_{ij} é definido como o segmento, ou face, do elemento de contorno T_i que é partilhada com o elemento vizinho T_j, e onde $\mathbf{n}_{ij}$ é o vetor unitário associado a esta face, com direção de T_i a T_j, uma discretização em *Volume Finito* (7.45) com *passo de tempo global* é dada por:

$$V_i^{n+1} C_i^{n+1} = V_i^n C_i^n - \Delta t \sum_{l=1}^{N_s} \lambda_{i,j(i,l)} F_{i,j(i,l)} + \Delta t S_C \tag{7.46}$$

onde o comprimento do segmento ∂T_{ij} é tomado como $\lambda_{i,j}$. O índice n indica o passo de tempo, $\Delta t = t^{n+1} - t^n$ é o passo de tempo *global* e F_{ij} é o fluxo numérico. O termo de perdas e ganhos pode obter um tratamento explícito, no caso de reações suaves (*smooth*), ou implícito no caso de reações rápidas (*stiff*). Em três dimensões, a Equação (7.46) pode ser reescrita como:

$$A_i \Delta z_{i,k}^{n+1} C_{i,k}^{n+1} = A_i \Delta z_{i,k}^n C_{i,k}^n - \Delta t \sum_{l=1}^{N_s} \lambda_{i,j(i,l)} F_{i,k,j(i,l)} + \Delta t S_{C\,i,k} \tag{7.47}$$

onde agora N_S deve levar em conta também os fluxos verticais entrando e saindo do elemento T_i. Diferentes métodos podem ser utilizados para avaliar o fluxo numérico na interface entre elementos em esquemas de volumes finitos. Para o cálculo deste fluxo, será utilizada uma formulação baseado no esquema *Upwind*:

$$\begin{aligned} F_{ij} &= F_{ij}((C_{ij}^-, \nabla C_{ij}^-), (C_{ij}^+, \nabla C_{ij}^+)) = \\ &\quad \frac{1}{2}\left((H_j^n u_j^{n+\theta})(C_{ij}^+ + C_{ij}^-) - \Gamma_j^n (\nabla C_{ij}^+ + \nabla C_{ij}^-)\right) \\ &- \frac{1}{2}\left(\left|H_j^n u_j^{n+\theta}\right| + 2\varphi \left|\Gamma_j^n\right|\right)\left(C_{ij}^+ - C_{ij}^-\right), \end{aligned} \tag{7.48}$$

onde H_j^n é a profundidade de água e $u_j^{n+\theta 1}$ é a velocidade e Γ_j^n é a difusividade no contorno do elemento, respectivamente. Na vertical, o componente advectivo

[1] $u^{n+\theta} = \theta u^{n+1} + (1-\theta) u^n$

do fluxo é calculado utilizando a respectiva velocidade vertical $w_{i,k}^{n+\theta}$. Note que H_j^n, $u_j^{n+\theta}$ e $w_{i,k}^{n+\theta}$ são disponibilizados pela solução hidrodinâmica e os índices são consistentes com a discretização da Equação da Continuidade (Eq. 7.21), resultando em conservação exata da massa no sistema (Casulli & Zanolli, 2005; Gross et al., 2002). C_{ij}^+ e C_{ij}^- são *valores reconstruídos na interface* do contorno ∂T_{ij} a partir da esquerda e direita, respectivamente. Estes valores podem ser aproximados utilizando valores medianos *contantes*, i.e., tomando $C_{ij}^+ = C_j^n$ e $C_{ij}^- = C_i^n$, resultando num esquema clássico de primeira ordem de *Godunov* (Toro, 2009). Outra aproximação é estimar estes valores utilizando uma reconstrução *espaço-temporal* linear dentro de cada elemento, resultando num esquema de segunda ordem do tipo *MUSCL* (van Leer, 1974).

7.4.1 Método MUSCL em grades não-estruturadas

Para simplificar a descrição do algoritmo, será apresentado primeiro a reconstrução de 2ª ordem do método MUSCL num contexto de passo de tempo *global*, onde o passo de tempo global é definido por $\Delta t = t^{n+1} - t^n$. O método MUSCL de van Leer (van Leer, 1979) é um solução precisa e robusta para leis de conservação, incluindo casos onde a solução exibe choques, descontinuidades ou grandes gradientes. A principal ideia é melhorar a reconstrução constante utilizada no esquema de primeira ordem de Godunov por uma reconstrução linear dos valores na interface, visando atingir uma maior ordem de precisão.

Ao contrário de ser utilizada apenas um valor contante na interface, os valores usados em cada elemento que divide a face "j" é aproximado usando uma reconstrução (ou interpolação) linear em ambos, espaço e tempo. Esta aproximação, também conhecida como método de MUSCL-Hancock (Toro, 2009), resulta na seguinte equação:

$$C_i(\mathbf{x}, t) = C_i^n + \nabla C_i^n \cdot (\mathbf{x} - \mathbf{x}_i) + \partial_t C_i^n \, (t - t^n), \tag{7.49}$$

onde o baricentro da célula T_i é representado por $\mathbf{x}_i$, C_i^n é o valor médio no elemento no passo de tempo t^n, ∇C_i^n é o gradiente espacial, que ainda precisa ser computado, e $\partial_t C_i^n$ é a primeira derivada com relação ao tempo, que pode ser diretamente computada a partir da EDP em sua forma primitiva uma vez que o gradiente ∇C_i^n é conhecido da seguinte maneira:

$$\partial_t C_i^n = -\mathbf{u}_i^n \cdot \nabla C_i^n . + \nabla \cdot (\mathbf{\Gamma_i^n} \cdot \nabla C_i^n) \tag{7.50}$$

onde $\mathbf{u}_i^n$ e $\mathbf{\Gamma}_i^n$ são definidos como o vetor velocidade e o tensor difusividade no baricentro do elemento T_i, respectivamente, ambos providos pela solução hidrodinâmica.

De acordo com o teorema de Godunov (Godunov, 1959), não há esquemas melhores que esquemas *lineares* de primeira ordem para equações de advecção, portanto esquemas lineares de alta ordem irão gerar soluções espúrias na vizinhança de grandes gradientes e descontinuidades. Visando evitar esta restrição, um esquema de alta ordem deve ser *não-linear*. Tendo isto em vista, nós utilizamos um *limitador de gradiente* não-linear, Φ_i, que é aplicado ao gradiente não limitado $\tilde{\nabla} C_i^n$ seguindo os procedimentos descritos por Barth e Jespersen em seu trabalho pioneiro (Barth & Jespersen, 1989). Em detalhes, deve-se primeiro computar um gradiente *não-limitado* $\tilde{\nabla} C_i^n$ a partir da equação:

$$\tilde{\nabla} C_i^n = \frac{1}{|T_i|} \sum_{j \in \mathcal{N}_i} \frac{1}{2} \left(C_i^n + C_j^n \right) \mathbf{n}_{ij}, \qquad \text{with} \qquad |T_i| = \int_{T_i} d\mathbf{x}. \tag{7.51}$$

A partir deste gradiente não-limitado, uma reconstrução espacial *preliminar* é dada por:

$$\tilde{C}_i(\mathbf{x}, t^n) = C_i^n + \tilde{\nabla} C_i^n \cdot (\mathbf{x} - \mathbf{x}_i). \tag{7.52}$$

De maneira alternativa, o calculo do gradiente pode ser realizado utilizando uma lei de conservação integral do polinômio espacial preliminar $\tilde{C}_i(\mathbf{x}, t)$ num *conjunto* de reconstrução $\mathcal{S}_i$ que consiste do elemento T_i e seus vizinhos diretos. A reconstrução correspondente é dada por:

$$\frac{1}{|T_j|} \int_{T_j} \tilde{C}_i(\mathbf{x}, t) d\mathbf{x} = C_j^n, \qquad \forall T_j \in \mathcal{S}_i. \tag{7.53}$$

O sistema de equações resultante (7.53) pode ser solucionado com um algoritmo de mínimos quadrados *restrito* (Dumbser et al., 2007), onde a restrição é dada pela necessidade de que o princípio da conservação (7.53) seja satisfeito para um dado elemento T_i.

A principal ideia do limitador de gradiente de Barth e Jespersen (Barth & Jespersen, 1989) é satisfazer o princípio do máximo discreto (do inglês: *discrete maximum principle*), isto é, encontrar o maior valor admissível para Φ_i para o qual os valores das variáveis reconstruídas (ou interpoladas) não exceda o valor máximo ou o mínimo encontrados no conjunto $\mathcal{S}_i = T_i \cup \mathcal{N}_i$. Então, é necessário calcular o valor máximo e o valor mínimo de C_i^n no conjunto $\mathcal{S}_i$ como:

$$C_i^{\min} = \min_{j \in \mathcal{S}_i} \left(C_j^n \right) \qquad \text{e} \qquad C_i^{\max} = \max_{j \in \mathcal{S}_i} \left(C_j^n \right). \tag{7.54}$$

Uma vez que é necessário que o polinômio utilizado para reconstrução permaneça entre os limites máximo e mínimo:

$$C_i^{\min} \leq C_i(\mathbf{x}, t^n) \leq C_i^{\max}, \tag{7.55}$$

o gradiente $\tilde{\nabla} C_i^n$ é modificado de forma que (7.55) seja satisfeita. Para reconstruções lineares, os valores extremos contidos num elemento triangular ocorrem nos vértices do triângulo (Barth & Jespersen, 1989). Ao longo do texto, iremos denotar o conjunto de vértices do elemento T_i como $\mathcal{V}_i$. Desta forma, para cada coordenada do vértice $\mathbf{X}_k$ do elemento T_i com $k \in \mathcal{V}_i$, é computado os valores nos vértices $\tilde{C}_i(\mathbf{X}_k, t^n)$ a partir de (7.52) utilizando o gradiente *não-limitado* $\tilde{\nabla} C_i^n$ para determinar o valor $\bar{\Phi}_{i,k}$ como segue:

$$\bar{\Phi}_{i,k} = \begin{cases} \min\left(1, \frac{C_i^{\max} - C_i^n}{\tilde{C}_i(\mathbf{X}_k, t^n) - C_i^n}\right), & \text{if } \tilde{C}_i(\mathbf{X}_k, t^n) - C_i^n > 0, \\ \min\left(1, \frac{C_i^{\min} - C_i^n}{\tilde{C}_i(\mathbf{X}_k, t^n) - C_i^n}\right), & \text{if } \tilde{C}_i(\mathbf{X}_k, t^n) - C_i^n < 0, \\ 1, & \text{if } \tilde{C}_i(\mathbf{X}_k, t^n) - C_i^n = 0. \end{cases} \tag{7.56}$$

A partir destes valores $\bar{\Phi}_{i,k}$ o valor do limitador de gradiente é obtido como $\Phi_i = \min_{k \in \mathcal{V}_i} \left(\bar{\Phi}_{i,k}\right)$. Após os cálculos de Φ_i, é obtido o gradiente limitado como:

$$\nabla C_i^n = \Phi_i \tilde{\nabla} C_i^n, \tag{7.57}$$

a partir do qual é possível calcular também a derivada temporal $\partial_t C_i^n$ de acordo com (7.50). Os valores reconstruídos C_{ij}^- e C_{ij}^+ utilizado para calcular o fluxo numérico (7.48) são então dados por:

$$C_{ij}^- = C_i(\mathbf{x}_{ij}, t^{n+\frac{1}{2}}), \qquad C_{ij}^+ = C_j(\mathbf{x}_{ij}, t^{n+\frac{1}{2}}), \tag{7.58}$$

onde $\mathbf{x}_{ij}$ é a coordenada do baricentro da face ∂T_{ij} compartilhada entre os elementos T_i e T_j e o passo de tempo intermediário é dado por $t^{n+\frac{1}{2}} = t^n + \frac{1}{2}\Delta t$. Na presença de termos viscosos, os mesmos podem ser levados em conta dentro do limitador de gradiente, seguindo as ideias de Casulli & Zanolli (2005) no contexto de limitadores de fluxos viscosos. A fim de garantir monotonicidade da solução discretizada, o limitador (7.56) e (7.57) devem ser aplicadas num segundo passo, de maneira análoga, no passo de tempo t^{n+1}, o mesmo sendo computado para o gradiente temporal $\partial_t C_i^n$.

7.4.2 Passo de Tempo Localizado

Utilizando um esquema clássico de passo de tempo global (GTS, do inglês: *Global Time Stepping*), o passo de tempo global Δt é escolhido de acordo com uma condição de estabilidade *global* relacionada ao tamanho do elemento h_i, a velocidade de advecção $\mathbf{u}_i$ e aos termos viscosos $\mathbf{D}_i$ em cada elemento:

$$\Delta t^n = \text{ CFL } \min_{T_j \in \Omega} \left(\frac{h_j}{\|\mathbf{u}_j\|} + \frac{h_j^2}{2\,\|\mathbf{D}_j\|} \right), \tag{7.59}$$

onde Δt^n é o passo de tempo global; CFL $< 1/d$ é o número de Courant-Friedrichs-Lewy, d é o número de dimensões espaciais; h_j é o comprimento característico do elemento, que neste caso é tomado como o diâmetro do círculo circunscrito ao triângulo T_j; $\mathbf{u}_j$ é o vetor velocidade em T_j e $\mathbf{D}_j$ é uma matriz diagonal de difusividade em T_j. É possível observar que (7.59) é um mínimo global tomado levando em conta todos os elementos do domínio. Ao se acoplar diferentes modelos entre si, como o caso onde hidrodinâmica e qualidade de água são simulados, por exemplo, esta restrição de passo de tempo global pode se tornar muito severa, e o passo de tempo do esquema numérico explícito usado na solução da Equação de Transporte pode até limitar o passo de tempo do modelo hidrodinâmico. Nestes casos, uma metodologia de *sub-intervalos* deve ser utilizada (Casulli & Zanolli, 2005; Wang et al., 2008), visando desacoplar o passo de tempo da solução numérica explícita para o transporte do passo de tempo utilizando na solução numérica semi-implícita do modelo hidrodinâmico (Casulli & Walters, 2000).

O algoritmo de Passo de Tempo Localizado (LTS, do inglês: *Local Time Stepping*) segue as ideias apresentadas pela primeira vez no contexto do método de elementos finitos de Galerkin Descontínuo (DG, do inglês: *Discontinuous Galerkin*) (Dumbser et al., 2007; Gassner et al., 2008; Lörcher et al., 2007; Taube et al., 2009). Nestes trabalhos, foi mostrado que o algoritmo LTS converge com alta ordem de precisão em ambos, espaço e tempo. A principal diferença entre o o algoritmo utilizado neste trabalho é o uso de um operador não-linear de reconstrução, que requer informações do conjunto de elementos vizinhos. Num contexto DG não-limitado, como usado em (Dumbser et al., 2007; Taube et al., 2009), um passo de reconstrução não é necessário. Em vez de usar um único passo de tempo global (7.59) cada elemento irá computar um *passo de tempo local* seguindo uma *condição de estabilidade local*, baseada no conjunto $\mathcal{S}_i$, isto é, o elemento e seus vizinhos diretos:

$$\Delta t_i^n = \text{ CFL } \min_{T_j \in \mathcal{S}_i} \left(\frac{h_j}{\|\mathbf{u}_j\|} + \frac{h_j^2}{2\,\|\mathbf{D}_j\|} \right), \tag{7.60}$$

onde Δt_i^n é agora o *passo de tempo local*. Em conformidade, a cada elemento também será associado um *tempo local* t_i^n. Para ser mais preciso, até os índices dependem do elemento, logo $n = n(i)$, mas visando simplificar a notação, iremos desprezar a dependência explícita de n no número do elemento, i.

Um algoritmo de passo de tempo local não é organizado em passos de tempo, mas nos chamados ciclos. Em cada ciclo, deve-se percorrer todos os elementos no domínio e verificar um chamado *critério de atualização* ou *condição de evolução* Dumbser et al. (2007); Lörcher et al. (2007), isto é, um elemento é atualizado se, e somente se, a seguinte condição for satisfeita:

$$t_i^n + \Delta t_i^n \leq t_j^n + \Delta t_j^n, \qquad \forall j \in \mathcal{N}_i. \tag{7.61}$$

Esta condição significa que o tempo futuro de um elemento deve ser menor ou igual ao tempo futuro dos elementos vizinhos e é um resultado direto do princípio da casualidade. É possível observar que o método de passo de tempo localizado apresentado aqui é *totalmente assíncrono*, onde não é necessário nenhum tipo de *sincronização* entre os elementos, a não ser a condição de evolução (7.61)dada anteriormente.

O intervalo de tempo no qual os fluxos numéricos são computados nos contornos do elemento são definidos como:

$$[t_{ij}^n, t_{ij}^{n+1}] = [\max(t_i^n, t_j^n), \min(t_i^{n+1}, t_j^{n+1}], \qquad \Delta t_{ij} = t_{ij}^{n+1} - t_{ij}^n, \qquad t_{ij}^{n+\frac{1}{2}} = \frac{1}{2}\left(t_{ij}^n + t_{ij}^{n+1}\right). \quad (7.62)$$

O esquema numérico em Volumes Finitos usando o LTS pode ser definido, para os elementos T_i que satisfazem (7.61) como:

$$V_i^{n+1} C_i^{n+1} = V_i^n C_i^n + M_i - \sum_{j \in \mathcal{N}_i} \Delta t_{ij}\, \lambda_{ij}\, F_{ij}\left(C_{ij}^-, C_{ij}^+\right), \qquad t_i^{n+1} = t_i^n + \Delta t_i^n. \quad (7.63)$$

Os valores extrapolados para as faces C_{ij}^- e C_{ij}^+ utilizados em (7.63) são computados a partir da reconstrução local espaço-temporal (7.49) como:

$$\begin{aligned} C_{ij}^- &= C_i^n + \nabla C_i^n\,(\mathbf{x}_{ij} - \mathbf{x}_i) + \partial_t C_i^n \left(t_{ij}^{n+\frac{1}{2}} - t_i^n\right), \\ C_{ij}^+ &= C_j^n + \nabla C_j^n\,(\mathbf{x}_{ij} - \mathbf{x}_j) + \partial_t C_j^n \left(t_{ij}^{n+\frac{1}{2}} - t_j^n\right). \end{aligned} \quad (7.64)$$

O termo M_i in (7.63) é a chamada *variável de memória*, que leva em conta fluxos em passos de tempo anteriores cruzando a face do elemento, isto é, a partir do tempo t_i^n ao tempo t_{ij}^n. Em prática, esta variável de memória é atualizada pelos *vizinhos* de um elemento, para garantir que o esquema seja conservativo e simples de implementar. Uma vez que o elemento é atualizado a partir da Eq. (7.63), sua própria variável de memória é reiniciada como valor nulo, e os fluxos que cruzam as fronteiras do elemento são adicionados às variáveis de memória dos seus vizinhos diretos, isto é:

$$M_i := 0, \qquad M_j := M_j + \Delta t_{ij}\, \lambda_{ij}\, F_{ij}\left(C_{ij}^-, C_{ij}^+\right). \quad (7.65)$$

O último obstáculo é como realizar a *reconstrução* do elemento T_i após ele ser atualizado no contexto do LTS, uma vez que os elementos vizinhos estão em tempos diferentes $t_j^n \neq t_i^n$. Uma vez que a reconstrução espaço-temporal (7.49) é válida dentro de todo volume de controle espaço-temporal $T_j \times [t_j^n, t_j^{n+1}]$, nós podemos em vez de utilizar (7.51), computar o gradiente não limitado $\tilde{\nabla} C_i^n$ com auxílio do preditor (7.49) nos elementos vizinhos utilizado os valores médios *virtuais* nas células, $\bar{C}_j^n$:

$$\tilde{\nabla} C_i^n = \frac{1}{|T_i|} \sum_{j \in \mathcal{N}_i} \frac{1}{2}\left(C_i^n + \bar{C}_j^n\right) \mathbf{n}_{ij}, \qquad \text{with} \qquad \bar{C}_j^n = C_j^n + \partial_t C_j^n (t_i^n - t_j^n). \quad (7.66)$$

Observe que o preditor está sempre disponível nas células vizinhas devido a condição de evolução (7.61). Após o cálculo do gradiente não-limitado a partir da Eq. (7.66), o gradiente limitado e o cálculo das derivadas temporais $\partial_t C_i^n$ são realizadas como descrito na Seção 7.4.1.

7.5 Modelo de Ecossistemas Aquáticos

7.5.1 Processos Descritos pelo Modelo

O modelo IPH-ECO pode ser utilizado de forma acoplada, onde hidrodinâmica e qualidade da água são avaliados, ou de forma separada, levando-se em conta apenas processos físicos (hidrodinâmica) ou biológicos (qualidade da água). No caso onde a simulação é realizada de forma acoplada, a solução da Equação de Transporte de Escalares (Eq. 7.6) é computada para cada parâmetro de qualidade da água simulado, alterando apenas o termo fonte em cada equação. Desta forma, o modelo é capaz de simular Temperatura da Água, dinâmica de nutrientes (e.g., C, PO_4, NH_4, NH_3, Si), gases (O_2, CO_2 e CH_4), e biomassa de comunidades aquáticas (e.g., fitoplâncton, macrófitas, peixes):

$$\frac{\partial T_{Água}}{\partial t} = \underbrace{f^{ROC}_{T_{Água}}(Alb, Rad)}_{\text{Rad. Ondas Curtas}} + \underbrace{f^{ROL}_{T_{Água}}(Nuv, T_{Ar}, T_{Água})}_{\text{Rad. Ondas Longas}} + \underbrace{f^{Evap}_{T_{Água}}(Evap)}_{\text{Evaporação}} + \underbrace{f^{Cond}_{T_{Água}}(W, T_{Ar}, T_{Água})}_{\text{Condução}} \tag{7.67}$$

$$\frac{\partial M_{Ino}}{\partial t} = \underbrace{f^{FE}_{MID}(Sed)}_{\text{Erosão}} + \underbrace{f^{FS}_{MID}(T, OD, W)}_{\text{Sedimentação}} \tag{7.68}$$

$$\begin{aligned}\frac{\partial COP}{\partial t} = &\underbrace{f^{Lise}_{COP}(\mathbf{XX})}_{\text{Lise Celular}} + \underbrace{f^{Mort}_{COP}(\mathbf{XX})}_{\text{Mortalidade}} + \underbrace{f^{Exc}_{COP}(\mathbf{XX})}_{\text{Excreção}} - \underbrace{f^{Hid}_{COP}(\mathbf{XX})}_{\text{Hidrólise}} - \underbrace{f^{CB}_{COP}(\mathbf{XX})}_{\text{Consumo Biológico}} \\ &\pm \underbrace{f^{Sed/Res}_{COP}(\mathbf{XX})}_{\text{Sedimentação/Resuspensão}}\end{aligned} \tag{7.69}$$

$$\begin{aligned}\frac{\partial COD}{\partial t} = &\underbrace{f^{Lise}_{COD}(\mathbf{XX})}_{\text{Lise Celular}} + \underbrace{f^{Exu}_{COD}(\mathbf{XX})}_{\text{Exudação}} + \underbrace{f^{Exc}_{COD}(\mathbf{XX})}_{\text{Excreção}} + \underbrace{f^{Mort}_{COD}(\mathbf{XX})}_{\text{Mortalidade}} + \underbrace{f^{Hid}_{COD}(\mathbf{XX})}_{\text{Hidrólise}} \pm \underbrace{f^{Fot}_{COD}(\mathbf{XX})}_{\text{Fotólise}} \\ &\pm \underbrace{f^{Dif}_{COD}(\mathbf{XX})}_{\text{Difusão}}\end{aligned} \tag{7.70}$$

$$\begin{aligned}\frac{\partial NH_4}{\partial t} = &- \underbrace{f^{CB}_{NH4}(Fit, Veg, T, NH4)}_{\text{Consumo Biológico}} + \underbrace{f^{Min}_{NH4}(T, OD, Det)}_{\text{Mineralização}} + \underbrace{f^{FS}_{NH4}(T, OD, W)}_{\text{Fluxo - Sedimento}} + \underbrace{f^{Nit}_{NH4}(T, OD, NH4)}_{\text{Nitrificação}} \\ &+ \underbrace{f^{Mort}_{NH4}(Fit, Veg, Zoo, Pei)}_{\text{Mortalidade}} + \underbrace{f^{Exc}_{NH4}(Fit, Veg, Zoo, Pei)}_{\text{Excreção}} + \underbrace{f^{Mort}_{NH4}(Pei, Aves)}_{\text{Egestão}}\end{aligned} \tag{7.71}$$

$$\begin{aligned}\frac{\partial NO_3}{\partial t} = &- \underbrace{f^{CB}_{NO3}(Fit, Veg, T, NO3)}_{\text{Consumo Biológico}} + \underbrace{f^{FS}_{NO3}(T, OD, W)}_{\text{Fluxo - Sedimento}} + \underbrace{f^{Nit}_{NO3}(T, OD, NO3)}_{\text{Nitrificação}} \\ &+ \underbrace{f^{Denit}_{NO3}(T, OD, Det, NO3)}_{\text{Denitrificação}}\end{aligned} \tag{7.72}$$

$$\frac{\partial P_{AIM}}{\partial t} = + \underbrace{f^{FS}_{PAIM}(T, OD, W)}_{\text{Fluxo - Sedimento}} + \underbrace{f^{Sor}_{PAIM}(MIno, OD, PO4, PAIM)}_{\text{Sorção}} \tag{7.73}$$

$$\begin{aligned}\frac{\partial PO_4}{\partial t} = &- \underbrace{f^{CB}_{PO4}(Fit, Veg, T, PO4)}_{\text{Consumo Biológico}} + \underbrace{f^{Min}_{PO4}(T, OD, Det)}_{\text{Mineralização}} + \underbrace{f^{FS}_{PO4}(T, OD, W)}_{\text{Fluxo - Sedimento}} + \underbrace{f^{Sor}_{PAIM}(MIno, OD, PO4, PAIM)}_{\text{Sorção}} \\ &+ \underbrace{f^{Mort}_{PO4}(Fit, Veg, Zoo, Pei)}_{\text{Mortalidade}} + \underbrace{f^{Exc}_{PO4}(Fit, Veg, Zoo, Pei)}_{\text{Excreção}} + \underbrace{f^{Mort}_{PO4}(Pei, Aves)}_{\text{Egestão}}\end{aligned} \tag{7.74}$$

$$\begin{aligned}\frac{\partial O_2}{\partial t} = &+ \underbrace{f^{Min}_{O2}(T, OD, Det)}_{\text{Mineralização}} + \underbrace{f^{Nit}_{O2}(T, OD, NH4)}_{\text{Nitrificação}} + \underbrace{f^{PP}_{O2}(Fit, Veg, T)}_{\text{Produção Primária}} + \underbrace{f^{Resp}_{O2}(Fit, Veg, T)}_{\text{Respiração}} \\ &+ \underbrace{f^{SOD}_{O2}(Min_{Sed}, Nit_{Sed})}_{\text{Demanda do Sedimento}} + \underbrace{f^{Reaer}_{O2}(T, W)}_{\text{Reaeração}}\end{aligned} \tag{7.75}$$

$$\frac{\partial CID}{\partial t} = \underbrace{f^{Resp}_{CID}(\mathbf{XX})}_{\text{Respiração}} + \underbrace{f^{Met}_{CID}(\mathbf{XX})}_{\text{Metanotrofia}} - \underbrace{f^{Fot}_{CID}(\mathbf{XX})}_{\text{Fotossítense}} \pm \underbrace{f^{Dif}_{CID}(\mathbf{XX})}_{\text{Difusão - Atmosfera}} \pm \underbrace{f^{Dif}_{CID}(\mathbf{XX})}_{\text{Difusão - Sedimento}} \tag{7.76}$$

$$\frac{\partial CH_4}{\partial t} = \underbrace{f^{Met}_{CH_4}(\mathbf{XX})}_{\text{Metanogênese}} - \underbrace{f^{Met}_{CH_4}(\mathbf{XX})}_{\text{Metanotrofia}} + \underbrace{f^{Diss}_{CH_4}(\mathbf{XX})}_{\text{Dissolução}} - \underbrace{f^{Dif}_{CH_4}(\mathbf{XX})}_{\text{Difusão - Atmosfera}} + \underbrace{f^{Dif}_{CH_4}(\mathbf{XX})}_{\text{Difusão - Sedimento}} \tag{7.77}$$

(7.78)

$$\frac{\partial Bac}{\partial t} = \underbrace{f_{Bac}^{Ass}(\mathbf{XX})}_{\text{Assimilação}} - \underbrace{f_{Bac}^{Resp}(\mathbf{XX})}_{\text{Respiração}} - \underbrace{f_{Bac}^{Mort}(\mathbf{XX})}_{\text{Mortalidade}} - \underbrace{f_{Bac}^{Pred}(\mathbf{XX})}_{\text{Predação}} - \underbrace{f_{Bac}^{Sed}(\mathbf{XX})}_{\text{Sedimentação}} \tag{7.79}$$

$$\frac{\partial Fit}{\partial t} = \underbrace{f_{Fit}^{PP}(Fit,T,N,P,I)}_{\text{Produção Primária}} + \underbrace{f_{Fit}^{Resp}(Fit,T)}_{\text{Respiração}} + \underbrace{f_{Fit}^{Mort}(Fit)}_{\text{Mortalidade}} + \underbrace{f_{Fit}^{FS}(T,OD,W)}_{\text{Fluxo-Sedimento}} + \underbrace{f_{Fit}^{Graz}(Fit,Zoo,T)}_{\textit{Grazing}} \tag{7.80}$$

$$\frac{\partial Veg}{\partial t} = \underbrace{f_{Veg}^{PP}(Veg,T,N,P,I)}_{\text{Produção Primária}} + \underbrace{f_{Veg}^{Resp}(Veg,T)}_{\text{Respiração}} + \underbrace{f_{Veg}^{Mort}(Veg)}_{\text{Mortalidade}} + \underbrace{f_{Veg}^{Graz}(Veg,Aves,T)}_{\textit{Grazing}} \tag{7.81}$$

$$\frac{\partial Zoo}{\partial t} = \underbrace{f_{Zoo}^{Graz}(Fit,Det,Zoo,T)}_{\textit{Grazing}} + \underbrace{f_{Zoo}^{Resp}(Zoo,T)}_{\text{Respiração}} + \underbrace{f_{Zoo}^{Mort}(Zoo)}_{\text{Mortalidade}} + \underbrace{f_{Zoo}^{Pre}(Zoo,Pei,T)}_{\text{Predação - Peixes}} \tag{7.82}$$

$$\frac{\partial Bent}{\partial t} = \underbrace{f_{Bent}^{Graz}(Fit_{Sed},Det_{Sed},Bent,T)}_{\textit{Grazing}} + \underbrace{f_{Bent}^{Resp}(Bent,T)}_{\text{Respiração}} + \underbrace{f_{Bent}^{Mort}(Bent)}_{\text{Mortalidade}} + \underbrace{f_{Bent}^{Pre}(Bent,Pei,T)}_{\text{Predação - Peixes}} \tag{7.83}$$

$$\frac{\partial Pei_{Jv}}{\partial t} = \underbrace{f_{Pei_{Jv}}^{Pred}(Zoo,Pei_{Jv},Pei_{Ad},T)}_{\text{Predação}} + \underbrace{f_{Pei_{Jv}}^{Rep}(Pei_{Ad})}_{\text{Reprodução}} + \underbrace{f_{Pei_{Jv}}^{Age}(Pei_{Jv})}_{\text{Envelhecimento}} + \underbrace{f_{Pei_{Jv}}^{Resp}(Pei_{Jv},T)}_{\text{Respiração}}$$
$$+ \underbrace{f_{Pei_{Jv}}^{Mort}(Pei_{Jv})}_{\text{Mortalidade}} \tag{7.84}$$

$$\frac{\partial Pei_{Ad}}{\partial t} = \underbrace{f_{Pei_{Ad}}^{Pred}(Zoo,Bent,Pei_{Jv},Pei_{Ad},T)}_{\text{Predação}} + \underbrace{f_{Pei_{Ad}}^{Rep}(Pei_{Ad})}_{\text{Reprodução}} + \underbrace{f_{Pei_{Ad}}^{Age}(Pei_{Jv})}_{\text{Envelhecimento}} + \underbrace{f_{Pei_{Ad}}^{Resp}(Pei_{Ad},T)}_{\text{Respiração}}$$
$$+ \underbrace{f_{Pei_{Ad}}^{Mort}(Pei_{Ad})}_{\text{Mortalidade}} \tag{7.85}$$

Equações onde alguns processos são indicados com **XX** estão em desenvolvimento. Devido a elevada complexidade dos processos envolvidos no metabolismo em ambientes aquáticos, serão apresentadas a seguir as principais equações que descrevem a dinâmica de temperatura na água e os fluxos metabólicos de produção e consumo de oxigênio. Mais informações sobre o equacionamento utilizado no módulo de limnologia do modelo IPH-ECO podem ser encontradas em Fragoso Jr. (2009) e a partir do material disponibilizado em www.ipheco.org.

7.5.2 Modelo de Temperatura da Água

O modelo de Temperatura da Água é baseado na dinâmica de calor descrita em Chapra (2008) para um reator concentrado. Na superfície da água, o fluxo de calor é descrito pelo balanço entre a Radiação de Onda Curta, Radiação de Onda Longa, Fluxo de Calor por Condução e Fluxo de Calor por Evaporação (Fig. 7.9).

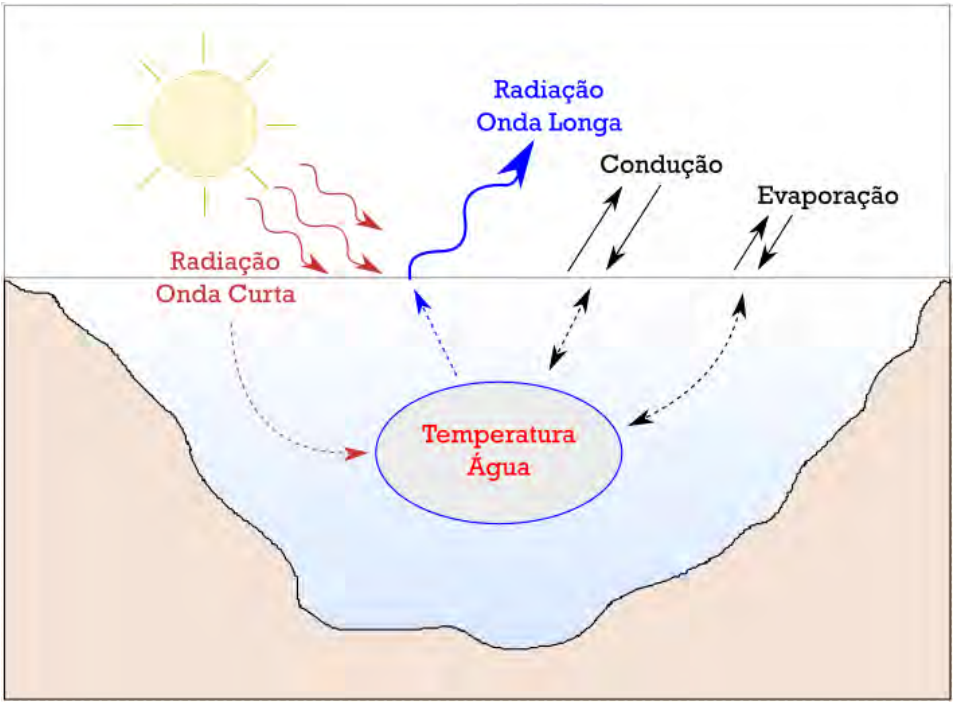

Figura 7.9: Principais parcelas do balanço de calor na superfície de corpos hídricos. Uma seta vermelha indica fluxo positivo, uma seta azul indica fluxo negativo, e as setas pretas indicam fluxos que variam entre positivo e negativo.

O balanço de calor na superfície da água é então descrito como:

$$H_s = Q_{sw} + Q_{lw} + Q_{cond} + Q_{evap} + Q_{transp} \tag{7.86}$$

onde H_s é o balanço de calor na superfície da água (W.m^{-2}); Q_{sw} é o fluxo de calor por radiação de onda curta (W.m^{-2}); Q_{lw} é o fluxo de calor por radiação de onda longa (W.m^{-2}); Q_{cond} é o fluxo de calor por condução na superfície (W.m^{-2}); Q_{evap} é o fluxo de calor por evaporação (W.m^{-2}); Q_{transp} é o transporte de calor por advecção, dado pela solução de equações de transporte. A relação entre fluxo de calor (ΔH_s) e alterações na temperatura da água (ΔT) é dado por:

$$\Delta H_s = \rho \cdot V \cdot c_p \cdot \Delta T \tag{7.87}$$

onde ρ é a densidade da água (Kg.m^{-3}); V é o volume da célula computacional (m^3); e c_p é o calor específico da água (J.Kg^{-1}.C^{-1}). O fluxo de calor na superfície é dado em unidades de área, logo a energia total transferida para uma célula computacional com área A_i num espaço de tempo Δt é dado por:

$$\Delta H_s = H_s \cdot A_i \cdot \Delta t \tag{7.88}$$

Desta forma, a alteração na temperatura da água pode ser descrita como:

$$\Delta T = \frac{H_s \cdot A_i \cdot \Delta t}{\rho \cdot V \cdot c_p} = \frac{H_s \cdot \Delta t}{\rho \cdot \Delta z \cdot c_p} \tag{7.89}$$

onde Δz é a espessura de água na célula computacional (m).

Radiação de Onda Curta

A radiação atmosférica de onda curta deve ser corrigida para levar em conta a parcela refletida pelo Albedo na superfície da água, sendo a quantidade que chega nas camadas do modelo dada por:

$$Q_{sw} = Q_{sw,atm} \cdot (1 - Alb) \tag{7.90}$$

Além disso, quando penetra nas camadas computacionais a intensidade da radiação de onda curta decai exponencialmente com a profundidade da água de acordo com a lei de Beer-Lambert:

$$Q_{sw}(z) = Q_{sw,atm} \cdot e^{-k_d \cdot z} \tag{7.91}$$

onde K_d é o coeficiente de extinção da luz (m^{-1}) e z é a profundidade de água medida a partir da superfície.

Radiação de Onda Longa

A radiação de onda longa é composta por duas componentes principais, a radiação a partir da água e a radiação a partir da atmosfera. A radiação atmosférica de onda longa é estimada a a partir da temperatura (T_{ar}) e umidade do ar (U_{ar}):

$$Q_{lw,atm} = -\sigma \cdot (T_{ar} - 273)^4 \cdot (A + 0.031\sqrt{e_{ar}}) \cdot (1 - Alb) \tag{7.92}$$

onde σ é a constante de Stefan-Boltzmann (5.669 W.m^{-2}.K^{-4}); A é um coeficiente calibrável (variando entre 0.5 e 0.7); e_{ar} é a pressão de vapor atmosférica (mmHg) que pode ser computada em função da umidade do ar e da pressão de vapor de saturação da água. A radiação da água de onda longa pode ser calculada em função da temperatura da superfície da água (T_s):

$$Q_{lw,agua} = -\epsilon \cdot \sigma \cdot (T_s - 273)^4 \tag{7.93}$$

onde ϵ é a emissividade da água. Finalmente, o fluxo de calor devido a radiação de onda longa é calculado pela soma das componentes atmosférica e da água:

$$Q_{lw} = Q_{lw,atm} + Q_{lw.agua} \tag{7.94}$$

Fluxo de Calor por Condução

O fluxo de calor por condução depende da intensidade do vento e do gradiente de temperatura entre a superfície da água e o ar:

$$Q_{cond} = c_1 \cdot f(U) \cdot (T_s - T_{ar}) \tag{7.95}$$

onde c_1 é o coeficiente de Bowen (mmHg.C^{-1}) e f(U) é uma função de velocidade do vento que descreve o efeito da turbulência superficial no fluxo de condução.

Fluxo de Calor por Evaporação

O fluxo de calor por evaporação depende da temperatura do ar e da umidade relativa, sendo descrito como:

$$Q_{evap} = f(U) \cdot (e_{sat} - e_{ar}) \tag{7.96}$$

onde e_{sat} é a pressão de vapor de saturação da água (mmHg).

7.5.3 Processos Metabólicos de Produção e Consumo

Os fluxos de GPP são compostos pela produção primária de diferentes grupos, a saber: Fitoplâncton, Macrófitas Aquáticas e Perifíton. O fluxo de produção primária do Fitoplâncton é descrito utilizando a seguinte equação:

$$Fito_{PP} = PP_{max} \cdot Fp \cdot f(I) \cdot f(T_{agua}) \cdot f(Nut) \cdot Biomass \tag{7.97}$$

onde PP_{max} é a taxa máxima de produção do Fitoplâncton; Fp é o fotoperíodo em h/24 hrs; $f(I)$, $f(T_{agua})$ e $f(Nut)$ são funções de limitação devido a iluminação, temperatura da água e nutrientes, respectivamente; e $Biomass$ é a biomassa de fitoplâncton. A função de limitação pela luz é computada a partir da Equação de Lehman:

$$f(I) = \frac{1}{C_{ext} \cdot H} \cdot \log\left(\frac{1 + \frac{LPAR0}{K_e}}{1 + \frac{LPARB}{K_e}}\right) \tag{7.98}$$

onde C_{ext} é o coeficiente de extinção da luz; H é a profundidade total de água; $LPAR0$ e $LPARB$ fazem referência a intensidade de luz no topo e no fundo da coluna d'água, respectivamente; e K_e é uma constante de meia saturação da intensidade da luz para o fitoplâncton. A função de limitação a pela temperatura da água é descrita como:

$$f(T_{agua}) = \exp\left(\frac{-0.5}{\sigma^2} \cdot \left((T_{agua} - T_{opt})^2 - (T_{ref} - T_{opt})^2\right)\right) \tag{7.99}$$

onde σ é um parâmetro descritivo da curvatura de Gauss utilizada para descrever a limitação por luz; T_{opt} é a temperatura ótima de crescimento do fitoplâncton; e T_{ref} é uma temperatura de referência. A limitação por nutrientes é descrita pela Equação de Droop na seguinte forma:

$$f(Nut) = \left(1 - \frac{NutMin}{rNutD}\right) \cdot \frac{NutMax}{NutMax - NutMin} \tag{7.100}$$

onde $NutMin$ e $NutMax$ são os conteúdos máximos de um determinado nutriente no fitoplâncton e $rNutD$ é a razão de composição desse nutriente com relação ao peso seco do fitoplâncton.

A produção primária das algas aderidas (perifíton) é modelada de maneira similar a utilizada para o fitoplâncton (Eq. 7.97), exceto na função de limitação de luz. Neste caso, a função não é integrada na vertical e apenas o valor da intensidade de luz no fundo da coluna d'água é utilizado.

A produção primária das Macrófitas Aquáticas também é calculada de maneira similar ao apresentado na Equação 7.97. Para o caso das Macrófitas Aquáticas, a limitação por luz é calculada levando em conta uma integração apenas na altura que a macrófita pode atingir, diferente do fitoplâncton onde toda a profundidade da coluna d'água é levada em conta. As macrófitas terão uma assimilação de nutrientes sendo realizada pelas raízes e pelo tronco. Isto deve ser levado em conta no cálculo da limitação por nutrientes (Eq. 7.100) sendo o valor computado ponderado pela biomassa do tronco e da raiz, respectivamente.

A respiração é calculada de maneira similar para todos os grupos simulados por meio seguinte relação:

$$R_e = K_r \cdot f(T_a) \cdot Biomass \tag{7.101}$$

onde K_r é uma taxa de respiração específica; $Biomass$ é a biomassa do grupo simulado (e.g., Fitoplâncton, Peixes, Zooplâncton); e $f(T_a)$ é uma função de correção para a temperatura que depende do grupo simulado.

Os processos microbianos de consumo de oxigênio (i.e., mineralização e nitrificação) são modelados levando em conta concentrações na coluna d'água e na camada de sedimento. O fluxo de mineralização na água e no sedimento é calculado da seguinte maneira:

$$Min_{Agua/Sed} = K_{min,Agua/Sed} \cdot \theta^{T_{agua}-20} \cdot [Det_{Agua/Sed}] \tag{7.102}$$

onde Min é o fluxo de mineralização; $K_{min,Agua/Sed}$ é uma taxa constante de mineralização; θ é um coeficiente para descrever o efeito da temperatura na mineralização; e $[Det_{Agua/Sed}]$ é a concentração de detritos na água ou no sedimento. O consumo de oxigênio durante o processo de mineralização é corrigido para levar em conta a concentração de oxigênio dissolvido disponível. O fluxo de oxigênio para

mineralização na coluna d'água é então descrito como:

$$O2_{Min,Agua} = Min_{Agua} \cdot PMO2\_C \cdot fCPS \cdot CorO2_{Agua} \tag{7.103}$$

onde $PMO2\_C$ é a razão entre os pesos moleculares de Oxigênio e Carbono ($\approx$ 2.667); $fCPS$ é a fração de Carbono no peso seco da matéria orgânica degradável ($= 0.4$); e $CorO2_{Agua}$ é uma correção da taxa de consumo levando em conta a concentração de oxigênio disponível, descrita por uma relação de Michaelis-Menten da forma:

$$CorO2_{Agua} = \frac{O2_{Agua}}{K_{O2} + O2_{Agua}} \tag{7.104}$$

onde $O2_{Agua}$ é a concentração de oxigênio dissolvido disponível para mineralização e K_{O2} é uma constante de meia saturação do oxigênio.

No sedimento, o consumo de oxigênio para mineralização é computado levando em conta a espessura da camada aeróbia, calculada da seguinte maneira:

$$Sed_{Aer} = \frac{ProfO2Sed}{ProfSed} \tag{7.105}$$

onde $ProfSed$ é a profundidade máxima da camada de sedimentos (assumida como 10 cm) e $ProfO2Sed$ é a profundidade de penetração do oxigênio no sedimento, calculada utilizando a concentração de oxigênio na coluna d'água, a taxa de difusão na interface água-sedimento e a demanda de oxigênio no sedimento:

$$ProfO2Sed = \sqrt{2 \cdot O2_{Agua} \cdot \frac{Dif_{O2}}{DOS}} \tag{7.106}$$

onde Dif_{O2} é o coeficiente de difusão de oxigênio na interface água-sedimento, que depende da difusividade molecular do oxigênio, da temperatura da água, da porosidade do sedimento e da turbidez; e DOS é a demanda de oxigênio no sedimento, calculada levando em conta os processos de mineralização e nitrificação no sedimento. Finalmente, o fluxo de mineralização no sedimento é computado como:

$$O2_{Min,Sed} = Min_{Sed} \cdot PMO2\_C \cdot rC - PS \cdot Sed_{Aer} \cdot (1 - fRefr) \tag{7.107}$$

onde rC_PS é quantidade de Carbono existente no Peso Seco e $fRefr$ é a fração refratária da concentração de Detritos no sedimento.

O fluxo de nitrificação na coluna d'água pode ser descrito como:

$$Nitr_{Agua} = K_{nit,Agua} \cdot \theta^{T_{agua}-20} \cdot CorO2_{Agua} \cdot [NH4_{Agua}] \tag{7.108}$$

onde $K_{nit,Agua}$ é uma taxa constante de nitrificação na coluna d'água; $\theta^{T_{agua}-20}$ é uma correção para a temperatura da água; $CorO2_{Agua}$ é uma correção pela

concentração de oxigênio dissolvido disponível para nitrificação; $[NH4_{Agua}]$ é a concentração de amônio na água. No sedimento uma equação similar é utilizada:

$$Nitr_{Sed} = K_{nit,Sed} \cdot \theta^{T_{agua}-20} \cdot Sed_{Aer} \cdot [NH4_{Sed}] \tag{7.109}$$

A partir do calculo dos fluxos de nitrificação na coluna d'água e no sedimento, é possível calcular a concentração de oxigênio necessária para nitrificação utilizando a seguinte equação:

$$O2_{Nitr,Agua/Sed} = rO2\_NH4 \cdot PMO2\_NH4 \cdot Nitr_{Agua/Sed} \tag{7.110}$$

onde $rO2\_NH4$ é a proporção de moléculas de O2 e NH4 utilizados no processo de nitrificação; $PMO2\_NH4$ é a razão do peso molecular de O2 por NH4; e $Nitr_{Agua/Sed}$ é o fluxo de nitrificação na coluna d'água ou na camada de sedimento.

Referências Bibliográficas

Antenucci, J. P., Tan, K. M., Eikaas, H. S., and Imberger, J. (2013). The importance of transport processes and spatial gradients on in situ estimates of lake metabolism. *Hydrobiologia*, 700:9–21.

Asaeda, T. & Van Bon, T. (1997). Modelling the effects of macrophytes on algal blooming in eutrophic shallow lakes. *Ecological Modelling*, 104:261–287.

Barth, T. J. & Jespersen, D. C. (1989). The design and application of upwind schemes on unstructured meshes. *27th Aerospace Science Meeting, AIAA*, pages 1–12.

Batt, R. D. & Carpenter, S. R. (2012). Free-water lake metabolism: addressing noisy time series with a kalman filter. *Limnology and Oceanography: Methods*, 10:20–30.

Boulion, V. V. & Hakanson, L. (2003). A new general dynamic model to predict biomass and production of bacterioplankton in lakes. *Ecological Modelling*, 160:91–114.

Brighenti, L. S., Staehr, P. A., Gagliardi, L. M., Brandão, L. P. M., Elias, E. C., Mello, N. A. S. T., Barbosa, F. A. R., and Bezerra-Neto, J. F. (2015). Seasonal changes in metabolic rates of two tropical lakes in the Atlantic forest of Brazil. *Ecosystems*, 18:589–604.

Brugnano, L. & Casulli, V. (2008). Iterative solution of piecewise linear systems. *SIAM Journal on Scientific Computing*, 30(1):463–472.

Brugnano, L. & Casulli, V. (2009). Iterative solution of piecewise linear systems and applications to flows in porous media. *SIAM Journal on Scientific Computing*, 31(3):1858–1873.

Casulli, V. (1990). Semi-implicit finite difference methods for the two-dimensional shallow water equations. *Journal of Computational Physics*, 84:56–74.

Casulli, V. (2009). A high-resolution wetting and drying algorithm for free-surface hydrodynamics. *International Journal for Numerical Methods in Fluids*, 60:391–408.

Casulli, V. & Cattani, E. (1994). Stability, accuracy and efficiency of a semi-implicit method for three-dimensional shallow water flow. *Computers & Mathematics with Applications*, 27(4):99–112.

Casulli, V. & Cheng, R. T. (1992). Semi-implicit finite difference methods for three-dimensional shallow water flow. *International Journal for Numerical Methods in Fluids*, 15:629–648.

Casulli, V. & Walters, R. A. (2000). An unstructured grid, three-dimensional model based on the shallow water equations. *International Journal for Numerical Methods in Fluids*, 32:331–348.

Casulli, V. & Zanolli, P. (2005). High resolution methods for multidimensional advection–diffusion problems in free-surface hydrodynamics. *Ocean Modelling*, 10:137–151.

Chapra, S. C. (2008). *Surface Water-Quality Modeling*. Waveland Press, Inc.

Chen, C., Liu, H., and Beardsley, R. (2003). An unstructured grid, finitevolume, three-dimensional, primitive equations ocean model: application to coastal ocean and estuaries. *Journal of Atmospheric and Oceanic Technology*, 20:159–186.

Cheng, R. T., Casulli, V., and Gartner, J. W. (1993). Tidal, Residual, Intertidal Mudflat (trim) model and its applications to San Francisco Bay, california. *Estuarine, Coastal and Shelf Science*, 36:235–280.

Cheng, R. T., Casulli, V., and Milford, S. N. (1984). Eulerian-Lagrangian solution of the convection-dispersion equation in natural coordinates. *Water Resources Research*, 20:944–952.

Cole, J., Prairie, Y., Caraco, N., McDowell, W., Tranvik, T., Striegl, R., Duarte, C., Kortelainen, P., Downing, J., Middelburg, J., and Melack, J. (2007). Plumbing the global carbon cycle: Integrating inland waters into the terrestrial carbon budget. *Ecosystems*, 10:171–184.

Cole, J. J. & Caraco, N. F. (1998). Atmospheric exchange of carbon dioxide in a low-wind oligotrophic lake measured by the addition of sf_6. *Limnology and Oceanography*, 43(4):647–656.

Cole, J. J., Pace, M. L., Carpenter, S. R., and Kitchell, J. F. (2000). Persistence of net heterotrophy in lakes during nutrient addition and food web manipulations. *Limnology and Oceanography*, 45(8):1718–1730.

Cole, T. & Buchak, E. (1995). *CE-QUAL-W2: A Numerical Two-Dimensional, Laterally Averaged, Hydrodynamic and Water Quality Model, Version 2.0 - User Manual*.

Coloso, J. J., Cole, J. J., and Pace, M. L. (2011). Short-term variation in thermal stratification complicates estimation of lake metabolism. *Aquatic Sciences*, 73:305–315.

Cremona, F., Kõiv, T., Kisand, V., Laas, A., Zingel, P., Agasild, H., Feldmann, T. o., Jarvalt, A., Nõges, P., and Nõges, T. (2014). From bacteria to piscivorous fish: Estimates of whole-lake and component-specific metabolism with an ecosystem approach. *PLoS ONE*, 9(7):e101845.

Devlin, S. P., Zanden, M. J. V., and Vadeboncoeur, Y. (2016). Littoral-benthic primary production estimates: Sensitivity to simplifications with respect to periphyton productivity and basin morphometry. *Limnology and Oceanography: Methods*, 14:138–149.

Dumbser, M., Kaser, M., and Toro, E. F. (2007). An arbitrary high-order discontinuous galerkin method for elastic waves on unstructured meshes – v. local time stepping and p-adaptivity. *Geophysical Journal International*, 171:695–717.

Fragoso Jr., C., Motta-Marques, D., and Ferreira, T. (2009). *Modelagem Ecológica em Ecossistemas Aquáticos*. Oficina de Textos, 1th edition.

Fragoso Jr., C. R. (2009). *Modelagem tridimensional da estrutura trófica em ecossistemas aquáticos continentais rasos*. PhD thesis, Universidade Federal do Rio Grande do Sul.

Fragoso Jr, C. R., Janse, J. H., van Nes, E. H., and Motta-Marques, D. (2009). IPH-TRIM3D-PCLake: A three-dimensional complex dynamic model for subtropical aquatic ecosystems. *Ecological Modelling & Software*, 24:1347–1348.

Fragoso Jr, C. R., Motta-Marques, D., Ferreira, T. F., Janse, J. H., and van Nes, E. H. (2011). Potential effects of climate change and eutrophication on a large subtropical shallow lake. *Ecological Modelling & Software*, 26:1337–1348.

Fringer, O. B., Gerritsen, M., and Street, R. (2006). An unstructured-grid, finite-volume,nonhydrostatic, parallel coastal ocean simulator. *Ocean Modelling*, 14:139–173.

Gassner, G., Lörcher, F., and Munz, C.-D. (2008). A discontinuous Galerkin scheme based on a space-time expansion II. viscous flow equations in multi dimensions. *Journal of Scientific Computing*, 34:260–286.

Gazeau, F., Duarte, C., Gattuso, J.-P., Barron, C., Navarro, N., Ruiz, S., Prairie, Y., Calleja, M., Delille, B., Frankignoulle, M., and Borges, A. (2005). Whole-system metabolism and CO_2 fluxes in a Mediterranean Bay dominated by seagrass beds (Palma Bay, NW Mediterranean). *Biogeosciences*, 2:43–60.

Godunov, S. (1959). A finite difference method for the computation of discontinuous solutions of the equations of fluid dynamics. *Matematicheskii Sbornik*, 47(3):271.

Gross, E. S., Bonaventura, L., and Rosatti, G. (2002). Consistency with continuity in conservative advection schemes for free-surface models. *International Journal for Numerical Methods in Fluids*, 38:307–327.

Gross, E. S., Casulli, V., Bonaventura, L., and Koseff, J. R. (1998). A semi-implicit method for vertical transport in multidimensional models. *International Journal for Numerical Methods in Fluids*, 28:157–186.

Ham, D. A., Pietrzak, J., and Stelling, G. S. (2005). A scalable unstrucutred grid 3-dimensional finite volume model for the shallow water equations. *Ocean Modelling*, 10:153–169.

Hamilton, D. P. & Schladow, S. G. (1997). Prediction of water quality in lakes and reservoirs. Part I - Model description. *Ecological Modelling*, 96:91–110.

Hanson, P. C., Bade, D. L., Carpenter, S. R., and Kratz, T. K. (2003). Lake metabolism: Relationships with dissolved organic carbon and phosphorus. *Ecological Modelling*, 48(3):1112–1119.

Hanson, P. C., Carpenter, S. R., Armstrong, D. E., Stanley, E. H., and Kratz, T. K. (2006). Lake dissolved inorganic carbon and dissolved oxygen: changing drivers from days to decades. *Ecological Monographs*, 76(3):343–363.

Hanson, P. C., Carpenter, S. R., Kimura, N., Wu, C., Cornelius, S. P., and Kratz, T. K. (2008). Evaluation of metabolism models for free-water dissolved oxygen methods in lakes. *Limnology and Oceanography:Methods*, 6:454–465.

Hipsey, M. R., Antenucci, J. P., and Brookes, J. D. (2008). A generic, process-based model of microbial pollution in aquatic systems. *Water Resources Research*, 44:W07408.

Hodges, B. R., Imberger, J., Saggio, A., and Winters, K. (2000). Modeling basin-scale internal waves in a stratified lake. *Limnology and Oceanography*, 45(7):1603–1620.

Holtgrieve, G. W., Schindler, D. E., Branch, T. A., and A'mar, Z. T. (2010). Simultaneous quantification of aquatic ecosystem metabolism and reaeration using a bayesian statistical model of oxygen dynamics. *Limnology and Oceanography*, 55(3):1047–1063.

Huebner, K. H., Dewhirst, D. L., Smith, D. E., and Byrom, T. G. (2011). *The Finite Element Method for Engineers*. Wiley & Sons, 4th edition.

Iskandarani, M., Haidvogel, D., and Levin, J. (2003). A three-dimensional spectral element model for the solution of the hydrostatic primitive equations. *Journal of Computational Physics*, 186:397–425.

Janse, J. H. (2005). *Model studies on the eutrophication of shallow lakes and ditches*. PhD thesis, Wageningen University.

Jorgensen, S. E. & Fath, B. D. (2011). *Fundamentals of Ecological Modelling*. Elsevier, 4th edition.

Karlsson, J., Berggren, M., Ask, J., Byström, P., Jonsson, A., Laudon, H., and Jansson, M. (2012). Terrestrial organic matter support of lake food webs: Evidence from lake metabolism and stable hydrogen isotope of consumers. *Limnology and Oceanography*, 57(4):1042–1048.

Kemp, W., Smith, E., Marvin-DiPasquale, M., and Boynton, W. (1997). Organic carbon balance and net ecosystem metabolism in Chesapeake Bay. *Marine Ecology Progress Series*, 150:229–248.

Kemp, W. & Testa, J. (2011). Metabolic balance between production and consumption. In Wolanski, E. and McLuski, D., editors, *Treatise on Estuarine and Coastal Science*, chapter 6. Elsevier.

Kluijver, A., Ning, J., Liu, Z., Jeppesen, E., Gulati, R., and Middelburg, J. (2015). Macrophytes and periphyton carbon subsidies to bacterioplankton and zooplankton in a shallow eutrophic lake in tropical China. *Limnology and Oceanography*, 60:375–385.

Laas, A., Nõges, P., Kõiv, T., and Nõges, T. (2012). High-frequency metabolism study in a large and shallow temperate lake reveals seasonal switching between net autotrophy and net heterotrophy. *Hydrobiologia*, 694:57–74.

Lauster, G. H., Hanson, P. C., and Kratz, T. K. (2006). Gross primary production and respiration differences among littoral and pelagic habitats in northern Wisconsin lakes. *Journal of Fisheries and Aquatic Sciences*, 63:1130–1141.

Liu, H., Benoit, G., Liu, T., Liu, Y., and Guo, H. (2015). An integrated system dynamics model development for managing lake water quality at the watershed scale. *Journal of Environmental Management*, 155:11–23.

Lörcher, F., Gassner, G., and Munz, C.-D. (2007). A discontinuous Galerkin scheme based on a space-time expansion. I. inviscid compressible flow in one space dimension. *Journal of Scientific Computing*, 32(2):175–199.

Lynch, D. & Werner, F. (1991). Three-dimensional hydrodynamics on finite elements. part ii: non-linear time-stepping model. *International Journal for Numerical Methods in Fluids*, 12:5077–533.

MacIntyre, S., Jonsson, A., Jasson, M., Aberg, J., Turney, D. E., and Miller, S. D. (2010). Buoyancy flux, turbulence, and the gas transfer coefficient in a stratified lake. *Geophysical Research Letters*, 37:L224604.

McCallister, S. L. & del Giorgio, P. A. (2008). Direct measurement of the δ^{13}C signature of carbon respired by bacteria in lakes: Linkage to potential carbon sources, ecosystems baseline metabolism, and CO_2 fluxes. *Limnology and Oceanography*, 53(4):1204–1216.

McNair, J. N., Gereaux, L. C., Weinke, A. D., Sesselmann, M. R., Kendall, S. T., and Biddanda, B. A. (2013). New methods for estimating components of lake metabolism based on free-water dissolved-oxygen dynamics. *Ecological Modelling*, 263:1130–1141.

McNair, J. N., Sesselmann, M. R., Kendall, S. T., Gereaux, L. C., Weinke, A. D., and Biddanda, B. A. (2015). Alternative approaches for estimating components of lake metabolism using the free-water dissolvedoxygen (fwdo) method. *Fundamental and Applied Limnology*, 186:21–44.

Obrador, B. & Petrus, J. L. (2013). Carbon and oxygen metabolism in a densely vegetated lagoon: implications of spatial heterogeneity. *Limnetica*, 32(2):321–336.

Obrador, B., Staehr, P. A., and Christensen, J. P. (2014). Vertical patterns of metabolism in three contrasting stratified lakes. *Limnology and Oceanography*, 59(4):1228–1240.

Odum, H. T. (1956). Primary production in flowing waters. *Limnology and Oceanography*, 1:103–119.

Park, R. A., Clough, J. S., and Wellman, M. C. (2008). Aquatox: Modelling environmental fate and ecological effects in aquatic ecosystems. *Ecological Modelling*, 213(1):1–15.

Read, J. S., Hamilton, D. P., Jones, I. D., Muraoka, K., Winslow, L. A., Kroiss, R., Wu, C. H., and Gaiser, E. (2011). Derivation of lake mixing and stratification indices from high-resolution lake buoy data. *Ecological Modelling & Software*, 26:1325–1336.

Rose, K. C., Winslow, L. A., Read, J. S., Read, E. K., Solomon, C. T., Adrian, R., and Hanson, P. C. (2014). Improving the precision of lake ecosystem metabolism estimates by identifying predictors of model uncertainty. *Limnology and Oceanography: Methods*, 12:303–312.

Rosman, P. C. (2001). Um sistema computacional de hidrodinâmica ambiental. In Silva, R. C. V., editor, *Métodos Numéricos em Recursos Hídricos - Volume 5*, chapter 1. ABRH - Associação Brasileira de Recursos Hídricos.

Sadro, S., Melack, J. M., and MacIntyre, S. (2011). Spatial and temporal variability in the ecosystem metabolism of a high-elevation lake: integrating benthic and pelagic habitats. *Ecosystems*, 14:1123–1140.

Sand-Jensen, K. & Staehr, P. A. (2007). Scaling of pelagic metabolism to size, trophy and forest cover in small Danish lakes. *Ecosystems*, 10:127–141.

Sand-Jensen, K. & Staehr, P. A. (2009). Net heterotrophy in small Danish lakes: a widespread feature over gradients in trophic status and land cover. *Ecosystems*, 12:336–348.

Shchepetkin, A. & McWilliams, J. (2005). The regional oceanic modeling system (ROMS): a split-explicit, free-surface, topography-following-coordinate, oceanic model. *Ocean Modelling*, 9:3447–404.

Silva, L. H., Huszar, V. L., Marinho, M. M., Rangel, L. M., Brasil, J., Domingues, C. D., Branco, C. C., and Roland, F. (2014). Drivers of phytoplankton, bacterioplankton, and zooplankton carbon biomass in tropical hydroelectric reservoirs. *Limnologica*, 48:1–10.

Smith, S. & Banke, E. (1975). Variation of the sea surface drag coefficient with wind speed. *Quarterly Journal of the Royal Meteorological Society*, 101:665–673.

Staehr, P. A., Baastrup-Spohr, L., Sand-Jensen, K., and Stedmon, C. (2012a). Lake metabolism scales with lake morphometry and catchment conditions. *Aquatic Sciences*, 74:155–169.

Staehr, P. A. & Sand-Jensen, K. (2007). Temporal dynamics and regulation of lake metabolism. *Limnology and Oceanography*, 52(1):108–120.

Staehr, P. A., Testa, J. M., Kemp, W. M., Cole, J. J., Sand-Jensen, K., and Smith, S. V. (2012b). The metabolism of aquatic ecosystems: history, applications, and future challenges. *Aquatic Sciences*, 74:15–29.

Taube, A., Dumbser, M., Munz, C., and Schneider, R. (2009). A high-order discontinuous Galerkin method with time-accurate local time stepping for the Maxwell equations. *International Journal Of Numerical Modelling: Electronic Networks, Devices And Fields*, 22:77–103.

Tedford, E. W., MacIntyre, S., Miller, S. D., and Czikowsky, M. J. (2014). Similarity scaling of turbulence in a temperate lake during fall cooling. *Journal of Geophysical Research: Oceans*, 119:4689–4713.

Tonetta, D., Staehr, P. A., Schmitt, R., and Petrucio, M. M. (2016). Physical conditions driving the spatial and temporal variability in aquatic metabolism of a subtropical coastal lake. *Limnologica*, 58:30–40.

Toro, E. (2009). *Riemann Solvers and Numerical Methods for Fluids*. Springer, 3th edition.

Trolle, D., Spigel, B., Hamilton, D. P., Norton, N., Sutherland, D., Plew, D., and Allan, M. G. (2014). Application of a three-dimensional water quality model as a decision support tool for the management of land-use changes in the catchment of an oligotrophic lake. *Environmental Management*, 54:479–493.

Vachon, D. & Prairie, Y. T. (2013). The ecosystem size and shape dependence of gas transfer velocity versus wind speed relationships in lakes. *Canadian Journal of Fisheries and Aquatic Sciences*, 70:1–8.

Vachon, D., Prairie, Y. T., and Cole, J. J. (2010). The relationship between near-surface turbulence and gas transfer velocity in freshwater systems and its implications for floating chamber measurements of gas exchange. *Limnology andd Oceanography*, 55(4):1723–1732.

van de Bogert, M. C., Bade, D. L., Carpenter, S. R., Cole, J. J., Pace, M. L., Hanson, P. C., and Langman, O. C. (2012). Spatial heterogeneity strongly affects estimates of ecosystem metabolism in two north temperate lakes. *Limnology and Oceanography*, 57(6):1689–1700.

van de Bogert, M. C., Carpenter, S. R., Cole, J. J., and Pace, M. L. (2007). Assessing pelagic and benthic metabolism using free water measurements. *Limnology and Oceanography:Methods*, 5:145–155.

van Leer, B. (1974). Towards the ultimate conservative difference scheme II: Monotonicity and conservation combined in a second order scheme. *Journal of Computational Physics*, 14:361–370.

van Leer, B. (1979). Towards the ultimate conservative difference scheme V: A second order sequel to Godunov's method. *Journal of Computational Physics*, 32:101–136.

Walters, R., Hanert, E., Pietrzak, J., and Le Roux, D. (2009). Comparison of unstructured, staggered grid methods for the shallow water equations. *Ocean Modelling*, 28:106–117.

Wang, B., Zhao, G., and Fringer, O. (2011). Reconstruction of vector fields for semi-lagrangian advection on unstructured, staggered grids. *Ocean Modelling*, 40:52–71.

Wang, C.-F., Wang, H. V., and Kuo, A. Y. (2008). Mass conservative transport scheme for the application of the elcirc model to water quality computation. *Journal of Hydraulic Engineering*, 134:1166–1171.

Wanninkhof, R. (1992). Relationship between gas exchange and wind speed over the ocean. *Journal of Geophysical Research*, 97:7373–7382.

Winslow, L. A., Zwart, J. A., Batt, R. D., Dugan, H. A., Woolway, R. I., Corman, J. R., Hanson, P. C., and Read, J. S. (2016). Multiyear measurements of ebullitive methane flux from three subarctic lakes. *Inland Waters*, 6:622–636.

Zhang, Y. & Baptista, A. M. (2008). SELFE: A semi-implicit Eulerian-Lagragian finite-element model for cross-scale ocean circulation. *Ocean Modelling*, 21:71–96.

Zhang, Y., Baptista, A. M., and Meyers III, E. P. (2004). A cross-scale model for 3d baroclinic circulation in estuary-plume-shelf systems: I. Formulation and skill assessment. *Continental Shelf Research*, 24:2187–2214.

Zimmer, K. D., Hobbs, W. O., Domine, L. M., Herwig, B. R., Hanson, M. A., and Cotner, J. B. (2016). Uniform carbon fluxes in shallow lakes in alternative stable isotopes. *Limnology and Oceanography*, 61:330–340.